Synthesis and characterization of Pb(V1-xMx)O3 compounds

Alexandru Okos

UNIVERSITÉ DE GRENOBLE

THÈSE

Pour obtenir le grade de

DOCTEUR DE L'UNIVERSITÉ DE GRENOBLE

préparée dans le cadre d'une cotutelle entre
l'*Université de Grenoble* et
l'*Université Babeş-Bolyai*

Spécialité : **PHYSIQUE DES MATERIAUX**

Arrêté ministériel : le 6 janvier 2005 -7 août 2006

Présentée par **Alexandru OKOS**

Thèse dirigée par **Pierre BORDET** et **Aurel POP**
codirigée par **Claire COLIN**

préparée au sein des **Laboratoires :**
Institut Néel, CNRS, SPMCE, MCMF
Laboratoires de l'Université Babeş-Bolyai

dans **les Écoles Doctorales :**
Ecole Doctorale de Physique, Grenoble
Ecole Doctorale de Physique, Cluj-Napoca

Synthèse et Caractérisation de composés de type $Pb(V_{1-x}M_x)O_3$, (M = Ti, Fe)

Thèse soutenue publiquement le **16.01.2014**,
devant le jury composé de :

Mr. Romulus TETEAN
Président du jury, Professeur - Université Babes-Bolyai, Cluj-Napoca
Mr. Mădălin BUNOIU
Rapporteur du jury, Professeur - Université de L'ouest, Timisoara
Mme. Christine MARTIN
Rapporteur du jury, Directrice de Recherche - Université de Caen
Mr. Pierre BORDET
Membre du jury, Directeur de Recherche - CNRS Grenoble
Mme. Claire COLIN
Membre du jury, Maitre de Conferences - CNRS Grenoble
Mr. Olivier ISNARD
Membre du jury, Professeur - CNRS Grenoble
Mr. Aurel POP
Membre du jury, Professeur - Université Babes-Bolyai, Cluj-Napoca
Mr. Viorel POP
Membre du jury, Professeur - Université Babes-Bolyai, Cluj-Napoca

Université Joseph Fourier / Université Pierre Mendès France /
Université Stendhal / Université de Savoie / Grenoble INP

Abstract

Recently, multiferroic compounds attracted huge interest due to their unique properties which make such materials very interesting for real life applications, from capacitors, sensors and actuators to computer memory devices. $PbVO_3$ is a very promising material. It is isostructural with $PbTiO_3$ which is a very well known and studied ferroelectric material and it also contains vanadium ions which carry a 1/2 spin so magnetic ordering can be expected. However, no sign of magnetic ordering could be observed which raises the following questions:

1) why is $PbVO_3$ not magnetic? and
2) could it be tuned so that it becomes magnetic?

The objective of the project was to provide some answer to the above questions by studying the synthesis and investigating of the physical properties of the $Pb(V,M)O_3$, M = Ti, Fe potentially multiferroic oxides.

We prepared two kinds of samples, polycrystalline and single crystals. The polycrystalline batch is larger containing two series, the titanium series and the iron series with the chemical compositions as follows.

$PbV_{1-x}Ti_xO_3$ with x = 0, 0.1, 0.25, 0.5 0.6, 0.75, 0.8, 1

$PbV_{1-x}Fe_xO_3$ with x = 0.1, 0.25, 0.3, 0.4, 0.5, 0.55, 0.6 0.65, 0.75

Single crystals were prepared only in the form of clean $PbVO_3$ in which no substitution was attempted.

The structure and the physical properties of the samples were studied and an attempt was made to correlate the results and try to formulate a model which could explain the intriguing and often apparently contradicting behaviours of our compounds. The present work discusses the results obtained during the study and attempts to shed some light on the subject, without asserting that it reaches a final and definitive conclusion.

The work is structured on five chapters.

The first chapter reviews the fundamental concepts of the physics behind the multiferroic compounds, emphasizing the exotic properties / phenomena that are connected to our compounds. The first chapter also deals with the data already published in literature for $PbVO_3$ and some substitution compounds.

The second chapter describes the experimental methods and investigation techniques used during the study.

The third chapter presents the preparation methods, the high pressure - high temperature equipments employed and the reaction conditions required for the synthesis of $PbVO_3$ (and the substitution counterparts). The discussion continues with the first investigations and results which are concerned with phase purity.

The fourth chapter discusses with somewhat greater details the structural properties of the samples.

The fifth chapter deals with the magnetic and dielectric properties of the potentially multiferroic $Pb(V_{1-x}M_x)O_3$ compounds.

Since the physical properties of these materials are strongly dependent on the structure of the samples, the chapters intertwine at times, in each chapter results from the other chapters being mentioned and some redundancy is thus unavoidable. The measurements of X-Ray absorption form the core of the work as these measurements confirmed the oxidation states of the B site cations (where the substitution takes places). From these observations almost the entire set of structural and physical properties can be explained. The substitution with titanium is thus shown to be isovalent which leads to the formation of the $PbVO_3$-$PbTiO_3$ solid solution and the dilution of the magnetic lattice of $PbVO_3$. On the other hand the substitution with iron is not isovalent and therefore the solid solution $PbVO_3$-$PbFeO_3$ (the latter compound was never reported) stops at $x = 0.5$. The disorder caused by the iron substitution leads to the formation of spin glass like magnetic states and ferroelectric relaxor states on these compounds.

As mentioned already, this is far from the final conclusion of the research on $PbVO_3$. New ideas and new questions develop as the research progresses so this work only provides (maybe) a starting point for future explorations.

Résumé

Les dernières années les composés multiferroïques ont attiré un grand intérêt en raison de leurs propriétés uniques qui rendent ces matériaux très intéressants pour des applications réelles, par exemple des condensateurs, des détecteurs et des actuateurs ou des dispositifs de mémoire d'ordinateur. Dans la recherche de multiferroïques, $PbVO_3$ est un matériel très prometteur. $PbVO_3$ est isostructural avec $PbTiO_3$ qui est un matériel ferroélectrique très bien connu et étudié et il contient également des ions de vanadium qui portent un spin 1/2, donc, un certain type d'ordre magnétique peut être attendu. Cependant, aucun ordre magnétique n'a pu être observé ce qui pose les deux questions suivantes:

1) pourquoi $PbVO_3$ n'est pas magnétique ?
2) est-ce que $PbVO_3$ peut être réglé de sorte qu'il devienne magnétique ?

L'objectif du projet était de fournir une réponse aux questions ci-dessus par l'étude de la synthèse et des propriétés physiques des oxydes potentiellement multiferroïques de type $Pb(V_{1-x}M_x)O_3$ où M = Ti, Fe.

Nous avons préparé deux types d'échantillons, échantillons polycristallins et monocristaux. Le batch polycristallin est plus grand et il contient deux séries: la série de titane et de la série de fer avec les compositions chimiques suivantes:

$PbV_{1-x}Ti_xO_3$ où x = 0, 0.1, 0.25, 0.5, 0.6, 0.75, 0.8, 1

$PbV_{1-x}Fe_xO_3$ où x = 0.1, 0.25, 0.3, 0.4, 0.5, 0.55, 0.6 0.65, 0.75.

Des monocristaux ont été préparés uniquement sous la forme de $PbVO_3$ dans lequel aucune substitution n'a été essayée.

La structure et les propriétés physiques des échantillons ont été étudiés et on a tenté de corréler les résultats et de formuler un modèle qui pourrait expliquer les comportements fascinants et souvent apparemment contradictoires de nos composés.

Cette thèse parle des résultats obtenus au cours de l'étude et tente de clarifier certaines questions au sujet de $PbVO_3$, sans affirmer qu'elle arrive à une conclusion finale et définitive.

Le document est structuré en cinq chapitres. Le premier chapitre passe en revue les concepts fondamentaux de la physique de derrière les composés multiferroïques, mettant l'accent sur les propriétés / phénomènes qui sont connectés à nos composés.

Le premier chapitre s'occupe également des données déjà publiées dans la littérature pour $PbVO_3$ et les composés substitués.

Le deuxième chapitre décrit les méthodes expérimentales et les techniques de mesure utilisées au cours de l'étude.

Le troisième chapitre présente les méthodes de préparation, les équipements de haute pression - hautes températures employées et les conditions de réaction nécessaires pour la synthèse de $PbVO_3$ (et ses homologues substitués). La discussion est continuée avec les premières investigations et les résultats qui traitent de la pureté de phase.

Le quatrième chapitre traite avec plus de détails les propriétés structurales des échantillons et le cinquième chapitre traite les propriétés magnétiques et diélectriques des composés potentiellement multiferroïques, $Pb(V_{1-x}M_x)O_3$.

Comme les propriétés physiques de ces matériaux sont fortement dépendantes de la structure des échantillons, les chapitres s'entrecroisent parfois, dans chaque chapitre, des résultats des autres chapitres sont mentionnés et une certaine redondance est donc inévitable. Les mesures d'absorption des rayons X forment le noyau de l'étude parce que ces mesures ont confirmé les états d'oxydation des cations du site B (où la substitution prend place). A partir de ces observations, presque toutes les propriétés structurales et physiques peuvent être expliquées. La substitution avec du titane, est donc révélée isovalente ce qui conduit à la formation de la solution solide $PbVO_3$-$PbTiO_3$ et à la dilution du réseau magnétique de $PbVO_3$. D'autre part, la substitution avec du fer n'est pas isovalente et donc la solution solide $PbVO_3$-$PbFeO_3$ (ce dernier composé n'a jamais été signalé) s'arrête à $x = 0.5$. Le désordre introduit par la substitution avec du fer conduit à la formation d'un état magnétique similaire à un verre de spin et d'un comportement diélectrique typique pour un relaxeur ferroélectrique.

Comme déjà mentionné, cette étude est loin d'être la conclusion définitive de la recherche sur $PbVO_3$. De nouvelles idées et de nouvelles questions se développent avec l'avancement de la recherche, donc ce travail fournit (peut-être) seulement un point de départ pour des explorations futures.

Table of contents

Chapter I. Multiferroic $PbVO_3$ perovskite

I.1. Multiferroic compounds, structure and properties

I.1.1. Introduction to multiferroics

A material is called functional if it presents a physical property that can be used in a real life application. The situation is much more interesting in the case of materials which present not just one, but several physical properties, exploitable at the same time in the same application or device. These are called multifunctional materials and their study attracted a lot of interest in the past few years first because of their wide range of possible applications.

Multiferroic compounds are multifunctional materials which contain simultaneously two or all three of the so called ferroic properties: ferromagnetism, ferroelectricity and/or ferroelasticity [1]. The "ferro" prefix comes from historical considerations and makes reference to iron which is a well known ferromagnetic material, that is to say it presents a spontaneous magnetization, M, which can be reversed with an external magnetic field. Similarly a ferroelectric material presents a spontaneous electric polarization, P, which can be switched by an external electric field and a ferroelastic material has a spontaneous deformation, e_{ij} which can be activated by an external mechanical stress. It should already be noted that the simultaneous presence of at least two ferroic properties is extremely rare. Therefore, the definition of multiferroic materials is extended to include antiferroic properties, namely antiferromangetism and antiferroelectricity [2]. With this change a material is by definition multiferroic if it presents two or more order parameters. We will be interested on the other hand only in materials which present magnetic and electrical ordering.

Then the question of the coupling of the order parameters comes into view. If such couplings between the magnetic and electric properties of a multiferroic material exist, that is to say if the magnetization can be controlled with an electric field and the

opposite, the polarization can be controlled with a magnetic field, that material is called a magneto-electric material [3].

The names awarded to these categories of materials can appear to be misleading but a representation with diagrams of the classes of materials discussed above helps to provide a clear image (figure 1.1).

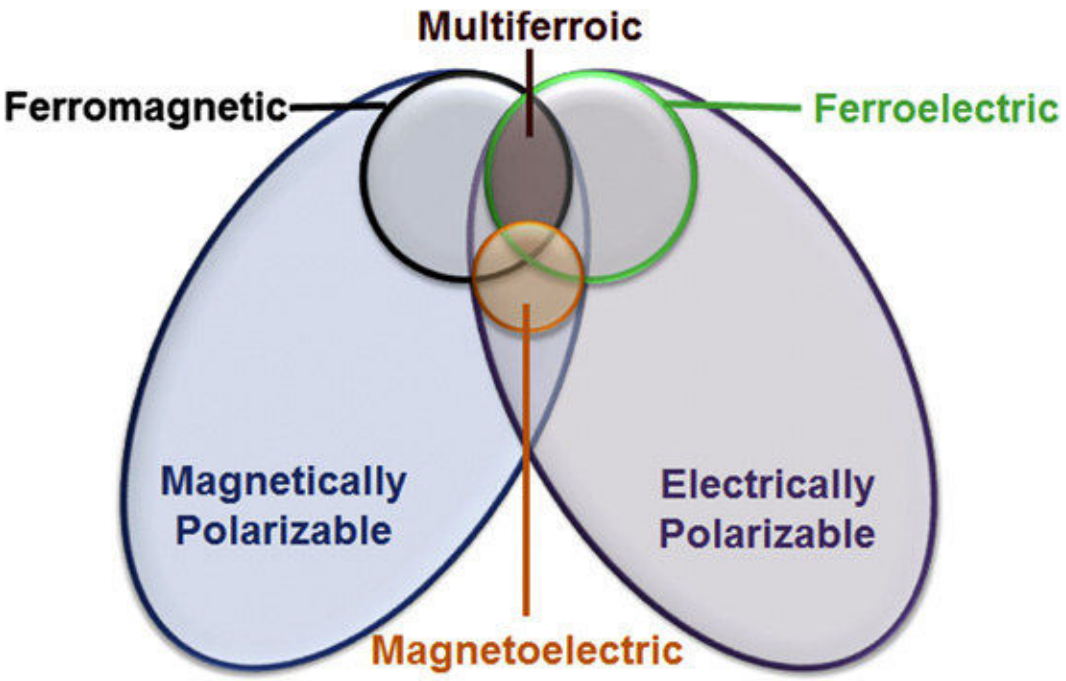

Fig. 1.1. Classification of multiferroic and magneto-electric materials [4].

There are two types of multiferroic materials, classified by their construction:

a) artificial multiferroics (or extrinsic multiferroics) are thin film hetero-structures composed of alternating layers of ferroelectric and ferromagnetic materials
b) single phase multiferroics (or intrinsic multiferroics) are materials in which the ferroelectric and ferromagnetic properties exist in the same phase [1]. These materials can be thin films or bulk samples but either way their synthesis implies the discovery of new chemical formulas.

The object of our study, $PbVO_3$, is potentially an intrinsic multiferroic.

There are two types of coupling between the ferroic properties in these materials.

The first type is observed for materials in which the ferroelectric and the magnetic orderings are associated to different sublattices. The typical example of a

material that displays this behaviour is $BiFeO_3$. For this material The Bi^{3+} sublattice is responsible for the onset of ferroelectricity while the Fe^{3+} sublattice generates weak magnetism at RT [5, 6].

The second type of coupling appears in materials for which the ferroelectric ordering is induced indirectly by a charge ordering or a magnetic ordering. This coupling is expected to be stronger because these electric dipoles can be directly switched by applying a magnetic field. The control of electric properties by a magnetic field has in fact been evidenced in system presenting frustrated magnetism. Unfortunately the opposite is not true as an electric field does not cause a great modification of magnetic properties [1].

Multiferroic materials, particularly intrinsic multiferroics, are very rare because the properties they contain exclude each other. When electrical and magnetic ordering mechanisms are present it is not unusual for the system to display complex magnetic (or electrical) structures. The simple structures, the complex structures and the requirements for a multiferroic material are discussed below.

I.1.2. Magnetic structures / behaviours

a) Ferromagnetism

The magnetism of matter is generated by the magnetic properties of the constituting atoms of the considered sample and this in turns is by the electronic configuration of the atoms. Without going into the details of the magnetism of the atom and the magnetism of the matter we will only review the fundamental mechanism of the magnetic phenomena.

Electrons are arranged in electronic shells called orbitals of different energies according to the Pauli Exclusion Principle and Hund's Rules. Unpaired electrons, if they exist, will generate a magnetic moment related to their spin.

Different types of magnetic states can exist, according to the presence or absence of magnetic moments and the presence or absence of interactions between these magnetic moments. The principal ones are: diamagnetism, paramagnetism, ferromagnetism, atiferromagnetism and ferrimagnetism.

A ferromagnetic material has a phase transition from a high temperature paramagnetic phase with no net macroscopic magnetic moment to a low temperature phase that has a spontaneous magnetization even in the absence of an external magnetic field. The transition temperature is called the Curie temperature. The temperature dependence of the magnetization in the region above the transition temperature is described by the Curie-Weiss law which states that

$$\chi = \chi_0 + c/(T-\theta),$$

where χ is the magnetic susceptibility and represents essentially the magnetic response function of the system to an applied magnetic field ($M = \chi * H$), χ_0 is a diamagnetic component.

b) Complex magnetic structures

Paramagnetism, ferromagnetism, antiferromagnetism, ferrimagnetism (and diamagnetism) are the basis of all magnetic structures. Other exotic structures like canted antiferromagnetism or spin glass exist but these are only variations of the standard ones.

Antiferromagnetism can sometimes generate frustrated lattices. Long range ordered magnetic systems display symmetries that simplify the analysis of their properties. Frustrated systems are intrinsically disordered and lack these symmetry properties, therefore complicating the interpretation of results obtained for such systems. This may lead to new types of broken symmetry and the breakdown of the thermodynamic limit of certain quantities and the emergence of new phenomena, for example unconventional temperature dependence of certain parameters [7].

A frustrated lattice is formed when the interactions of the magnetic moments are conflicting and there is no spin configuration that can simultaneously satisfy all the couplings [7]. For example this happens when the next nearest neighbour magnetic interaction has about the same strength as the nearest neighbour interaction (J_1/J_2 = 0.5) [1-3]. The simplest example of a frustrated magnetic structure is the case of a triangular arrangement of antiferromagnetically interacting ising spins (figure 1.2). In this case two spins can align antiparallel to each other but the third one cannot align antiparallel at the same time with both the other spins. Energetically any direction the third spin would choose is equivalent because it will lead to an antiparallel alignment to one of the previous spins and a parallel alignment to the other.

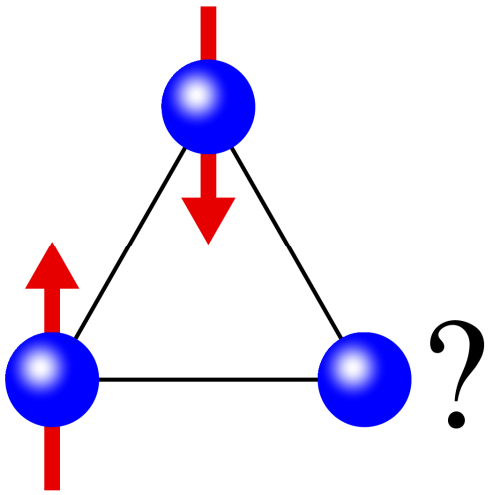

Fig. 1.2. Frustrated magnetism in triangular lattice [8].

It can be seen that the system is degenerate, and such a degeneracy of the ground state is one of the most striking features of frustrated systems. For example, the Hamiltonian of a system of ising spins on a triangular lattice, written as:

$H = J \sum \sigma_i \sigma_j$

can be minimised in more than one way, for more than one arrangement of the spins. This causes the degeneracy and the existence of multiple ground states is the characteristic of frustrated systems.

Suppose an arrangement of spins like the one in figure 1.3.

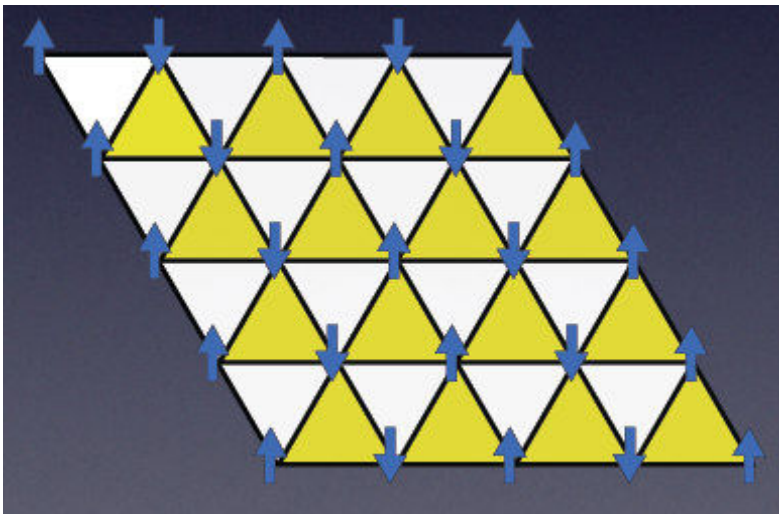

Fig. 1.3. Example of arrangement of ising spins on a triangular lattice [9].

There is no triangle in which all the spins point in the same direction and there is one frustrated bond per triangle. This bond is highlighted with red in figure 1.4.

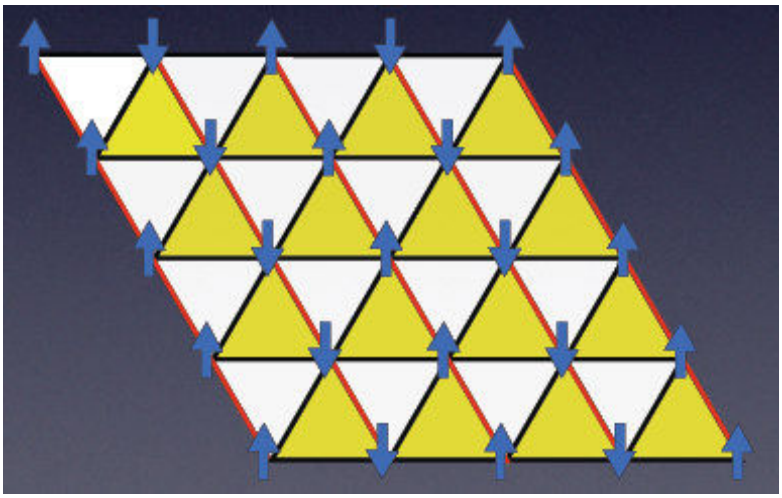

Fig. 1.4. A possible arrangement of spins in a triangular lattice red lines mark ferromagnetic correlations [9].

It can be easily seen that this is not the only possible configuration. While maintaining the 1 frustrated bond per triangle the system of spins can be arranged as in figure 1.5.

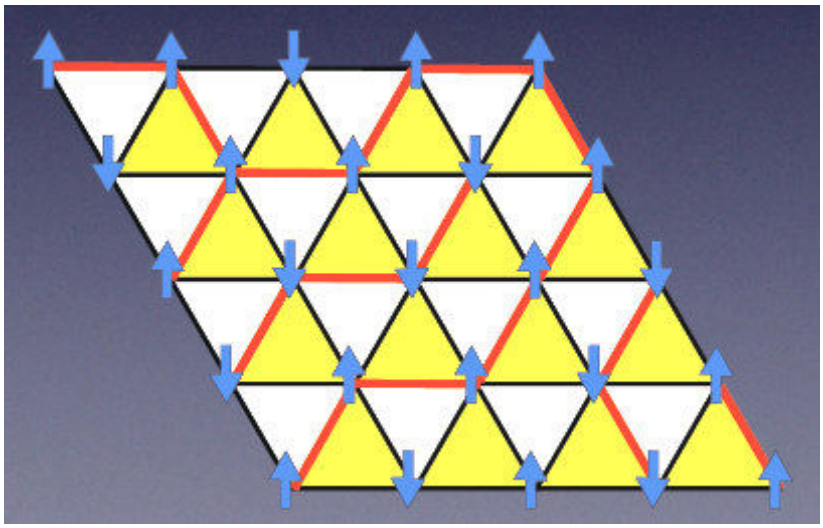

Fig. 1.5. Another possible arrangement of spins in a triangular lattice red lines mark ferromagnetic correlations [9].

The number of ground states increases exponentially with the number of magnetic moments. Wannier determined the number of ground states in 1950 with the equation:

$\Omega = \exp(S/k_B)$, where $S \approx 0.34\ Nk_B$ for the triangular lattice.

Other examples of frustrated systems include the checkerboard lattice (a) with $S \approx 0.21\ Nk_B$, the kagome lattice (b), $S \approx 0.5\ Nk_B$ and the pyroclore lattice (c), $S \approx 0.203\ Nk_B$ (figure 1.6).

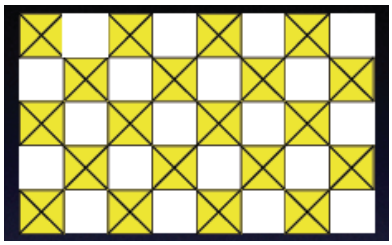

a)

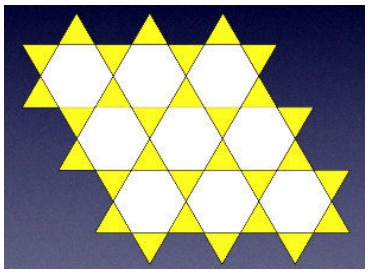

b)

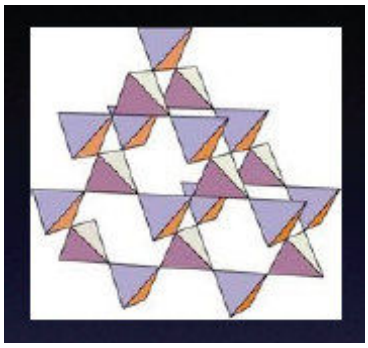

c) *Fig. 1.6. Examples of frustrated systems [10].*

Frustration is also found in spin glass systems. A spin glass is a system with magnetic moments characterized by quenched randomness and magnetic frustration, i.e. a pair of localized moments has the same probability of having ferromagnetic or antiferromagnetic interactions.

The magnetic behaviour of spin glass systems is different from the one of a ferromagnet or a paramagnet in the time response. Above the Curie temperature both ferromagnets and spin glasses present a paramagnetic behaviour. When cooled under a magnetic field these systems become magnetized. When the external field is removed the differences become striking. A ferromagnet remains magnetized to the value of the remanent magnetization while the magnetization of a paramagnet quickly drops to zero. A spin glass is found between these two behaviours presenting a remanent magnetization that slowly decays with time by a complicated, non-exponential law.

The fingerprint of a spin glass system is found in the AC magnetic susceptibility of the sample. The low field $\chi_{AC}(T)$ graph presents a cusp at a temperature, T_f, that is dependent on the frequency of the signal used to probe the sample. The specific heat of a spin glass shows no singularity but only a rounded maximum at a temperature slightly above T_f. Magnetic neutron powder diffraction indicates that at low temperature the spins are frozen on random orientations (at least at the timescale of the diffraction experiment). The magnetic disorder is reminiscent of the atomic disorder of a common glass. For this reason the systems with these properties were named spin glasses [7, 11].

I.1.3. Ferroelectric structures

a) ferroelectrics

In many aspects ferroelectricity is similar to ferromagnetism, replacing the magnetic moments with electric dipoles. The formal definition of a ferroelectric is that of a material which undergoes a phase transition from a high temperature phase that behaves as a normal dielectric (in which the electric polarization increases linearly with the external electric field and returns to zero when the field is removed) to a low temperature phase that has a spontaneous polarization that can be switched by an external electric field. Analogous to the ferromagnetic materials, the ferroelectric materials present domains, in which the electric dipoles follow a parallel alignment and their polarization shows a hysteresis response to the applied electric field. However there are also notable differences. The domain walls of ferroelectric materials are much narrower than the domain walls of ferromagnets. Another difference is that there is no equivalent for the spin / magnetic moment. The existence of the electric dipole is related to the structure of the ferroelectric material and comes from the displacement of a positively charged ion relative to the centre of negative electric charge produced by the surrounding anions. Another important difference is that for ferroelectric ordering there is no true equivalent for the exchange integral of ferromagnetic materials.

Now that the introduction of the ferroelectric materials and ferroelectricity as the manifesting phenomenon of these materials is set we will analyze in more detail the fundamental physical properties of ferroelectric crystals.

Let us assume an oversimplified model of a ferroelectric crystal with the chemical composition AB and a simple 2D square lattice [12] (figure 1.7).

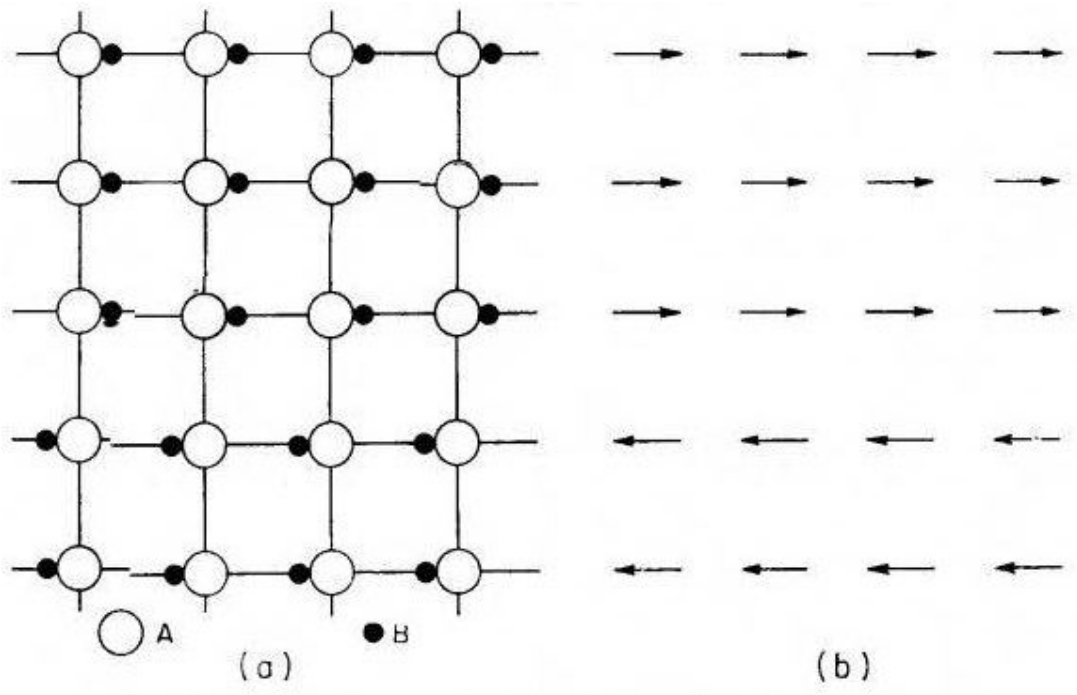

Fig. 1.7. Structure of model ferroelectric crystal (a) and orientation of electric diploes in the same crystal (b) [12].

Suppose the A ions carry a negative charge and the B ions a positive one. The AB pair is considered an electric dipole so the structure can be described in terms of these dipoles (fig1.7.b). If at a certain temperature all the B ions are close to the A ions on their left the crystal is spontaneously polarized. This alignment extends only in one region of the crystal while in others the alignment follows another direction. Polarization domains are hence formed.

The equilibrium position of the B ion is such that it stays closer to one A ion that to another A ion. The potential between the two A ions has the aspect of a double well (fig 1.8).

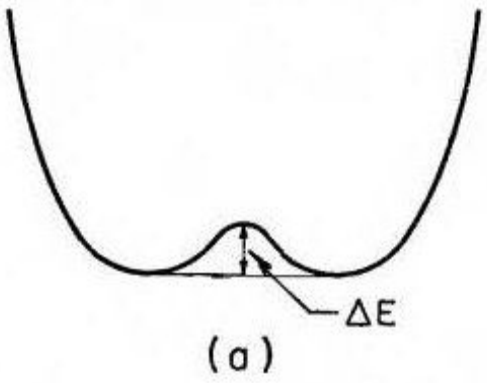

Fig. 1.8. Double potential well describing the crystal in figure 1.7 [12].

There are therefore two minima in the potential well (corresponding to two equilibrium positions that the B ions can occupy) and the B ions can jump from one position to the other one provided that they are supplied sufficient energy to go over the energy barrier.

If an electric field is applied to the crystal in the horizontal direction (fig.1.7) the dipoles that are already aligned with the field will remain so but the diploes that have an antiparallel alignment with respect to the field will tend to reverse their orientation. If the field is strong enough the energy barrier will be broken and the diploes will switch in the direction of the filed. The reversal takes place by nucleation and domain wall motion and generates a hysteresis of polarization (P) in function of the applied electric field (E). For small values of the filed, the energy supplied to the system is not sufficient to cause the reversal of domains thus the polarization grows linear with the filed, just like in a dielectric material. When the field is increased a number of domains will switch and the polarization will increase rapidly until saturation is reached (all the domains are aligned to the filed). When the filed is reduced the polarization does not fall to zero but remains at the value of the remanent polarization. In order to reduce the polarization to zero the field must be applied in the opposite direction. At the coercive filed, Ec, the polarization becomes zero and a further increase in the magnitude of the field restarts the entire process in the negative direction.

The P-E hysteresis loop (figure 1.9) is the most important characteristic of a ferroelectric material because this is what actually defines a material as ferroelectric. The existence of a spontaneous polarization is not sufficient for a material to be labelled ferroelectric. A material is ferroelectric if it has a spontaneous polarization that can be reversed by an electric field.

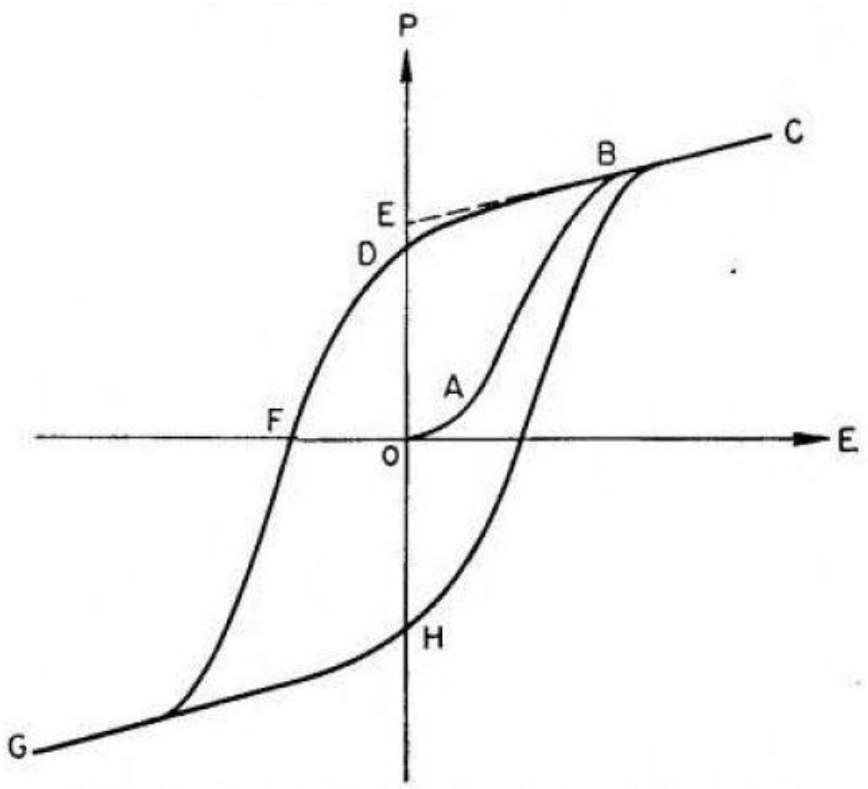

Fig. 1.9. P-E hysteresis loop [12].

The observation that the polarization can be switched by an electric field indicates the fact that the shift of the B ions is small. This means that the energy barrier is low.

If the energy barrier is so small that it can be exceeded by applying and electric field it can be expected that the barrier can be overcame by temperature. Indeed at a sufficiently high temperature the B ions can jump from one position into the other without the need of an electric field. Statistically, the B ions will therefore be symmetrical to the A ions. Also it is possible that the potential changes from a double well to a single well with the equilibrium position midway between the A ions. The two situations are producing the same effect, i.e. the crystal is no longer polar and will behave as a normal dielectric. The temperature that marks the transition from the ferroelectric behaviour to the normal dielectric behaviour is called the ferroelectric Curie temperature.

Another consequence of the small shift in the position of the B atom is observed to the behaviour of the dielectric constant as a function of temperature. The dielectric

constant (ε) is defined as the derivative of the dielectric displacement (D) with respect to the electric filed (E).

The connection between the dielectric displacement, filed and polarization is:

$$D = \varepsilon_0 E + P$$

and the derivative of the polarization P with respect to the E filed is the dielectric susceptibility (χ_e), therefore, the connection between the dielectric constant and the dielectric susceptibility is:

$$\chi_e = \varepsilon_r - 1$$

This definition of the dielectric constant works for dielectric materials, which have a linear dependence between D and E even at large fields. For ferroelectrics the D(E) is the hysteresis loop so the definition of the dielectric constant needs to be adjusted to take into account the more complicated dependence. One possibility is to define ε as the slope of the D(E) graph at the origin.

$$\varepsilon = (\partial D / \partial E)_{E=0}$$

The dielectric constant is therefore measured in small AC fields as to not reverse any domains. As the potential well between two A atoms changes with the temperature the polarizability of the B ions also changes and as a result some anomaly of the dielectric constant is expected to be seen at the transition temperature.

In some ferroelectrics the dependence of ε on temperature, above the transition temperature is found to be described by a law similar to the Curie-Weiss law of ferromagnetism:

$$\varepsilon = \varepsilon_0 + \frac{C}{T - T_0}$$

C is the Curie constant, T_0 is the Curie-Weiss temperature and ε_0 is the temperature independent part and it can usually be neglected. Close to T_0 the

dielectric constant becomes very large and can be connected to the dielectric susceptibility by:

$\varepsilon \approx \chi_e$

In ferroelectrics that undergo a phase transition of the second kind T_0 is essentially equal to T_C but this is not always the case as for ferroelectric materials that undergo a phase transition of the first order T_0 is no longer equal to T_C.

It should be noted that the results discussed so far are based on a simplified model that differs from actual materials by two aspects.

Firstly, the dipole moment is attributed to atom pairs arbitrarily picked and defined as the product of charge and separation. However in a real material, even though every unit cell carries a dipole moment, the moment cannot be attributed to any specific pair of atoms as it is related to the charge distribution within the unit cell. Therefore the dipole moment is written as:

$\mu = \iiint q(r) * r * dv$

Secondly, the dipole moment of each unit cell does not consist only of ionic charges but instead it may also contain charge separation that might eventually appear through the distortion of the electronic cloud of a given atom. This is a major difference between ferroelectricity and ferromagnetism. In ferroelectric crystals the moments are imbedded in a highly polarizable medium while in ferromagnetism the magnetic moments due to the spin cannot be influenced by the medium.

We will now discuss the crystallographic restrictions that are imposed on a material for it to be ferroelectric.

There are 32 crystal classes (point groups) under which any crystal can be categorized according to the symmetry elements it comprises. 11 of the 32 point groups contain a centre of inversion and therefore cannot contain ferroelectric materials for the reason that a centrosymmetric crystal cannot possess polar properties. An electric field applied to a centrosymmetric crystal will cause it to change its shape but the strain remains unchanged when the field is reversed. The effect is said to be quadratic, meaning that the strain depends on the square of the

filed. This is the electrostriction and it actually occurs in all (!) substances, whether crystalline or amorphous, solid or fluid [12].

The remaining 21 classes do not have a centre of symmetry and (with one exception) display the piezoelectric effect. (Piezoelectricity is the property of a crystal to develop charge separation when it is subjected to stress.) The piezoelectric effect is a linear effect.

10 of the 20 classes that display the piezoelectric effect have a unique polar axis. Crystals from these classes are spontaneously polarized with the value of the polarization dependent on temperature. When the temperature is changed the polarization also changes and the pyroelectric effect is observed, i.e. electric charges are observed on the crystal faces that are perpendicular to the unique polar axis.

Ferroelectric materials belong to the pyroelectric class. A necessary condition for a material to be ferroelectric is to belong in one of the 10 polar point groups but this is not a sufficient condition as reversibility of the polarization must also occur. A ferroelectric crystal can thus be defined as a pyroelectric crystal with reversible polarization [12].

This constitutes another important difference between ferroelectricity and ferromagnetism. In ferromagnetism the moments can always be reversed by a magnetic field whenever they are spontaneously aligned. Therefore the phenomenon is interesting particularly because of the spontaneous alignment. By contrast ferroelectricity is interesting only when the moments are loosely aligned and the interactions are so delicate that an external electric field can reverse the spontaneous polarization.

The ferroelectric effect was first observed in the Rochelle salt, $KNa(C_4H_4O_6)*4H_2O$ but the complex structure of this material and the large number of ions made an in-depth understanding of the physical processes governing ferroelectricity hard to achieve. Therefore the most widely studied ferroelectrics, for which coherent theories were formed, are ABO_3 perovskite oxides. The simplest structure of the sort is the cubic perovskite structure. This structure is define by large A cations that occupy the corners of the cube and a small B cation located in the centre of the structure, surrounded by an oxygen octahedron. Below the ferroelectric Curie temperature there is a distortion of the cubic structure to a lower symmetry structure, distortion that is accompanied by an off-centre shift of the small cation. It is this shift that forms the electric dipole [13, 14]. Figure 1.10 shows the structure of a

classic perovskite and the deformation it undergoes below the paraelectric (or dielectric rather) – ferroelectric phase transition temperature.

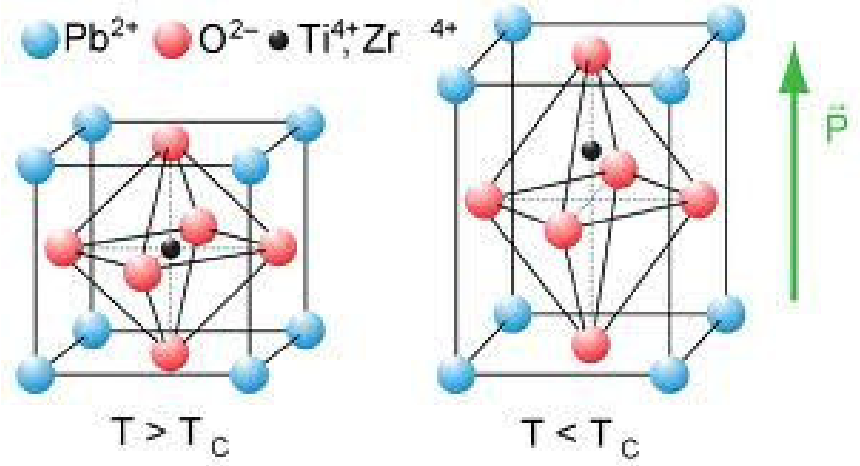

Fig. 1.10. Typical perovskite structure and cubic to tetragonal / paraelectric to ferroelectric phase transition for PZT, a well known ferroelectric material [14].

The parallel alignment of electric dipoles is then responsible for the development of the spontaneous polarization in ferroelectric materials.

b) ferroelectric relaxors

Relaxor ferroelectrics are the equivalents of spin glasses from magnetism [15]. Usually relaxor ferroelectrics appear as centro-symmetric cubic structures even below the Curie temperature (Tc) with only small, local, off-centre distortions that average to zero and are barely detectable with X-Ray diffraction. As in the case of the spin glasses, randomly distributed clusters are formed. A distinguishing feature of relaxor ferroelectrics is that measurements of dielectric constant in function of temperature present a peak and that peak shifts to higher temperature when the frequency of the AC current used in the measurement is increased. At the same time the intensity of the peak decreases with increasing frequency. The width of this peak is much larger for a relaxor ferroelectric than the peak corresponding to the ferroelectric transition for a conventional ferroelectric material [16-18]. Associated to this peak in the dielectric constant is a giant piezoelectric effect, which makes relaxor ferroelectric very interesting for applications.

I.1.4. Multiferroism (and requirements for multiferroism)

We can now try to explain why there are only few multiferroic materials available.

A multiferroic material must be by definition at the same time ferroelectric and ferromagnetic. In that case the allowed structural and physical properties for such a material are restricted to those that occur both in ferroelectric and ferromagnetic materials and this is exactly what makes the choice of materials so limited because the requirements for either ferroic order property exclude the other. Whatever makes a material ferroelectric excludes the possibility of having ferromagnetism in the same material and the other way around, ferromagnetism tends to destroy the ferroelectric ordering [2]. There are several factors that make the ferroic properties mutually exclusive and these factors are discussed below.

The first problem comes from the symmetry of the crystal structure of the material. As mentioned above a primary requirement for ferroelectricity is a structural distortion that removes the centre of symmetry and allows the formation of an electric polarization. There are 31 point groups that allow the off-centre distortion and other 31 point groups that allow the formation of a magnetic polarization. Only 13 point groups belong in both classes, theoretically allowing the existence of ferromagnetism and ferroelectricity. However, not all the materials that crystallize in these 13 groups are multiferroics, meaning that other constraints, apart from symmetry must exist [2].

Another problem is related to the electrical properties of the materials. A potential ferroelectric material has to be firstly an electric insulator in order to keep the electric charges separated. Otherwise free charges will rearrange and the electric polarization will vanish. However, no such requirement is imposed on ferromagnets and most magnets are metals and therefore electric conductors. The driving force for ferromagnetism in Fe, Ni, Co and their alloys is a high density of states at the Fermi level which also induces metallic conduction. However, ferrites (ferrimagnetic materials) antiferromagnets and canted antiferromagnets are in fact insulators but even so there are only a few materials at the same time antiferromagnetic and ferroelectric. Therefore, the lack of a great number of multiferroic materials cannot be blamed on the lack of insulating magnets alone [2].

A third restriction refers to the electronic structure of constituent atoms. This is also referred to in textbooks as the d^0 / d^n problem. Generally, magnetism is set by unpaired electrons that occupy d orbitals. With empty d shells there can be no ferro-, ferri-, antiferro-, or any other type of magnetic ordering since there are no magnetic moments. However, empty d shells are required in the common perovskite oxides on the B cation in order to have the off-centre distortion that generates electric diploes. As soon as the d shell of the B site cation begins to fill with electrons the tendency of that cation to induce a distortion that removes the centre of symmetry is eliminated. There are a few possible explanations as to why the presence of electrons in d orbitals reduces the tendency for off-centre displacement, however no complete answer to the question was provided so far [2].

I.1.5. Known multiferroics

We will now review some examples of multiferroic materials already reported in literature.

At the start of the chapter we mentioned extrinsic and intrinsic multiferroic materials. We will now concentrate only on intrinsic multiferroics which in turn can be classified in two main categories. On one hand are type 1 (or proper) multiferroics that order magnetically and electrically by independent means and therefore show weak magneto-electric coupling, and on the other hand are type 2 (or improper) multiferroics that present strong magneto-electric coupling and electric polarization induced by a magnetic ordering transition [1]. Although the coupling in type 2 multiferroics can be very strong, the electrical polarization is generally very small. Therefore type 1 multiferroics for which the electrical polarization may be quite large still present a lot of interest, although they remained largely unexplored until recently [1, 5].

Among the "classical" type 1 multiferroics the $BiMO_3$ (M = Mn, Fe, Cr) materials are the most promising for applications [5].

The ABO_3 type perovskite structure allows a wide range of possible oxidation states of the cations (for example $A^{2+}B^{4+}O_3$ or $A^{3+}B^{3+}O_3$) [3] and the possibility of

tuning the properties of the material simply by substituting the cations on the A site or the B site [3].

One tuning possibility is to attempt to construct a material in which the A site cation (Pb, Bi,…) contains a stereochemically active lone electron pair and so is responsible for ferroelectric ordering and the B site cation (transition metal) contains partially filled d shells and therefore is responsible for magnetism. These materials are known as proper multiferroics [19-24]. Because the ferroelectricity and the magnetism of these compounds are generated by different sublattices the correlation between the electrical and magnetic properties is weak. $BiFeO_3$, $BiMnO_3$, $YCrO_3$, $PbVO_3$ are reported examples of such materials [19-20].

$BiFeO_3$ is essentially the only single phase multiferroic that simultaneously posses ferroelectric ($T_C \approx 1100$ K) and antiferromagnetic ordering ($T_N \approx 643$ K) at RT [3, 5, 6]. $BiMnO_3$ is ferromagnetic below 105 K but it seems its space group is C2/c which is centrosymmetric therefore eliminating the possibility of ferroelectricity [5]. $BiCrO_3$ has an orthorhombic phase with the space group Pnma at high temperature (transition temperature at 430 K) and a monoclinic phase on the C2/c space group at RT. Below 114 K $BiCrO_3$ is a G type AFM [5].

Another approach, suggested by Smolenskii, is the substitution with magnetic ions of the B site cations of a known non-magnetic ferroelectric. The product thus obtained will contain on the same B site two cations, one with empty d shells for ferroelectricity and one with partially filled d shells for magnetism. This is the case for $PbMn_{0.5}Nb_{0.5}O_3$ or $PbFe_{0.5}Nb_{0.5}O_3$. The materials of this type tend to have low magnetic phase transition temperatures because of the dilution of the magnetic ions [19, 20].

The polarization can be induced by other mechanisms and this is the case of improper multiferroics. There are 3 categories of improper multiferroics: geometric multiferroics, electronic multiferroics and magnetic multiferroics.

Geometric multiferroics generate the electric polarization by complex lattice distortions. This is the case of the hexagonal $RMnO_3$ (R = rare earth) where electric polarization is induced by the tilting of MnO_5 pyramids and buckling of the R-O plane. $BaMF_4$ (M = Mn, Fe, Co, Ni) presents a similar behaviour, inducing ferroelectricity by rotation of MF_6 octahedra and displacement of Ba cations along the c axis.

Charge ordering can generate frustrated magnetism and small atom displacement as the distance between parallel spins tends to be shorter and than the distance between the spin aligned anti-parallel tends to be longer (figure 1.11). This is the case for $Pr_{1-X}Ca_XMnO_3$ for x between 0.4 and 0.5 or $LuFe_2O_4$ (which presents mixed oxidation states Fe^{3+} and Fe^{2+}) [20].

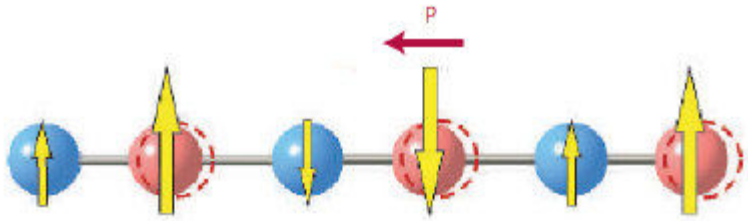

Fig. 1.11. Charge ordering of ↑↑↓↓ type resulting in electric polarization [21].

Ferroelectricity can also be induced by magnetic ordering. Materials from this class are very promising for applications due to their strong correlation between the electrical polarization and the external magnetic field. However, their polarization is small, about 6 orders of magnitude smaller than the polarization of normal ferroelectrics. This is the case of Cr_2BeO_4, $TbMnO_3$, $Ni_3V_2O_8$, $CuFeO_2$, $MnWO_4$ and CuO [20-24] or $TbMn_2O_5$ [25].

Table 1.1 gives a review of the methods by which ferroelectricity and magnetic ordering can be merged in a single sample and several examples for each method. Figure 1.12 presents a diagram of the most common oxides, grouped as simple oxides, magnetically polarizable oxides, electrically polarizable oxides and finally multiferroic oxides.

Table 1.1 Review of mechanisms responsible for multiferroism [20, 26, 27]

	Pathway to	Mechanism for multiferroism	Examples
Type I	A-site driven	Stereochemical activity of A-site lone pair gives rise to ferroelectricity and magnetism arises from B-site cation	$BiFeO_3$, $BiMnO_3$
	Geometrically driven	Long-range dipole–dipole interactions and oxygen rotations drive the system towards a stable ferroelectric state	$YMnO_3$, $BaNiF_4$
	Charge ordering	Non-centrosymmetric charge ordering arrangements result in ferroelectricity in magnetic materials	$LuFe_2O_4$
Type II	Magnetic ordering	Ferroelectricity is induced by the formation of a symmetry-lowering magnetic ground state that lacks inversion symmetry	$TbMnO_3$, $DyMnO_3$, $TbMn_2O_4$

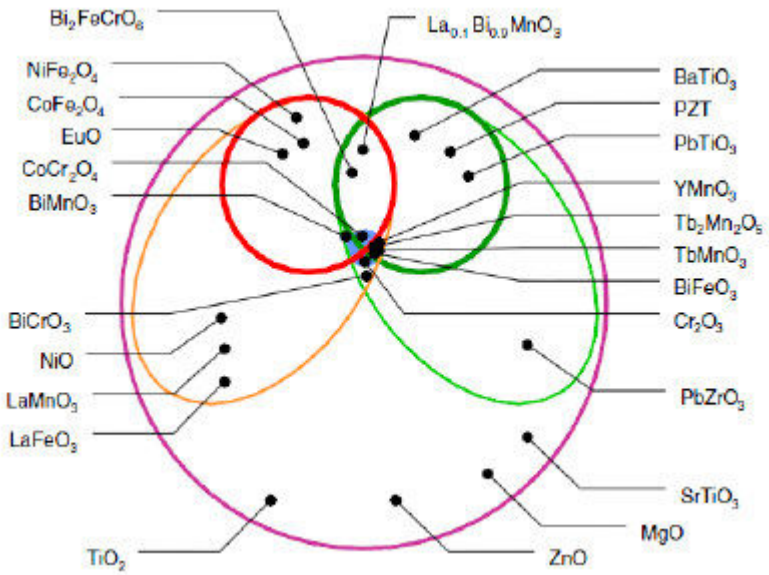

Fig. 1.12. Classification of oxides [28].

I.1.6. Applications for multiferroics

While devices which make use of ferroelastic-ferroelectric or alternatively ferroelastic-ferromagnetic materials do exist, for example, piezoelectric transducers, so far, no application for materials presenting ferroelectric-ferromagnetic properties was ever put to work. However, applications are envisaged in the fields of computer memories, actuators, transducers and capacitors [2, 24]. This is reflected by the huge number of articles written on the topic of multiferroic materials in the past few years. Fig 1.13 presents a plot of the number of articles in function of their publishing year.

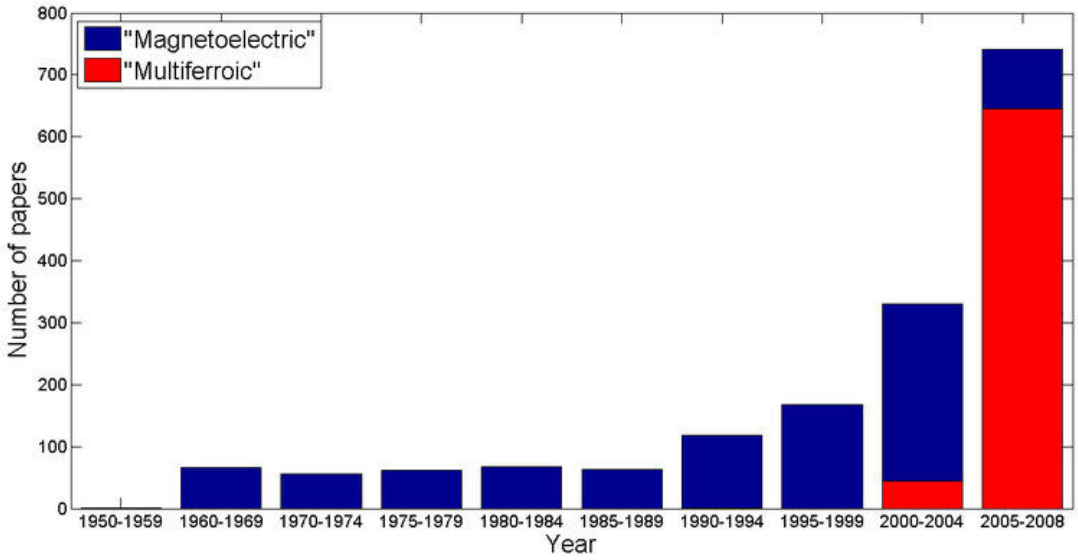

Fig. 1.13. Number of articles on multiferroic oxides by year of publication [29].

The first multiferroic materials were reported in the 1960's by Russian scientists and since then research in this field remained at a relatively constant pace, without any significant increase in the number of publications. However in 2000 an explosion in the number of articles was observed with the discovery of the coexistence of ferromagnetism and ferroelectricity in $BiFeO_3$.

One idea for an application of multiferroics in computer memory devices is to exploit the fact that both the magnetization M and the polarizability P can be used independently to store the value of a digit. This way a memory bit can have 4 different logical states as opposed to only 2 (0 and 1) for conventional computers. The interesting fact about such a device is that it does not necessitate a strong coupling between M and P. In fact, for this application a strong coupling would be disastrous. Figure 1.14 shows a schematic representation of the 4 logical values a digit from a multiferroic memory device may have [1].

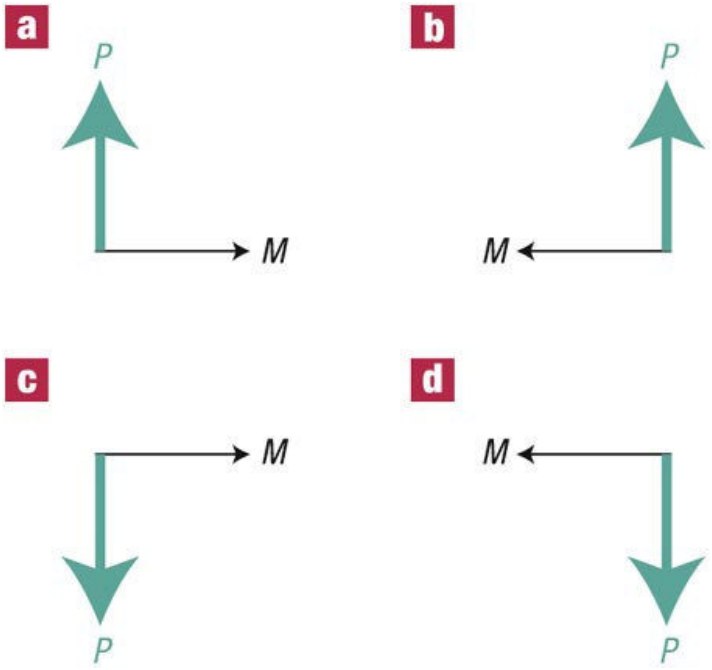

Fig. 1.14. Logical states for a potential 4 bit memory device constructed on the basis of a multiferroic material [30]. Each bit (a, b, c, d) is defined by the combination of the two possible orientations of the magnetization and the polarization.

On the other hand, another idea, in the eventuality of a strong correlation between M and P is the construction of a memory than can be written by an electric field and read by a magnetic sensor. This will dramatically increase the speed and reduce the power consumption of computing devices since it is easier and less costly to control an electric filed than a magnetic one. Such an advantage is particularly important in the context of increased miniaturization of electronic devices [1-3].

On top of that, the very understanding of the physics of the mechanisms which govern the behaviour of multiferroic materials is equally, if not more, interesting than the quest for increased computing power.

I.2. Results reported on $PbVO_3$

$PbVO_3$ has stirred a lot of interest in the past few years as a strong candidate for a new multiferroic oxide, one which might come closer to the ultimate target of multiferroics research, i.e. the successful fabrication of a single phase material presenting ferromagnetic and ferroelectric ordering at room temperature and a reasonably strong coupling between the two types of order [2]. $PbVO_3$ is so promising because it crystallizes in the non-centre-symmetric space group P4mm just like the ferroelectric $PbTiO_3$, so ferroelectricity is assured by the structure, but, on top of that, the V^{4+} ion in $PbVO_3$ carries a ½ spin and therefore a magnetic moment. The addition of magnetic moments to an already ferroelectric structure can be expected to result in multiferroicity of the novel compound, $PbVO_3$. However, up to now, no long range magnetic ordering was found for this material [31, 32, 33, 34].

Results already published on $PbVO_3$ are discussed in this chapter. Four aspects will be discussed on the matter of the history of $PbVO_3$. The discussion will follow the synthesis, the structure, the properties of the compound and the theories that explain the properties.

I.2.1. Sample Synthesis

The preparation of $PbVO_3$ was reported first in 2004 by Bordet et al. [31]. Bordet et al. [31] synthesized $PbVO_3$ samples under HP-HT conditions from a mixture of PbO, PbO_2 and V_2O_3. Typical reaction parameters were HP = 4.5 GPa, HT = 750° - 850° C and reaction time t = 3h. Single phase samples were obtained at 825° C for a non-stoichiometric mixture corresponding to the composition of $PbVO_{2.8}$.

The structure of the material was solved by means of X-Ray powder diffraction. It was found that $PbVO_3$ is isostructural to $PbTiO_3$. High temperature XRD indicated decomposition of the compound above 330°C in air. The magnetic properties of $PbVO_3$ were investigated by magnetization measurements and by neutron powder diffraction (NPD). No magnetic transition was detected [31].

However, the first published article to report the synthesis of $PbVO_3$ appeared from a Russian team lead by Shpanchenko [32] in 2004.

Shpanchenko et al. [32] reported for the synthesis of $PbVO_3$, a new compound in the $PbTiO_3$ family, prepared by solid state reaction under extreme conditions of pressure and temperature [32]. Shpanchenko [32] prepared his samples in a lens type apparatus from a mixture of PbO and VO_2 or alternatively PbO and V_2O_3 / V_2O_5 mixed in 1:1 ratio. The reactions took place at pressures of 40 – 80 kbars, temperatures of 650-1000° C and dwell times of 5 to 240 minutes [32].

Another very important aspect highlighted by Shpanchenko [32] and encountered in almost all the article on $PbVO_3$ is the constant presence of secondary phases. This is a major drawback as some of the impurities are magnetic which causes a great deal of trouble in interpreting magnetic measurements. The most frequently observed impurities are $Pb_3V_2O_8$, and hydrocerussite, $Pb_3(CO_3)_2(OH)_2$, which are not magnetic and therefore do not impede the acquisition of magnetic measurements to a great extent. Another impurity is PbV_6O_{11} which is antiferromagnetic. Because of the AFM signature of PbV_6O_{11} the presence of this impurity in the samples complicates the interpretation of results from magnetization measurements. Other impurities include VO_2 which does not react and this oxide also presents a strong magnetic signal at high temperatures. Also Shpanchenko [32] reported that $PbVO_3$ decomposes in air at about 300° C.

In 2005 Belik [33] synthesized in a similar way new $PbVO_3$ samples of better quality by employing a second HP-HT treatment which dramatically reduced the quantities of impurities present in the samples after only the first HP-HT treatment [33].

After the works of Shpanchenko [32] and Belik [33] some attempts were made to prepare and characterize $PbVO_3$ thin films. This approach was used notably by Lane W. Martin [35, 36] who reports the successful growth of epitaxial $PbVO_3$ thin films on a LAO ($LaAlO_3$) substrate using the PLD (pulsed laser deposition) technique in a reductive environment from a target of $Pb_2V_2O_7$. AFM ordering at about 130K is observed in $PbVO_3$ thin films [34, 35]. The films present a piezoelectric coefficient d = 3.1 pC/N [36] but the lattice parameters of $PbVO_3$ in thin films are very different from the parameters observed in bulk samples, c=5.02 Å in film and 4.67 Å in bulk so the properties of films can be greatly different from the ones observed in bulk samples [34].

Another very interesting direction in the research on $PbVO_3$ was taken in 2008 by Kengo Oka and Mikio Takano [37] with the synthesis of $PbVO_3$ single crystals [37]. The method of synthesis used by Oka [37] is called the hydrothermal method in high pressure conditions. It consists in the addition of 10% weight of distilled water to the mixture of oxides and the slow cooling of the sample. Oka [37] grew his crystals from mixtures of PbO, V_2O_3 and V_2O_5. Water was added to the mixture of powder oxides and the entire slurry was subjected to a pressure of 6 GPa and heated to 1223 K and slowly cooled to 973 K. Figure 1.15 shows the single crystals he obtained.

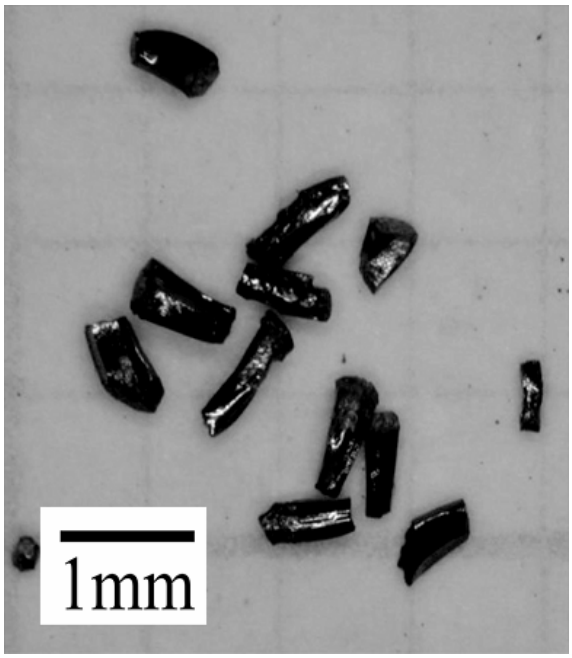

Fig. 1.15. $PbVO_3$ single crystals obtained by Kengo Oka [37].

Also in 2008 Tsirlin [34] prepared $PbVO_3$ samples from a mixture of PbO and VO_2 compressed at 5 GPa and heated to 950° C [34]. He used the samples to explore the possibility that $PbVO_3$ has a magnetic frustrated square lattice by performing susceptibility and specific heat measurements on polycrystalline $PbVO_3$ samples. Details about his results are discussed in the properties subchapter.

The latest articles include the works of Atahar who studied the thermal properties of $PbVO_3$ in 2012 [38] and Zhou also in 2012 who investigated structural properties of $PbVO_3$ under high pressure [39]. Atahar prepared $PbVO_3$ samples in the 40 – 60 kbar pressure range and at temperatures of 700° - 750° C [38].

Zhou [39] prepared $PbVO_3$ samples by a new method. His method was the decomposition of $Pb_2V_2O_7$ under high pressure and high temperature. $Pb_2V_2O_7$ was prepared from a mixture of PbO and V_2O_5. The mixture was placed in a platinum crucible and melted at 800° C for 2 hours. The sample was then cooled to 700° C where it underwent another dwell for 3 hours followed by quenching to RT. The $Pb_2V_2O_7$ sample was pressed into a pellet of 60 μm diameter and 15 μm thickness and loaded into the pressure chamber. The pellet was then pressurized to 30 GPa and heated with a YAG laser to 1500 – 2000 K. Zhou reports that $Pb_2V_2O_7$ has reacted to form $PbVO_3$ by the reduction of vanadium from V^{5+} to V^{4+} [39].

Up to this point the discussion was centred on $PbVO_3$ in which no substitution is performed. However, there is a number of interesting articles that are concerned with substitutions at the site of V in $PbVO_3$.

There is one article (up to date) that treats the V-Fe substitution, although not for the entire series but just for $PbV_{1/2}Fe_{1/2}O_3$. The article was published in 2009 by Takeshi Tsuchiya [40]. He prepared his samples using two different compositions, both sets of conditions found in HP-HT region at HP = 7 GPa and temperatures ranging from 800 to 1000° C. The first starting mixture is made of simple oxides, PbO, V_2O_5 and Fe_2O_3. The second starting product uses a precursor ($Pb_4V_2O_9$) which is ground and mixed with Fe_2O_3. The $Pb_4V_2O_9$ precursor is prepared by conventional solid state reaction from a mixture of PbO and V_2O_5 pressed into a pellet and heated at 600° C for 9 hours [40].

The V-Ti substitution is also discussed in two articles published in 2008 and respectively 2011 by Arévalo [41]. In these articles, Arévalo talks about the V-Ti substitution in the context of study of the complex system $PbM_{1-x}M'_xO_3$ where M and M' are Ti, Cr and V. He prepared his samples from stoichiometric mixtures of PbO,

VO_2 and TiO_2. The mixture was placed in a gold capsule and heat treated in a belt type apparatus at temperatures between 800° and 1200° C under pressures between 20 and 80 kbar [41].

I.2.2. Structure

The structure of $PbVO_3$ was solved by Bordet et al. [31] in 2004. The XRD diagram was indexed in the tetragonal system with the unit cell parameters a = 3.805 Å, c = 4.672 Å. The structure was refined in the P4mm non centrosymmetric space group and was found similar to that of the RT tetragonal phase of $PbTiO_3$. The Pb atom is at the origin of the system occupying the 1a (0, 0, 0) position and V is found in the off-centre position 1b (0.5, 0.5, 0.568). Oxygen atoms form a square pyramid with the apical oxygen O1 in 1b at (0.5, 0.5, 0.245) and the oxygen atoms forming the base, O2, at 2c (0.5, 0, 0.696).

In order to obtain more precise positions and occupancies of the oxygen atoms NPD experiments were performed at the D2B-ILL instrument, Grenoble, using a 1.594 Å wavelength. Vanadium atoms are not strong scatterers for neutrons so the structure was obtained using a joint refinement of XRD and NPD diagrams. Figure 1.16 shows the Rietveld refinements for the NPD respectively XRD data. Table 1.2 shows the atom positions in the $PbVO_3$ unit cell and the anisotropic atomic displacement parameters for the Pb and oxygen atoms. No oxygen vacancies were observed in these XRD-NPD experiments.

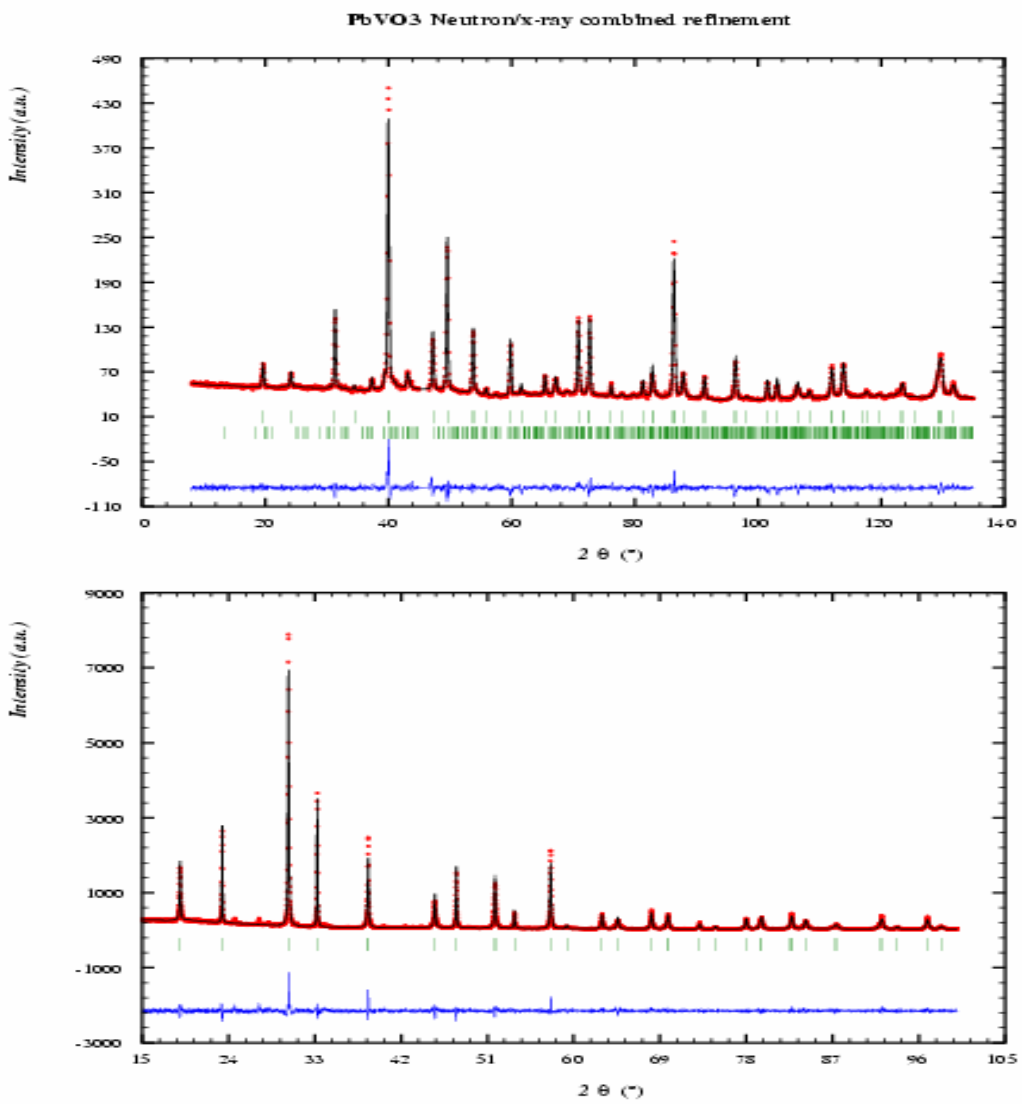

Fig. 1.16. $PbVO_3$ NPD (top) and XRD (bottom) refinement made by Dr. Bordet. The second row of ticks in the NPD pattern marks the reflections of $Pb_3V_2O_8$ [31].

Table 1.2. Atom coordinates in $PbVO_3$ structure at RT [31]

Atom	**Wyck.**	**x**	**y**	**z**	**U_{11} (Å ^{2})**	**U_{22} (Å ^{2})**	**U_{33} (Å ^{2})**
Pb	1*a*	0	0	0	0.011(2)	0.011(2)	0.030(2)
V	1*b*	1/2	1/2	0.5695	0.0127		
O1	1*b*	1/2	1/2	0.232(5)	0.017(9)	0.017(9)	0.035(18)
O2	2*c*	1/2	0	0.688(3)	0.015(4)		

NPD diagrams were recorded at temperatures of 300 K and 1.5 K. The low temperature diagram was collected in order to detect any structural phase transition or magnetic ordering that might occur in $PbVO_3$. No difference appeared between the

diagrams collected at the two temperatures showing that $PbVO_3$ does not undergo any structural or magnetic phase transition in that temperature range.

$PbVO_3$ is described as a distorted perovskite structure in the space group P4mm, similar to the structure of $PbTiO_3$. Such a distortion is typical for a ferroelectric compound, such as $PbTiO_3$. However in $PbVO_3$ the distortion is much greater than in the Ti counterpart as shown by the c/a ratio which is 1.23 for $PbVO_3$ but only 1.06 in $PbTiO_3$. The representation of the $PbVO_3$ structure is shown in figure 1.17. In the representation 8 unit cells are stacked generating a 3D picture of the atom arrangement. The cuboctahedron of oxygen atoms surrounding the Pb atom is highlighted. For simplicity only the oxygen structure surrounding a single Pb atom is shown.

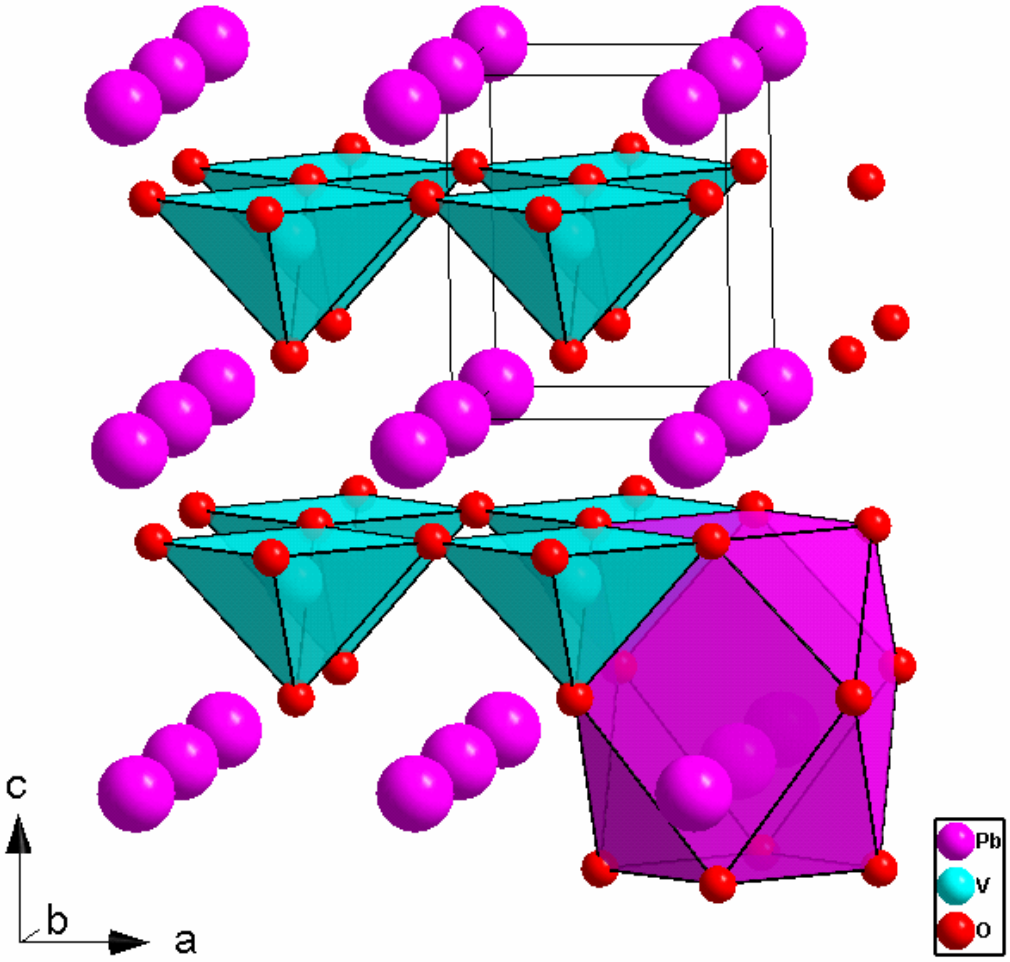

Fig. 1.17. Representation of the $PbVO_3$ structure, made by Bordet [31].

The oxygen cuboctahedron surrounding the Pb atoms is shown by Bordet [31] to be strongly elongated along the c-axis, with the Pb atoms are shifted from the centre 0.88 Å. The coordination of the Pb atom becomes 8-fold, with 4 O2 anions at 2.40 Å and 4 O1 at 2.90 Å. The next 4 O2 are shown to be much farther away at 3.73Å. In $PbTiO_3$ the shift of the Pb atom is only 0.49 Å.

The V^{4+} cation coordination is a square pyramid with 4 O2 at 1.98 Å and one apical O1 forming a vanadyl bond at 1.58 Å, which is typical for V^{4+} compounds. Bordet [31] observed that the oxygen pyramid has roughly the same dimensions in $PbVO_3$ as in $PbTiO_3$, but due to the formation of the vanadyl bond, the V^{4+} cation is closer to the apical oxygen (Ti-O=1.77 Å in $PbTiO_3$). He explains that the formation of the vanadyl bond between V and O1 decreases the strength of the Pb-O1 bond, therefore causing the Pb cations to be displaced towards the O2 plane, in order to reach charge balance. Table 1.3 shows the most important inter-atomic distances calculated by Bordet [31].

Table 1.3. Inter-atomic distances in $PbVO_3$ [31].

bond	length (Å)	bond	length (Å)
V—O1	3.094(24	Pb—O1 (x4)	2.899(9)
V—O1	1.576(24)	Pb—O2 (x4)	2.396(9)
V—O2 (x4)	1.980(4)	Pb—O2 (x4)	3.734(12)

Shpanchenko [32] also solved the structure of $PbVO_3$ by means of XRD and came up with very similar results. In its XRD patterns, Shpanchenko [32] noticed an unusual broadening of the diffraction peaks and he attributed this effect to the mechanical strain, present in the samples.

Belik [33] collected XRD at low temperatures on a conventional diffractometer, energy dispersive XRD under HP conditions and refined the structure from XRD obtained using synchrotron radiation.

The low temperature XRD was performed from room temperature (RT) to 12 K and showed no phase transition. However, the tetragonality of $PbVO_3$ (c/a ratio) is shown to be decreased with the temperature. Figure 1.18 shows the plot of the c and a parameters through this temperature range.

Belik [33] first reported a pressure induced phase transition at room temperature in $PbVO_3$ from tetragonal to cubic symmetry (T-C transition). Figure 1.19 shows the energy dispersive XRD patterns registered by Belik [33] on a $PbVO_3$ sample at various pressures from 1 GPa up to 6 GPa and back to ambient pressure. The T-C phase transition begins at about 2 GPa at RT on increasing pressure.

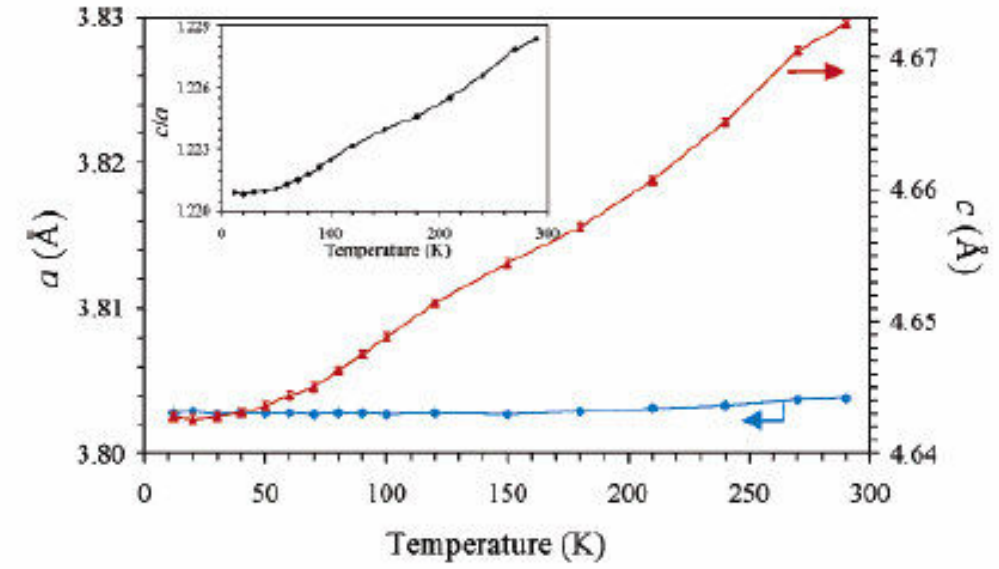

Fig. 1.18. Variation of lattice parameters in function of temperature for $PbVO_3$. The "c" parameter is plotted in red and the "a" parameter in blue. The insert shows the evolution of the tetragonality (c/a ratio) in function of temperature [33].

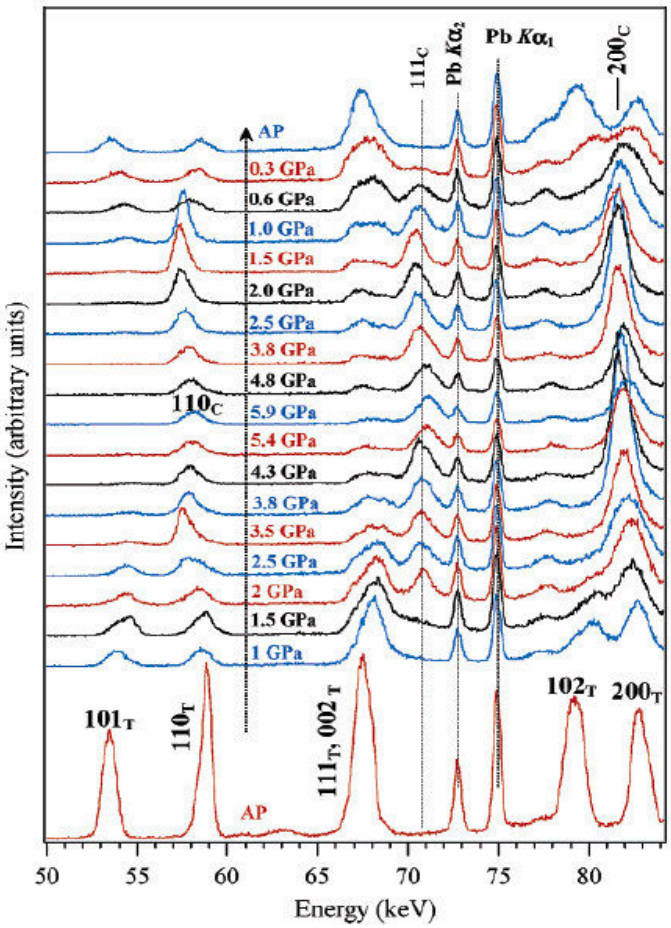

Fig. 1.19. HP-XRD patterns for $PbVO_3$. The first two diffraction peaks correspond to the (1 0 1) and (1 1 0) reflections of the tetragonal phase. The two reflection merge towards each other and eventually become equivalent in the cubic phase [33].

These are the main structural studies conducted on $PbVO_3$ pristine samples. The results reported in articles that discuss partial substitutions in $PbVO_3$ are discussed below.

In the article dealing with the V-Fe substitution, Tsuchiya [40] presented the XRD pattern of well crystallized sample. The Rietveld refinement plot is shown in figure 1.20 [40].

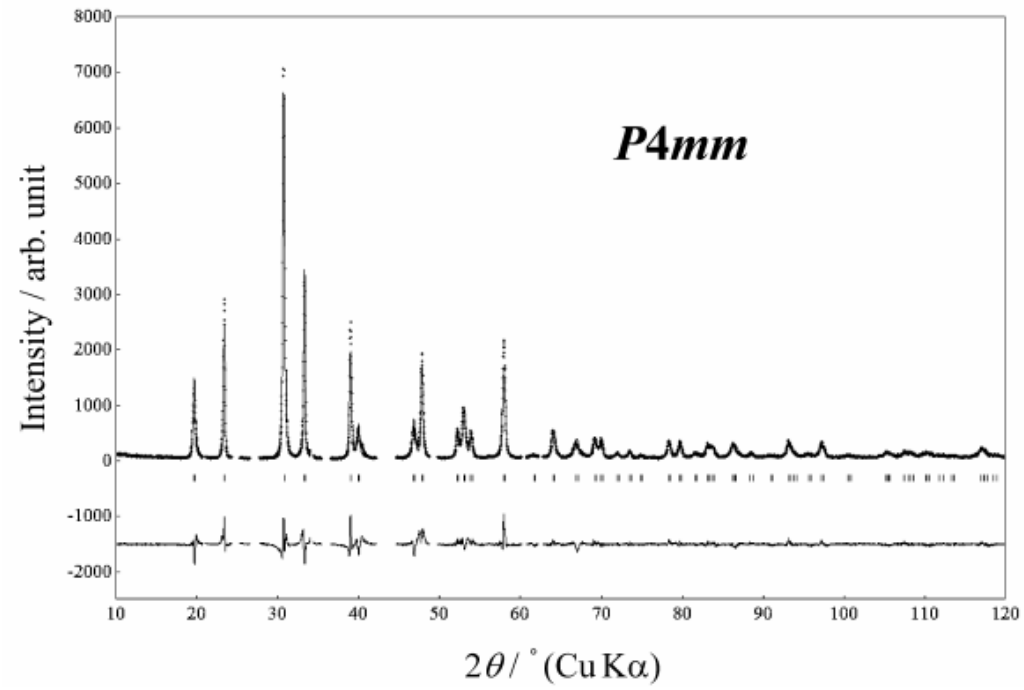

Fig. 1.20. XRD and Rietveld refinement for $PbV_{1/2}Fe_{1/2}O_3$. The upper curve marked in dots is the observed data. The continuous line overlapped to the observed data is the calculated pattern and the lower curve is the difference between the observed and calculated diffraction patterns [40].

He indexed the diffraction peaks of the main phase with a tetragonal unit cell with the lattice parameters a = 3.8 Å and c = 4.51 Å. The tetragonality observed for PVFO is c/a = 1.186, much smaller than for $PbVO_3$, although both compounds are isostructural with space group P4mm.

Table 1.4 shows the atom coordinates for Tsuchiya's structure [40]. The atomic positions indicate a less distorted structure than that of $PbVO_3$ and no sign of V/Fe ordering could be detected.

Table 1.4. Atom coordinates in the unit cell of $PbV_{1/2}Fe_{1/2}O_3$ [40].

Atom	Site	*g*	*x*	*y*	*z*	*B*/Å^2
Pb	1*a*	1.0	0	0	0	0.58(9)
$Fe_{0.5}$ $V_{0.5}$	1*b*	1.0	1/2	1/2	0.543(2)	0.01 ± 0.14
O1	2*c*	1.0	1/2	0	0.650(2)	1.0(3)
O2	1*b*	1.0	1/2	1/2	0.182(4)	1.0(3)

Arévalo [41] worked on the V-Ti substitution and showed that a solid solution is formed in the $PbV_{1-x}Ti_xO_3$ system. x can take any value between 0 and 1 so any V-Ti degree of substitution exists in between $PbVO_3$ and $PbTiO_3$ with smooth, linear variations of lattice parameters with the increase of the Ti concentration. No phase transition is observed as none is expected, considering that both $PbVO_3$ and $PbTiO_3$ crystallize in the same space group, P4mm. Figure 1.21 shows the displacement of the (1 0 1) and (1 1 0) diffraction peaks for the two materials. This reflects the smooth, linear change of lattice parameters with the composition.

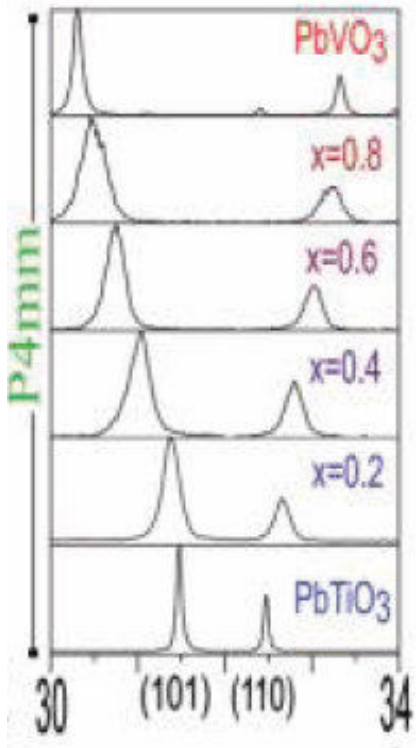

Fig. 1.21. Modification in peak position (caused by variation of lattice parameters) for the $PbTiO_3$ – $PbVO_3$ solid solution [41].

I.2.3. Properties

The first prediction of the electric properties of $PbVO_3$ was made by Bordet [31] in an evaluation of the spontaneous polarization that $PbVO_3$ should have. In his model, the pyramids of oxygen atoms form layers perpendicular to the c-axis by corner-sharing with all the vanadyl bonds pointing in the same orientation. The distance, δz, between the V cation position and the O2 plane was used to obtain an estimation of the spontaneous polarization, Ps [42] by the relation Ps = kδz. k is a constant and its value for $PbVO_3$ was considered equal to the value it has for $PbTiO_3$ as determined by Glazer et al. [42] ((k= 2.90 C. m^{-2} .$Å^{-1}$). Using the constant k for $PbTiO_3$, the spontaneous polarization for $PbVO_3$ was found to be Ps=1.6 C*m^{-2} [42].

Shpanchenko [32] investigated the resistivity of $PbVO_3$ and reported that $PbVO_3$ behaves like a semiconductor with a very large resistivity at room temperature, resistivity which further increases by two orders of magnitude between 300 K and 30 K up to the point in which it becomes almost impossible to measure. The results of his measurements are shown in figure 1.22.

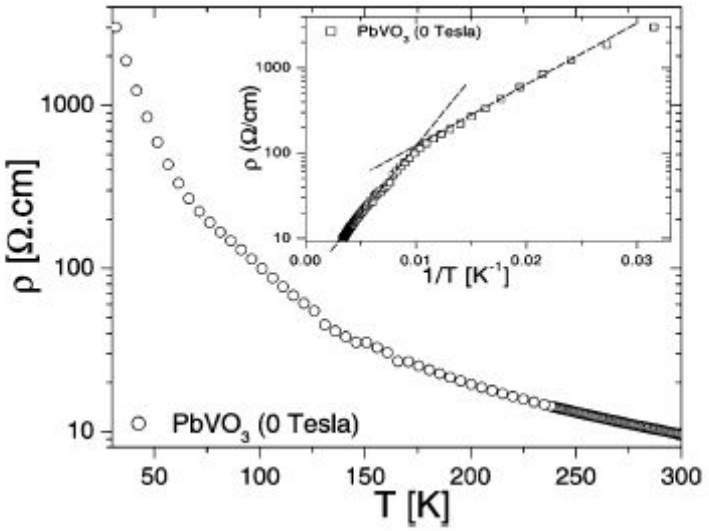

Fig. 1.22. Resistivity measurement in function of temperature for $PbVO_3$. The insert shows the 1/T plot in which Shpanchenko highlights a change in the slope which he assigns to two regions of activated behaviour [32].

Shpanchenko [32] also attempted to conduct measurements of magnetic susceptibility but he could not extract any reliable information because the measurements were dominated by the contribution of ferromagnetic impurities.

However he investigated the magnetism of $PbVO_3$ by neutron powder diffraction (NPD) and observed neither the presence of extra peaks nor any change in the intensity of already existing peaks in the NPD diagrams down to 1.5 K.

Belik [33] used his samples for resistivity measurements at high pressure and also DTA, magnetic susceptibility and specific heat measurements and he tried to evidence the presence of a P-E hysteresis curve.

Correlated to the structural T-C phase transition, Belik [33] observed a change in the behaviour of the electric resistivity of $PbVO_3$. At ambient pressure $PbVO_3$ is a semiconductor but under high pressure, the electric resistivity of $PbVO_3$ gains a metallic behaviour. The tetragonal/semiconductor – cubic/metal transition is slow and occurs over an extended range of pressures and a hysteresis in the ρ as function of P plot is observed. This hysteresis, observed by Belik [33], is shown in figure 1.23.

In addition to the resistivity measurements, Belik [33] tried to show the presence of a P-E hysteresis curve for $PbVO_3$ but, unfortunately he was unable to do so due to the presence of impurities in his samples, impurities which lowered the electric resistivity of the sample too much.

Magnetic susceptibility measurements made by Belik [33] reveal no magnetic transition between 570 and 2 K. The specific heat measurements again, present no transition in about the same temperature range (400 K to 0.4 K). These observations led Belik [33] to the conclusion that $PbVO_3$ is an antiferromagnet with the Néel temperature located above the decomposition temperature for this material, which is approximately 570 K.

Above 570 K $PbVO_3$ decomposes to $Pb_2V_2O_7$. Belik [33] studied the decomposition with the DTA technique and determined from the amount of oxygen absorbed into the reaction that the average oxidation state of vanadium in $PbVO_3$ is 4+.

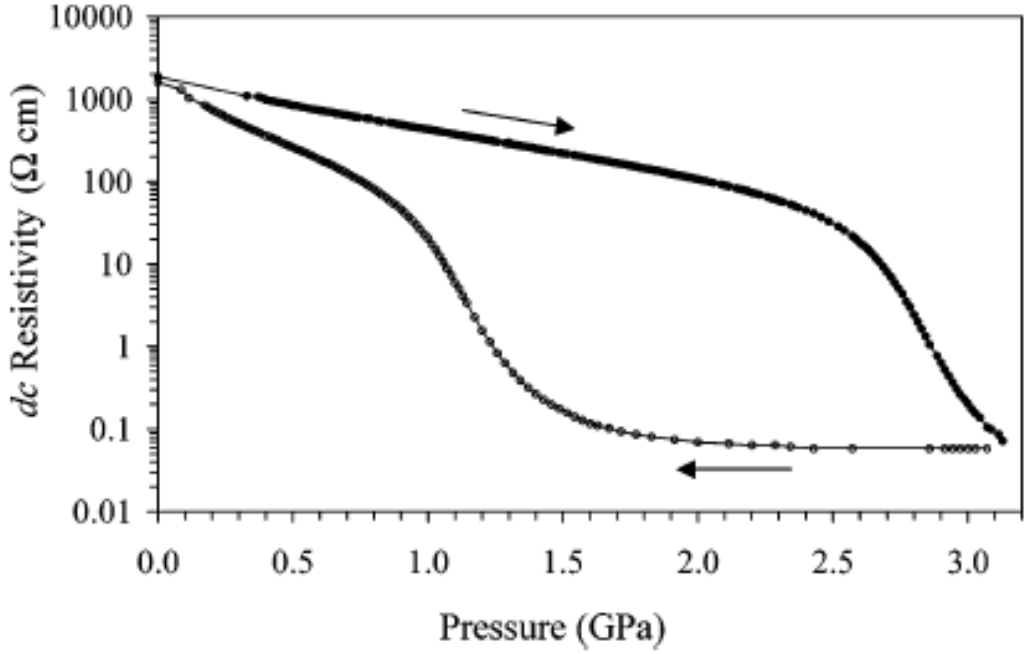

Fig. 1.23. Electric resistivity in function of pressure for $PbVO_3$ [33].

Oka [37] also looked into the magnetic properties of $PbVO_3$ as he used his crystals in measurements of magnetic susceptibility and μSR. In the susceptibility measurements he observed a splitting between the zero field cooled (ZFC) – field cooled (FC) measurements and some anomalies at about 40-50 K. The rest of the susceptibility curve is dominated by a broad peak centred at about 200 K. He explained these anomalies as a sign of antiferromagnetic ordering and fitted the broad peak in the susceptibility data with the results predicted by a 2D antiferromagnetic model having an ordering temperature of 42.5 K. The same type of behaviour was obtained from μSR measurements. However, the fit works well only on the 200 K to 300 K region. Figure 1.24 shows his susceptibility data. The magnetic susceptibility was not measured along a certain direction of the crystal. Instead Oka [37] used a bundle of randomly oriented crystals as the sample for the SQUID magnetometer employed in the measurements.

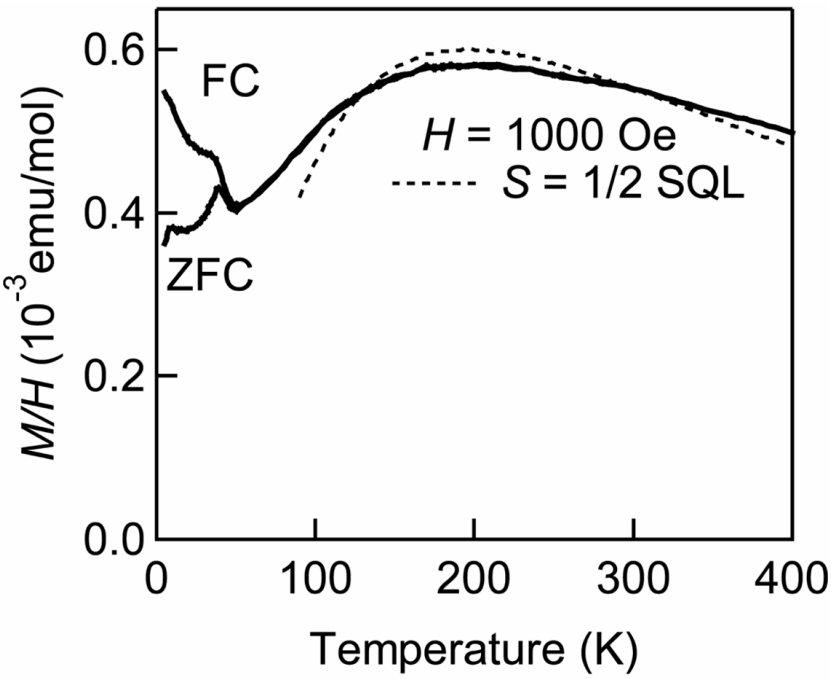

Fig. 1.24. Magnetic susceptibility – continuous line and AFM square lattice fit – dashed for $PbVO_3$ single crystals [37].

The magnetic susceptibility measurements made by Tsirlin [34] present the same broad peak at 200 K and some anomalies at 40-50 K just like in the measurements made by Oka [37]. The region after the peak is fitted with two 2D antiferromagnetic models (simple and frustrated, see the next section for descriptions of the two models). Contrary to Oka [37], Tsirlin [34] explains the anomalies at 40-50 K as an effect caused by trapped oxygen which undergoes condensation at about 50 K. Tsirlin's measurements [34] are shown in figure 1.25. Just like in the measurements made by Oka [37], the fit comes very close to the observed data but the match is not perfect. Tsirlin [34] explains that one possible cause for the difference between the observed and calculated susceptibility data is the relatively short range of data available for the fit. The low temperature region is dominated by the AFM interactions and possibly trapped oxygen while the high temperature region is dominated by the contributions of magnetic impurities such as PbV_6O_{11} and VO_2 that was not consumed in the reaction.

Measurements of specific heat reveal no transition what so ever. Figure 1.26 shows the specific heat curve observed by Tsirlin [34].

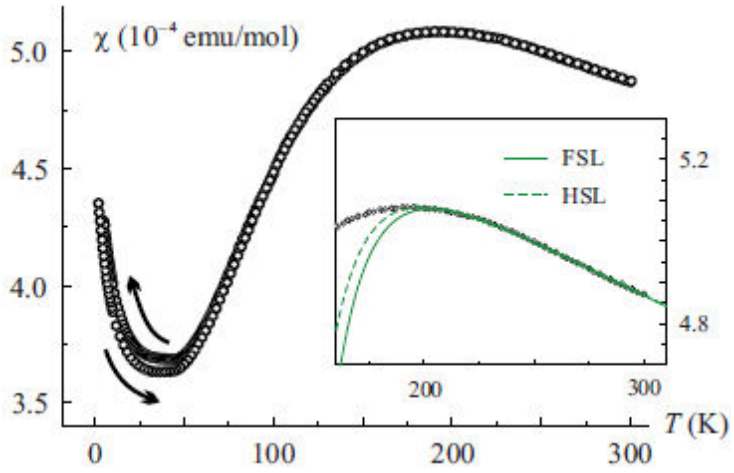

Fig. 1.25. χ(T) measurement for $PbVO_3$ powder. The insert is the fit with the two 2D AFM models (simple, HSL and frustrated, FSL) [34].

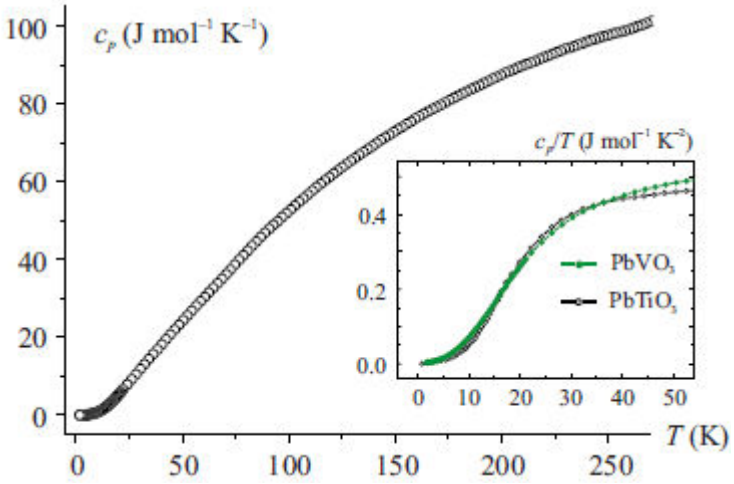

Fig. 1.26. Specific heat for $PbVO_3$. The insert shows the comparison between $PbVO_3$ and $PbTiO_3$ [34].

$PbVO_3$ was also investigated by means of computational techniques, however, these results will not be discussed here. Complicated calculations were made in 2009 by Yoshitaka Uratani [43] and 2012 by Solovyev [44] with the aim of explaining the magnetic behaviour of $PbVO_3$ (and $BiCrO_3$). Also in 2012 Atahar [38] studied experimentally but also through calculations the thermal properties of $PbVO_3$ and confirms the observations made by Tsirlin [34]. Other calculations were performed aiming to explain the structural T-C transition by Xing Ming in 2010 [45] and Zhou performed in 2012 [39] a series of XRD measurements again looking at the structural transition of $PbVO_3$. Te most recent results are from 2013 and belong to Aleksandar S. Miloševic who determined from ab inito calculations the electronic structure and optical properties of $PbVO_3$ (and $BiCoO_3$) [46].

For the substitution samples, Tsuchiya [40] performed magnetic susceptibility measurements on a $PbV_{1/2}Fe_{1/2}O_3$ sample that was free from magnetic impurities. The $\chi(T)$ and $1/\chi(T)$ from Tsuchiya's article [40] are shown in figure 1.27.

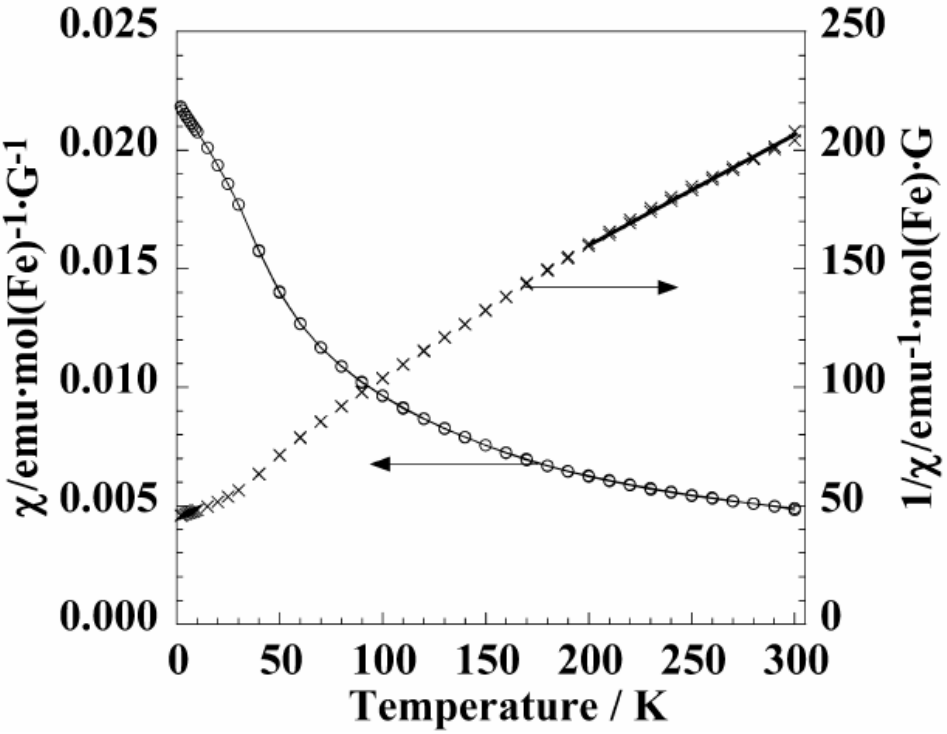

Fig. 1.27. Temperature dependence of magnetic susceptibility for $PbV_{1/2}Fe_{1/2}O_3$ [40].

The temperature dependence of the magnetic susceptibility was found not to obey the Curie-Weiss law and to reveal AFM interactions.

Tsuchiya [40] measured the dielectric constant of the $PbV_{1/2}Fe_{1/2}O_3$ at 9 K and obtained an almost constant value (ε_r = 174-177) regardless of the frequency of me measurement between 1 kHz and 500 kHz. The dielectric constant was found to increase however as the temperature increases and disperse with frequency (ε_r = 24000 at 1 kHz and ε_r = 6000 at 500 kHz).

DTA showed that PVFO decomposes in air at 700 K into $Pb_4V_2O_9$ and Fe_2O_3. Notice the increase in decomposition temperature, relative to $PbVO_3$.

I.2.4. Theory and interpretations

The first explanation of the mechanism that led to the formation of the $PbVO_3$ structure was provided by Bordet [31]. He explains that the distortions of the Pb^{2+} environment are caused by the lone pair of p electrons of the Pb cation. The distortions then induce an asymmetric coordination for V^{4+}. This explains the large tetragonal distortion of the unit cell and leads to the localization of the vanadium d electrons. Because of the localization the compound is expected to present magnetism of localized spins in a ferroelectrically distorted structure [31]. His model was described in greater detail under the structure subchapter (I.2.2.).

Shpanchenko [32] reached a similar conclusion from his experimental results and from his energy band calculations. He considers the lone electron pair of the Pb^{2+} responsible for the tetragonal distortion as it is present both in $PbVO_3$ and in $PbTiO_3$. In $PbTiO_3$ the Ti forms a short bond with one apical oxygen atom and a longer one with the other but the coordination remains 6. In $PbVO_3$ one of the oxygen atoms can be pushed at a nonbonding distance so the coordination of V becomes 5 fold with the formation of the vanadyl bond and this further elongates the structure. Therefore both the lone pair of Pb electrons and the formation of the vanadyl bond contribute to the elongation. However Shpanchenko [32], points out, no such vanadyl bond is found in other $A^{2+}VO_3$ compounds. From band energy calculations he explained the magnetic properties of $PbVO_3$ and observed that the compound is more stable in an AFM structure than in a FM structure. He also observed the appearance of an energy band gap due to the localization of the vanadium d electrons and predicted the value of the gap at Eg = 0.28 eV, typical for a semiconductor. This is in contrast to the $SrVO_3$ which is cubic and presents a metal conduction. The interaction between VO2 layers was found by Shpanchenko [32] to be weak from the delocalization of electrons in the region from V^{4+} and O^{2-} from neighbouring layers. His conclusion is supported by calculation of exchange parameters which differ by one order of magnitude between in plane and perpendicular to plane (inter-plane) interactions. Shpanchenko [32] considers that the transformation from the $SrVO_3$ 3D structure with octahedron coordination of V to the 2D $PbVO_3$ structure with the short vanadyl bond is the structural reason for the change in resistivity behaviour. The reduction in dimensionality is attributed by Shpanchenko [32] to the replacement of Sr^{2+} cations

by Pb^{2+} cations by a similar mechanism to the one found on the compounds with the $Sr_{n+1}V_nO_{3n+1}$ composition. In that series $SrVO_3$ shows metallic conduction and Pauli paramagnetism while Sr_2VO_4 has semiconductor resistivity and follows a Curie-Weiss law for the magnetic susceptibility. The differences between these two materials are attributed to the change in dimensionality of the structure.

Oka [37] proposed another model for explaining the large tetragonal distortion in $PbVO_3$. The model is based on their magnetic studies. The V^{4+} ion has a d^1 electronic configuration and energy band calculations (LDA) show that a d^1 electron in a pyramidal coordination will generally occupy the nondegenerate d_{xy} orbital. This is because if a Jahn-Teller distortion somehow causes the V-O bonds to expand in the z direction the energy of the d_{xy} orbital should be higher than the energies of the degenerate d_{xz} and d_{yz} orbitals. At this point the degeneracy remains since the d electron occupies the lower energy d_{xz} and d_{yz} orbitals. In the $V\text{-}O_5$ pyramidal coordination the bond to the apical oxygen is considerably shorter that the bond to the in plane oxygen atoms and the d electron of V tends to avoid the close oxygen, therefore the energy of the d_{xy} orbital is lowered. The d electron then occupies the d_{xy} orbital and thus the degeneracy is lifted. In octahedron (VO_6) coordination all 3 d orbitals have the same energy. The formation of the pyramidal coordination lifts the degeneracy. Figure 1.28 shows the energy levels of the d orbitals in the 3 cases discussed above as they are treated in Oka's article [37]. The s^2 lone electrons of Pb are aligned along the c direction and further enhance the distortion and prevent the formation of a Jahn-Teller distortion that might shrink the octahedron along c [37]. This scenario explains the pressure induced change in resistivity behaviour of $PbVO_3$ from semiconductor/insulator to metallic. The insulating nature is due to the ordering of d_{xy} orbitals. In cubic $PbVO_3$ all 3 d type orbitals will have the same energy so metallic conduction is expected as in the case of $SrVO_3$ (which is cubic with the V from $SrVO_3$ having octahedral coordination). This observation is in good agreement with experimental data. Oka [37] also explains the magnetic properties of $PbVO_3$ by the same 2D model. First-principle calculations performed by Oka [37] predict that $PbVO_3$ should be a 2D (two dimensional) antiferromagnet due to the ordering of d_{xy} orbitals but the system is also frustrated due to the fact that next nearest neighbour interactions are not negligible with the ratio of the nearest neighbour interaction (J1 or NN) and next nearest neighbour interactions (J2 or NNN) being J1/J2 = 0.32. Theoretic calculations show that the system lies at the boundary between AFM

ordering and spin glass (estimates of the boundary run from J1/J2 = 0.38 to 0.24 [37]), however AFM ordering is thought to dominate from results of magnetization measurements and μSR. The ordering temperature of the 2D AFM is estimated by Oka [37] to be at 50 K from susceptibility measurements and at 43 K from μSR. This in contrast to the expected results of Belik [33] who considers $PbVO_3$ to be an AFM with the Néel temperature above the decomposition temperature of $PbVO_3$ (decomposition occurs at about 570K). The absence of magnetic diffraction peaks in NPD diagrams of $PbVO_3$ (peaks that would indicate long range ordering) is explained by Oka [37] through the small spin S= 1/2 and the shrinkage of the ordered moment due to the reduction in dimensionality.

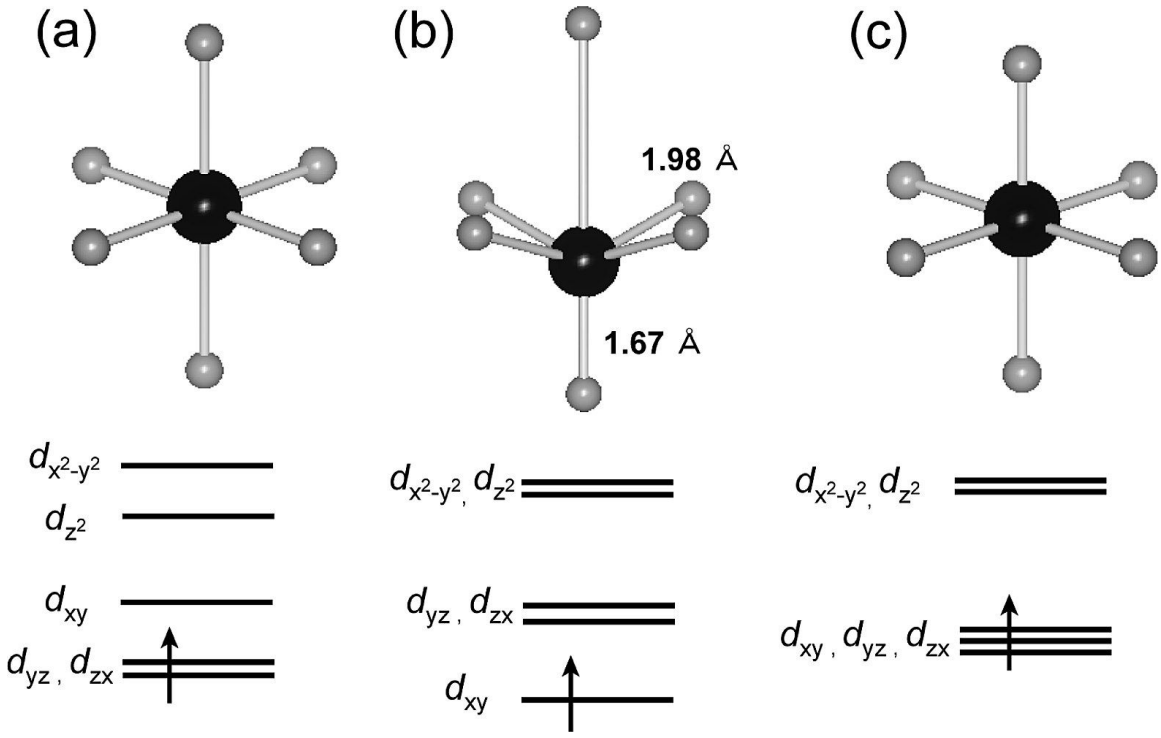

Fig. 1.28. Energy levels of d orbitals for V cation corresponding to the coordination of the V cation, a) Jahn-Teller distortion, b) pyramidal coordination, c) no distortion [37].

Tsirlin [34] used two models to explain the properties of $PbVO_3$. These models are the Heisenberg Square Lattice model (HSL) which takes into account only NN (J1) interactions and the Frustrated Square Lattice model (FSL) which takes into account both NN (J1) and NNN (J2) interactions and these interactions are antiferromagnetic. The magnetic susceptibility data is consistent with the HSL and the

FSL models so Tsirlin [34] looked for computational model in order to better describe the system and also performed specific heat measurements (figure 1.26.) He tried to separate the magnetic contribution to the specific heat curve by comparing the data for $PbVO_3$ to the data of a diamagnetic material with the same structure. Therefore he compared the specific heat curve for $PbVO_3$ to the specific heat curve of $PbTiO_3$ (insert of figure 1.26.). The difference between the two curves was found to be considerable, as defined by crossing points of the two specific heat graphs in the low temperature region. Tsirlin [34] attributes this effect to the different phonon spectra of the two materials so the subtraction could not be performed. Energy band calculations performed by Tsirlin [34] reveal a significant of d_{xy} orbitals, consistent with the pyramidal coordination of V and with the results obtained by Oka [37]. Tsirlin's [34] first estimations of the interaction energies reveal t1 = 0.132 eV for NN and t2 = 0.077 eV for NNN [34]. Long range in layer hopings are found to have very small energy (under 0.004 eV) and the inter-layer hoping interactions are found to be even smaller, under 0.0012 eV [34]. Tsirlin [34] then considers that these two contributions can be neglected, thus demonstrating the strong two-dimensionality of the $PbVO_3$ system. The α ratio, α=t1/t2, which controls the magnetic properties of the system is 0.34 and this supports the FSL scenario. Tsirlin [34] considers that the frustration in $PbVO_3$ plays a crucial role and suppresses the long range ordering, transforming the ground state of the system in a spin-liquid state. This is in contrast to Oka's conclusions [37] who believed the system to be a 2D long range ordered AFM.

These are the main models explaining the structural, magnetic and dielectric properties of $PbVO_3$. Regarding the magnetic properties it is important to mention Solovyev article from 2012 [44]. By superb calculations Solovyev [44] predicts the magnetic structure of $PbVO_3$ to be a spiral structure. The analysis of the calculations is beyond the objectives of the work and therefore will not be discussed here.

We will now turn our attention to the articles that discuss substitutions.

Tsuchiya [40] calculated the bond lengths and bond angles from the XRD data and observed that there are great differences between the bonds of the B site cation to the apical oxygen ions (here labelled O2). From these results he concluded that the B site cation has a pyramidal coordination. The values of the bond lengths in the square pyramid are only average values as Tsuchiya [40] adopted a disordered model for the arrangement of Fe and V ions. The coordination of separated V and Fe cations could not have been calculated. The tetragonal distortion, which is still large in PVFEO (the

c/a = 1.18, placed between the values of 1.23 for $PbVO_3$ and 1.06 for $PbTiO_3$) is considered by Tsuchiya [40] to be a second order Jahn-Teller effect caused by the electronic configuration of the V^{5+} ion and the lone electron pair of the Pb^{2+} ion. This explanation is supported by XPS measurements which return the oxidation states for the cations. According to the XPS data the cations the oxidation states for Pb, Fe and V are Pb^{2+}, Fe^{3+}, V^{5+}.

Concerning the magnetic properties, Tsuchiya [40] concluded that the $PbV_{1/2}Fe_{1/2}O_3$ compound is an antiferromagnet [40]. He calculated the effective moment of the Fe ion from the data collected between 200 and 300 K. The effective moment was found to be $\mu_{eff} = 4.14\ \mu_B$ which is considerably smaller than the predicted moment from the electronic structure of Fe^{3+} $\mu_{eff} = 5.92\ \mu_B$. Considering a disordered distribution of Fe and V cations Tsuchiya [40] explains that iron rich regions are formed and within these regions the Fe ions are arranged by antiferromagnetic super-exchange interactions that function through the oxygen anion. He observed that the effective moment decreases with decreasing temperature and attributes this observation to the fact that with the decline in the thermal disturbance the AFM interactions become the main contribution to the magnetic behaviour (i.e. decrease in effective moment).

By using the ionic model and the structural data of the $PbV_{1/2}Fe_{1/2}O_3$ compound Tsuchiya [40] estimated the spontaneous polarization for the material to be Ps = 88 $\mu C/cm^2$. This a la larger value than the one in $PbTiO_3$, Ps = 57 $\mu C/cm^2$, but lower than the estimated value for $PbVO_3$, Ps = 150 $\mu C/cm^2$.

Arévalo [41] studied a complex set of substitutions including the V-Ti substitution in the $PbVO_3$ - $PbTiO_3$ solid solution, which is of interest on our own study. Therefore more attention will be paid to this substitution, however not neglecting the other substitutions. The V-Ti substitution is regarded by Arévalo [41] as the substitution with V on $PbTiO_3$ rather than the opposite (which is our study). The composition of his samples is written as $PbTi_{1-x}V_xO_3$ while that of our samples is $PbV_{1-x}Ti_xO_3$. This is an important difference since it will cause a great deal of confusion.

Again the large tetragonal distortion from both $PbTiO_3$ and $PbVO_3$ is explained by Arévalo [41] as an effect of the lone electron pair of Pb^{2+}. The lone electron pair occupies approximately the same volume as an oxygen ion so when all the pairs align

to the same direction the effect is a strong distortion [41]. He also considers that the B site cation has a considerable contribution to the tetragonal distortion and connects this contribution to the ion size. He observed that when the B site cation of a pristine tetragonal material is substituted by a smaller size cation the c axis and the volume of the unit cell decrease. When the substitution degree is sufficient the symmetry of the material is changed, becoming cubic. For example, in the $PbV_{1-x}Cr_xO_3$ this effect is produced at x = 0.4 [41]. The introduction of the smaller (here Cr) cation causes disorder in the arrangement of the lone pair electrons of Pb^{2+} and this eventually changes the symmetry of the unit cell [41]. No phase transition is observed for the samples from the V-Ti substitution with the samples of the series presenting almost no strain (strain is observed for examples in samples with Cr substitutions as these samples undergo a tetragonal to cubic phase transition). However the x = 0.3 remains a threshold point, marking the sample where strain is minimum [41].

Another interesting fact observed by Arévalo [41] is that $PbTi_{0.8}V_{0.2}O_3$ has a temperature induced phase transition form tetragonal to cubic at T = 730 K. It should be remembered that $PbTiO_3$ also has a tetragonal to cubic transition activated by temperature but $PbVO_3$ however does not as it decomposes (under ambient pressure) at about 570 K, before it reaches the transition temperature. When higher V concentrations are reached the samples again decompose into $Pb_3V_{2-x}Ti_xO_8$ and/or $Pb_2V_{2-x}Ti_xO_7$ [41].

I.2.5. Synthesis / Review

The main characteristics reported in literature for $PbVO_3$ and $PbV_{1-x}M_xO_3$ (M = Fe, Ti) have been discussed so far. In a quick review these data are organized into the following table, table number 1.5.

year	research group	sample preparation	measurements	results	model
2004	Bordet [31]	$PbVO_3$ powder starting materials: oxides PbO, PbO_2, V_2O_3 HP = 4.5 GPa HT = 750 - 850° C t = 3 h	XRD HT XRD electron diffraction NPD magnetic susceptibility DTA	lattice parameters a = 3.805 Å c = 4.672 Å space group P4mm structure accurate determination of atomic positions no transition observed in NPD calculation of bond lengths decomposition temperature at 330° C	V cation has a 5 fold pyramidal coordination forming a vanadyl bond with the apical oxygen vanadyl bond correlated with the Pb^{2+} lone pair generates the very large tetragonal distortion
2004	Shpanchenko et al. [32]	$PbVO_3$ powder starting materials: oxides PbO, VO_2 mixture (1:1) of V_2O_3 and V_2O_5 HP = 40-80 kbars HT = 650-1000° C t = 5-240 min purest samples obtained at 40 – 60 kbar and 700 – 750°C	XRD resistivity measurements NPD energy band calculations	lattice parameters strain effects structure semiconducting behaviour NPD reveals no magnetic structure predicted Eg and magnetic ordering decomposition temperature for $PbVO_3$ calculation of bond lengths	Pb^{2+} and vanadyl bond produce large tetragonal distortion Eg = 0.28 eV AFM ordering more likely than FM ordering 2D system
2005	Belik [33]	$PbVO_3$ powder	low	lattice constants +	AFM with Néel

		starting materials: oxides: PbO, V_2O_5, V_2O_3 HP = 6 GPa HT = 973-1223 K t = 30-120 min quenching to RT second HP-HT treatment	temperature XRD synchrotron radiation XRD HP XRD HP resistivity measurements P-E hysteresis DTA magnetic susceptibility specific heat	temperature dependence structure tetragonal semiconductor to cubic metallic transition oxidation for V is +4 decomposition temperature for $PbVO_3$ no phase transition observed in magnetic susceptibility or specific heat calculation of bond lengths	temperature above decomposition temperature
2008	Kengo Oka [37]	$PbVO_3$ single crystals starting materials: oxides: PbO, V_2O_5, V_2O_3 10 % wt distilled water hydrothermal reaction HP = 6 GPa HT = 1223 K t_1 = 30 min slowly cooled to HT = 973 K t_2 = 12 h release pressure	HP XRD magnetic susceptibility μSR energy band calculations	in situ observation of the reaction forming $PbVO_3$ broad maximum at 200 K ZFC-FC difference AFM transition at 40-50 K	large tetragonal distortion due to V d orbitals degeneracy lift 2D AFM but with frustrations AFM dominates and leads to long range ordering ordering not visible by NPD due to small spin
2008	Tsirlin [34]	$PbVO_3$ powder starting materials: oxides: PbO, VO_2 HP = 5 GPa HT = 950°C t = 2 h	magnetic susceptibility specific heat energy band calculations	broad maximum at 200 K anomalies in magnetic susceptibility at 40-50 K	frustrated square lattice (FSL) model frustration breaks long range ordering

				no transition visible in specific heat measurements	liquid spin ground state
2009	Tsuchiya [40]	$PbV_{1/2}Fe_{1/2}O_3$ powder starting materials: PbO, V_2O_5, Fe_2O_3 or $Pb_4V_2O_9$, Fe_2O_3 HP = 7 GPa HT = 800-1000° C	XRD / XRD at HT XPS magnetic susceptibility dielectric constant DTA	lattice parameters + temperature variation space group P4mm structure calculation of bond lengths oxidation states Pb^{2+}, Fe^{3+}, V^{5+} AFM transition smaller than expected effective moment constant ε_r aat 9 K dispersion of ε_r with f at high temperature decomposition temperature 700 K	pyramidal coordination of B site ion disordered arrangement of V and Fe ions Fe-Fe AFM interactions predicted spontaneous polarization Ps = 88 $\mu C/cm^2$
2011	Angel Arévalo Lopez [41]	$Pb(M_{1-x}M'_x)O_3$ M; M' = Ti; V; Cr powder samples starting materials: PbO, VO_2, TiO_2, (CrO_2) HP = 20-80 kbar HT = 1073-1473 K	XRD electron diffraction HRTEM magnetic susceptibility	solid solution $PbVO_3$ - $PbTiO_3$ no strain effects	lone electron pair of Pb^{2+} correlated to electronic structure and size of B site cation responsible for tetragonality and tetragonal - cubic phase transition

I.2.6. Conclusions

$PbVO_3$ presents interesting structural and magnetic properties with interplay of magnetic and electric phenomena rarely observed. It can be synthesized in the form of bulk samples only by HP-HT at pressures from 2 to 8 GPa and temperatures from 650 to 1200° C. While the structure of $PbVO_3$ is well known and considered fairly simple, the question about the magnetic properties remains to be solved. The magnetic moment of V (V^{4+}) is not clearly observed for $PbVO_3$ samples. Experimental data is scarce and incomplete due to the difficulties of sample synthesis. The magnetization measurements reveal a very weak signal while specific heat measurements and NPD show no phase transition. Several models explaining these properties exist. These models describe $PbVO_3$ as an AFM with a high transition temperature that cannot be reached without destroying the sample or as a 2D long range ordered AFM or a spin glass or even an AFM spiral system. The dielectric properties of the sample are also important to investigate.

In the present work, we will attempt to shed some light on the problem of the magnetic structure of $PbVO_3$ by the partial substitution of V with Ti and with Fe. In the theory of the magnetic frustration, disorder induced by the substitution might release the frustration and lead to magnetic ordering. On the other hand if the weak magnetism is caused by the 2D arrangement of the V cations (due to the formation of the vanadyl bond), the substitution could reduce the tendency of the system to form a 2D lattice and could lead to the onset of a 3D magnetic ordering.

Therefore part of our study consisted in the synthesis and characterization of $PbVO_3$ as the witness sample. For $PbVO_3$ another objective was to advance the studies on single crystals, namely to refine the structure using single crystal X-Ray diffraction and to use the superior insulating properties of the crystals in the measurement of electrical properties. Another part of the study, as anticipated above, dealt with the effects of the partial substitution at the site of Vanadium by Titanium and Iron, i.e. V-Ti substitution and V-Fe substitution.

Chapter II. Experimental methods for sample analysis

II.1. XRD and NPD for structural characterization

By far the most widely used technique in this work is the X-ray powder diffraction measurement (XRD). Although XRD is an old technique, now having 100 years since it was discovered (1912), it still remains one of the most powerful and most widely used techniques in the field of material science for determining the structural and also microstructural properties of a crystalline sample.

In a crystal atoms are arranged with a certain periodicity and this periodic array of atoms acts as a diffraction grid for impinging X-ray radiation. X-rays are waves of electromagnetic radiation. When this radiation reaches the electrons of an atom, the electric component of the radiation causes these electrons to oscillate and this oscillation generates a new front of secondary X-ray radiation. This is in a simplified, semi-classical view the mechanism of elastic scattering of X-rays on the atoms of a crystal. These atoms therefore become new emitters of radiation. Since they are placed in a regular array, they generate a regular array of spherical waves which interfere and cancel each other out on most directions except a few specific directions in which the waves add up and produce a constructive interference. These directions are given by Bragg's law:

$2d\sin(\theta) = n\lambda$, where d is the distance between scattering planes of atoms, i.e. the interreticular distance, θ is the angle along which the constructive interference is formed (and is equal to the incidence angle), n is an integer defining the diffraction order and λ is the wavelength of the X-ray radiation used. Figure 2.1 shows a representation of the path of rays forming constructive interference for a set of inter-atomic planes spaced at d. This is the basis of the XRD technique. X-rays, rather than visible radiations, are very well suited for this type of measurements because the wavelength of X-ray radiation is the same order of magnitude as the inter-atomic spacing, i.e a few Å. For example the Cu Kα1 radiation wavelength is 1.5406

Å and the distance between (100) atomic planes in a typical perovskite oxide is about 4 Å.

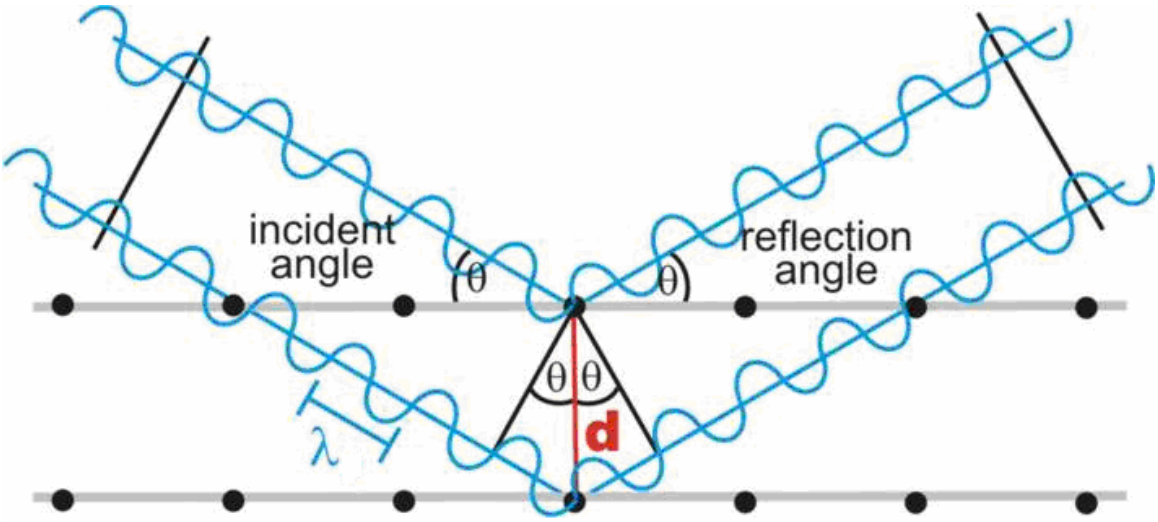

Fig. 2.1. Diffraction of X-rays on a set of atomic planes. Constructive interference is observed when the difference in the paths taken by the two reflected waves (upper and lower) is an integer multiple of λ [47].

The diffraction mechanism on the crystallographic planes is not limited only to the X-ray radiation. Neutrons and electrons can also be used in diffraction techniques since these particles possess an associated wavelength of the same order of magnitude as the inter-reticular distance in between the atoms of a crystal. Even though the nature of the interaction between neutrons and matter (or electrons and matter) is different from that of the X-ray – matter interaction, the very principle is the same.

The method described above is the classical diffraction technique, called the angular diffraction technique, or the diffraction at constant wavelength. This is however not the only diffraction technique available. Energy dispersive X-ray (EDD) diffraction or time of flight diffraction for neutrons also exist and present their own advantages and limitations. For instance energy dispersive X-ray diffraction is very useful in confined environments and in situations in which fast data acquisition is required. Such is the case in the studies of chemical reactions that take place at high pressures.

In this work, we will focus only on the conventional, constant wavelength diffraction methods. Ideally, XRD is conducted on a single crystal as single crystal

XRD offers more structural information in a more straightforward manner but this requires the preparation of a single crystal of good quality and reasonable dimensions (typically 100µm in diameter) and this is not always obtainable, therefore, most of the time diffraction measurements are carried out on powders. The procedure employed for single crystal XRD data collection and analysis will be described in the corresponding part of chapter IV. A powder is defined as a sample divided into small homogenous particles called crystallites or grains. An ideal powder for XRD is made of a large number of small crystallites (< 20 µm) randomly oriented. In that case there will always be some crystallites properly oriented to respect the condition for diffraction.

It is generally easier to have a sample in powder form and the very process of XRD measurement itself is far simpler for powder samples than for single crystals. On the other hand the data interpretation can be more complex in the case of powder XRD and the precision obtained is poorer. That is because in the case of single crystal XRD, the user measures directly the position and intensity of each Bragg peak, which allows reaching high counting statistics and thus high precision an accuracy. In the case powder XRD, the counting statistics is much less and Bragg reflections tend to overlap, which limits the precision at which they can be measured.

Further on we will discuss the data acquisition with respect to the geometry of the diffractometer we used and we will review the steps in data interpretation.

II.1.1. X-Ray diffractometers

An X-ray powder diffractometer consists in an X-ray source (X-ray tube or synchrotron), a sample holder, a detector which measures the number of X-ray photons that arrive on it and, the heart of the machine, a goniometer which measures the angle at which the detector is rotated, relative to the X-ray source – sample direction. As already implied, the X-ray source shoots a beam of collimated (and sometimes monochromated) X-rays onto the sample. The sample then diffracts, shooting the X-rays at specific directions, specific angles by the mechanism discussed in the previous section. Since the powder grains are randomly oriented, each reflection at a given d_h will produced a cone of diffracted beam at the corresponding Bragg angle. The detector is then rotated in the plane formed by the incident beam

and the normal to the surface of the sample in an angular range of usually 10 to 120 degrees. By convention this angle is labelled the θ angle. In doing so the detector intersects the cones of diffracted beams of X-ray radiation and records the intensity of the beams he cuts. At the same time the goniometer measures the position, i.e. the angle of the detector. The two data (angle and intensity) are then correlated by a computer and consequently generate the XRD diffraction pattern, the XRD diagram, of the sample that is studied. Figure 2.2 shows a typical configuration of a diffractometer. Two main configurations exist. These are the so called reflection geometry and the transmission geometry. In the symmetrical reflection geometry (also called Bragg-Brentano geometry) the source and the detector are placed on the same side of the flat sample and the radiation is "reflected" by the sample from the source into the detector. In symmetrical transmission geometry the source and the detector are located on either side of the flat sample and the source shoots the X-ray beam through the sample. Another type of transmission geometry is the so-called Debye-Scherrer geometry, where the sample is contained in a cylindrical capillary placed along the goniometer rotation axis. Nowadays, the entire process of data acquisition is automated. High precision stepper motors are used to accurately determine the position of the detector and linear detectors are used to gather more information on a single pass. However, in the basic design and functionality the diffractometer evolved little from the early machines used by von Laue.

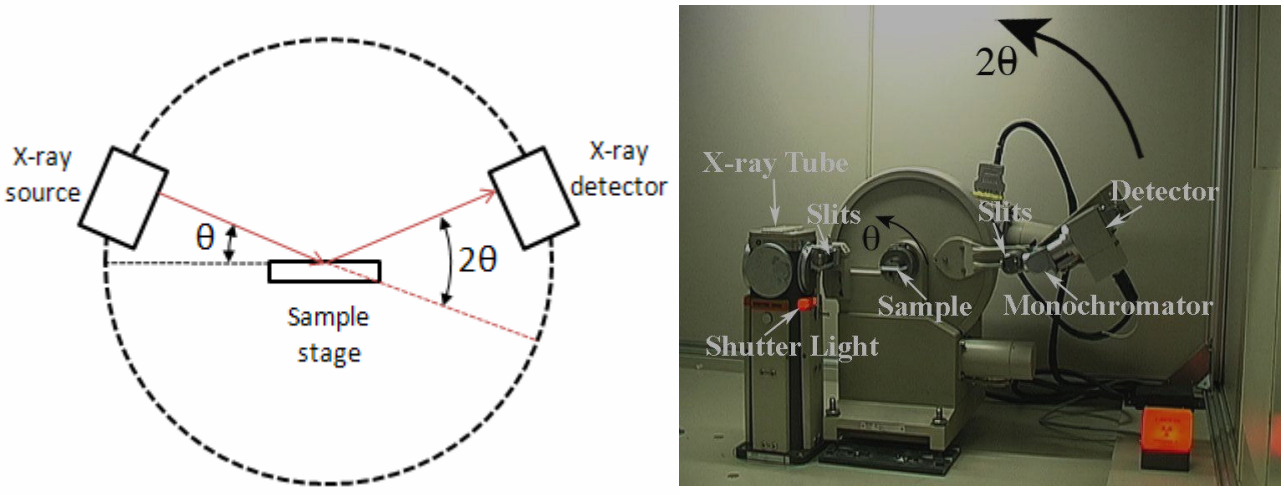

a) b)

Fig. 2.2. components of a diffractometer working in reflection geometry a) schematic representation [48], b) actual diffractometer (Philips X'Pert X-ray Diffractometer) [49]. The large wheel in the centre of the image is the diffractometer's goniometer.

II.1.2. Diffraction data interpretation

By the process described above, the raw data obtained in a diffraction measurement (the diffraction pattern of a powder sample) is nothing more than just a list of intensities collected at regular angular intervals. Further on, the work of the experimentalist is to turn somehow that list of numbers into parameters that have a physical meaning, for example the lattice parameters, the size and aspect of the crystallites, the angles and distances between the atoms of the unit cell, the purity of the sample and so on. Back in the day this was done by hand and it was a very laborious task. Nowadays the treatment of a diffraction pattern is done on a computer.

An X-ray powder diffraction pattern presents a series of peaks located at specific angles. There are 4 observable parameters on a diffractogram, three of which determine the peaks and one which describes the background between the peaks. The three parameters that define the diffraction peaks are the position, the width and the intensity of the peaks in cause (sometimes peaks are called reflections). Each one of these observable carries specific information about the sample.

a) position of the peaks

The position of the peaks relates directly to the inter-reticular distance through Bragg's law, which can be rewritten as $\lambda = 2d_h\sin\theta_h$ (for n = 1). For every set of interatomic planes defined by the Miller indices (h, k, l) there is an interreticular (interplanar) distance d_{hkl}. If the Bragg law can be respected (no systematic extinctions or other constraints) this distance will generate a diffraction peak labelled again (h, k, l) at a precise angle, θ_{hkl}. Going backwards, from the precise measurement of the θ_h angle where (h = h,k,l) the d_h distance can be calculated and this distance is related to the lattice parameters of the sample in question. In principle, with a sufficient number of determined d_h distances it is possible to deduce the lattice parameters.

Naturally for such a calculation to work it is necessary to have a sample containing ideally a single phase or, if this is not possible, a sample that contains at least 95 % the desired phase, considering 5 % as the limit at which an impurity phase can still give a clear signal in the diffraction pattern. If impurities are present in the sample that is under investigation the problem becomes far more complicated.

Another requirement is to have a very well adjusted, very well calibrated diffractometer to reduce the number of systematic errors. It should also be mentioned that strain and structural defects such as stacking faults can affect the position of the peaks, making the calculation of inter-reticular distances more complicated

b) width and shape of the reflections

The width and shape of the reflections give information about the microstructure of the sample. How it does that and how to extract the information is an art in itself. Without having any chance to give a complete description of the phenomenon some guidelines are presented nevertheless. The width of a reflection is defined by the FWHM parameter (full width at half maximum), which represents the extent of the peak at the half of the peak's height, or by the integral width (marked as β) which is the width of a rectangle with the same area as that of the peak and a length equal to the height of the peak. The latter has the advantage to be independent from the peak shape and is generally used for description of microstructure effects.

Roughly speaking there are two contributions to the width of the reflection. There is an unavoidable instrumental broadening, or the contribution given by the machine itself and a sample broadening, a contribution given by physical effects in the sample in question. Each contribution may be more or less empirically described by an analytical function and the convolution of these two functions gives the profile of a reflection, or in other words, the function which describes the distribution of the intensity in function of the θ angle, in the vicinity of the Bragg reflection position. This function is often noted $\Omega(2\theta)$.

For an X-ray powder diffractometer or for a high resolution neutron diffractometer the instrumental contribution is quite small so the sample broadening effects become sizeable and must be taken into account.

Over the years, several profile shape functions have been proposed to describe the shape of the diffraction peaks, each function having specific advantages and disadvantages. The choice of the most convenient one will depend on factors such as instrumental resolution, degree of sample broadening effects, need for accurate microstructural information, etc. The profile function widely accepted as the best approximation to most observed reflection profiles is the Voigt function, which is convolution between a Gaussian and a Lorentzian function. The expression of the Voigt function is the following:

$$\Omega(2\theta) = \Phi_0 \frac{1}{\sqrt{\pi}H} \int_{-\infty}^{+\infty} \frac{\exp(-t^2)}{\phi^2 + (\frac{2\theta - 2\theta_h}{H} - t)} dt$$

where

2θ is the angle at which the function is calculated

$2\theta_h$ is the position of the centre of the Bragg peak

H is the FWHM

Φ=H/β is the form parameter [50].

This function is complicated and a model based on this function requires a lot of computing time and power. Therefore, often an approximation of the Voigt function is used instead. The light-version of the Voigt function is called the pseudo-Voigt and consists in a weighed summation of the Gaussian and Lorentzian functions. The expression of the pseudo-Voigt type of function is:

$$\Omega(2\theta) = \eta.L(2\theta, H_L) + (1-\eta).G(2\theta, H_G)$$

G and L are functions and represent the Gaussian and Lorentzian components of the pseudo-Voigt function, with their respective widths at half maximum, H_G and H_L and η is a mixing parameter showing how much of the Gaussian and of the Lorentzian components are induced into the pseudo-Voigt. The values for η go between 0 and 1 with η = 0 meaning only Gaussian function and η = 1 meaning full Lorentzian function [50].

The expressions for the Gaussian and Lorentzian functions are:

$$G(2\theta, H_G) = \frac{2}{H_G}\left[\frac{\ln 2}{\pi}\right]^{1/2} \exp(\frac{-4\ln 2}{H_G^2}(2\theta - 2\theta_h)^2)$$

$$L(2\theta, H_L) = \frac{2}{\pi H_L}\left[1 + \frac{4}{H_L^2}(2\theta - 2\theta_h)^2\right]^{-1}$$

In a simplified view, the Gaussian part deals with the instrumental contribution while the Lorentzian is concerned with the sample contribution, with the microstructural properties of the sample. The two components can in principle be separated due to the fact that their behaviour with respect to the Bragg angle differs. It has been shown by

Cox that H_G and H_L vary differently with the diffraction angle. This has lead to the development of the Thomson-Cox-Hastings (TCH) function [50, 85], which gives the variation of the width and shape of the reflections according to the angle at which they appear. In this model the Gaussian widening varies according to the expression:

$$H_G = \left[U.\tan^2\theta + V.\tan\theta + W + P/\cos^2\theta\right]^{1/2}$$

This is the so-called Cagliotti law which defines the general form of a spectrometer resolution function. In principal, the values of U, V and W can be calculated from the instrumental set up.

The Lorentzian widening part is described by:

$$H_L = X.\tan\theta + Y/\cos\theta$$

Here, the first term describe the effect of mechanical strain on the reflection width, while the second is related to particle size and is similar to the well-known Scherrer equation.

Both contributions may be used in the refinement of a diffraction pattern, in which case the refinable parameters are U, V, W, X and Y (the term in P is rarely used). Another possibility is to consider the widths of two contributions equal, $H_G = H_L = H$. In that case the refinable parameters remain just H and η. The choice of the two possible ways of refining the data depends on what the user aims at and the quality of the XRD diagram. The TCH function / option is more complicated (has more parameters that can be adjusted) and is better suited for extracting accurate structural and microstructural information about the sample when a high resolution diffractometer has been used, while the second option, the one with fewer parameters allows for an easier refinement and is better suited for less sophisticated data processing such as the phase identification in a sample or for lower resolution experiments.

c) intensity of the diffraction peaks

The intensity of the diffraction peaks gives information about the structure of the material, about the manner in which atoms are stacked in the unit cell. This is the third parameter which describes a peak in “our model” and the last peak related measure directly obtained from the diagram. The diffracted intensity I_{hkl} can be obtained in principal by integrating the diffraction profile for each (h, k, l) reflection. This method is however limited to the cases where the peaks do not overlap. That is

seen in very high resolution diagrams or in diagrams measured for samples presenting a simple, high symmetry and small cell structure. In the more frequent situation in which the peaks do overlap, the extraction of the intensity will be much more accurate and precise if done by a full profile refinement of the data, i.e. the Rietveld or the LeBail methods.

On the other hand, when a model of the structure is known, the intensities of the Bragg peaks can be calculated. The equation that returns the diffracted intensity has many different terms and different expressions depending on the geometry of the diffractometer and the type of radiation (X-rays or neutrons) employed.

For example, for the widely used Bragg-Brentano geometry, the intensity of the reflections can be calculated from the following equation:

$$I_h = \left(\frac{I_0 \lambda^3 l_s}{64\pi R}\right)\frac{1}{\mu}\left(\frac{e^2}{m_e c^2}\right)^2 \frac{j_h}{V_c^2} Lp\left|F_h\right|^2$$

For the transmission or Debye-Scherrer geometries the first constant terms will be slightly different but the general form remains the same.

Deducing the meanings of the constants is fairly straightforward task for most of them. For example the meaning of some of the parameters seen in the above equations is listed below:

- I_0 – the intensity of incident radiation
- λ – wavelength of the radiation used in the experiment
- l_s – size of detector slits
- R – sample to detector distance
- V – volume of sample irradiated by the beam
- e – electron charge
- m_e –mass of electron
- c – speed of light
- V_c – unit cell volume [50].

With the constant terms regrouped the equation for the diffracted intensity can be rewritten in a condensed form:

$$I_h = S.j_h.Lp.\left|F_h\right|^2$$

where:

- S is a scale factor, common to all the reflections
- j_h is the multiplicity of the reflection h, since all reflections with the same d_h are superimposed on a powder pattern
- Lp is the Lorentz-polarization factor. The Lorentz term is related to the speed at which the reflections cross the Ewald sphere, while the polarization term depends on the nature and polarization of the radiation and on the type of monochromator used (if any). These terms can be calculated from known instrumental parameters.
- F_h is the structure factor for the reflection h [50].

The structure factor is the most interesting one since it reflects the arrangement of atoms in the unit cell. The structure factor can be viewed as the Fourier transform of the atomic motif of the crystal. It has the following expression for the h = (h, k, l) reflection:

$$F_{hkl} = \sum_{j \subset cell} f_j T_j \exp(2i\pi(hx_j + ky_j + lz_j))$$

The first term, f_j, is the atomic scattering factor for the j atom of coordinates (x_j, y_j, z_j). For x-rays this is known as the form factor of the atom and for neutrons as the Fermi length, b_j [50].

T_j is the Debye-Waller term which describes the static and dynamic displacement of atoms about their mean positions. For an isotropic harmonic thermal displacement (oscillations of the atom inside an isotropic parabolic potential well centred about its equilibrium position) the atomic displacement factor is written as:

$T_j = \exp\{-B_j * (\sin^2\theta) / \lambda^2\}$ where B_j is the atomic displacement in $Å^2$. $B_j = 8*\pi^2*\langle U_j^2 \rangle$ where $\langle U_j^2 \rangle$ is the root mean square of the amplitude of oscillation.

Finally, the exponential term of the structure factor contains the information about the atom positions in the cell.

d) background

The background is the fourth type of observable in a diagram (after the 3 ones which determined the diffraction peaks, namely, position, widening and intensity). It

is the least interesting part of the diffractogram and the effort is made to increase the peak to background ratio but, it can nevertheless provide some additional information about the sample. The background too is composed of two contributions, an instrumental one and a sample-related one.

The instrumental background can be generated by stray X-ray photons which can be residual radiation of other wavelengths still present or diffuse scattering from air or the environment of the diffractometer.

The sample generated background can be the result of other scattering interactions from the sample, such as fluorescence or Compton scattering, or some peculiarity of the sample's structure (such as short-range order) or simply the presence of an amorphous phase in the sample. Short-range ordering effects and amorphous phases may generate a more or less structured background while the other sources produce only a monotone noise.

In practice, in usual diffraction experiments the background is simply excluded from the diagram and/or modelled with a more or less complicated polynomial function. However, in more specialized application the study of the background and of the phenomena that generate it can be a useful tool, but this is an entirely different field and consequently those methods will not be discussed in this work.

II.1.3. Rietveld Refinement

In the previous section we discussed some models used to describe an XRD diagram. Now we will discuss the way in which those models are used to fit an experimental set of XRD data. While physical properties of interest can be calculated "by hand" from an XRD, again computers and crystallography go hand in hand and stylish computing codes are employed in order to retrieve the information about the respective properties. An initial model of the structure of the material is inserted into the PC and the code then simulates a diffraction pattern based on the provided model. The code compares the calculated (simulated) diagram with the experimental one and attempts to re-adjust the initial model, to change some parameters from the model, in order to reduce the differences between the calculated and observed diagrams. This process is called the full profile refinement of an XRPD pattern, also known as the

Rietveld method. The method was derived in 1969 by Rietveld for the refinement of NPD patterns and was later extended to XRPD. Further improvements have been made and now the method is also extended to energy dispersive X-ray diffraction and time of flight neutron diffraction.

As mentioned earlier, some initial "guess" about the structure of the sample under investigation is required. If the material is absolutely new, if no previous reference about even a similar material exists then the user needs to start from scratch and for that refinement codes have only a limited use. Then a starting structural model has to be found using sophisticated crystallographic structure solution methods (direct methods, use of the Patterson function, charge flipping, etc.) in combination with other techniques (for example electron diffraction/microscopy). Since we did not used them, these methods for ab initio structure determination will not be discussed here.

One of the most successful and widely used codes for the Rietveld refinement of XRPD or NPD data, is the Fullprof program, which is part of the Fullprof_Suite software suite which allows performing most types of crystallographic calculations. This is the program we have used throughout our studies for crystal structure refinements.

The greatest problem faced in any powder diffraction experiment is the overlapping of peaks as this may render highly inaccurate the retrieval of information from the diffraction peaks. That is why XRPD was long time limited only to simple structures of high symmetry which will not generate overlapping peaks. However improvements in computation techniques made it possible to use XRPD in the study of more and more complicated systems. In this context, the greatest achievement of the Rietveld refinement was the fact that it could do just that, it could allow avoiding the problem of overlapping peaks leading to accurate determination of the peak characteristics (position, width/shape, intensity).

Unlike other, previous methods which focus on one individual peak, the Rietveld refinement plays on the entire diffraction pattern at the same time using as variables the instrumental characteristics of the diffractometer and the structural and microstructural parameters of the sample. On these variables the program builds a calculated diagram.

In the simulated diagram, the intensity at every angular point i is calculated as the sum of the background intensity and of all the peaks that superimpose on point i:

$$y_{ci} = y_{bi} + \sum_{\phi=1}^{N} S_{\phi} \sum_{k=k1}^{k2} j_{\phi k}.Lp_{\phi k}.O_{\phi k}.M.\left|F_{\phi k}\right|^2.\Omega_{i\phi k}$$

In this equation one can recognize the overall aspect and some of the terms from equation X that was used to define the intensity of a Bragg reflection. The terms are as follows:

- y_{ci} is the calculated intensity at point i
- y_{bi} is the intensity of the background
- S_{Φ} is the scale factor for the phase Φ
- $j_{\Phi K}$ is the multiplicity of the reflection k
- $Lp_{\Phi K}$ is the Lorentz-polarization factor
- $O_{\Phi K}$ describes the effect of preferential orientations
- M describes the absorption and/or microabsorption
- $F_{\Phi K}$ is the structure factor
- $\Omega_{i\Phi K}$ is the profile shape function [50].

The first summation is calculated over all the crystallographic phases present in the sample and the second one over all the reflections overlapping in the point i.

The Rietveld refinement is a least-squares method and works by minimizing the residue which is:

$$M = \sum_i w_i (y_i - y_{ci})^2$$

Where y_i, and yc_i are the observed and calculated counts at point i, and w_i is the statistical weight defined as $w_i=1/y_i$. The sum extends over all the points in the pattern.

The quality of the refinement is check by using different agreement factors. The most important ones are:

$$Rwp = \left[\sum_i wi(yi - yci)^2 / \sum wi.yi^2 \right]^{1/2}$$

which determines the quality of the full profile agreement. Rwp is supposed to reach at convergence the value of Rexp, which depends on statistics only. The other reported agreement factor is the so-called χ^2:

$$\chi^2 = M/(N-P+C)$$

$$R\exp = Rwp/\sqrt{\chi^2} = \left[(N-P+C)/\sum_i wi.yi^2\right]^{1/2}$$

Where M is the function to minimize defined above, N is the number of observations (points in the diagram), P and C are the number of parameters and constraints between them.

II.1.4. Guidelines for usage of the Rietveld refinement

The Rietveld Refinement uses the least square method to approach the structural and microstructural model of the sample to the actual specimen. However, such a method tends to stop at the first minimum it encounters, regardless of whether that point is an absolute minimum or just a local minimum. The program for handling the Rietveld code is at a first glance fairly simple. The user is presented with a list of parameters from which he can choose which parameters to "freeze" and which parameters to "release" for the refinement. Freeze and release refer to locking a parameter to a fixed value or allowing the value of that parameter to be adjusted by the program so that the model fits the experimental data as best as possible. This in itself is not something very hard to do but under the friendly interface there are a lot of hidden traps and the refinement can quickly become unstable or can return aberrant values for some parameters while still keeping the calculated diagram very closed to the experimental one. In order to avoid such problems, some simple, common sense, principles can be followed:

1. Know very well your diffractometer! The best results are obtained when the instrumental resolution function (the IRF) is known, that is when the evolution of the widening of diffraction peaks with respect to the 2θ angle is known. That function can be determined by measuring a "standard sample", a sample which gives no significant contributions to the width of the reflections. That way, the width observed is due "only" to the machine. Such a measure is particularly important in the case/study of a completely unknown sample. With the IRF known, the program is able to return valuable information about the microstructure of the sample (crystallite size and/or presence of mechanical strain)

2. Use the best possible model to start the refinement! The program does the refinement of a model. It does not provide a model out of the blue. If you start with some random initial values the program will not be able to untangle itself and bring the random initial values to reasonable limits/dimensions. If the structural model is unknown or only vaguely known it sometimes helps to start with a Le Bail refinement which doesn't take into consideration the positions of the atoms in the unit cell and only plays on the dimensions of the unit cell (the lattice parameters) and the microstructure of the sample. Once these parameters are determined the user can try to tackle the atomic coordinates in the Rietveld refinement (which is sensitive to the intensity of the reflection, in turns related to the arrangement/stacking of atoms in the unit cell).

3. Do not refine all the parameters at the same time! Parameters have different effects on the diagram. They must be refined in successive, logical order. For example, it would be foolish to try and refine the parameters controlling the widths of reflections before those controlling their positions. Moreover, some parameters have very strong effects on the pattern while others only have minor effects. Therefore it makes sense to first refine the parameters that have a drastic effect on the refinement and leave the finishing touches for the last steps of the refinement. For example, for x-rays, one must refine the parameters describing the position of a lead atom before those related to oxygen, because the former is a much stronger scatterer. A general sequence of steps is listed below.

- scale factor and background
- sample displacement / or zero shift of diffractometer + lattice parameters
- profile shape function and asymmetry
- atomic coordinates and $B_{overall}$ (overall Debye-Waller factor)
- individual isotropic thermal displacement factors
- site occupancy if required
- individual anisotropic thermal displacement factors if required (rarely for powder diffraction)

4. Constantly check your progress! Most of the times a visual examination is the fastest and easiest way to check the refinement for rough errors. In FullProf the difference curve between the observed and calculated XRD patterns is plotted automatically. In an ideal case that curve is only a white noise signal. Many times

though this is not the case but the simple visual examination of the difference curve can provide clues as to what is not working in the refinement. Of course, looking at the agreement factor's values is also good practice.

5. Check the values of the refined parameters! If some parameters have large fluctuations (above 50%) or reach unphysical values, try to refine those parameters separately, at least during the early stages of the refinement.

II.1.5. Neutron powder diffraction (NPD)

Neutrons present the wave-particle duality and therefore wave-like properties which make (thermal) neutrons suited for diffraction in the same way that X-rays are used for the purpose. There are fundamental differences between the NPD and XRD techniques in what concerns the nature of the interaction of the radiation with the matter. While X-rays interact with the electronic cloud, neutrons interact with the nuclei of the atoms. This difference makes it possible to obtain complementary information from neutron powder diffraction experiments and from the classic XRPD. Also, neutrons interact with the magnetic moments that exist in the sample (if any) due to the fact that they carry a spin and this interaction provides information about the magnetic ordering of the material.

Several neutron scattering techniques are available (for example the time of flight diffraction method) yet further on we will discuss only the constant wavelength neutron diffraction and the way it is used in the refinement of the crystallographic (not magnetic) structure of our material.

The disadvantage of neutron diffraction techniques is the need for large sample quantities and fairly sophisticated installations. The need for large samples is simply related to the fact that neutrons are scarce and the direct beam flux is much smaller than even for a classical laboratory x-ray source. This has to be compensated by using a much larger sample and keeping reasonable resolution to maintain an acceptable flux.

A neutron powder diffractometer still has the "same" block units as an X-ray diffractometer, namely it consists of a radiation source equipped with a monochromator and filters to block unwanted radiation, some sort of a sample holder

and a detector to record the scattered radiation. But, the radiation source has to be a nuclear reactor or a spallation source, the sample holder is often equipped with a cryostat operating on liquid helium and finally the detector is a much larger and much more sophisticated piece than in a classic X-ray diffraction machine. In order the compensate for the relatively low neutron flux, NPD instruments use large position sensitive detectors which collect data on the entire 2θ range simultaneously, unlike the point detectors from XRD. The NPD detectors maybe also equipped with vibrating slits which block any radiation that does not arrive at the detector from the centre of the machine (from the sample) while not blocking any useful signal either.. Further technical details will be presented in the next section, with reference to the D1B diffractometer at ILL, Grenoble, which was used in this study.

In contrast to X-rays, absorption of neutrons by matter is generally quite small (except in the case of some elements as for example boron or gadolinium). Typical values for the absorption coefficient, μ are about 0.3 cm^{-1} for neutrons which are small, compared to values of about 500 cm^{-1} for X-rays. A few examples of travelling lengths, t defined as $t = 1/\mu$, corresponding to an attenuation of the incident radiation by 1/e are presented in table 2.1. The low absorption means that neutrons scan a large volume of the sample, therefore allowing large samples to be used, as well as bulky ancillary equipments. In a NPD instrument, the sample is placed in a cylindrical tube of several millimetres in diameter. The combination of this geometry and the large sample volume scanned by the neutrons makes the technique less sensitive to a possible texturing of the sample, which constitutes an advantage over XRD.

Table 2.1 Penetration depths for some common elements.

element	X-rays (cm)	neutrons (cm)
Al	0.0078	125
Mn	0.0005	1.7
Fe	0.0004	8.3
Ni	0.0025	4
La	0.0005	7.1
Pb	0.0004	333

As already said, one important aspect of neutron diffraction is the fact that neutrons interact with the nuclei of atoms and not with the electronic cloud (like X-rays). For X-rays the scattering power of the elements increases with the Z number. For neutrons the scattering power of the elements depends on the cross section of their nucleus and this varies almost randomly in the periodic table. Because of the linear increase in the Z number, X-rays can be unable to distinguish between neighbouring elements and are little sensitive to low Z elements. For neutrons a strong contrast may be observed between the same neighbour elements, or even between different isotopes of the same element. For example the scattering power (scattering length) for Mn is b = $-0.373*10^{-12}$ cm and for Fe is b = $0.945*10^{-2}$ cm. Figures 2.3 and 2.4 show the scattering power of various elements and a comparison between the scattering cross sections "seen" by X-rays and neutrons for a few common elements.

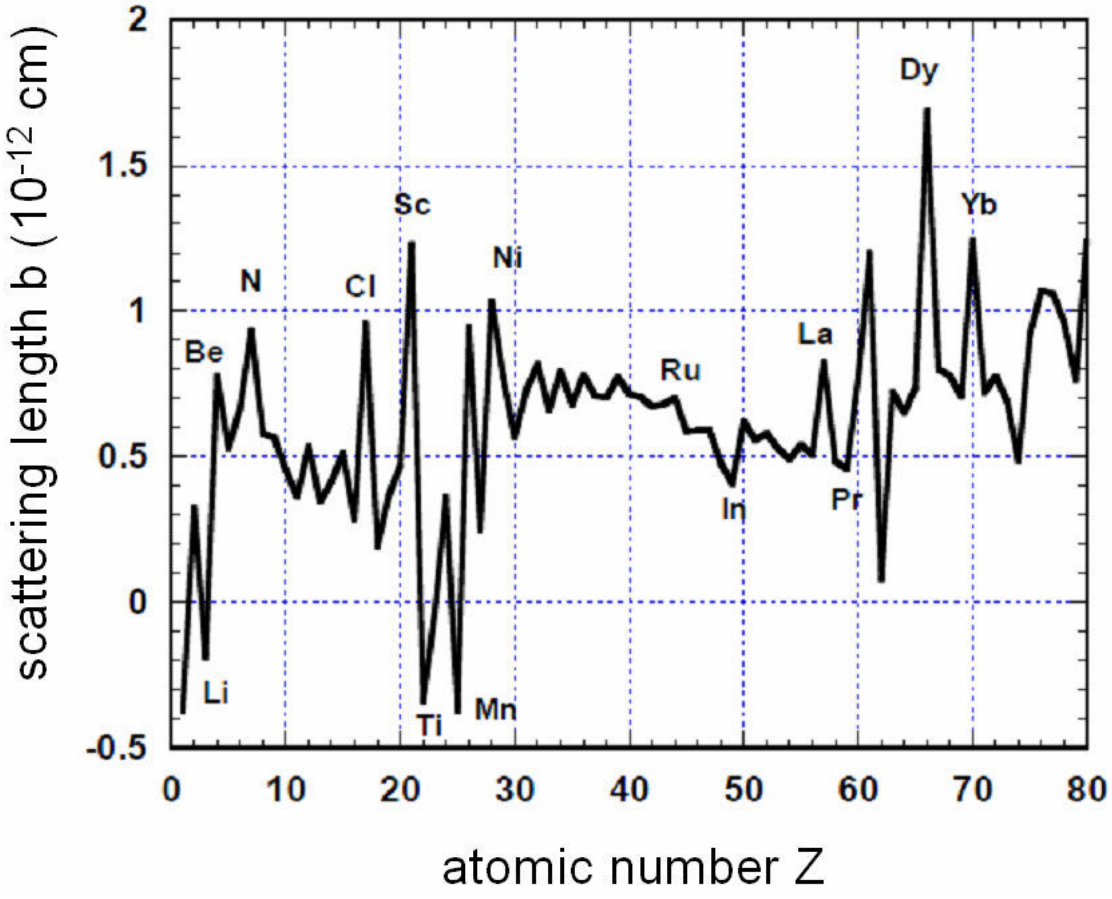

Fig. 2.3. Variation of the scattering length with the atomic mass [50].

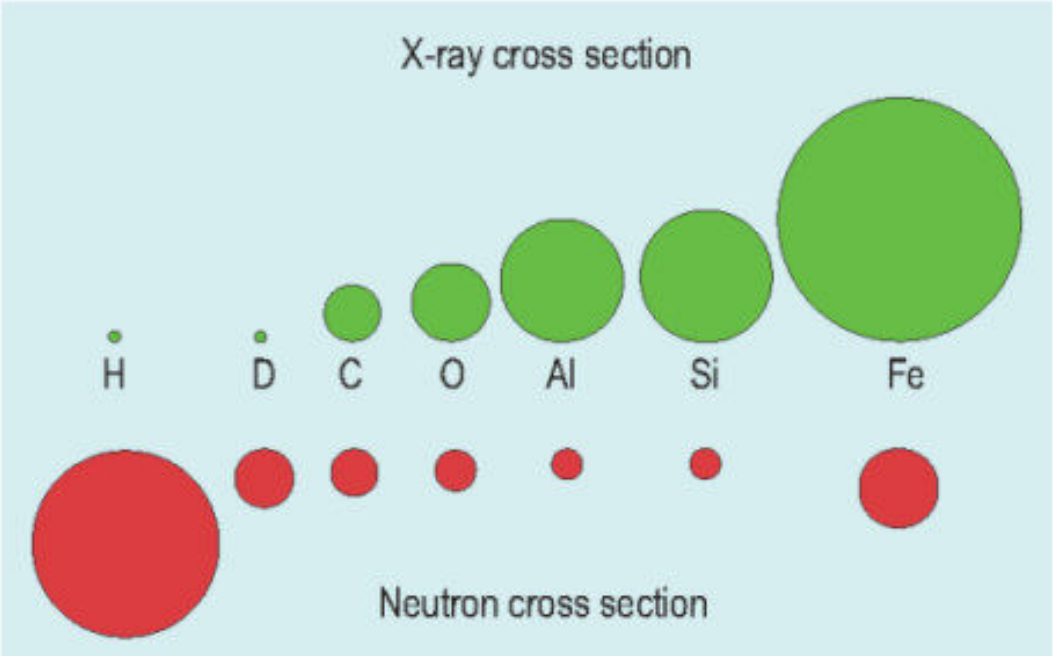

Fig. 2.4. Different scattering cross areas for X-rays and neutrons. The scattering cross sections for X-Rays are represented by green circles and the scattering cross sections for neutrons are represented by red circles [51].

In general NPD measurements are conducted on structures for which a model has been already determined by other techniques and the neutrons are used only to obtain more precise parameters for light atoms, distinguish between neighbouring atoms or investigate phase transitions, etc. Neutrons are very sensitive to the oxygen ions (and most of the other anions), approximately to the same extent as for the heavy cations which means that often cation-anion distances can be determined with better precision from NPD than from XRPD.

II.1.6. The D1B neutron diffractometer

Most of the NPD measurements were performed at the Laue-Langevin Institute (ILL) in Grenoble at the D1B diffractometer, although the D2B diffractometer from the same institute was also employed. A diagram with the main components of the D1B and a picture containing an overall view of the machine are provided in figures 2.5 and 2.6.

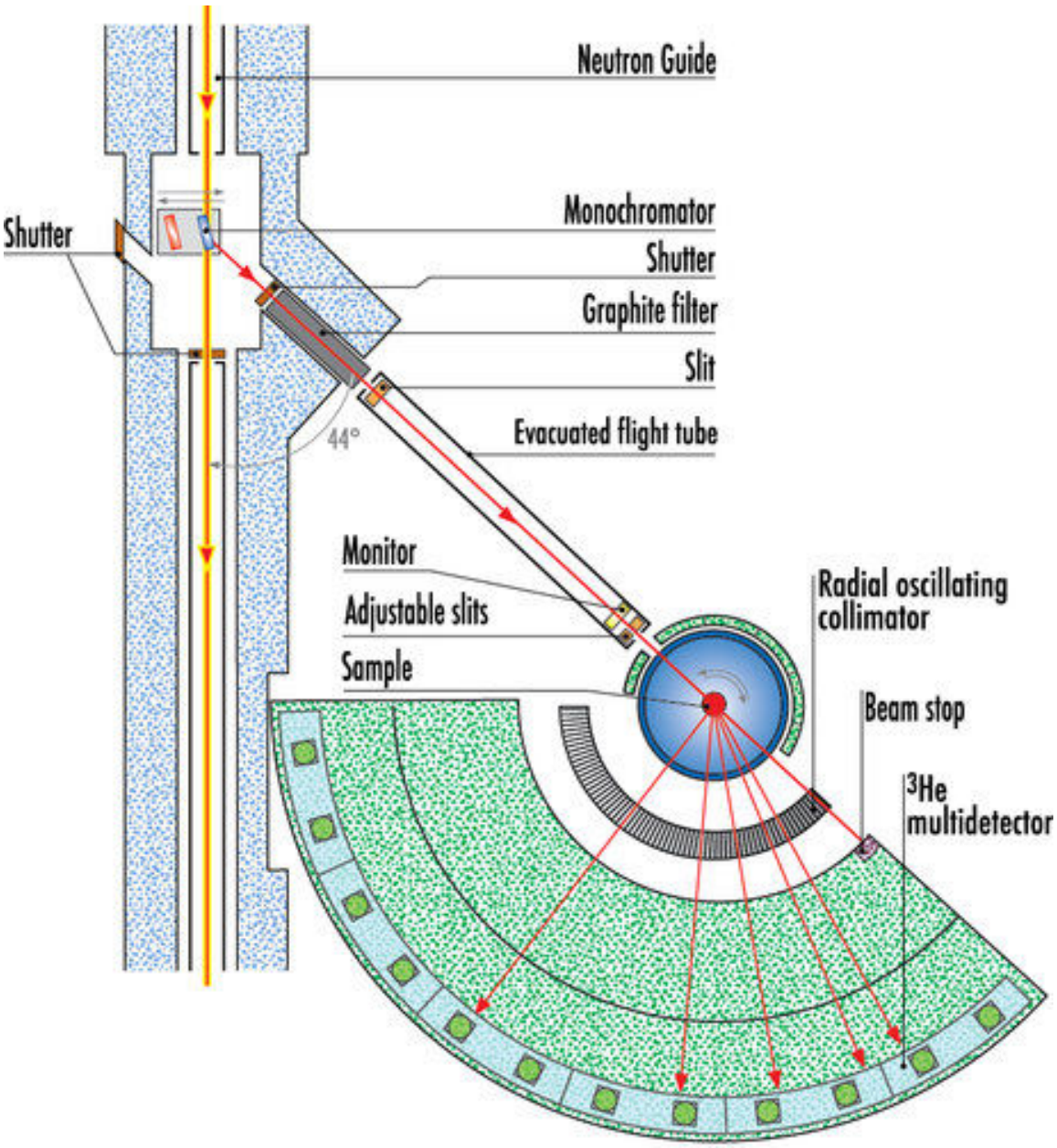

Fig. 2.5. The most important components of the D1B neutron diffractometer [52].

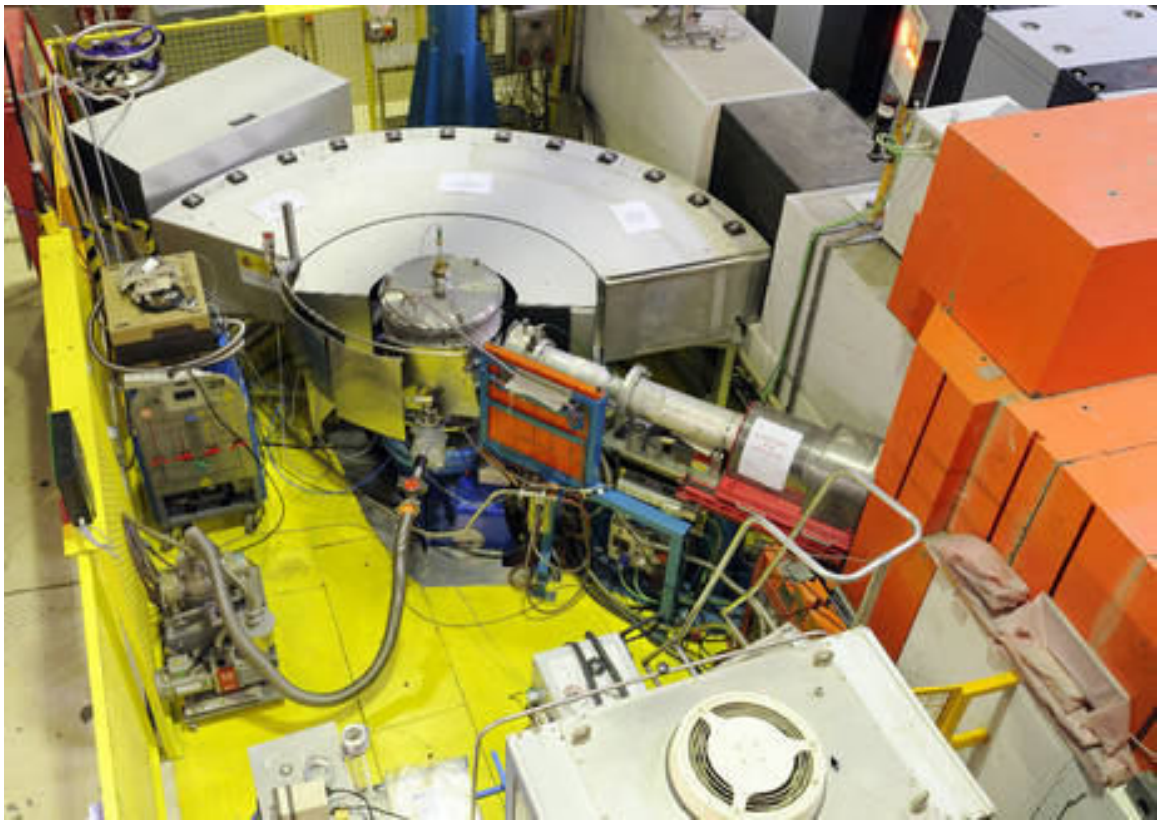

Fig. 2.6. Bird's-eye-view of the D1B diffractometer. One can easily identify the main parts from the diagram above. The sample is located in a furnace installed at the centre of the detector. A cryostat can also be installed in the place of the furnace [52].

This apparatus was designed to work at a high flux of neutrons and collect the scattered radiation on the 2θ range of 0.8° to 128.8°. Two wavelengths are available, namely 1.28 Å and 2.52 Å with the latter provided at a flux density 10 times larger than the former. The 2.52 Å wavelength is used in magnetic studies. The high intensity of the neutron beam is obtained at the expense of the high resolution but high resolution is less important for the magnetic diffraction since the (magnetic) signal is present only at low angles where the peaks are always well separated [50]. Therefore the gain in flux intensity far outweighs the loss in resolution. For an illustration of the loss of resolution, calculated diagrams for the same sample measured at the D1A (high resolution) and D1B (average resolution) are compared below, in figure 2.7.

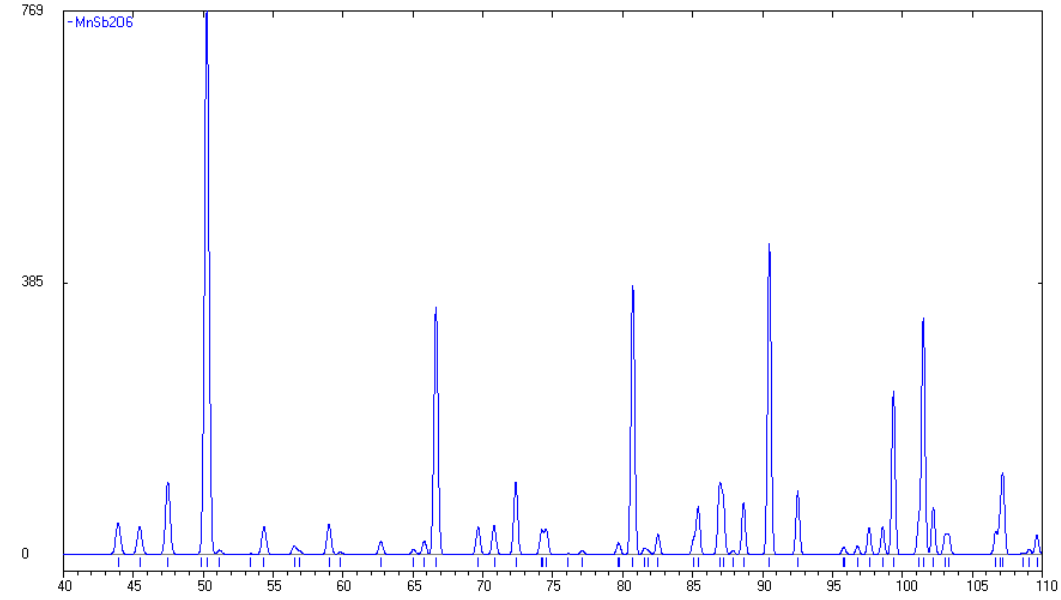

a)

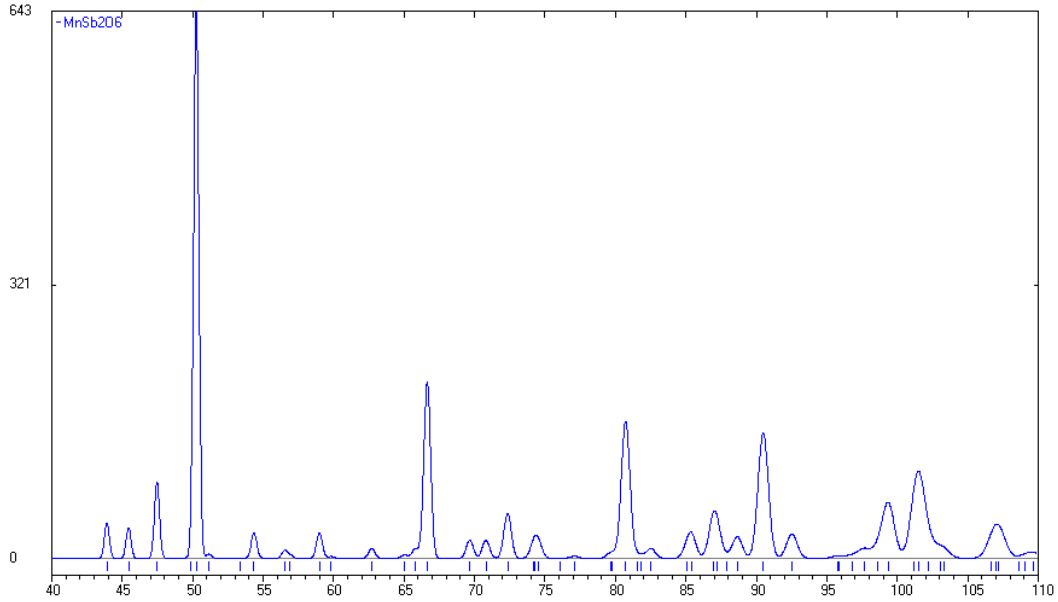

b)

Fig. 2.7. Calculated diffraction patterns for the diffractometers a) D1A and b) D1B [50].

A worsening of the resolution can be observed, particularly around 100° where the peaks are no longer resolved and begin to overlap instead.

II.2. SEM and EDX for morphology and chemical composition

The second most employed tool was the scanning electron microscope (SEM). The SEM was used intensively for the morphological and microstructural characterization of the samples. The energy dispersive X-ray spectroscopy (EDX) setup, built into the SEM was also put into action for the determination of the chemical composition and homogeneity of the samples. The principles of operation of the SEM and EDX are discussed below.

A scanning electron microscope produces an image of the sample under study by sweeping the sample with a focused beam of electrons and collecting as response the particles ejected by the sample.

The resolution of a microscope is limited by the wavelength of the radiation it utilizes and by the quality of the lens. When the size of the studied specimen has the same order of magnitude as the wavelength employed, diffraction effects start to become important and lead eventually to the point at which separate spots are no longer resolved. The associated wavelength of the electrons used in a SEM is much shorter than the wavelength of visible light, used in an optical microscope therefore the resolution of the SEM is much higher, in between 0.4 to 20 nm. By contrast, with an optical microscope details can be seen down to only 0.1–0.2 μm.

A SEM is essentially constructed from the following components:

- an electron gun which supplies a stream of electrons. The electron gun consists in an electron source and a Wehnelt cage that attempts to already reduce the dispersion of the beam of electrons.
- an electronic column which consists in a series of electromagnetic lenses and has the role of focusing the electrons into a fine beam
- a sample holder (called a stage) which allows the movement of the sample on the 3 axes + rotation around the vertical axis + tilt…
- a set of detectors that collect the particles (electrons and/or photons) emitted by the sample as a result of the electron-matter interaction
- vacuum pumps which maintain a pressure of about 10^{-5} - 10^{-6} mbarr in the chamber of the microscope.

Figure 2.8 shows the main components of a SEM.

Details about the coils found in the column are seen in the picture. These are the electromagnetic lenses that focus the more or less randomly emitted electrons from the electron gun into the fine beam of electrons that sweeps the sample. SEM images are obtained by synchronizing the coil which sweeps the beam of electrons on the surface of the channel with the coil that sweeps the beam of electrons on the screen of a cathode ray tube (CRT). This determines of the coordinates of a pixel from an SEM image with respect to the position of the scanning electron beam on the surface of the sample. The intensity of the pixel is determined by the number of electrons collected at the detector.

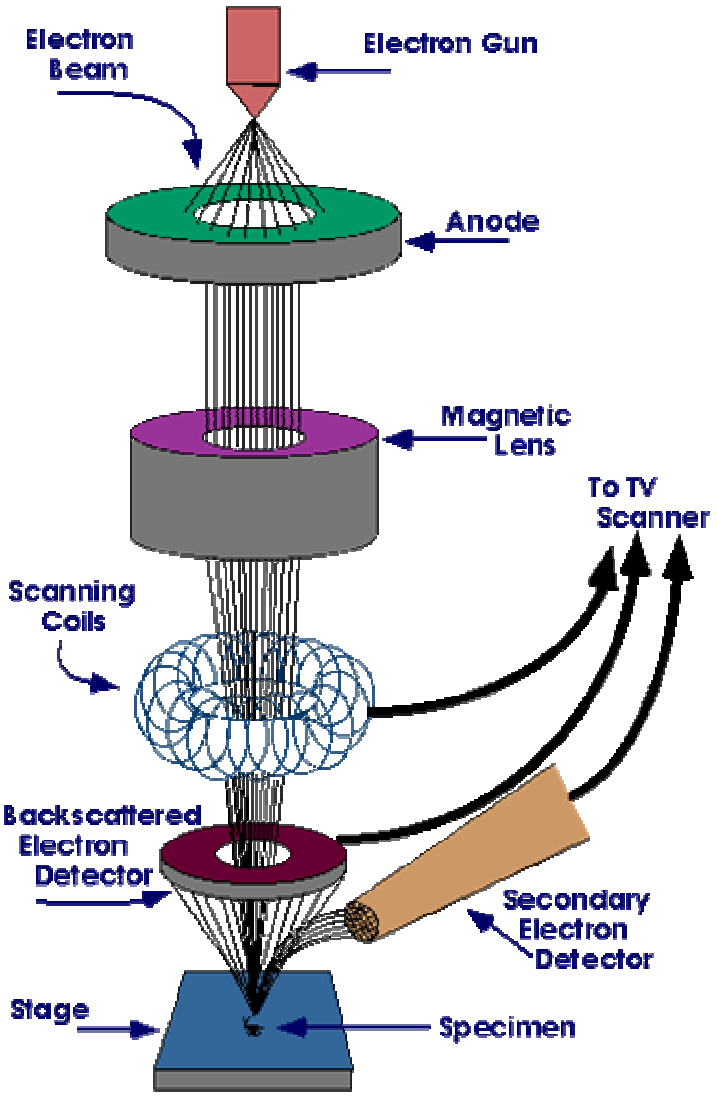

Fig. 2.8. Schematic representation of the main components of an SEM [53].

II.2.1. Electron beam – matter interaction

From the interaction of the incident electrons with the sample several types of electrons and photons are re-emitted. The different particles are collected with specialized detectors and the consequent signals are treated independently since different particles provide different types of information about the sample. Examples of re-emitted particles are secondary electrons, backscattered electrons, Auger electrons, visible light photons (cathodoluminescence), X-ray photons (figure 2.9). Of these particles only secondary electrons (SE), backscattered electrons (BSE) and characteristic X-ray photons will be discussed. Figure 2.10 shows the three types of particles and the region of the interaction volume from the sample from where they are emitted.

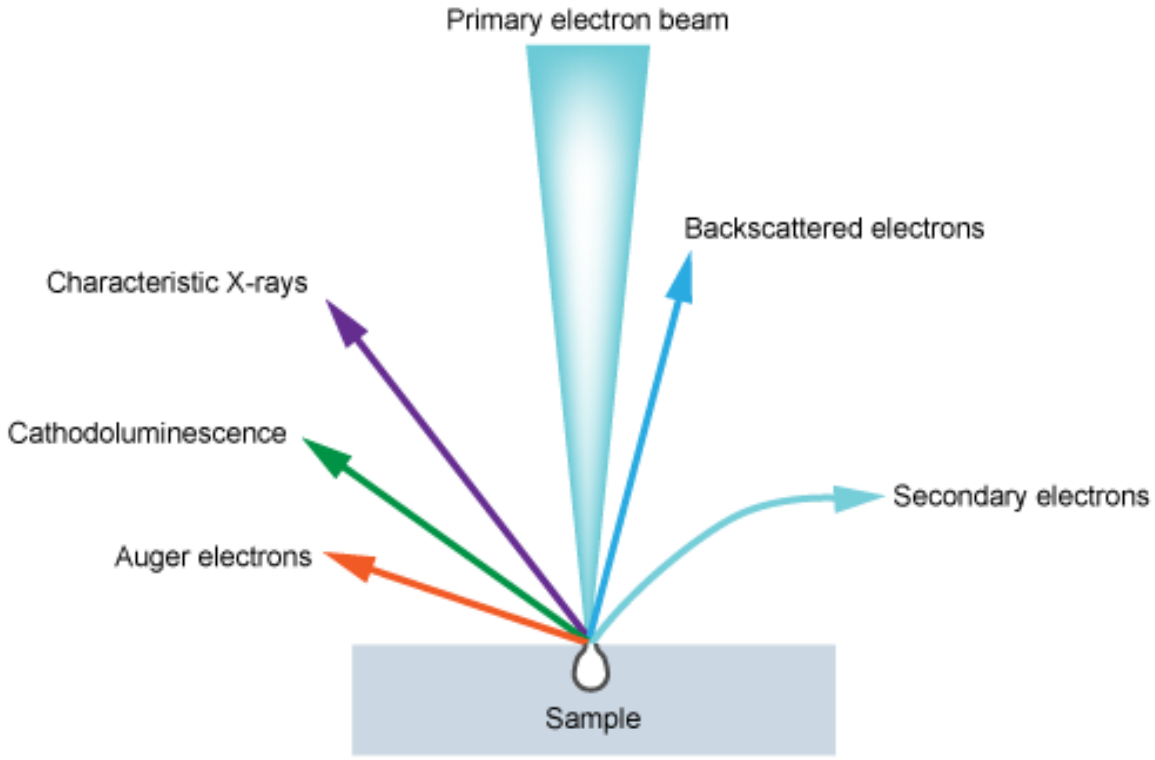

Fig. 2.9. The 5 main type of particles resulted from the interaction of the incident electron beam with the sample. It can be observed that the trajectory of secondary electrons is not straight unlike the trajectory of the BSE. This effect has applications on imagery (see below) [54].

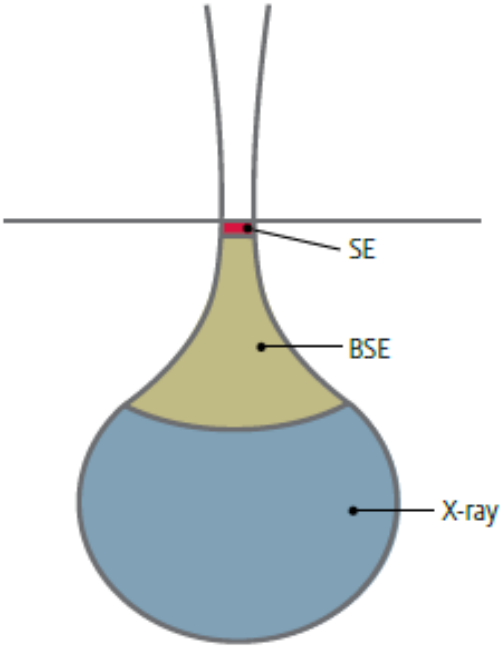

Fig. 2.10. The structure of the volume of sample that interacts with the electrons from the incident beam. The regions of the interaction volume which act like sources id SE, BSE and X-rays are highlighted [55].

a) Secondary electrons are electrons that used to belong to the sample, ejected by the collision with electrons from the beam. The energy of the secondary electrons is fairly low, of about 50 eV so these electrons are easily collected (or repelled) by applying a small positive (or negative) potential to the detector. Given the low energy from the collision, the SE are only emitted from a thin layer of the sample, typically below 10 nm. Since they are emitted from the surface of the sample they are very sensitive to the topography of the specimen. This makes SE very well suited in the acquisition of high resolution images of the sample as the number of SE emitted depends greatly on any tilt, or step of the surface of the sample.

b) Backscattered electrons are electrons from the beam which interact with the nuclei of the atoms and are elastically scattered on a direction close to the incident path. The energy of BSE is high, much higher than the one of SE and almost identical to the energy of the incident beam. Due to the higher energy BSE can travel through a thicker portion of the sample and are emitted from a larger interaction volume. Therefore, the image obtained in BSE has a lower resolution than the image obtained in SE. On the other hand, unlike SE which travel in a more or less random path, BSE

travel in a straight line and this property can be exploited in obtaining shadow effects which can give additional information about the morphology of the sample.

BSE are sensitive to the atomic number of the atoms from the sample. Heavier atoms re-emit more electrons than lighter ones so regions containing heavy atoms will appear brighter than regions made up from lighter atoms. This property gives what is known as the phase contrast and used in conjunction with EDX can give information about the homogeneity of the sample.

BSE are also used in a type of electron diffraction (EBSD) and can provide information about the structure and orientation of crystallites.

c) X-Ray photons are emitted by the following mechanism. A high energy electron from the beam ejects an electron from the inner shells of an atom from the sample. Another electron, from an outer shell, falls back to occupy the now available state. When this electron descends from the initial high energy state to the final low energy state it emits an X-ray photon. The energy of the X-ray photon thus created depends on the energy levels of the electron shells and is characteristic for every atomic species. The study of this characteristic radiation is the basis of the energy dispersive X-ray spectroscopy, or EDX (see next section).

Figure 2.11 shows a review of the ways in which SE, BSE and X-Ray photons are generated in a sample investigated by means of SEM.

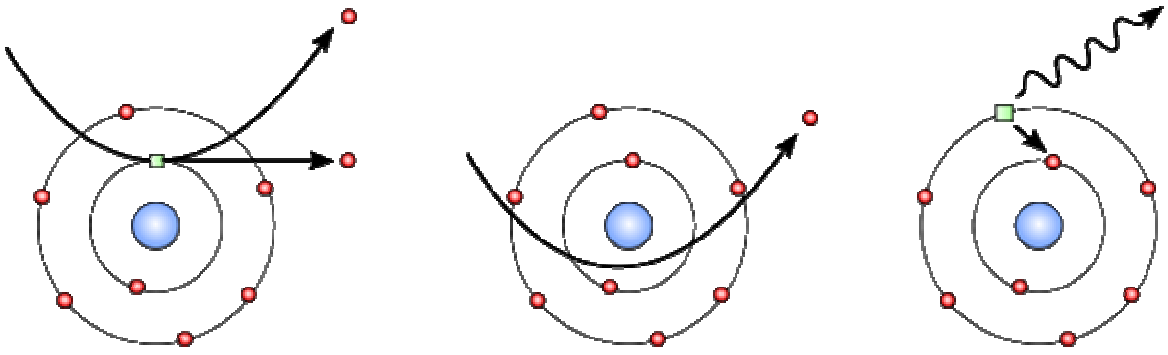

Fig. 2.11. Representations of the emission mechanisms discussed above [56].

II.2.2. Energy dispersive X-ray spectroscopy

In a broader perspective EDX is an investigation technique used for elemental identification or chemical characterization of a sample which works by analyzing the characteristic radiation emitted by the atoms of a sample as a result of the interaction with an ionizing beam. Each atom genus has a unique electronic structure that allows a unique set of transitions which are translated as a unique set of peaks in the EDX spectrum. Figure 2.12 shows a schematic representation of the principle of EDX and figure 2.13 shows an example of a typical EDX spectrum. The EDX spectra are obtained by converting the X-Ray photons into electrical signal in a solid state detector. The photon generates electron-hole pairs in the detector with the number of pairs proportional to the energy of the photon. With the number of charge carriers increased the current that passes through the detector also increases. This current can be measured and from it, the energy of the incident X-Ray phonon can be determined.

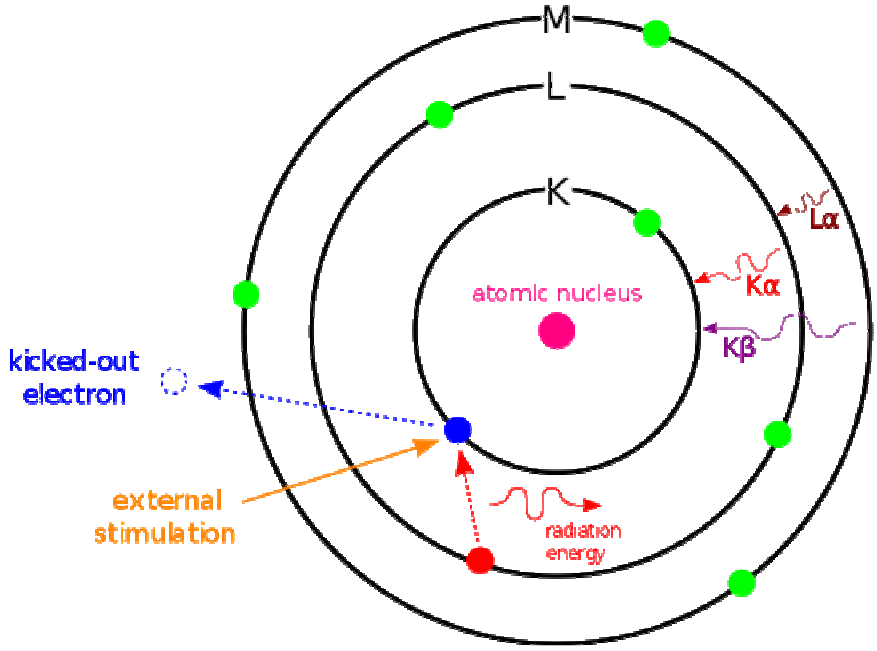

Fig. 2.12. Schematic representation of the process of characteristic X-ray emission, as used in EDX [57].

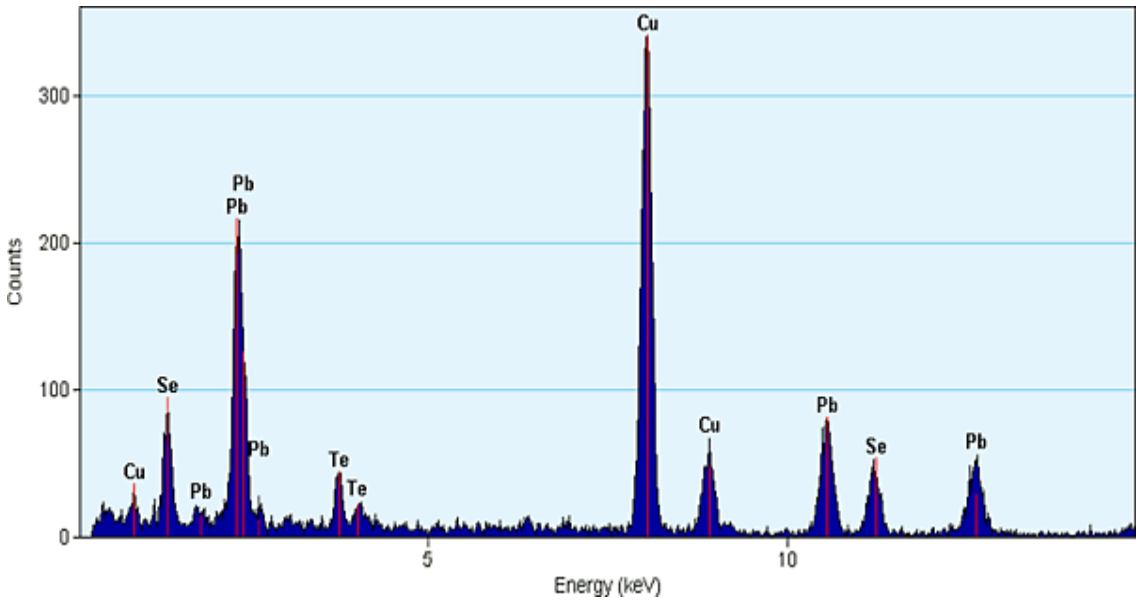

Fig. 2.13. Example of EDX spectrum [58].

An EDX spectrum is made from a series of peaks defined by their position, with and intensity and a background connecting the peaks.

The energy of the characteristic radiation determines the position of the peaks in the EDX spectrum. The intensity of the peaks is determined by the number of counts, i.e. the number of photons that reach the detector. Qualitative and quantitative determinations are made based on these two values, position and intensity.

The width of the peak is given by the energetic resolution of the detector. For EDX the resolution is about 130-150 eV.

The background is caused by the fact that the electronic bombardment also produces a continuum spectrum of X-ray radiation from the interaction between the incident electrons and the atomic nuclei. The intensity of the background decreases with increasing energy.

II.2.3. Interpretation of EDX spectra

The qualitative determination consists in identifying the chemical elements present in an unknown sample or to check for possible contaminations in a sample of known composition. This is most of the times a straightforward task which requires only the knowledge of the position of the peaks, taking into account that the energies of the characteristic radiation for the various elements are well known and given in tables. Ambiguities can almost every time be solved by taking into account additional lines.

Qualitative determination on the other hand is more sophisticated with the reliability of the result dependent on many parameters. For this the intensities of the peaks must be measured. Already it is clear that such a measure is affected by the statistics.

The acceleration voltage must be able to provide a kinetic energy of the incident electrons at least twice as high as the greatest characteristic X-ray energy of any element present in order to have an adequate intensity.

The current of the electron beam plays another crucial role. Higher current means more electrons which will generate more photons and thus greater intensity. But, there are some limitations with some samples that can be damaged by the current.

In addition, the sample preparation is important. A thin coating of an electrically conductive material needs to be applied sometimes on insulating samples to provide a path for the electrons to reach the ground and to avoid the build up of static charge on the surface of the sample.

It has been shown (by Castaing in 1951 [59]) that the relative intensity of an EDX peak is approximately proportional to the mass concentration of the element responsible for that peak. This is true because the mass of the sample scanned by the incident electrons is almost constant, regardless of the composition. An apparent concentration can be calculated from a standard sample with the equation:

$$C' = \left(\frac{I_{sp}}{I_{st}} \right) C_{st}$$

C’ is the concentration of the element in the sample, the apparent concentration. C_{st} is the concentration of that element in the standard sample. I_{sp} and I_{st} are the intensities of the peaks for the sample under study and standard respectively.

In order to obtain a more accurate concentration some corrections need to be employed. There are 4 such corrections. The first correction deals with the fact that the mass scanned by electrons is not strictly constant but is affected by the stopping power of the different elements. The second correction is concerned with the loss of incident electrons. Electrons that are backscattered can no longer be counted upon for the generation of radiation. The third takes into account the absorption of X-rays by the sample as they emerge from a finite depth in the material. The fourth correction deals with the X-ray fluorescence of the sample. There are different models to calculate these corrections. One very common model is the ZAF correction. ZAF stands for correction for the atomic number effects (Z), absorption (A) and fluorescence (F) [60].

II.3. SQUID for magnetic characterization

Magnetic measurements were performed in a Quantum Design SQUID magnetometer. The SQUID is currently the most sensitive device available for measuring magnetic fields. It can detect magnetic fields as low as 10^{-14} T. The sensitivity of the SQUID device allows it to detect changes in the magnetic field associated to one flux quanta.

The acronym SQUID is derived from superconducting quantum interference device and makes reference to the detection system based on Josephson junctions. The detector is the core of the machine and it is the part which gives the SQUID its remarkable sensitivity. A SQID has 4 main components: a large superconducting field coil, detection coils, the SQUID detector and a magnetic shield.

a) The field coil is a solenoid built from a superconductor wire. The job of the field coil is to produce a uniform magnetic field which magnetizes the sample. This is the external magnetic filed. The field coil is mounted inside a cryostat and is cooled with liquid helium. Electrical power is supplied to the coil from a power source that can reverse its polarity and therefore the direction of the current through the coil. This way the uniform magnetic field can be oriented on either way along the axis of the coil.

b) The detection coils system is a simple piece of superconducting wire wound in a second order gradiometer configuration, figure 2.14 (b). This configuration contains of 3 counter-winding coils. The entire system is placed in the centre of the field coil and the sample is placed in the centre of the detection coil assembly. The sample is mounted on a rod that travels along the axis of the coils. The sample is magnetized by the external field produced by the large filed coil and is moved through the 3 segments of the detection coils. By electromagnetic induction a voltage develops at the terminals of the detector coil assembly. The voltage measured at the terminals depends on the position of the sample relative to the coils. The dependence is shown in figure 2.14 (a). When the sample passes through the first turn of wire the voltage has one direction, when the sample passes through the second winding the voltage has the opposite direction and twice the absolute value and when the sample finally reaches the third winding, the voltage returns to sign and value it had at the first winding.

The SQUID measures the voltage in function of the position of the sample to the coil and fits the data. From the fit it returns the magnetization of the sample in electromagnetic units.

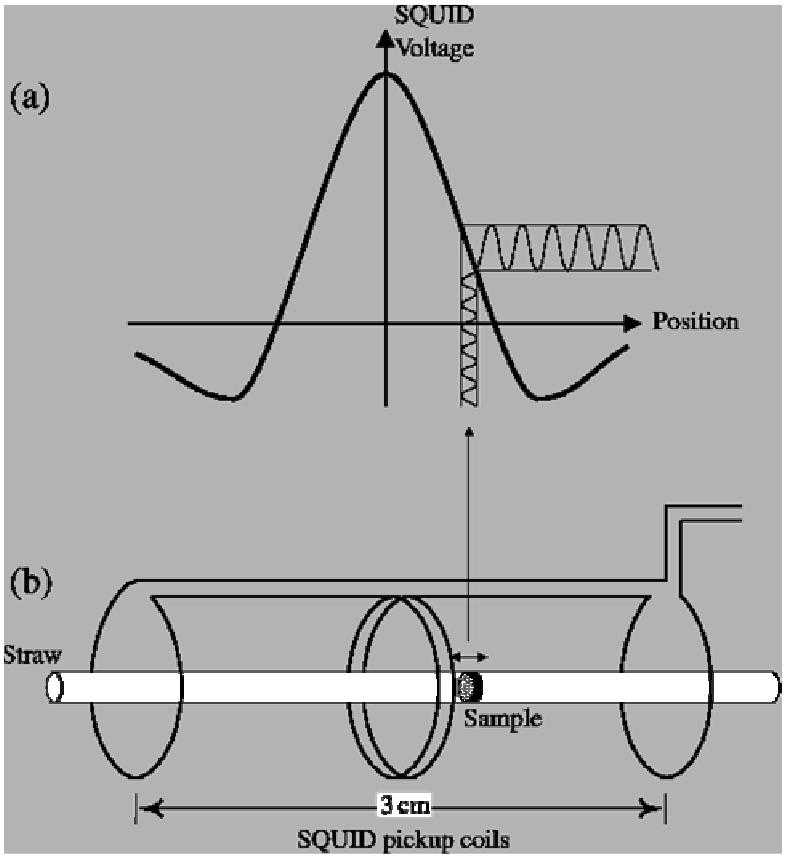

Fig. 2.14. a) SQUID raw signal, detected voltage in function of sample position. b) movement of the sample [61].

c) The SQUID proper is the core of the machine. It uses superconducting Josephson junctions to measure the voltage induced in the pick-up coils. The theory of the Josephson junctions is quite complicated and far from the objectives of this work but, essentially, the Josephson junctions used in the SQUID act like a very sensitive voltage to frequency converter. Since frequency can be measured with high accuracy, the voltage that generated the respective frequency can be measured far more precisely by this method than by using a conventional voltmeter.

There are two kinds of Josephson effects, the DC effect and the AC effect. A Josephson junction is made from two superconductors separated by a thin insulating layer, as represented in figure 2.15. Cooper pairs can pass through the insulating layer

from one superconducting side into the other by the tunnelling effect. The Cooper pairs can pass from one side to the other without any bias applied to the superconductors. This is the DC effect. Instead of a voltage bias, the driving mechanism for the current of Cooper pairs is the phase difference between the wavefunctions of the electrons on each side of the insulating barrier.

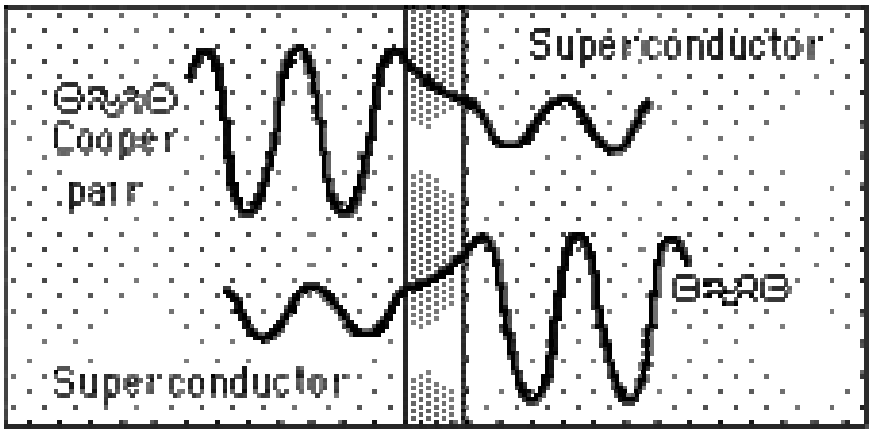

Fig. 2.15. Josephson junction [62]. The sine curves represent the wavefunctions of the Cooper pairs. The grey middle zone represents the insulating layer separating the two superconductors.

In the AC Josephson effect a bias is applied to the junction and this causes the current of Cooper pairs to oscillate with a characteristic frequency proportional to the voltage applied across the junction. The frequency is related to the voltage through the equation:

$$f_{Josephson} = \frac{2e\ \Delta V}{h}$$

d) The magnetic shield protects the detection coils of the SQUID from outside interference and blocks the intense magnetic field generated by the field coil to exit the machine.

II.4. Electrical resistivity and dielectric constant measurements

The dielectric properties of the samples were investigated by performing measurements of electrical resistivity, dielectric constant and electrical polarization, although the latter only managed to prove the evidence of a polarization hysteresis curve, rather than returning exact values for the saturation or remanent polarization. The setups and procedures for these measurements will be discussed below.

II.4.1. Resistivity measurements

Resistivity measurements were performed in DC or AC by the 2 contacts method in temperatures ranging from 500 to 4.2 K. Using the 2 contacts method the resistivity of a sample is calculated using Ohm's law as:

$$R = \frac{V}{I}$$

A constant voltage power supply injects a current through the sample and that current is measured with an ammeter. Figure 2.16 shows the wiring diagram for the circuit. The resistivity of the sample can be determined, if the geometry of the sample is known. The resistivity is given by the equation:

$$\rho = R\frac{A}{\ell}$$

, where R is the electrical resistance, A is the cross section of the sample and l is the length of the sample.

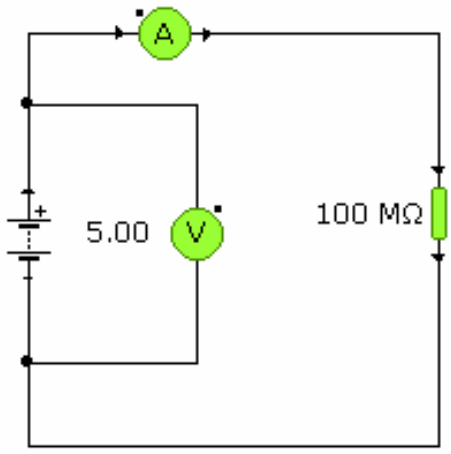

Fig. 2.16. Wiring diagram for DC resistivity measurements in the 2 contacts configuration.

II.4.2. Dielectric constant

Dielectric constant measurements are performed using an impedance meter. A pellet is polished in the shape of a cylinder with a thickness of about 500 μm. The two parallel surfaces are covered in silver paste thus forming a capacitor. The capacitor will present an impedance which consists of a real component, i.e. the ohmic resistance of the capacitor and an imaginary part which is the capacitive reactance. The electric impedance is a complex number given by

$Z = R + jX$, where Z is the impedance, R is the ohmic resistance and x is the reactance (which in this case is capacitive) and j is the imaginary unit which in electronics is not noted with "i" to avoid confusions with the electric current.

The impedance meter describes the sample with the model of a resistor connected in parallel with an ideal capacitor and returns the values of the resistance and the capacity of the sample.

Both R and C are measured in function of temperature and at different frequencies. Any change in the dielectric constant of the sample, ε_r, will result in a change of the capacity of the sample. The capacity is given by the equation:

$$C = \varepsilon_r \varepsilon_0 \frac{A}{d}$$

, where C is the capacity, ε_r is the dielectric constant, ε_0 is the electric permeability of vacuum, A is the cross surface of the capacitor armature and d is the distance between the armatures.

The reactive capacitance depends on the capacity by the equation:

$$X_C = \frac{1}{2\pi f C}$$

, where X_c is the reactive capacity, f is the frequency of the AC voltage used in the measurement and C is the capacity. When the capacity changes the reactive capacitance is also changed and this modification is visible as a change in the impedance of the sample.

The behaviour of the sample can be (better) evidenced by the examination of the phase shift it induces.

The phase shift (the phase of the impedance) and is marked by the δ angle in the phasor representation of the impedance. The tangent of the phase is calculated with the equation: $\tan(\delta) = X_c / R$.

II.4.3. The electrical polarization hysteresis

The electrical polarization hysteresis was evidenced using a Sawyer – Tower circuit which consists in two capacitors connected in series to an AC high voltage source. The diagram of the circuit is shown in figure 2.17. One capacitor is the sample and the other capacitor is a reference capacitor.

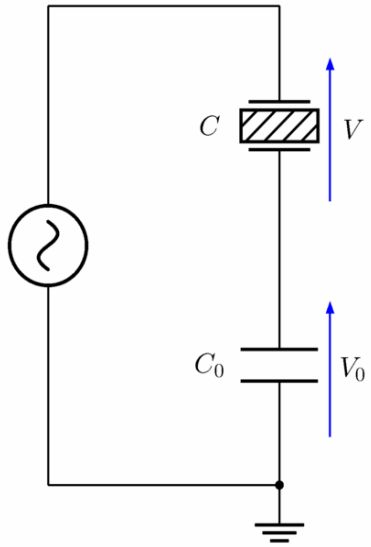

Fig. 2.17. Sawyer – Tower circuit. C is the capacity of the sample and C_0 is a reference capacity [63].

The capacity of a sample prepared in the manner described in the previous section is typically of a few pF. The capacity of the reference is in the order of a few μF. When the two capacitors are connected in series to a voltage source most of the voltage will be recovered on the terminals of the sample. In other words, V on the figure 2.17 will be almost equal to the voltage of the power source and much larger than V_0. The high value of the voltage applied to the sample, correlated to the relative small thickness of the sample ensure the establishment of a high electric field E, required to reach the saturation of a ferroelectric sample. Both the voltage and the thickness are known so the electric field can be determined, knowing that E = V/d. The polarization can be determined from the charge that builds up on the armature of the capacitor. The charge has the same value for both capacitors and it is determined from V_0. The voltage measured on the sample is applied (through a voltage divider) to the X channel of an oscilloscope and the voltage on the reference is applied to the Y channel of the oscilloscope. The hysteresis circuit can then be read directly on the screen of the oscilloscope.

II.5. XANES-EXAFS for local structure characterization

X-Ray absorption spectroscopy (XAS) measurements were performed at the BM 30 beamline at the ESRF facility in Grenoble, France. The basic operation principle of XAS is discussed below.

XAS explores the variation of the absorption coefficient of matter in function of the photon energy. The dominating mechanism for absorption in an XAS setup (beam energy 1-50 KeV) is the photoelectric effect in which a core electron is ejected by the collision with a high energy X-ray photon. In solids, the photoelectron interacts with the surrounding atoms and this interaction causes oscillations in the absorption coefficient. From the analysis of these oscillations the coordination of the studied atom can be determined.

The intensity of the radiation decreases exponentially as it traverses the sample, with the decrease governed by the equation:

$$I = I_0 e^{-\mu t}$$

, where I is the transmitted intensity, I_0 is the incident intensity, μ is the absorption coefficient and t is the thickness of the sample.

μ depends both on the material properties and the photon energy. As the energy increases the absorption decreases until a critical point is reached when in increases abruptly, as in a step. This step in the absorption is known as the absorption edge. It occurs when the photon energy reaches the threshold (E_0) at which the core electron is ejected, or in other words the threshold of the binding energy of the core electron. This gives XAS element selectivity since the absorption edge energy depends on the binding energy of the core photoelectrons which in turn depends on the type of atom on which these core electrons are located.

A typical XAS spectrum contains four regions called the pre-edge region, XANES, NEXAFS and EXAFS. Analysis of the XANES part yields information about the oxidation state of the element. The NEXAFS and EXAFS regions give information about inter-atomic distances. At this point our study was concerned only with the pre-edge and XANES parts. A peak is observed on the pre-edge region and the position of that peak relates to the oxidation state.

II.6. EPR for magnetic local structure characterization

Electron Paramagnetic Resonance (EPR) is another very useful and very sensitive technique for probing the local structure of matter. The method can only be applied to the study of materials with unpaired electrons since only these electrons produce an EPR signal.

Every electron has a magnetic moment and a spin quantum number. In an external magnetic field B_0 the spin / electron magnetic moment can take only two orientations, parallel (m_s = -½) or anti-parallel (m_s = ½) with respect the applied field. The two possible orientations do not have the same energy. The energy of the parallel orientation is lower than the energy of the anti-parallel orientation. The splitting of an energy level in a magnetic field is called the Zeeman effect. The energy of each level is given by:

$E = m_s g_e \mu_B B_0$, where g_e is the electron's g factor and μ_B is the Bohr magneton. The energy difference between the two levels is therefore

$$\Delta E = g_e \mu_B B_0$$

It can be observed that the energy difference, or the splitting of the energy levels, depends on the strength of the magnetic field. Transitions from one level to the other are allowed at the expense of the absorption or emission of a photon of energy E = hν, if the energy of the photon equals the energy difference, ΔE, between the two levels. This gives the fundamental equation of EPR:

$$h\nu = g_e \mu_B B_0$$

Figure 2.18 shows a diagram of the splitting of the energy levels, highlighting the ΔE gap. The frequency of the photon that verifies the resonance condition of EPR is in the domain of the microwave radiation. The fundamental equation of EPR allows a high number of possible combinations of magnetic fields and radiation frequencies that still verify the equation but in practice, in an EPR spectrometer, the frequency is kept fixed and the magnetic field is swept, thus increasing the gap until it matches the energy of the radiation. This is because it is relatively easy to control the strength of a

magnetic field (by controlling the current that passes through a coil) but it is fairly hard to change the frequency of radiation in that frequency domain.

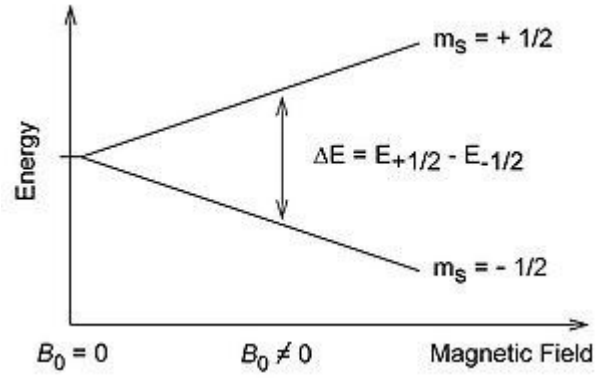

Fig. 2.18. Splitting of an energy level of an unpaired electron in two new levels in the presence of a magnetic field, each level corresponding to an orientation relative to the external magnetic field [64].

This effect is analogous to the one used in NMR (nuclear magnetic resonance) with the difference that in NMR the magnetic moments of the nuclei respond to the magnetic field. The same splitting mechanism also works in NMR but the difference in energy is smaller and therefore the frequency of the radiation is in the order of several MHz, in the domain of RF (radio frequency).

The parallel orientation is more energetically favourable so the population in the parallel state is much larger that the population in the anti-parallel state. When the resonance condition is reached, $h\nu = g_e\mu_B B_0$, electrons from the lower energy state are promoted to the higher energy state resulting in an overall absorption of energy and it is this absorption that produces the EPR spectra. Usually it is not the absorption that is represented but rather the first derivative of the absorption. Figure 2.19 shows an example of an EPR absorption graph and its derivative.

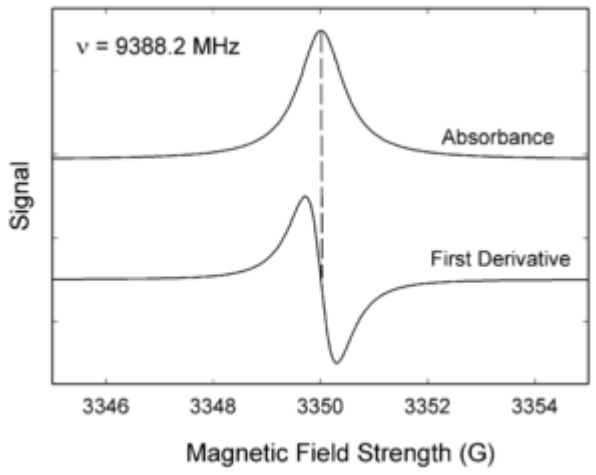

Fig. 2.19. Typical EPR spectrum. The derivative of the absorption graph (as opposed to the absorption graph directly) is typically employed in the analysis of EPR spectra [64].

The Electron Paramagnetic Resonance measurements presented during this document were carried out on a Bruker Elexsys E500 spectrometer in X band (at 9.4 GHz) and in function of temperature. Figure 2.20 shows the setup used for the EPR data acquisition.

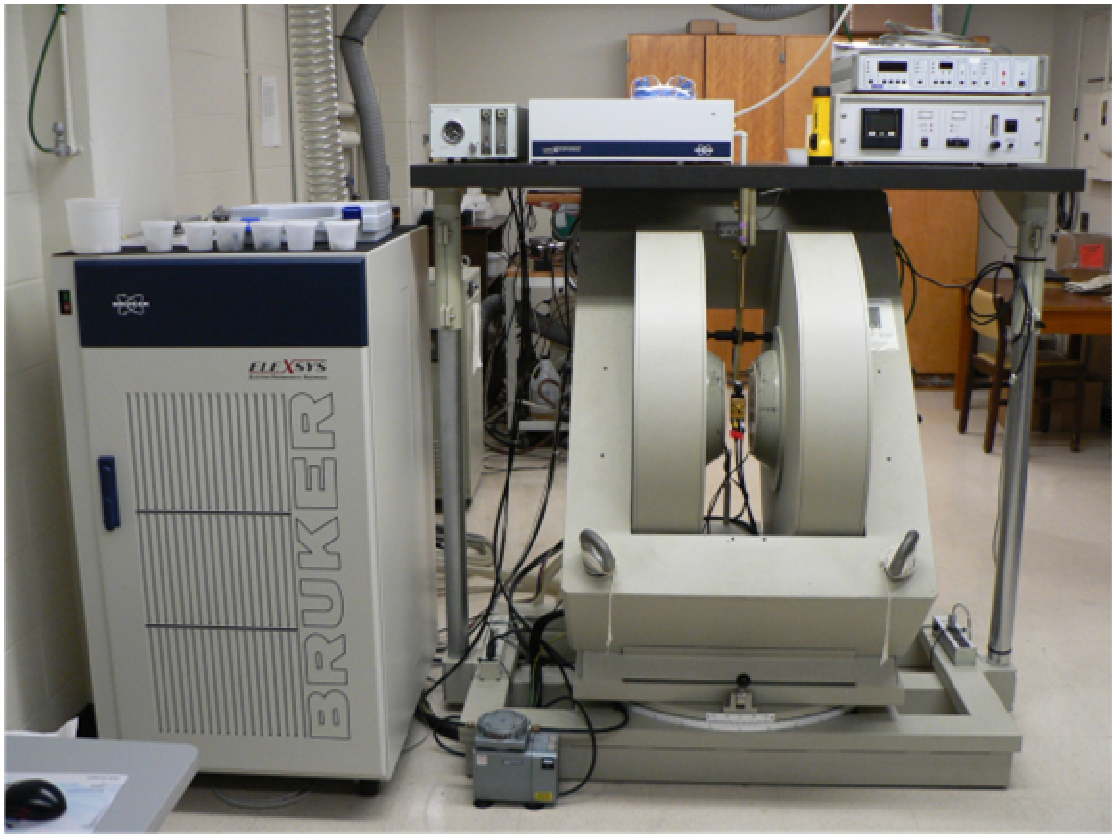

Fig. 2.20. Bruker Elexsys E500 EPR spectrometer.

II.7. Raman spectroscopy

Raman spectroscopy is a vibration spectroscopy used in condensed matter physics research in obtaining additional structural information (to the one obtained by conventional methods such as XRD) about the phonon modes present in the sample which relates to the inter-atomic distances and strength of the bond between the atoms. Raman scattering by a crystal can provide information about the orientation of that crystal, if the structure of the material is known.

The technique relies on the inelastic scattering of the light from a laser. The light scattered by the sample at the wavelength of the laser radiation is blocked by filters and the inelastically scattered light, which is seen at slightly different wavelengths than the laser radiation, is collected and focused on the detector.

Figure 2.21 shows the transitions between vibration energy levels of a molecule and the way the Raman spectrum is formed.

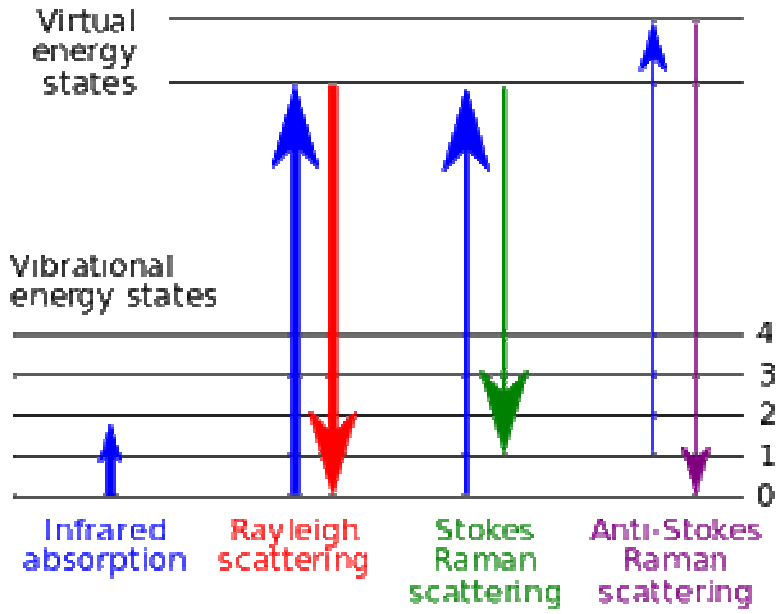

Fig. 2.21. Transitions responsible for the generation of a Raman spectrum [65].

Raman spectra are collected by making use of laser radiation. Typically, when a photon of the appropriate energy hits a molecule it promotes that molecule to a higher energy level. The molecule does not remain there for an indefinite time interval and instead it descends back to the initial level. This is the elastic, or Rayleigh scattering.

Most of the photons re-emitted by the sample follow this rule. In Raman scattering the incident photon promotes the molecule to a higher, virtual, energy state from which the molecule descends rapidly to a lower energy level that is different from the initial, departure, level.

If the final energetic level is located higher than the initial one the spectral line produced by the transition is called the Stokes line. Inversely, if the final level is placed lower than the initial level the spectral line generated is called the Anti-Stokes line. The Stokes and Anti-Stokes lines are distributed symmetrically on both sides of the main spectral which is the Rayleigh line (Rayleigh scattering).

The efficiency of the Raman scattering is very small. Only about 1 photon in every 10^6 photons is scattered inelastically. The number of Stokes events is larger than the number of Anti-Stokes events therefore the intensity of the Stokes lines is higher than the intensity of the Anti-Stokes.

The Raman spectra used on our study were recorded using a Renishaw inVia Raman Microscope. The HeNe laser emitting at 633 nm with a power of 50 mW was used. The spectral resolution of the recorded spectra was ~4 cm-1. For all normal Raman measurements a 40x objective and the 10% neutral density filter was used. The registered spectra are the average of 9 accumulations with 10 s integration time. Figure 2.22 shows the setup used.

Fig. 2.22. Renishaw inVia Raman Microscope.

Chapter III. Synthesis, chemical characterization and morphology of $PbVO_3$ type multiferroic samples

III.1. Experimental setup of HP-HT: Solid state reaction method for powder and hydrothermal method for crystal

III.1.1. The need for high pressure

On many instances, in the research field of condensed matter, samples are prepared by solid state reaction. In this technique, and in its variations, the starting products are solids and remain in their solid form throughout the entire reaction. A solid-solid interface is formed between the particles of the starting products. This interface and the problems related to it will be discussed in more detail in the subsequent segments. The engine that drives the solid-solid reaction is the diffusion of atoms from one solid into the adjacent solid. This is a thermally activated process so, usually, in solid state reactions high temperatures are employed (typically 1000°C to 1800°C) and long reaction times and regrinding of the products. The dwell time can be on the order of magnitude of days or even weeks.

An additional thermodynamic parameter alternative to high temperature is high pressure. The high pressure increases the diffusion and reduces the reaction time. After just 30 minutes, which was the typical dwell duration of our synthesis experiments, the reaction is complete.

The material we focused our attention on belongs in the family of ABO_3 type perovskite multiferroic oxides, more specifically, $PbVO_3$ in which the atom at the Vanadium site was partially substituted with iron or titanium. Therefore, the use of lead and vanadium oxides is unavoidable. In the phase diagram of Lead and Vanadium oxides high pressure is required for the synthesis of $PbVO_3$. It is reported that any attempt at synthesising bulk $PbVO_3$ samples by conventional solid state reactions has failed [33] and only high pressure proves to works [33]. Interestingly enough, this is not the case though for closely related $PbTiO_3$ oxide. Unlike $PbVO_3$,

$PbTiO_3$ can be prepared both under high pressure – high temperature conditions and using the conventional solid state reaction in a sealed tube. The mixed compound $PbV_{1-x}Ti_xO_3$ exists and can only be prepared by HP – HT solid state reaction. The attempt to synthesize this compound by the conventional solid state reaction method has failed, even for relatively low amounts of vanadium added to the mixture, more precisely for x = 0.9, or 10 % vanadium. This seems to suggest that it is the nature of the vanadium atom that implies the need for HP – HT methods.

III.1.2. High pressure – high temperature equipment

Two specially designed presses were used at the Institute Néel. These are a BELT X type press, used for trial reactions, in which the reaction conditions were tested and a CONAC type press used again for trials but also the production of larger quantities of representative samples. The BELT type press is of an American design while the CONAC press is a Russian conception.

a) BELT press

The BELT press is a high pressure high temperature device capable of reaching pressures up to 8 GPa and temperatures as high as 1500° C (fig 3.1). It is important to note that the press can maintain these extreme conditions for extensive periods of time (hours or days).

The principle of operation of the BELT is the following. Two conical shaped tungsten carbide pistons push into each side of a specially designed tungsten carbide chamber [66]. The pistons and the chamber are held in place and strengthened by hardened steel binding rings. The binding rings are tapered and are forced into each other, which causes them to stretch close to their elasticity limit [66]. The chamber with the corresponding binding rings forms a toroidal belt around the sample, hence the name of the device. A water cooling circuit is constructed into the toroidal belt.

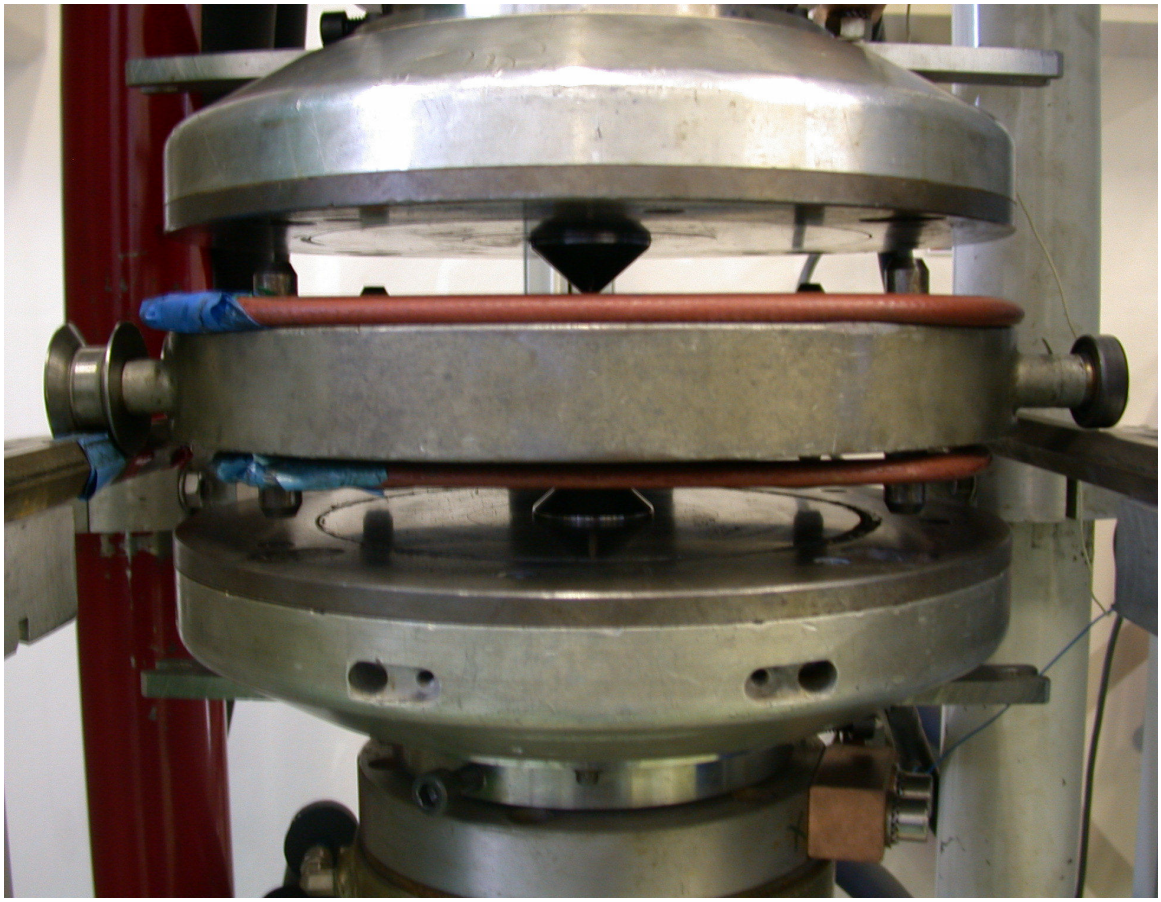

Fig. 3.1. The constructions of the BELT press. The middle section is the toroidal belt of the machine, housing the chamber and the cooling system (not visible in the picture). The two, upper and lower, small conical parts are the tungsten carbide pistons themselves. Concentric circles are visible on the structures supporting the pistons and these circles are the edges of the hardened steel binding rings.

The sample is located in the centre of the chamber in a pressure cell. The pressure is transmitted to the sample through two halves of a pyrophyllite gasket which also provide electric and thermal insulation.

At the same time in which pressure is applied by the two pistons, high temperature is achieved by means of an oven built into the pressure cell. The heating element of the oven is a graphite cylinder through which a high intensity electric current (hundreds of amps) is injected from the pistons.

The pressure cell is assembled on site before the machine is launched with the reaction conditions program. After the program has finished the cell is completely

destroyed and cannot be reused. A diagram of the pressure cell is presented in figure 3.2.

Some of the parts of the pressure cell are already discussed. The other parts include insulators which are stacked in a certain sequence.

The first part is the metal (Au or Pt) capsule containing the mixture of starting oxides. A special device is used to fill the capsule and slightly compress the powder in order to make the powder more compact by eliminating some of the air trapped inside the powder during the grinding / mixing process.

The capsule is 3 mm in diameter, the small size being necessary in order to achieve high pressures without the need of exaggeratedly large forces. However, this is the drawback of the system as the volume of material that can be prepared is relatively small, only 0.04 cm^3.

Further on the capsule is placed inside the graphite oven (discussed above) and insulation of the capsule from the oven is provided by a pyrophyllite cylinder. Two alumina disks are used to seal the entire system. Finally the oven now containing the sample is placed inside the double sided pyrophyllite gasket (discussed above) which represents the pressure transmitting medium. Two polytetrafluoroethylene (PTFE) gaskets maintain the pyrophyllite inside the BELT chamber during the HP – HT treatment.

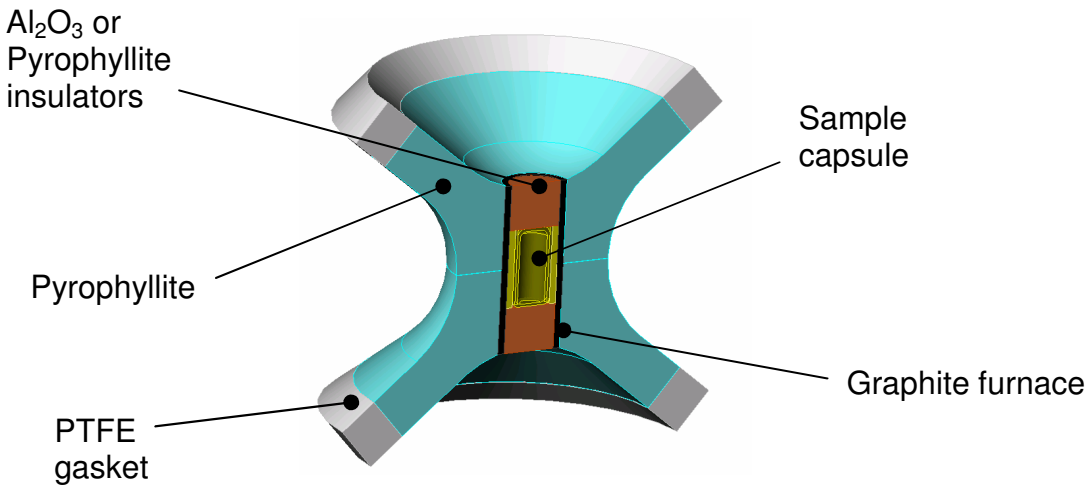

Fig. 3.2. Cut through the pressure cell of the BELT type press [67].

There are tree design features that give the BELT the amazing performances it is capable of. These are the two sided pyrophyllite “sandwich gasket”, the double ending and the conical shape of the pistons and the chamber [66].

The sandwich gasket increases the stroke of the pistons which increases the available sample volume and ultimately the maximum pressure. The double ending, or in other words the fact that two pistons push from two sides has a similar effect, namely the increase of the stroke but also, this configuration increases the symmetry which has the effect of eliminating some stress concentration points.

A (pyrophyllite) gasket can be compressed up to the point in which the thickness of that gasket is reduce to a minimum value, typically 2 to 4 thousands of an inch. Beyond that point, additional press load cannot bring the pistons (anvils) closer together so the maximum pressure is reached. However, if the gasket is arranged at an angle, θ, less then 90° to the direction of compression the thickness along the compression line can be increased. This is one reason why the pistons and chamber are conical in shape. The smaller the θ angle can be made the greater the stroke can be increased. The limiting factor in the smallness of θ is set by the tangent friction forces at the interface of the tungsten carbide parts with the pyrophyllite gasket. If the angle is too steep the frictions become too small and the gasket is blown out of the chamber [66].

Also, a conical piston has much more strength than a classical cylindrical piston and has a higher tolerance for miss-alignments in between the chamber and the pistons themselves.

b) CONAC press

The other press used during the study is the CONAC press. The principle of operation of the CONAC press is similar to the one of the BELT but the construction of the “pistons” (the correct term would be anvils) and the pressure cell is different.

The main difference consists in the much larger volume of sample that can be prepared with the CONAC press. There are two possible configurations for the CONAC (28 and 40, where the number refers to the size of the sample containing capsule) which can handle samples of 0.17 (CONAC 28) or 0.8 (CONAC 40) cm^3.

The machine can reach pressures up to 7.5 (CONAC 28) or 6 (CONAC 40) GPa and temperatures of 1500° C. The specifications of the CONAC are comparable to the ones of the BELT in terms of maximum pressure and temperature but it is interesting to note that the force required to achieve such high pressures is much greater for the larger CONAC press. The maximum force that can be applied on the pistons of the CONAC is 1500 tons-force (!) whereas for the BELT, the maximum force is "merely" 300 tons [67-73].

The pressure structure of the CONAC press is composed of two identical facing dies constructed from tungsten carbide, each die supported by three hardened steel tapered rings press fitted into each other. These dies are constructed with a cone shape hole which contains the pressure cell.

A picture of the CONAC dies is presented in figure 3.3 and a diagram of the pressure cell is given in figure 3.4.

Fig. 3.3. The lower die of the CONAC 40 press. The cone shaped hole is clearly visible in the centre of the die.

The pressure cell is composed in a solid pressure transmitting medium made from calcite ($CaCO_3$), a graphite resistive heater, similar to the one used in the BELT, thermal and electrical insulators in pyrophyllite and calcite, conductors in steel and molybdenum which transmit the electric current from the dies to the furnace and the metal capsule containing the sample [68-73].

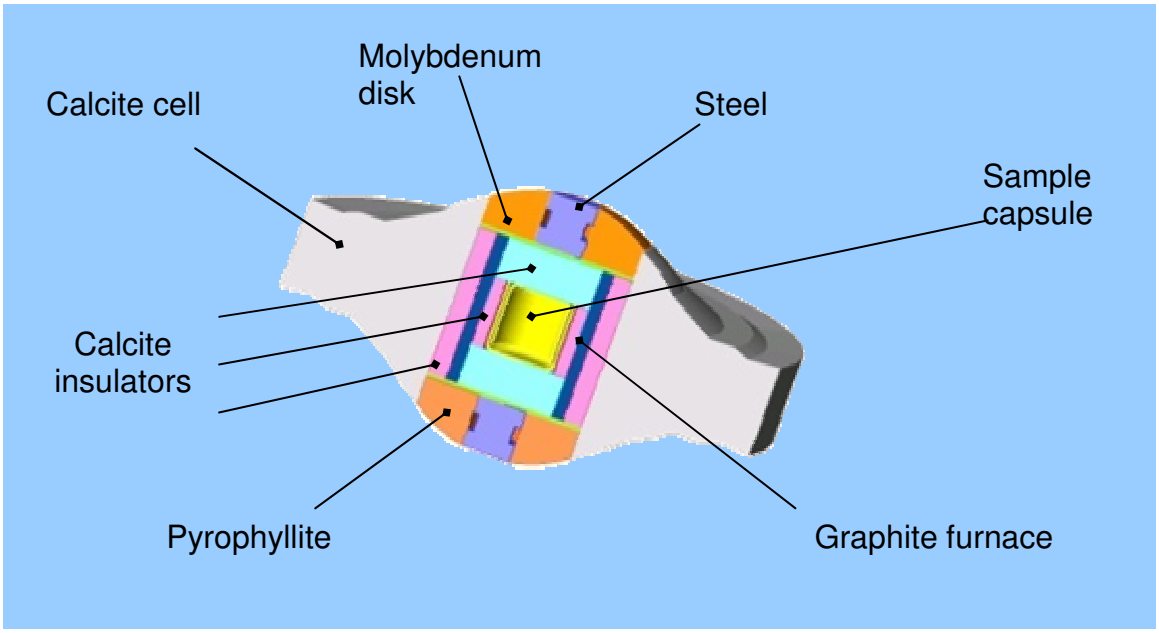

Fig. 3.4. Diagram showing the assembly of the pressure cell for the CONAC press [67].

There is an alternative way of using the CONAC pressure cell. While the BELT cannot handle the large volume capsules of the CONAC, the opposite is true. The compartment of the pressure cell designed to contain the sample capsule is large enough to accommodate two smaller size BELT capsule. In that case a specially built BN (boron nitrate) cylinder takes the place of the sample capsule in the diagram above. Two holes are drilled into this cylinder and a 3 mm BELT capsule is placed in each. Thus smaller sized capsule can be successfully used.

A similar, but much more complicated, setup containing two capsules was previously constructed by Doctor Céline Goujon at the Néel Institute, Grenoble and it is used for HP – HT, in-situ DTA measurements [68].

c) Calibration of the press

During a standard synthesis experiment in either of the two HP – HT devices, the pressures exerted on the sample are controlled through the force applied on the anvils / pistons of the machine. In the same way, the temperature is controlled by the power supplied to the oven. There is no direct measurement of the pressure and temperature within the pressure cell. Instead graphs relating force to pressure and wattage input to temperature are used.

The force-pressure and power-temperature graphs are obtained from the calibration of the press. The temperature calibration is made by placing a thermocouple in the pressure cell. The calibration in pressure is carried out by investigating the pressure induced phase transitions of bismuth [68]. These transitions are marked by changes is the resistivity of bismuth so for the calibration the electrical resistance of a bismuth wire is measured and plotted as a function of the pressure. A sharp decrease in resistance is observed at 24800 atmospheres [66] corresponding to the Bi I – Bi II transitions and a slight increase in resistance is noted at 26200 atmospheres as bismuth passes from Bi II to Bi III [66]. As a result, the variation in the resistance of the bismuth wire marks the points in which the high pressures (needed for the occurrence of the Bi phase transitions) are reached.

d) Role of the capsule in HT-HP experiment

Special attention must be paid to the capsule that serves as the reaction chamber. The choice of ceramic, porous capsules which might allow outside oxygen to react with the mixture of oxides does exist. There are special capsules made from BN. However these cannot be used for $PbVO_3$ because $PbVO_3$ decomposes in air at 300° C [32]. This is a relatively low temperature, at least when it is compared to the reaction temperature which is close to 1000° C. Another problem in using BN capsules is the diffusion of the material in the walls of the capsule and the other way around. After the reaction the capsule is practically indistinguishable from the product material.

The “default” material for the capsule is gold but there is also the option of a platinum capsule. Metallic capsules provide good insulation and form an airtight seal but even so there are some shortcomings as materials normally considered inert, such as gold or platinum, can react with some starting products under HP – HT conditions. Lead is one example of such a starting material. Pb-Au or Pb-Pt alloys do exist and since lead oxides are used as reactants, it can be expected to have some reactions with the walls of the capsule at the contact of the walls with the mixture of powder. It is also possible to have diffusion of grains of pure gold into the mixture of staring oxides (and hence in the final product) but no reaction between the Au and the starting products. The same is true for Pt. Based on results from XRD and EDX we speculate that we have simple diffusion of Au in the sample and perhaps the formation of a Pb-Pt alloy (or even a Pb-Pt oxide). Figure 3.5 shows a cut into a gold capsule containing the sample and in that cut it is possible to see grains of gold which have diffused from the capsule into the sample.

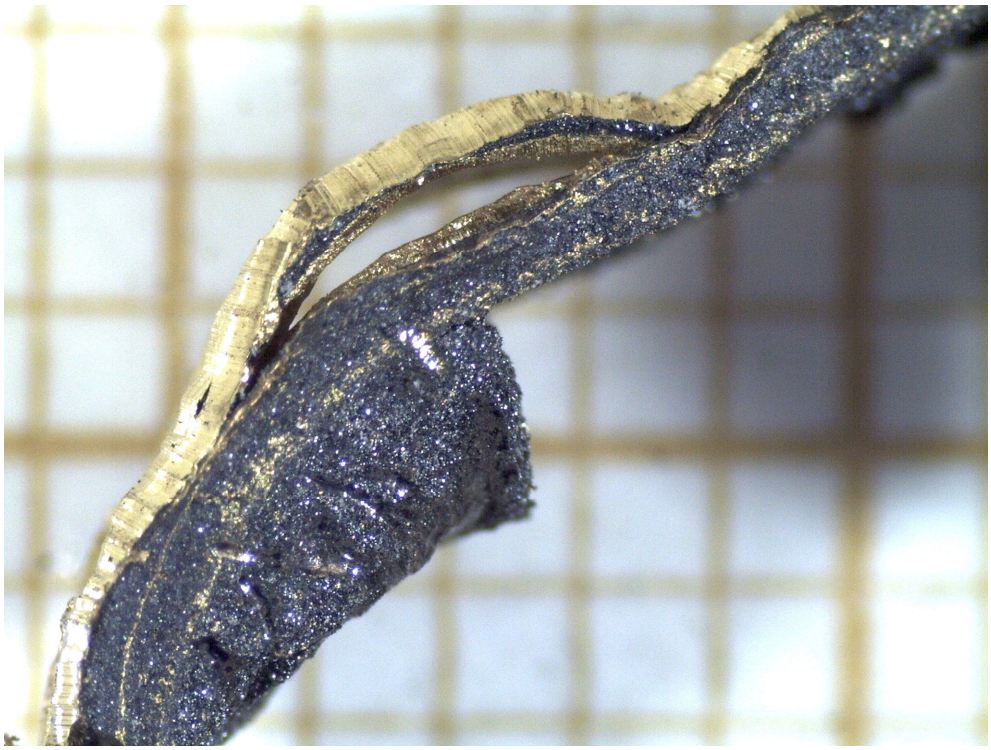

Fig. 3.5. Gold diffusion from the walls of the reaction chamber. Grains and wires of gold can be seen into the black sample (this is the PVO_009 sample).

III.1.3. Solid state reaction for powder

The solid state reaction technique consists in grinding the staring materials and mixing the powders as to create a solid-solid interface. Ideally, neither solid will remain chemically identifiable after the reaction is complete. The atoms in solids are less mobile than the atoms in liquids so the time scale at which the atoms in a solid move is very slow which in turn will require small particles, thus small reaction distances, higher temperatures and higher pressures in order to have reasonable reaction times.

In the simple case of just 2 solid phases (fig.3.6.) the atoms are tightly packed by comparison to the situation in liquids or gases.

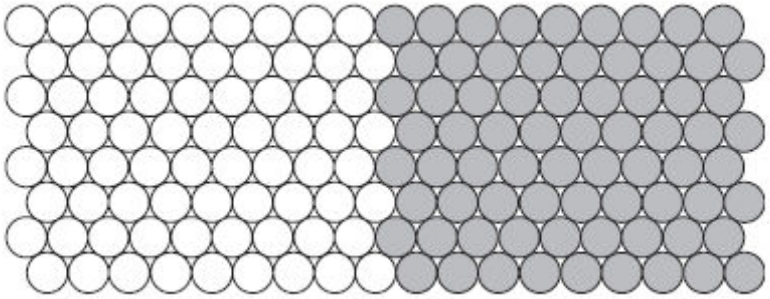

Fig. 3.6. Two solid phases prior to the reaction [74].

This is an oversimplified model because it does not take into account vacancies or interstices but the presence of vacancies is required in order to move atoms from one phase into the other one. The displacement of atoms from one side and their accommodation in the other phase requires a large expense of energy. The mechanism which drives the atoms migration is the diffusion. The diffusion coefficients in solids are smaller than the ones in liquids or gases by several orders of magnitude, typical values being of about 10^{-20} cm^2/s whereas in liquids $D = 10^{-5}$ cm^2/s and $D = 10^{-1}$ cm^2/s in gases. At these coefficients, the rough estimation of the scale of the length travelled by an atom gives, in one minute in average $7.7*10^{-10}$ cm for an atom in a solid and for comparison 0.02 cm in a liquid.

The displacement is connected to the diffusion coefficient through

$$<\Delta x^2> = 2Dt$$

and D, the diffusion coefficient has a temperature dependence following an Arrhenius behaviour seen in chemical reactions.

$D(T) = D(0)\exp -E_A/RT$, where E_A is the activation energy.

Higher temperatures mean greater diffusion coefficients and smaller particle size means smaller $<\Delta x>$, lesser distance required for atoms to travel in order to have a complete reaction. For these reasons high temperatures are employed and the reactants are brought into play in the form of fine powders.

This is known as the ceramic method. Very often oxides with high melting points are used as reactants so the reaction conditions are extreme due to the refractory nature of these materials.

For the example shown in the previous figure (fig. 3.6.), in the early stage of the reaction, a white atom must dislodge itself from the white phase and find a place in the grey phase. The same is true for grey atoms which have to diffuse in the white phase material. At this point the situation becomes more complicated as a white atom must not only extract itself from his coordination site but must also travel a significant distance through the product material formed at the interface. Figure 3.7 illustrates this.

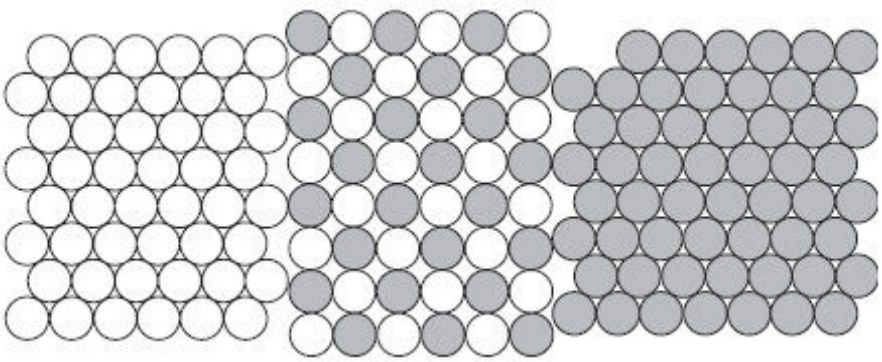

Fig. 3.7. Solid state reaction (ceramic method) in progress showing the reaction product forming at the interface of the reactants, separating them [74].

To solve this problem, the reaction process is interrupted from the outside, the sample is retrieved from the reaction chamber, crushed, re-ground and re-mixed to ensure homogeneity. This creates new interfaces for the grains of the starting products so the reaction can continue, ideally until the complete exhaustion of the reactants.

III.1.4. HP-HT hydrothermal method for single crystal growth

Single crystals can be shaped in the same capsule type in which polycrystalline samples are formed by controlled cooling and the addition of a small amount of water to the mixture of starting oxides. The quantity of water needed is approximately 10% of the weight of the powder [37]. This process is called the hydrothermal method.

Without going into many details the hydrothermal method can be described as a crystallization process in which water is used as a solvent [74]. The material is re-crystallised or synthesised from a solution in a sealed container above ambient pressure and temperature.

These reactions take place above the critical point of the solvent, water, in our case.

Figure 3.8 shows a typical phase diagram, not necessarily for water, which highlights the presence of the critical point.

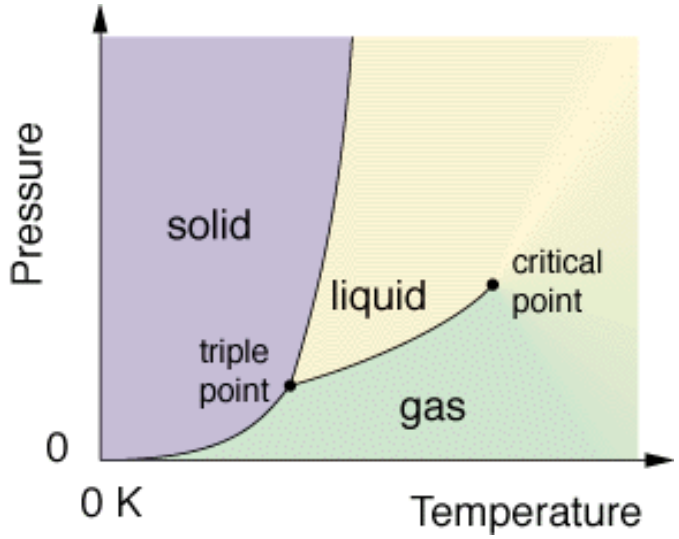

Fig. 3.8. Critical point on the phase diagram. For water, the critical point is located at 373.94° C and 217.7 atmospheres [75].

Near the critical point the physical properties of water are considerably different from the properties of water at ambient pressure and temperature. The high pressure disrupts the hydrogen bonds between the water molecules which dramatically reduces the water density (0.3 g/cm^3 at the critical point). The diminishing of the number of hydrogen bonds is a noteworthy effect because it increases the solubility of the solvent.

III.2. Synthesis of $PbV_{1-x}M_xO_3$ (where M = Fe, Ti) and phase characterization

III.2.1. Choice of starting products, chemical equations

A number of approximately 40 samples in the form of powders and single crystals were produced.

There are three classes of samples according to the type of substitution as follows.

The first class consists in the clean $PbVO_3$ without any substitution. Samples in this class are called the PVO series.

The second class is formed by samples in which in the structure of $PbVO_3$ the vanadium was partially substituted with titanium. Thus the chemical compositions of these samples should be written as $PbV_{1-x}Ti_xO_3$. These samples are called the PVT series

Finally, the third class consists in samples in which another partial substitution was performed. This time, in the structure of $PbVO_3$ vanadium was substituted with iron. Therefore the chemical composition of these samples is $PbV_{1-x}Fe_xO_3$. These are called the PVF series. The values of x (the degree of substitution) in either class are already mentioned in the introductory part.

The samples were prepared from stoichiometric mixtures of high purity oxides. The oxides used were PbO, PbO_2, V_2O_3, V_2O_5, TiO_2 and Fe_2O_3. Of course, not all the oxides were used at the same time but rather specific combinations appropriate for each sought composition or sample.

Even at this stage complications inherent to the HP – HT synthesis begin to emerge. The amount of oxygen has to be taken into account prior to the reaction and multiple choices of combinations which lead to the same final product are available. The possible choices for starting products reported in literature and tested by us during the master research stage or during this work are summarized in tables.

Table 3.1 The types of samples and substitutions tried, arranged by their occurrence / existence. Each line of the table marks an entire set of samples, therefore each one of these lines will de detailed in the following tables.

prepared samples	literature	master	thesis
$PbVO_3$	✓	✓	✓
V-Ti substitution	✓	☒	✓
V-Fe substitution	✓	✓	✓

a) $PbVO_3$

The chemical equation for the synthesis of simple (no substitution) $PbVO_3$ is the following.

$$4\ PbO + V_2O_3 + V_2O_5 \rightarrow 4\ PbVO_3$$

The valence of oxygen is always 2- so in $PbVO_3$ this is no exception. The valence of lead in $PbVO_3$ is 2+. The existence of Pb^{4+} is not impossible but it is unlikely and it is excluded for now. In order to have equilibrium of the valences the vanadium should take on the 4+ valence, hence the choice of oxides. By having a mixture of V_2O_3 (valence/oxidation of vanadium 3+) and V_2O_5 (vanadium oxidation 5+) an average valence of 4+ for the vanadium is achieved. This however is not the only possibility. Vanadium will rapidly oxidize to the highest valence, 5+ if it has the chance. Therefore an equation of the form:

$$PbO + PbO_2 + V_2O_3 \rightarrow 2PbVO_3$$

should also work. In this case PbO_2 provides the "supplementary" oxygen required for the oxidation of vanadium from 3+ to 4+. Indeed the reaction does occur, $PbVO_3$ is formed but the results are less encouraging. This reaction path was previously tested by Marie France from the team lead by Dr. Bordet at that time [31] and retested by us during my masters research stage and was found to yield greater quantities of impurities, mostly $Pb_3V_2O_8$, than the first path, the mixture of V_2O_3/V_2O_5.

Table 3.2 Summary of reaction conditions and choice of starting products for $PbVO_3$ samples (the first line of table 3.1)

$PbVO_3$ synthesis literature			
author	starting products	reaction conditions	observations
Bordet [31]	PbO, PbO_2, V_2O_3	HP = 4.5 GPa HT = 750 - 850° C t = 3 h	tried non-stoichiometric mixtures: $PbVO_{2.8}$
Shpanchenko [32]	PbO, VO_2 or PbO, V_2O_3, V_2O_5	HP = 40-80 kbars HT = 650-1000° C t = 5-240 min	
Belik [33]	PbO, V_2O_3, V_2O_5	HP = 6 GPa HT = 973-1223 K t = 30-120 min	second HP-HT treatment
Tsirlin [34]	PbO, VO_2	HP = 5 GPa HT = 950° C t = 2 h	
Oka [37]	PbO, V_2O_3, V_2O_5	HP = 6 GPa HT = 1223 K t_1 = 30 min slowly cooled to HT = 973 K t_2 = 12 h release pressure	add 10 % wt distilled water to powder mixture
$PbVO_3$ synthesis master			
sample choice	starting products	reaction conditions	observations
1	PbO, PbO_2, V_2O_3	HP = 4 GPa HT = 900° C t = 30 min	
2	PbO, VO_2	HP = 4 GPa HT = 900° C t = 30 min	
3	PbO, PbO_2, V_2O_3	HP = 4 GPa HT = 900° C t = 30 min	non stoichiometric mixture $PbVO_{2.75}$
$PbVO_3$ synthesis thesis			
sample type	starting products	reaction conditions	observations

powder	PbO, PbO_2, V_2O_3	HP = 6 GPa HT = 950° C t = 90 min	
powder	PbO, V_2O_3, V_2O_5	HP = 6 GPa HT = 950° C t = 90 min	non stoichiometric mixture $PbVO_{2.7}$
powder	PbO, V_2O_3, V_2O_5	HP = 6 GPa HT = 950° C t = 90 min	second HP-HT treatment
single crystals	PbO, V_2O_3, V_2O_5	HP = 6 GPa HT = 950° C t = 90 min cool to TH = 700° C during t_2 = 12 h pressure release	+ 10 % wt distilled water to powder mixture

b) $PbV_{1-x}Ti_xO_3$

In the case of the vanadium – titanium substitution the equations for the reactions are relatively easy to write because in TiO_2 the valence of titanium is already 4+. Thus the general equation is the following:

$$4\ PbO + (1-x)\ V_2O_3 + (1-x)\ V_2O_5 + 4x\ TiO_2 \rightarrow 4\ PbV_{(1-x)}Ti_xO_3$$

Table 3.3 Summary of reaction conditions and choice of starting products for samples of the V-Ti substitution (line 2 of table 3.1)

$PbV_{(1-x)}Ti_xO_3$ synthesis (V-Ti substitution)			
how / where	starting products	reaction conditions	observations
literature Arévalo [41]	PbO, VO_2, TiO_2	HP = 20-80 kbar HT = 1073-1473 K	
thesis	PbO, V_2O_3, V_2O_5, TiO_2	HP = 6 GPa HT = 950° C t = 90 min	no re-annealing required
thesis	PbO, V_2O_3, V_2O_5, TiO_2	HP = 6 GPa HT = 730° C t = 90 min or 30 min	❖ conditions found accidentally ❖ equally good samples

c) $PbV_{1-x}Fe_xO_3$

For the vanadium – iron substitution the situation becomes more complicated. The problem is a bit anticipated here, and will continue to re-appear throughout the entire work and will be re-discussed in subsequent chapters. The core of the problem resides in the fact that iron in Fe_2O_3 has the valence 3+ and it is used to replace V^{4+} cations.

At the level of planning of chemical reactions, this implies the changing of the starting oxides as the degree of substitution is increased. In order to highlight the need for the modifications in the choice of oxides, it is interesting to follow the changes in the required quantities of starting products through a segment of the series.

For example, the equations for the synthesis of samples containing 20, 30 and 40 % iron are:

$4\ PbO + 0.6\ V_2O_3 + 1\ V_2O_5 + 0.4\ Fe_2O_3 \rightarrow 4\ PbV_{0.8}Fe_{0.2}O_3$ for 20% Fe

$4\ PbO + 0.4\ V_2O_3 + 1\ V_2O_5 + 0.6\ Fe_2O_3 \rightarrow 4\ PbV_{0.7}Fe_{0.3}O_3$ for 30% Fe

$4\ PbO + 0.2\ V_2O_3 + 1\ V_2O_5 + 0.8\ Fe_2O_3 \rightarrow 4\ PbV_{0.6}Fe_{0.4}O_3$ for 40% Fe.

It can be seen that as the quantity of iron is increased, less and less V_2O_3 is needed for the reaction as the V_2O_3 is formally replaced by Fe_2O_3. This works until the limit of 50% Fe content is reached.

At 50 % Fe there is a turning point. The choice of oxides species can no longer be maintained (and still have a "clean stoichiometry") since there is no way to accommodate for the V_2O_3 oxide, the presence of which is no longer needed. The equation can be written as:

$4\ PbO + V_2O_5 + Fe_2O_3 \rightarrow 4\ PbV_{0.5}Fe_{0.5}O_3$.

This however is not the only choice. A small amount of V_2O_3 can be added at the cost of slightly lowering the oxygen content in the final product. Also a mixture of PbO/PbO_2, V_2O_3 and Fe_2O_3 [40] can be employed and yet another option consists in the usage of a precursor ($Pb_4V_2O_9$) mixed with Fe_2O_3 [40]. We have tested the synthesis path proposed by Tsuchiya [40] and we have obtained the best results by using the first mixture, composed of PbO, V_2O_5 and Fe_2O_3.

For even higher degrees of substitution a new change occurs. This time, the only source of vanadium left in the equation is V_2O_5. Whenever the amount of V_2O_5 is lowered (in order to account for more iron and less vanadium) the available quantity of oxygen is also lowered. The three oxygen atoms in the Fe_2O_3 can not replenish the

lost five oxygen atoms from V_2O_5. Instead PbO_2 is added to supply for the needed oxygen. Therefore, the equation for the synthesis of the sample containing 60% Fe for example becomes:

$$3.6\ PbO + 0.4\ PbO_2 + 0.8\ V_2O_5 + 1.2\ Fe_2O_3 \rightarrow 4\ PbV_{0.4}Fe_{0.6}O_3.$$

It can be noticed that the amount of lead remains the same but the lead oxides effectively bring more oxygen into the reaction to compensate for the missing oxygen caused by the lowering of the quantity of V_2O_5 (sub unitary coefficient) caused in turn by the increase in Fe_2O_3.

With the alternative source of oxygen (form the PbO/PbO_2 mixture) a reaction containing the five starting oxides (PbO, PbO_2, V_2O_3, V_2O_5 and finally Fe_2O_3) can be written but it is redundant. Such a reaction was in fact tested but it did not produce any major improvement in the quality of the final product.

Table 3.4 Summary of reaction conditions and choice of starting products for samples of the V-Fe substitution (line 3 of table 3.1)

$PbV_{(1-x)}Fe_xO_3$ synthesis (V-Fe substitution)			
how / where	starting products	reaction conditions	observations
literature Tsuchiya [40]	PbO, V_2O_5, Fe_2O_3	HP = 7 GPa HT = 800-1000° C	
literature Tsuchiya [40]	$Pb_4V_2O_9$, Fe_2O_3	HP = 7 GPa HT = 800-1000° C	
master	PbO, PbO_2, V_2O_3, Fe_2O_3	HP = 4-6.5 GPa HT = 900-1000° C t = 30 min	
master	$Pb_4V_2O_9$ + Fe_2O_3	HP = 4 GPa HT = 1000° C t = 30 min	
thesis	PbO, V_2O_3, V_2O_5, Fe_2O_3	HP = 6 GPa HT = 950° C t = 90 min	no re-annealing required
thesis	PbO, V_2O_3, V_2O_5, Fe_2O_3	HP = 6 GPa HT = 730° C t = 90 min or 30 min	❖ conditions found accidentally ❖ equally good samples
thesis	PbO, (PbO_2), V_2O_3, Fe_2O_3	HP = 6 GPa HT = 950° C (or 730° C) t = 90 min (or 30 min)	at (or above) 50% Fe

III.2.2. Sample preparation and reaction conditions

The staring products came in the shape of powders. These powders were weighted on an electronic balance then mixed and ground in an agate mortar for approximately 30 minutes without the use of any solvent. The powder was the placed inside a gold (or platinum) capsule and compacted using a device built for that purpose. Then the capsule as closed and placed in the pressure cell (rigorously speaking the pressure cell is built around the capsule) in the manner described in the previous subchapter. After that the pressure cell was placed inside the corresponding press and a program which drives the HP – HT apparatus and controls the reaction conditions was launched.

While the chemical composition of the mixture of starting oxides was varied considerably in order to produce the substitution series, the reaction conditions were never changed. There was just one minor, accidental modification of the dwell temperature but this proved to have no effect over the quality of the samples. Two types of programs were used, a program of a relatively short duration, used for the synthesis of polycrystalline samples and a second program of a much longer duration used for the growth of single crystals. Schematic representations of the HP – HT treatments corresponding to the two programs are shown in figures 3.9 and respectively 3.10. Both programs had their core in a dwell of 30 (to 90) minutes at 6 GPa and 950° C, which are the reaction conditions used for virtually all the samples, but there are important differences between the two programs in what concerns the rate of cooling.

a) Powders

The BELT press can produce 8 GPa of pressure and a temperature of 1500° C. The COANC press with the type 28 capsule can produce 7.5 GPa of pressure and the same temperature of 1500° C, as the BELT.

The program for the synthesis of powders runs in the following sequence. Pressure is slowly applied until the 6 GPa value is reached. A short waiting period (roughly 2 minutes) follows and this allows for the pressure to stabilize. After the

waiting period the temperature is raised to 950° C where it is maintained for 90 minutes. This is followed by a rapid quench at room temperature and only after the quench the pressure is slowly released.

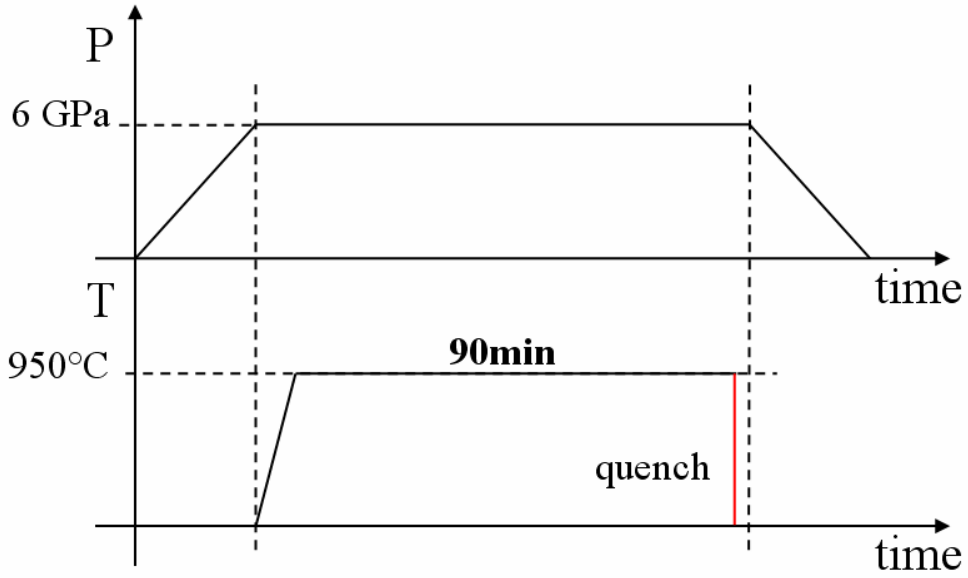

Fig. 3.9. Schematic representations of the HP – HT treatment, the program employed for polycrystalline samples.

b) Single crystals

Single crystals were synthesised by the hydrothermal method. For the synthesis the capsule contained the mixture of starting oxides to which 10% weight of water was added.

The program for the growth of single crystals starts the same as the program used for the synthesis of powders. The sample/capsule is brought up to pressure, then to temperature, again at 6 GPa and 950° but the dwelling time is reduce to 30 minutes. Further on, the dwell is followed by a slow cooling from 950° C to 700° C over a time range of 12 hours. The sample is then quenched from 700° C to RT after which the pressure is finally released.

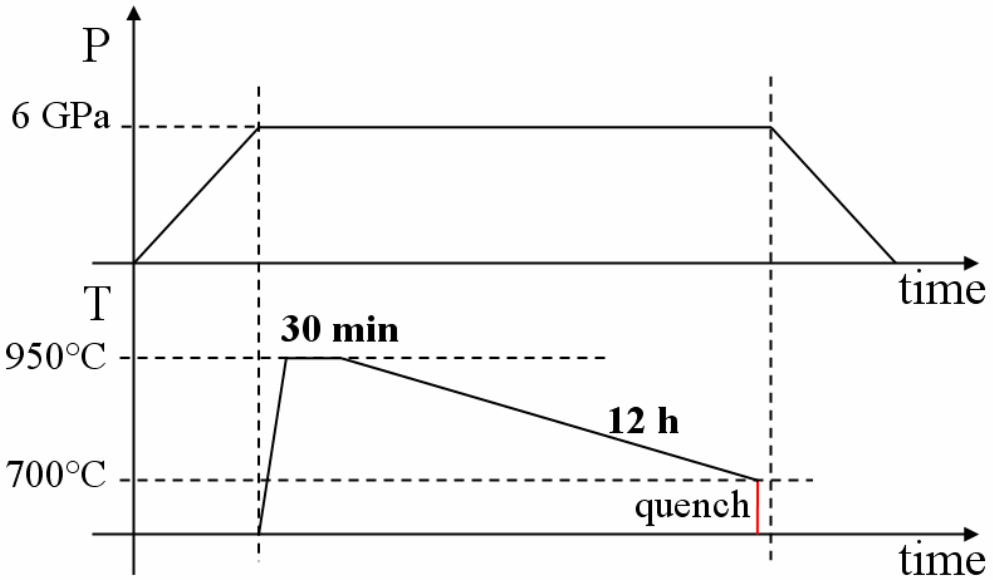

Fig. 3.10. Schematic representations of the HP – HT treatment, the program designed for the synthesis of single crystals. The time scale is not the same in the two diagrams.

Side note

The standard reaction conditions were 6 GPa / 950° C / 90 min for either type of press. The temperature is achieved by supplying 660 W of electrical power to the oven of the CONAC press or alternatively 640 W to the oven of the BELT. Accidentally it was observed that samples can be prepared in the BELT press at a slightly lower power input of 540 W. The 6 GPa pressure translates to a force of 800 tons applied to the anvils of the CONAC or 115 tons applied to the pistons of the BELT. Thus the reaction parameters can be translated into 800t / 660 W / 90 min for the CONAC and 115t / 640 W / 90 min for the BELT.

It can be seen that the conditions are extreme and under these high pressures, explosions of the pressure cells or failures of the components of a press are not unusual. Figures 3.11 and 3.12 present the aftermath of such explosions.

Fig. 3.11. The explosion of a CONAC pressure cell. Notice the radial trajectories caused by the flying debris.

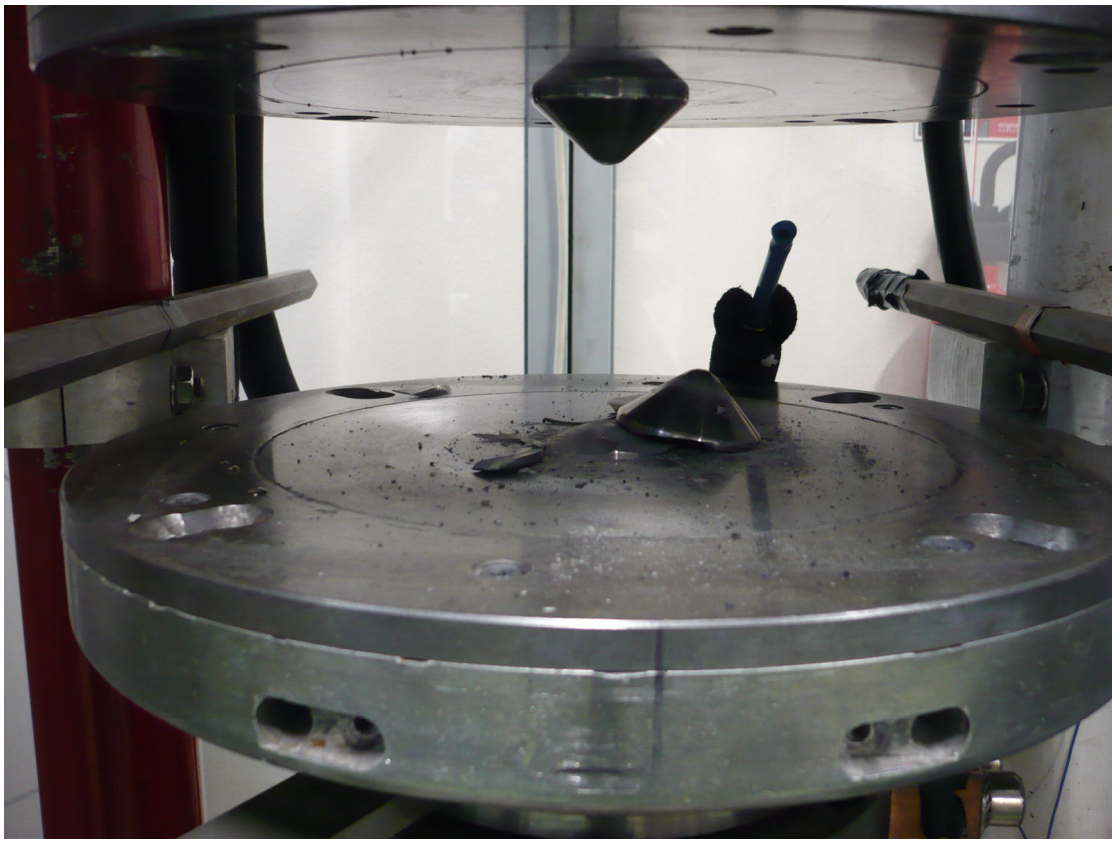

Fig. 3.12. Broken lower piston of the BELT press.

III.2.3. The first results – phase characterization

XRD is used as the first investigation technique in order to confirm (or not) the formation of the required phase and the presence or absence of starting products and/or secondary phases in the final product. For phase identifications XRD patterns recorded with a short counting time of 1 second / step (step size is 0.016°) or less are sufficient.

XRD is not the only technique employed. Also a Zeiss scanning electron microscope (SEM) equipped with a microanalysis probe (EDX) is used to check the morphologic aspect of the powder and their chemical composition and even the chemical distribution of the elements in the sample. This last feature is a very useful tool as it can detect regions in the sample in which one chemical element is found in concentrations greater than expected, i.e. an impurity that may not be visible in the XRD pattern. An even more insightful approach is to check the magnetic fingerprint of the sample in a SQUID magnetometer as the SQUID is very sensitive to even the tiniest amounts of impurities, where as XRD requires the presence of about 5 % of a secondary phase in order to make that secondary phase visible in the diffraction pattern.

The series of investigations, XRD, SEM, EDX and SQUID were performed for virtually every sample. However, data from the SQUID will not be treated here but in the chapter dedicated to magnetism. Also, not all the samples are presented but only a few representative ones and the emphasis will be only on the phase identification at this stage.

a) $PbVO_3$

Diffraction patterns for the best samples in the synthesis of $PbVO_3$ are presented below in figures 3.13 and 3.14. In the case of $PbVO_3$ a re-annealing treatment was found to provide samples of higher purity. For the re-annealing, $PbVO_3$ samples produced in two separate experiments were mixed and ground together. The powder thus obtained was used to fill a new gold capsule and the HP – HT treatment was carried out again. Some powder is lost during the opening of a capsule, therefore two initial capsules of $PbVO_3$ are required to prepare and fill a third capsule for a re-annealing HP – HT treatment.

Figure 3.13 shows the XRD pattern and Rietveld refinement for a $PbVO_3$ sample after the first HP – HT treatment. The red points are the experimental data, the diagram recorded by the diffractometer. The black line is the calculated diagram. The coloured short vertical lines mark the positions of the Bragg reflections in the calculated diagram. Lastly, the blue line is the difference between the observed and calculated diagrams.

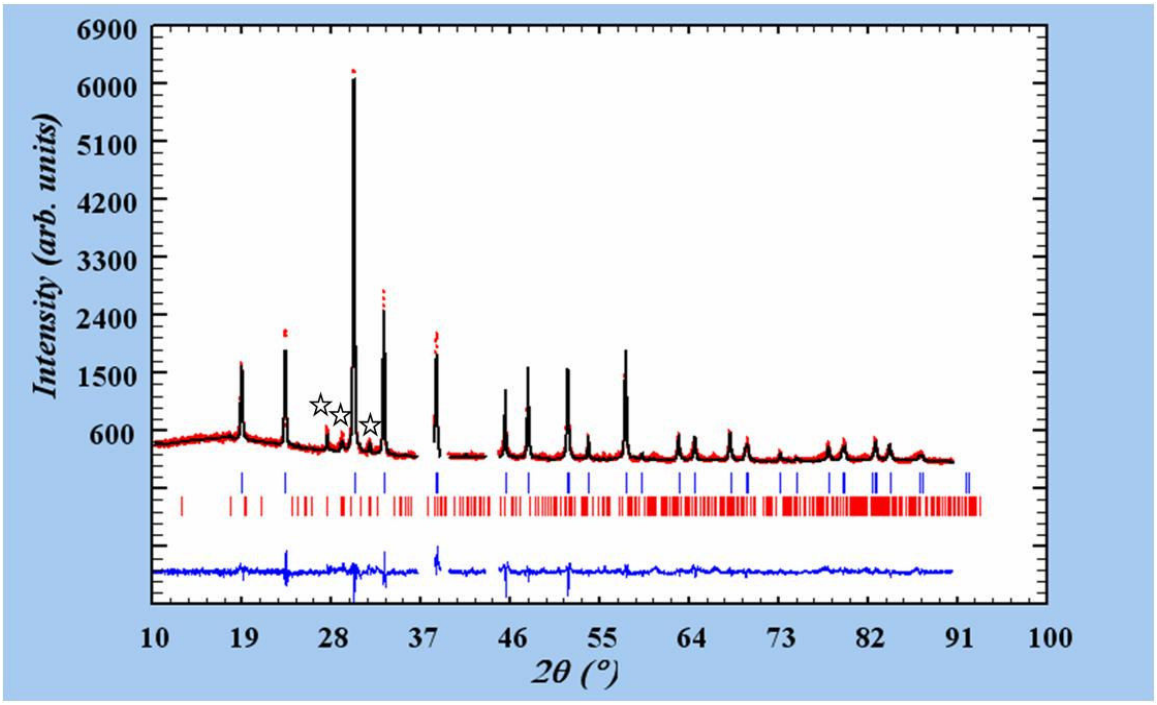

Fig. 3.13. $PbVO_3$ sample (PVO_003) before re-annealing (HP-HT 6 GPa / 950 °C / 90 min). The peaks of the secondary phase are marked with stars.

It can be seen from the red and blue tics that a secondary phase is present in the sample. Upon closer investigation a few other peaks which remain unexplained can also be seen. The excluded regions (the cuts in the XRD pattern) hide peaks which were found to be a contribution of the instrument.

The main phase (blue tics) is identified as $PbVO_3$ and is indexed with data available in literature [32] namely, a tetragonal structure with the space group P4mm, lattice parameters a = b = 3.8 Å and c = 4.67 Å. The second phase is the monoclinic $Pb_3V_2O_8$ (space group P21/c, from reference [76, 77]). This phase re-appears in almost every sample and it is easily identified by several diffraction peaks located near the highest intensity peak of $PbVO_3$.

The phase percentage is estimated to 92 % main phase, or $PbVO_3$ and 7 % impurity phase, $Pb_3V_2O_8$.

After the re-annealing treatment the XRD diagram of the $PbVO_3$ sample is the one presented in figure 3.14.

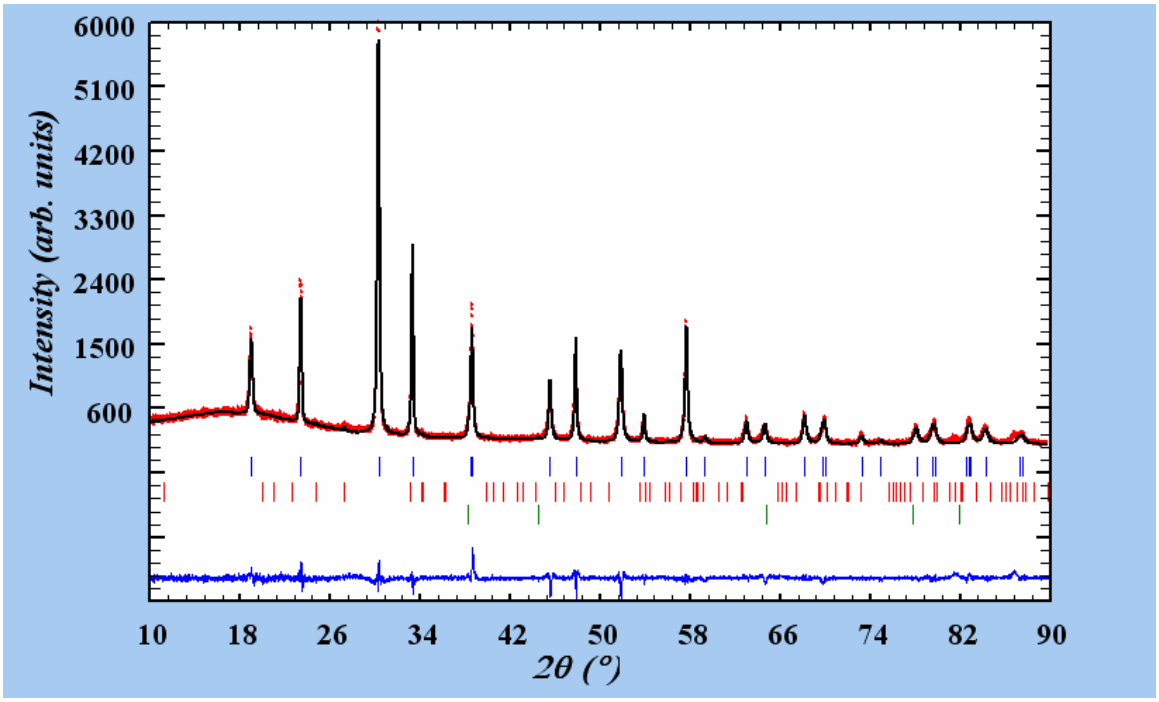

Fig. 3.14. $PbVO_3$ sample (PVO_005) after re-annealing (HP-HT 6 GPa / 950 °C / 90 min).

The amount of impurities has greatly reduced and the characteristic peaks of $Pb_3V_2O_8$ mentioned above have completely disappeared. With increased zoom on the region between 2θ = 25° and 35° three small peaks are visible. These peaks are given by a lead carbonate, namely hydrocerussite which has the composition $Pb_3(CO_3)_2(OH)_2$ [78]. The estimated percentage of hydrocerussite in the sample is approximately 2.8 %, however since this value is under the roughly 5% limit, it can not be considered a reliable value. The row of green tics marks the presence of a third impurity. This one is identified as a gold contamination resulted from the capsule. There are two ways in which gold could have entered into the sample. The first is the gold diffusion discussed in the previous pages and the second path consists simply in a slight contamination of the powder during the opening of the capsule. In either way,

the gold is not considered as part of the powder and is not counted as a "proper" impurity therefore the sample contains practically a single phase.

b) $PbV_{1-x}Ti_xO_3$

When vanadium is substituted with titanium (or iron) there is no need for re-annealing. Single phase samples are obtained from a single experiment. For illustrating this, diagrams for the samples substituted with 10% Ti and 30% Fe are shown in the next figures.

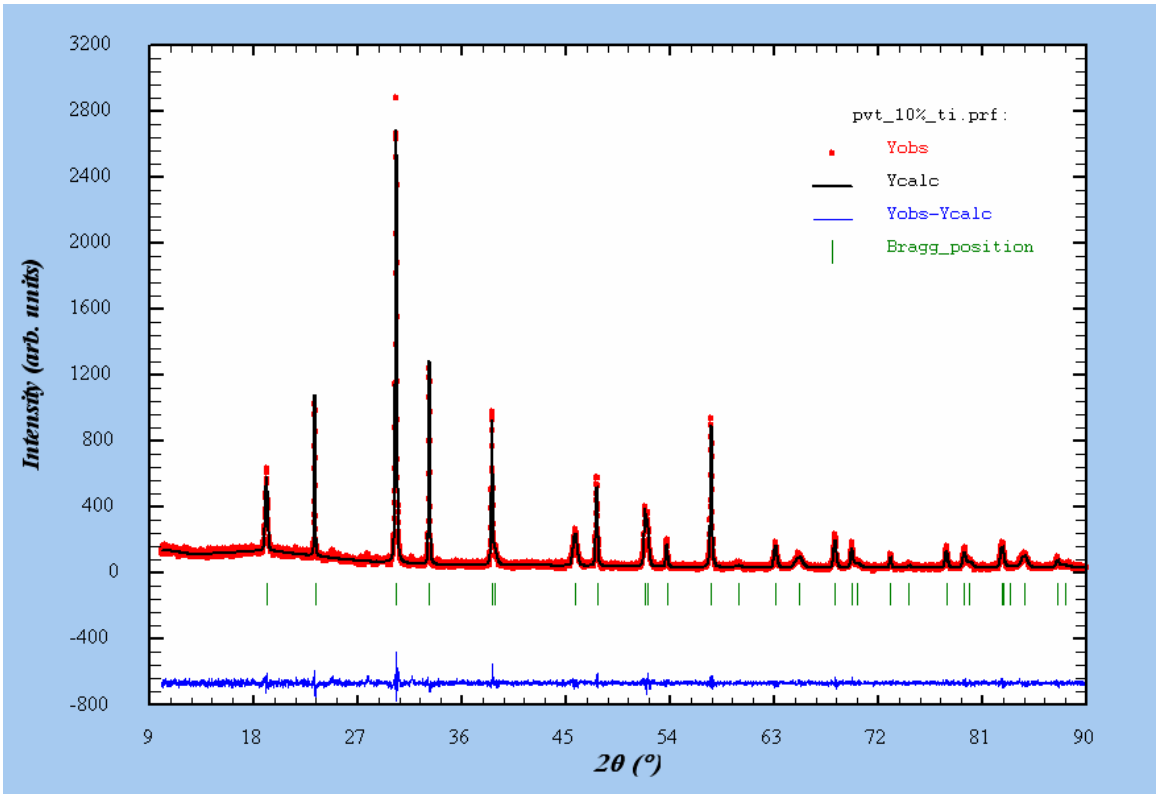

Fig. 3.15. XRD and Rietveld refinement for $PbV_{0.9}Ti_{0.1}O_3$ (HP-HT 6 GPa / 950 °C / 90 min). This sample is labelled PVT_007.

The sample contains no visible amounts of impurities. The diffraction peaks can be indexed with the same tetragonal structure and the same space group (P4mm) as for $PbVO_3$ but with different lattice parameters (a = 3.82 Å c = 4.56 Å) indicating the fact that the titanium is absorbed into the structure.

c) $PbV_{1-x}Fe_xO_3$

Similarly for the sample in which the vanadium is substituted by iron no impurities are visible in the XRD diagram.

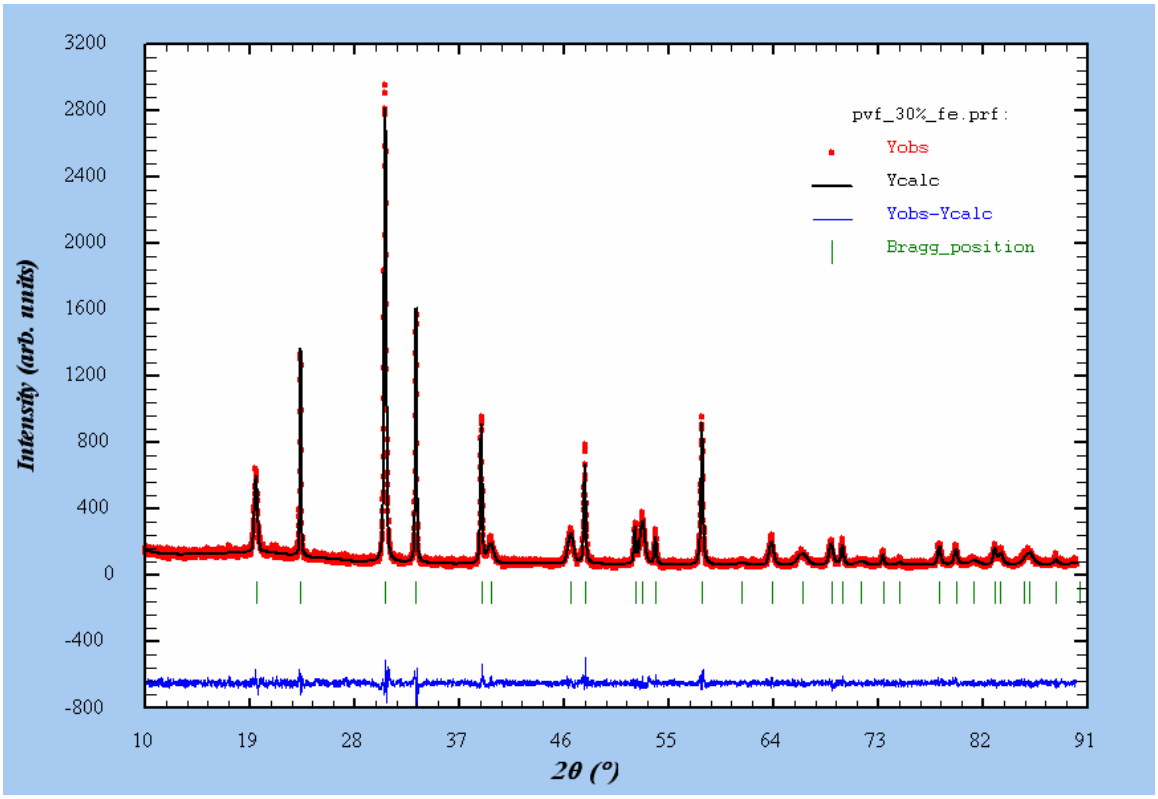

Fig 3.16. XRD and Rietveld refinement for $PbV_{0.7}Fe_{0.3}O_3$ (HP-HT conditions 6 GPa / 950 °C / 90 min), sample label PVF_004.

Again the diagram is indexed by a tetragonal structure with the pace group P4mm but different lattice parameters from $PbVO_3$ (a = 3.8 Å c = 4.53 Å). The change in lattice parameters is proof that iron, this time, is absorbed into the structure. Details about the variation of lattice parameters will be given in the following chapters.

III.3. Chemical characterization by Energy dispersive X-Ray spectroscopy, EDX

The chemical composition of the samples was quickly using standardless EDX measurements. This method is fast, easy to use and the preparation of the sample for the measurement is simple but it has the disadvantage of not having an excellent precision. Therefore, the average of several determinations actually comes close to the actual chemical composition but even so, the technique is suitable for the confirmation of the stoichiometry of a sample.

One sample from each series is chosen as an example. All the samples were characterised in the optimum conditions which are 8 mm working distance (WD) and 20 KV acceleration voltage.

a) $PbVO_3$

For $PbVO_3$ the EDX spectrum shows the characteristic peaks for lead and vanadium and one small peak from carbon which is not marked for clarity.

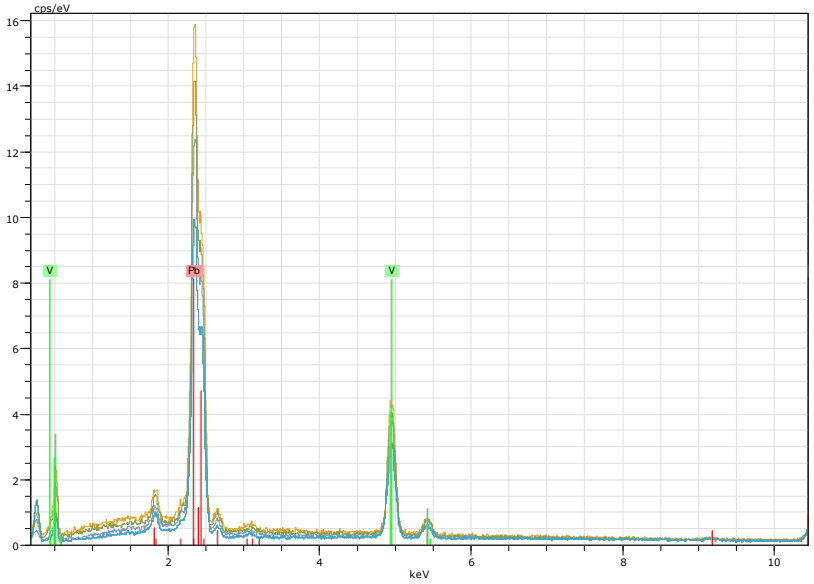

Fig. 3.17. EDX spectrum for $PbVO_3$ sample label PVO_010.

The ratio of lead to vanadium atoms is 50:50, expressed in atomic percentages without taking into account the oxygen atoms. The observed atomic ratio, calculated from the spectrum is close to the theoretic value in the margin of error of +/- 3%. Table 3.5 gives the atomic ratios found in various points on the surface of the sample and the apparent chemical composition corresponding to the respective points.

The average value over the four points returns an atom ratio of Pb:V = 48.62: 50.01 which is close within the precision of the method to the 50: 50 theoretic ratio. It is interesting nevertheless to pay attention to each individual point in which the EDX analysis is conducted because this can highlight the presence of a grain of a different phase, with a different chemical composition.

Table 3.5 Atomic ratio and corresponding chemical composition for a $PbVO_3$ sample. The chemical composition is normalised to the element found in the highest concentration.

composition $PbVO_3$			
theoretic atomic ratio (%) Pb: V = 50: 50			
observed atomic ratio (%)		corresponding composition	
Pb	V	Pb	V
52.09	42.46	1	0.81
46.45	53.55	0.86	1
48.53	51.47	0.94	1
47.44	52.56	0.90	1
Mean value			
48.62	**50.01**	**0.97**	**1**

b) $PbV_{1-x}Ti_xO_3$

For the titanium substitution series, the sample were the substitution is 50% provides a good example. The EDX spectra, showing the characteristic peaks of lead vanadium and titanium (carbon not marked for clarity) is provided along with the chart showing the observed chemical composition.

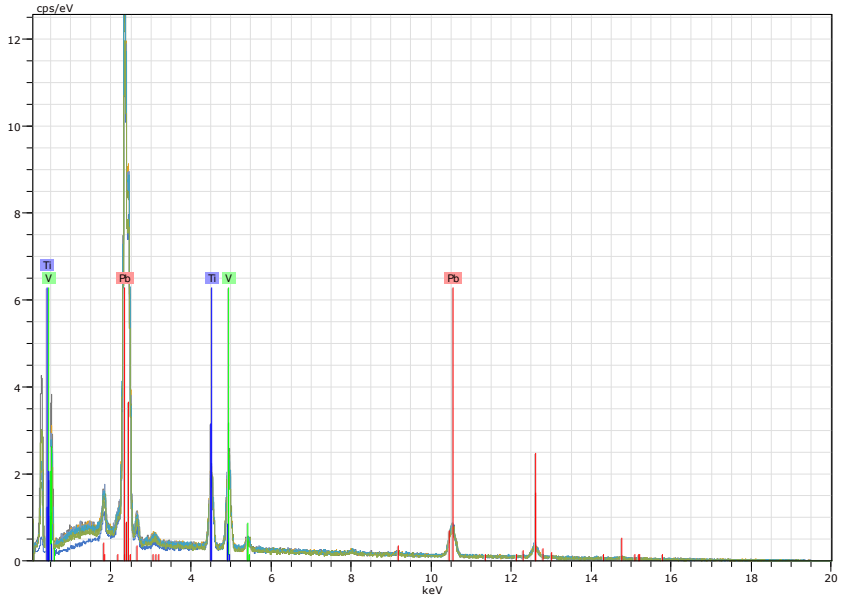

Fig. 3.18. PVT_002 EDX spectrum. Nominal composition is $PbV_{0.5}Ti_{0.5}O_3$. Lead is represented in red, vanadium in green and titanium in blue.

Table 3.6 Atomic ratio and chemical composition for $PbV_{0.5}Ti_{0.5}O_3$.

composition $PbV_{0.5}Ti_{0.5}O_3$					
theoretic atomic ratio (%) Pb: V: Ti = 50: 25: 25					
observed atomic ratio (%)			corresponding composition		
Pb	V	Ti	Pb	V	Ti
46.74	27.63	25.63	1	0.59	0.54
46.73	27.15	26.13	1	0.58	0.55
46.41	27.35	26.24	1	0.58	0.56
46.77	26.93	26.30	1	0.57	0.56
48.51	27.34	24.15	1	0.56	0.49
47.49	27.84	24.67	1	0.58	0.51
48.75	22.90	28.34	1	0.46	0.58
Mean value					
47.34	**26.73**	**25.92**	**1**	**0.56**	**0.54**

The same atomic ratio is found on all the measurements demonstrating the homogeneity of the sample. The observed atom ratio is very close to the expected one proving that stoichiometric composition of the sample is indeed the composition that

was aimed. For the case of the $PbV_{0.5}Ti_{0.5}O_3$ sample, the average on all the measure points yields a composition that contains the same amount of V and Ti, in good agreement with the sought composition

c) $PbV_{1-x}Fe_xO_3$

On the iron substitution series, the best example is provided by $PbV_{0.9}Fe_{0.1}O_3$ or, the 10% Fe sample. The same representation is employed for this sample. The EDX spectra shows the peaks corresponding to lead, vanadium and iron in figure 3.19 and the observed atomic ratios and calculated corresponding stoichiometries are presented in table 3.7.

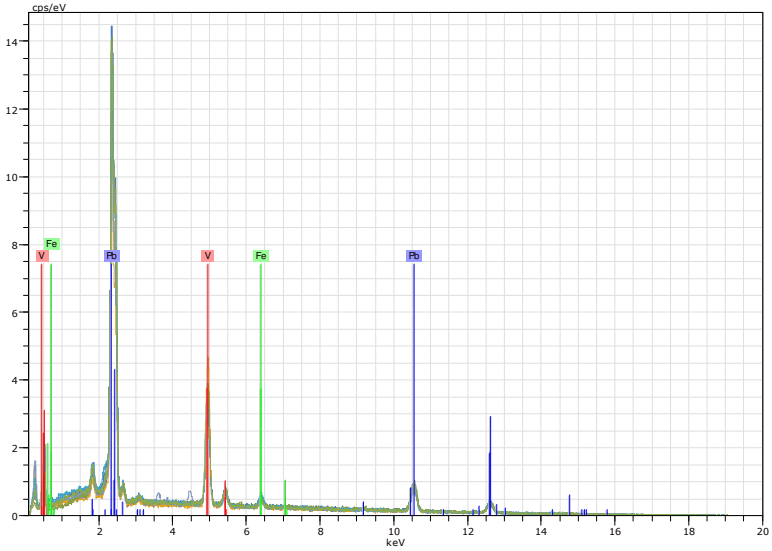

Fig. 3.19. PFV_002 EDX spectrum. The nominal composition of the sample is $PbV_{0.9}Fe_{0.1}O_3$. The peaks corresponding to lead are marked with blue lines, the ones for vanadium with red and the peaks from iron with green.

Table 3.7 Atomic ratio and calculated chemical composition for $PbV_{0.9}Fe_{0.1}O_3$.

composition $PbV_{0.9}Fe_{0.1}O_3$					
theoretic atomic ratio (%) Pb: V: Fe = 50: 45: 5					
observed atomic ratio (%)			corresponding composition		
Pb	V	Fe	Pb	V	Fe
44.13	47.33	8.53	0.93	1	0.18
53.06	42.47	4.46	1	0.80	0.08
48.31	45.89	5.79	1	0.94	0.11
48.62	45.35	6.03	1	0.93	0.12
48.03	46.42	5.55	1	0.96	0.11
45.31	50.19	4.50	0.90	1	0.08
Mean value					
47.91	46.27	5.81	0.97	0.93	0.11

Within the error margins of the EDX spectrometer the same composition is found in all the places in which the EDX spectra are gathered. This gives evidence of the homogeneity of the sample. The observed stoichiometry corresponds to the nominal stoichiometry. For this example the sample has the nominal stoichiometry $PbV_{0.9}Fe_{0.1}O_3$ and the observed average stoichiometry is $Pb_{0.97}V_{0.93}Fe_{0.11}O_3$. It should be noted however that the measurements and calculations include only the metal atoms but not the oxygen atoms.

III.4. Morphology and surface characterization by SEM

At the level of morphological investigation all the samples have the aspect of very well compacted, well sintered powders. This is an expected result in the synthesis under high pressure, in agreement with the literature [33]. A few SEM images are provided in order to help form an idea about the degree of packing of the powders.

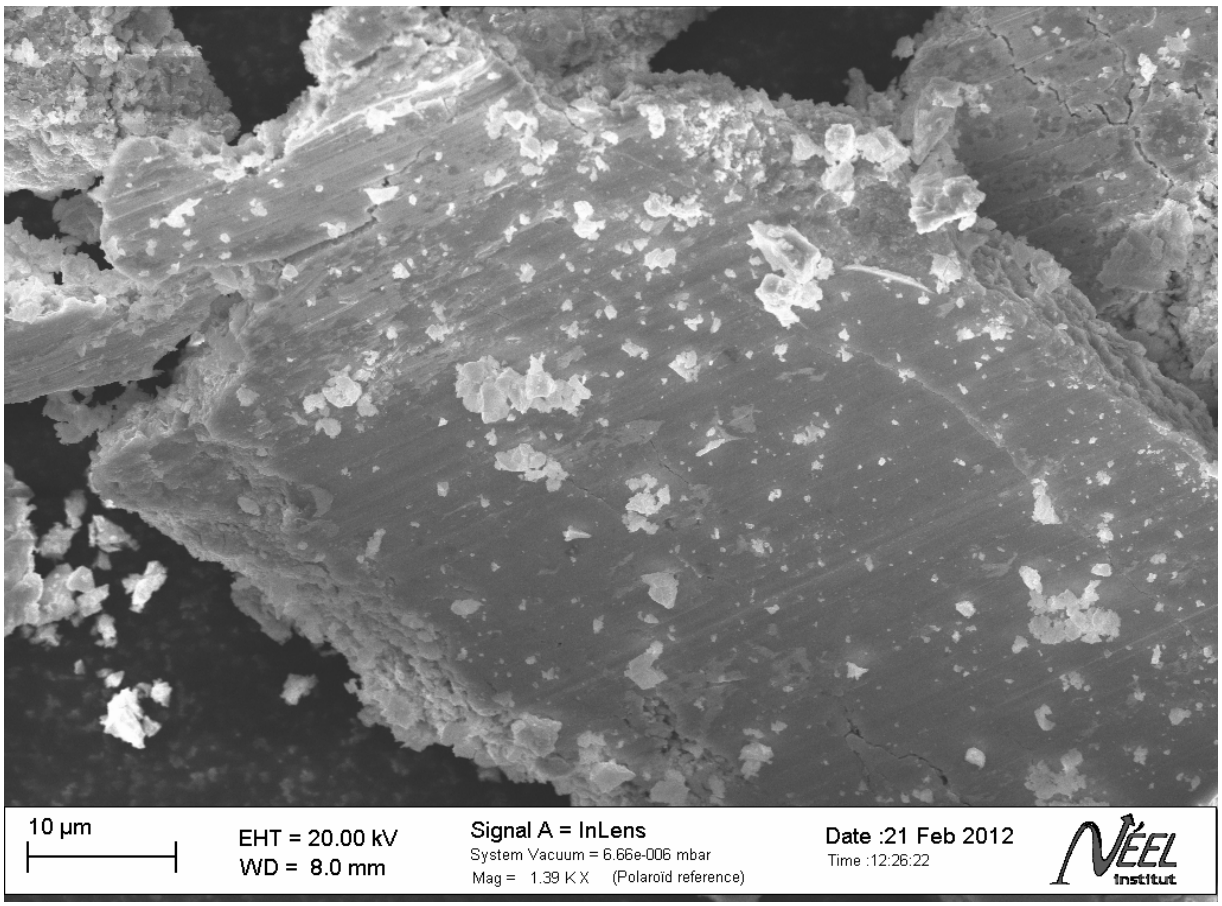

Fig. 3.20. Grains of $PbVO_3$ sample PVO_005. Parallel scratches can be observed on the surface of the grain.

Sometimes tiny isolated cubes can be seen, such as the one shown in figure 3.21 which belongs to the sample with the 25% Fe substitution.

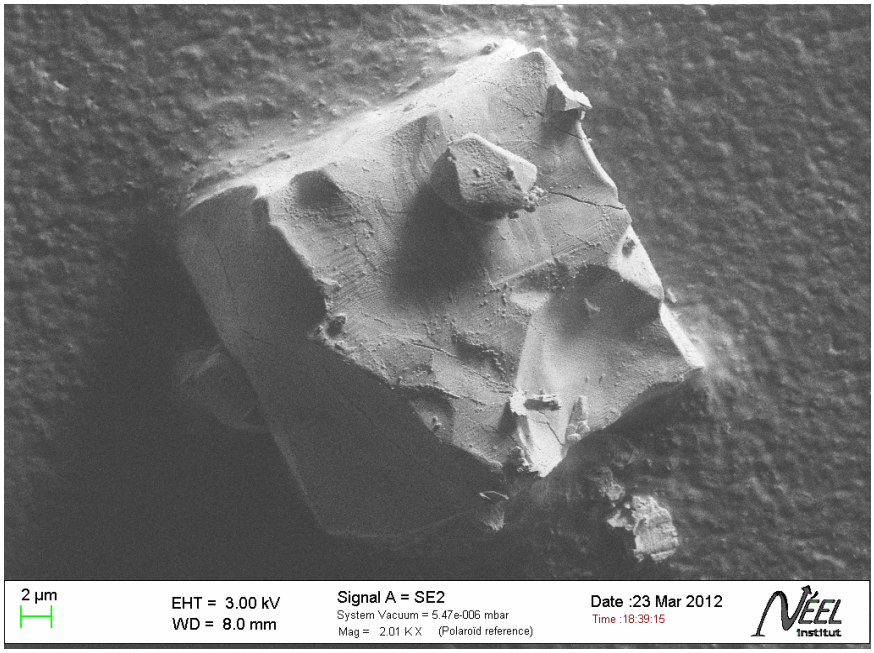

Fig. 3.21. Tiny cube of $PbV_{0.75}Fe_{0.25}O_3$ (PVF_001).

In other samples clean surfaces can sometimes result and this allows for the observation of the crystallites which form the sample. This is the case of the 40% Fe sample, shown in the picture below. Average crystallite sizes are in the range of 0.5 µm to 20 µm.

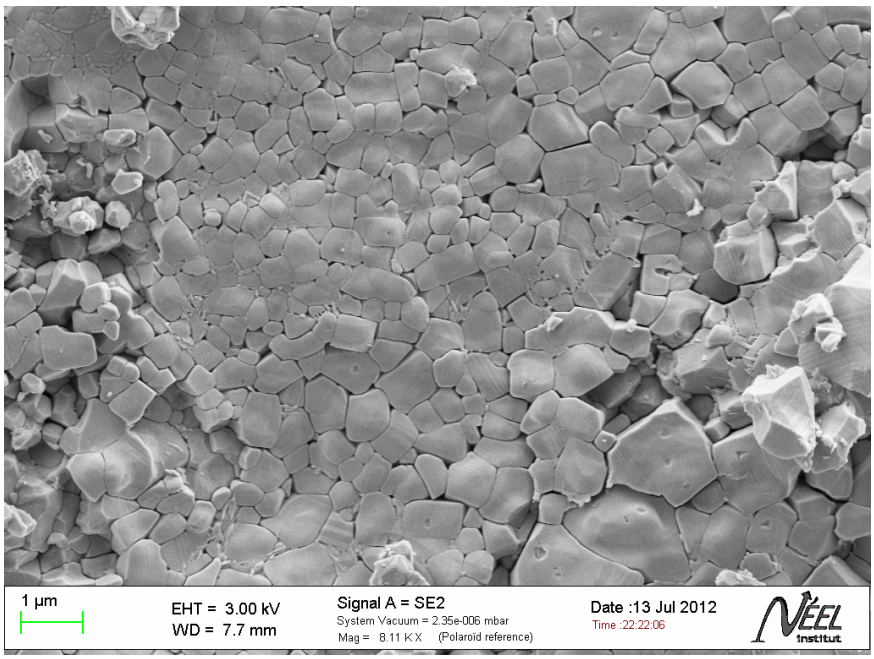

Fig. 3.22. Crystallites clearly seen on the $PbV_{0.6}Fe_{0.4}O_3$ sample. Sample label PVF_010.

The problem of the size of the crystallites is however more complicated and will be addressed in the chapter reserved for X-Ray diffraction measurements.

Single crystals were examined by scanning electron microscopy and also under a stereoscope. The shape of the crystals is that of a distorted prism. The average lengths of the crystals are between 100 to 500 μm and the width of the crystals is approximately 50 μm, in agreement with the literature [37].

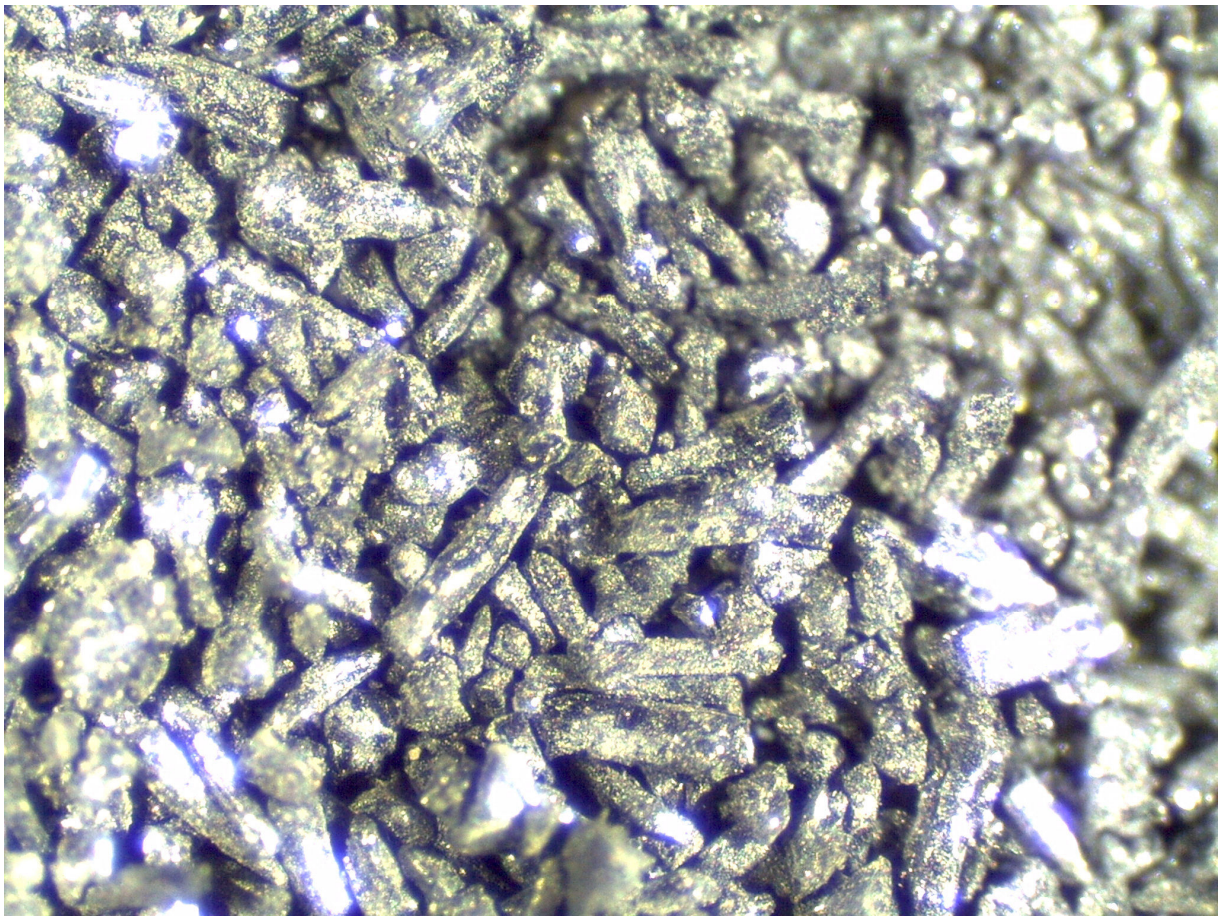

Fig. 3.23. $PbVO_3$ single crystals (PVO_011).

III.5. Local structure investigated by XANES

The magnetic and dielectric properties of the $PbVO_3$ samples and the samples with Ti or Fe substitutions can not be explained on the basis of only the average structure. For a better understanding of the physical properties of the samples it is necessary to probe their local structure. A very useful tool for such an investigation is the X-Ray Absorption Spectroscopy (XAS). The absorption edge of V was investigated on a number of samples at the BM32 FAME French CRG beamline at the ESRF synchrotron facility in Grenoble, France.

In this work only the XANES data obtained for the absorption edge of V in 4 representative samples is discussed. These samples are the following: $PbVO_3$, $PbV_{0.75}Ti_{0.25}O_3$ (25% Ti), $PbV_{0.75}Fe_{0.25}O_3$ (25% Fe) and $PbV_{0.5}Fe_{0.5}O_3$ (50% Fe). The absorption spectrum for these samples is shown in figure 3.24.

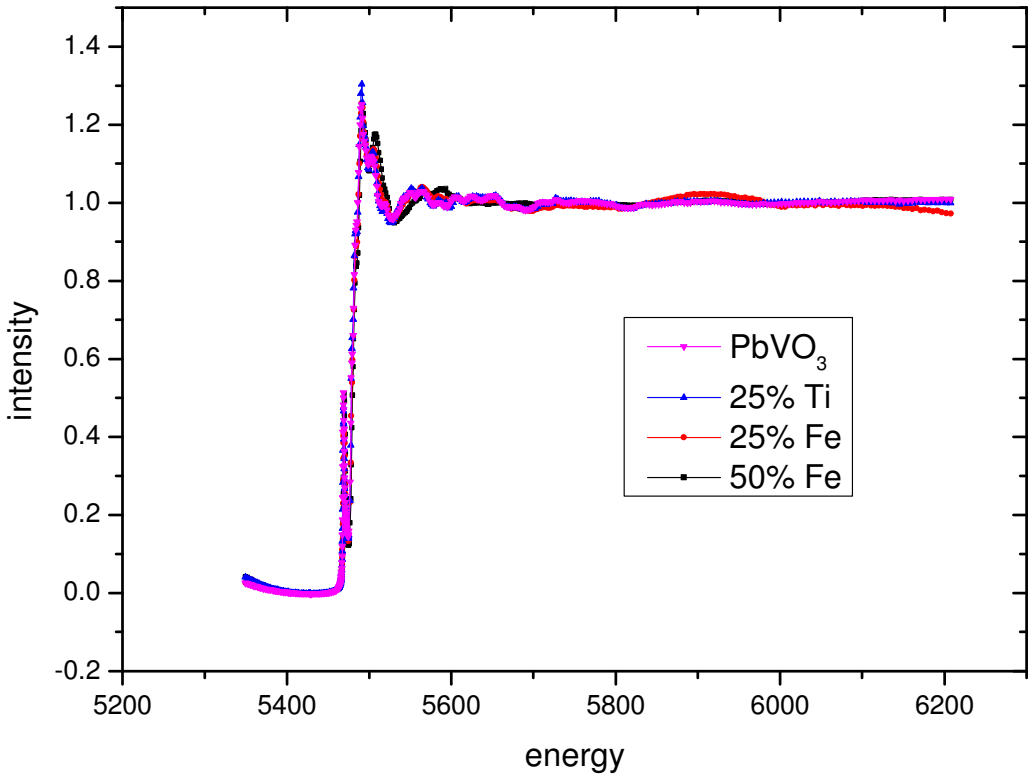

Fig. 3.24. XAS for $PbVO_3$ and substitution samples: 25% Ti, 25% Fe, 50% Fe.

The objective of this measure was to determine the oxidation state that Vanadium takes in the four samples. This can be observed from the shift of the pre-peak, located at about 5470 eV. A zoom on the pre-peak is shown in figure 3.25.

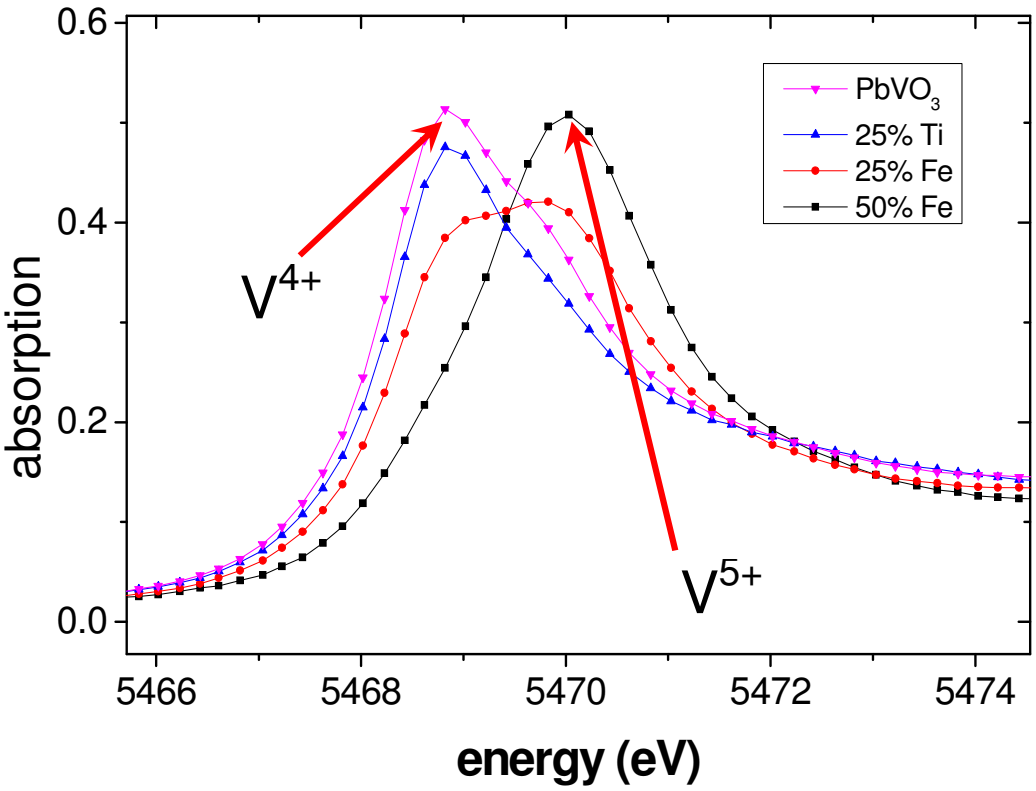

Fig. 3.25. XANES region for XAS of $PbVO_3$, and substitution samples.

The positions of the peaks corresponding to the oxidation states of V are indicated on the figure by arrows. The peak on the right corresponds to the 5+ oxidation state and the peak on the left is generated by vanadium oxidized to V^{4+}. It is observed that the position of the peak changes depending on the type and degree of substitution. More specifically a change in the degree of oxidation of V is observed in the case of the Fe substitution but no such change appears for the Ti substitution.

For $PbVO_3$ (the pink line) the oxidation of V is 4+, as predicted by considering the valence of Pb to be 2+ and that of oxygen 2-. In the case of the Ti substitution, Titanium is also 4+ oxidized so a Ti^{4+} ion replaces a V^{4+} ion and other than that no modification occurs. The peak of the 25% Ti sample (blue line) is at the same energy as the one of $PbVO_3$ meaning that indeed in the Ti series, the Vanadium ions remain 4+. The substitution with Ti is therefore isovalent and this is what allows the

formation of the complete solid solution, seen by XRD. The formula of the compounds from the Ti series should in fact be written as $\mathbf{Pb(V^{4+}_{1-x}\,Ti^{4+}_{x})O_3}$.

Iron is generally Fe^{3+}. Fe^{4+} also exists but it is unstable so, in a first approximation we can assume that the Fe induced in the PVF samples is Fe^{3+}. We also assume that Fe takes the place of V and not Pb so the substitution remains only at the B site cation. In this assumption, there is an immediate problem because an Fe^{3+} ion has to replace a V^{4+} and this leads to a great imbalance in valence. In order to restore the balance another vanadium ion from the sample increases its oxidation state to 5+ (vanadium will always go to 5+ if it has the opportunity) so the average oxidation state at the B site remains 4+. That means that strictly speaking for every Fe^{3+} ion introduced in the sample two V^{4+} ions are "removed". The first V^{4+} to be removed is the ion directly replaced by Fe^{3+} and the second V^{4+} that is removed is the V^{4+} that oxidizes to V^{5+}. In that case, the formula of the product is $\mathbf{Pb(V^{4+}_{1-2x}\,V^{5+}_{x}\,Fe^{3+}_{x})O_3}$. This explains why the solid solution stops at 50% Fe since at 50% Fe practically all the V^{4+} ions are exhausted. All the vanadium that remains in the 50% Fe sample is vanadium 5+. This can be verified in the peak position of the respective sample (the black line), which shows that the oxidation state of Vanadium is 5+. The sample with 25% Fe is half way into the solid solution and contains both V^{4+} and V^{5+}. The peak of the 25% Fe (red line) has the shape of the convolution of two other peaks (namely the peaks of V^{4+} and V^{5+}) which confirms the presence of both types of vanadium ions in the sample and the validity of the theory. This model also justifies the choice in the method of calculating the effective moment in the Fe series as: $\mu^2_{eff} = (1-2x)*\mu^2_V + x*\mu^2_{Fe}$.

III.6. Sample review

A table containing the essential information (composition, label, synthesis conditions and impurities) about all the samples that are discussed during this work is provided below. The labels and the compositions will be used for the identification of the samples throughout the work. The table contains 4 parts. The first 3 parts deal with the pristine samples and the samples of the two substitutions. The last table provides the list of the samples that were mixed together for usage at NPD.

Table 3.8 Identification of the samples

a)

$PbVO_3$				
short composition	extended composition	sample label	synthesis conditions	impurities
$PbVO_3$	$PbVO_3$	PVO_005	6 GPa / 950°C / 90 min + reannealing	$Pb_3(CO_3)_2(OH)_2$, Au
$PbVO_3$	$PbVO_3$	PVO_009	6 GPa / 950°C / 90 min	$Pb_3V_2O_8$, Au
$PbVO_3$	$PbVO_3$	PVO_010	6 GPa / 950°C / 90 min + reannealing	$Pb_3(CO_3)_2(OH)_2$, Au
$PbVO_3$ single crystals	$PbVO_3$	PVO_010	6 GPa / 950°C / 12 h (+temperature ramp)	maybe $Pb_3(CO_3)_2(OH)_2$

b)

Ti substitution $PbV_{1-x}Ti_xO_3$				
composition		sample label	synthesis conditions	impurities
short	extended			
10% Ti	$PbV_{0.9}Ti_{0.1}O_3$	PVT_007	6 GPa / 950°C / 90 min	-
25% Ti	$PbV_{0.75}Ti_{0.25}O_3$	PVT_001	6 GPa / 950°C / 90 min	-
50% Ti	$PbV_{0.5}Ti_{0.5}O_3$	PVT_002	6 GPa / 950°C / 90 min	-
60% Ti	$PbV_{0.4}Ti_{0.6}O_3$	PVT_004	6 GPa / 950°C / 90 min	-
75% Ti	$PbV_{0.25}Ti_{0.75}O_3$	PVT_006	6 GPa / 950°C / 90 min	not identified, visible at SQUID
80% Ti	$PbV_{0.2}Ti_{0.8}O_3$	PVT_005	6 GPa / 950°C / 90 min	-
100% Ti	$PbTiO_3$	S-PTO_001	850°C / 24h (sealed tube synthesis)	-

c)

Fe substitution $PbV_{1-x}Fe_xO_3$				
composition		sample label	synthesis conditions	impurities
short	extended			
10% Fe	$PbV_{0.9}Fe_{0.1}O_3$	PVF_002	6 GPa / 950°C / 90 min	$Pb_3V_2O_8$
20% Fe	$PbV_{0.8}Fe_{0.2}O_3$	PVF_007	6 GPa / 950°C / 90 min	$Pb_3V_2O_8$, $Pb_3(CO_3)_2(OH)_2$
25% Fe	$PbV_{0.75}Fe_{0.25}O_3$	PVF_001	6 GPa / 950°C / 90 min	-
30% Fe	$PbV_{0.7}Fe_{0.3}O_3$	PVF_004	6 GPa / 950°C / 90 min	-
40% Fe	$PbV_{0.6}Fe_{0.4}O_3$	PVF_010	6 GPa / 950°C / 90 min	-
40% Fe	$PbV_{0.6}Fe_{0.4}O_3$	PVF_014	6 GPa / 950°C / 90 min	Fe_2O_3
40% Fe	$PbV_{0.6}Fe_{0.4}O_3$	PVF_020	6 GPa / 750°C / 90 min	-
50% Fe	$PbV_{0.5}Fe_{0.5}O_3$	PVF_011	6 GPa / 950°C / 90 min + reannealing	the cubic phase

d) samples used for NPD

name	composition	samples mixed
PVO	$PbVO_3$	PVO_005, PVO_010, PVO_011
PVT_25	$PbV_{0.75}Ti_{0.25}O_3$	PVT_001, PVT_008, PVT_010, PVT_011, PVT_012
PVF_25	$PbV_{0.75}Fe_{0.25}O_3$	PVF_001, PVF_008, PVF_009, PVF_013
PVF_40	$PbV_{0.6}Fe_{0.4}O_3$	PVF_010, PVF_014, PVF_020, PVF_022

Chapter IV. Crystalline structure from XRD and NPD measurements

So far we have discussed the state in which the research on $PbVO_3$ has reached and the investigation techniques used in our study, and described the synthesis and characterization of our samples. In the following chapters the results obtained in our investigation of structural and physical properties will be discussed.

We will begin by the study of the evolution of the $PbVO_3$ structure upon substitution of V with Fe and Ti. The knowledge of these structural changes will be important in order to understand the evolution of the physical properties with substitution. The study has been carried out by a combination of X-ray and neutron powder diffraction. X-ray single crystal diffraction was also used in the case of $PbVO_3$, for which we were able to grow single crystals of sufficient size.

IV.1. Crystalline structure of $PbVO_3$

Before testing the substitution samples it is important to investigate the "clean" sample, that is, $PbVO_3$ for which no substitution was made.

$PbVO_3$ is a perovskite-type oxide which crystallises in a structure with tetragonal symmetry, space group P4mm (no. 99) and has the lattice parameters a~3.8 Å and c~4.67Å. The $PbVO_3$ compound is isostructural to the well-known $PbTiO_3$ ferroelectric compound, but in the case of $PbVO_3$ the ferroelectric distortion is larger (c/a = 1.06 for $PbTiO_3$ and c/a = 1.23 for $PbVO_3$). The Pb atoms occupy the 1a (000) position at the corners of the unit cell and the V atoms are located at the 1b (1/2 12/ z~0.57) position strongly displaced from the centre of the cell along the c axis. The oxygen atoms are also largely displaced from the face centres they would occupy in the archetypal cubic perovskite structure with O1 at 1b (1/2 1/2 z~0.22) and O2 at 2c (1/2 0 z~0.69). They form a strongly elongated octahedron which is shifted from the unit cell centre along the c axis. As a result, the vanadium coordination can be

considered as square pyramidal with a quite short V-O1 distance (1.65 Å) and four longer V-O2 distances (1.98 Å). A sixth V-O1 much longer bond (3.1 Å) completes the octahedron. As a result of the oxygen anion displacements along c, the Pb cations are located inside a square antiprism with four short (2.4 Å) bonds to O2 and four long bonds (2.9 Å) to O1 [31]. Figure 4.1 shows a representation of the structure of $PbVO_3$.

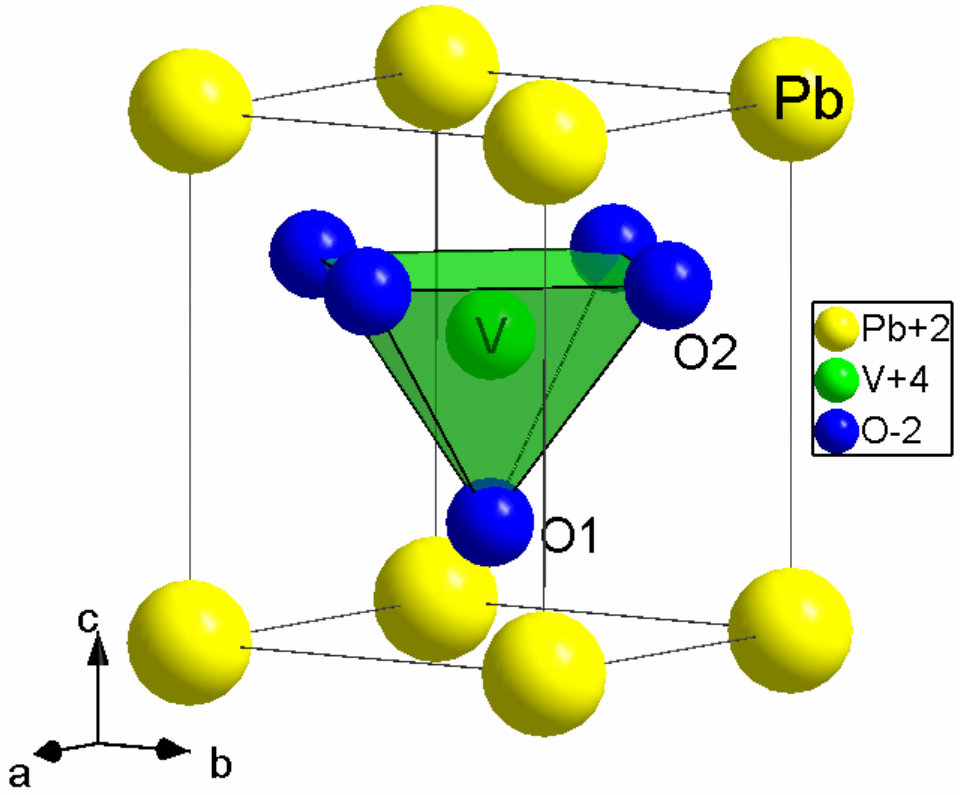

Fig. 4.1. Structure of $PbVO_3$. The Pb^{2+} cations (yellow) occupy the corners of the structure. The V^{4+} cation (green) is close to the centre of the structure and it is surrounded by 5 O^{2-} anions (blue) forming a pyramid. The faces of the oxygen pyramid are also represented (green).

IV.1.1. $PbVO_3$ single crystal structure refinement

Whenever possible, the use of single crystal diffraction to study the structure yields more accurate and precise results than what can be obtained by using powders. This is mainly because a much larger number of Bragg peaks can be individually measured up to a far better accuracy using a single crystal diffractometer. The present study provides the first report of a single crystal structural determination of $PbVO_3$. Previous determinations of the structure, reported in literature, were always made on powder samples.

Single crystal X-Ray diffraction data were collected and analysed with the help of Dr. Pierre Bordet and Dr. Olivier Leynaud.

The X-Ray diffraction data were collected using a Bruker Kappa Apex II diffractometer equipped with an Incoatec microsource generator providing a beam focused on the sample and monochromatized by a multilayer optics. The AgKα radiation was used (λ = 0.56087 Å) and the beam diameter at the sample position was approximately 100 µm (at half width). The sample is glued to a quartz fibre and mounted on a translation head. The head is attached to the three goniometer rotation stages (phi, omega, kappa) which allow reaching any orientation of the crystal placed at the goniometer centre. A diffraction image is then formed by shining the x-ray beam on the sample while it is rotating about a chosen axis. The Bragg peaks diffracted by the crystal are recorded on the Apex II CCD camera carried by the goniometer theta axis. The distance DX between sample and detector can also be chosen.

In order to collect a complete and accurate set of Bragg peak intensities for the structure solution and refinement, a typical data collection consists in performing several scans of the crystal. The type and ranges of the scans to be performed are chosen in order to provide optimal completeness and redundancy of the data collection. Completeness is defined as the ratio of symmetry-unique reflections actually measured in a given theta range over the theoretical number of such reflections determined from the unit cell and point group symmetry. Completeness should be as close to unity as possible. Redundancy is defined as the average number of symmetry-equivalent reflections which are measured. Although a redundancy of 1 should be sufficient in theory, redundant data are in fact very useful to check the point

group symmetry and to perform empirical absorption for anisotropic effects such as absorption of non spherical crystals, beam inhomogeneities, etc… The scans to be performed are determined by the software from the knowledge of the unit cell, symmetry and orientation matrix of the crystal, the desired theta measurement range and the expected values of completeness and redundancy.

Since each scan range can extend over 10's of degrees, they are divided in smaller ranges in order to not have too many reflections present on each measured frame (image) and thus to avoid overlapping of peaks. The typical frame width ranges between 0.5 and 2°. The measurement time is typically of the order of a few seconds to a few minutes per degree, depending on the sample diffracting power.

The experiment thus consists in the following steps:

Mounting and centring of the crystal on the goniometer

Examination of crystal quality by making a single diffraction image

Short data collection allowing determining the unit cell and orientation matrix

Calculation of the optimal scanning sequence, frame width and frame time.

Details about the synthesis of $PbVO_3$ single crystals are given in chapter II. A $PbVO_3$ singe crystal was glued at the end of a quartz tube which was placed in the sample holder.

The first requirement for obtaining good data from diffraction measurements is to have a good quality single crystal. In our case the acquisition of the data was hampered by the access to a suitable crystal. The average length of the typical crystals was 100 µm and the average width 25 µm. The small size of the crystals was backed by their fragility and this made them hard to handle. Also, when retrieved from the capsule, the crystals were covered by some impurities and therefore did not present the smooth, mirror-like surface expected from a crystal. The impurities were removed by washing the crystals using ethanol in an ultrasonic bath. Figure 4.2 shows a surface of a $PbVO_3$ single crystal, before the ultrasonic bath.

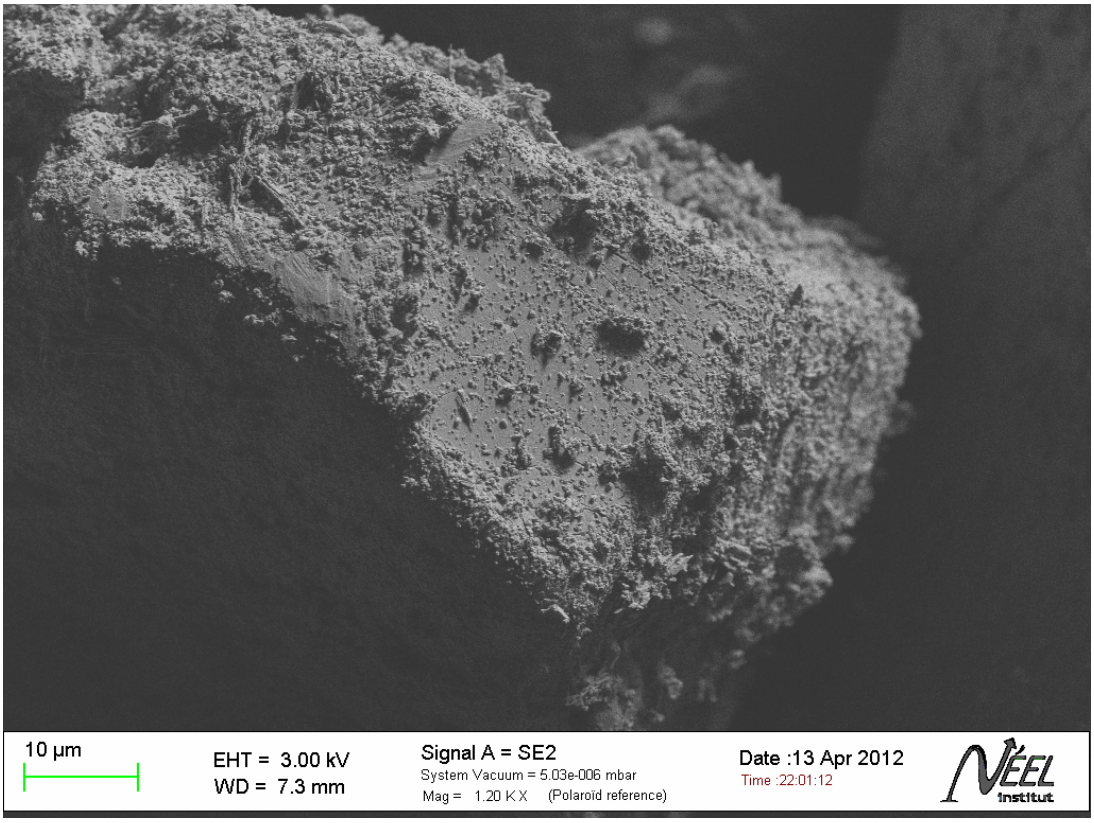

Fig. 4.2. $PbVO_3$ single crystal from the PVO_011 sample before any cleaning process. It can be observed that the surface of the crystal contains many grains of an unidentified impurity phase.

Most of the crystals obtained were quite visibly bent, very probably because they were affected by mechanical strain, which also explains their brittleness. Strain locally changes the inter-atomic distances and this has the effect of broadening the diffraction spots. In our case this was enough to render the diffraction figure useless. Apart from strain, another problem was the aggregation of crystals which was easily detected on the diffraction images by the presence of multiple diffraction spots.

By inspection of the diffraction images of several samples, a single crystal of sufficient quality was eventually found. One can expect to somewhat release mechanical strain by a re-annealing of the sample at a relatively high temperature. However, for $PbVO_3$ this is not possible because $PbVO_3$ is not stable above 300° C [32]. When heated in air it decomposes into the chervetite phase, $Pb_2V_2O_7$. One possible alternative to high temperature is long time so we tried to apply a heat treatment to the crystals in an oven at 210° C for one week. This re-annealing

treatment appears to have worked somehow because after the treatment we were able to find a crystal that yields a suitable diffraction pattern.

A synthetic diffraction figure obtained for this crystal is presented in figure 4.3. This image is artificially reconstructed from the experimental frames measured during data collection and provides a view of the (a*,b*) reciprocal plane.

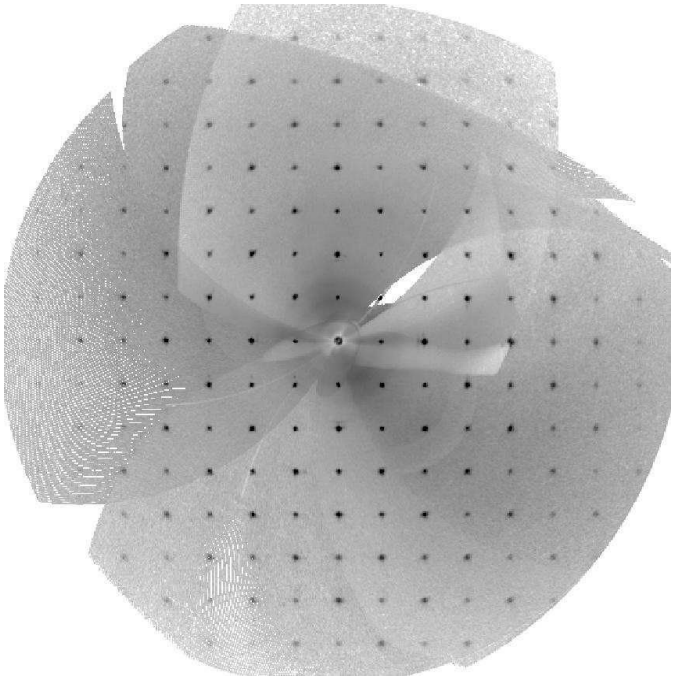

Fig. 4.3. (hk0) Synthetic precession diffraction image of a $PbVO_3$ single crystal from the PVO_011 sample.

After crystal centring and orientation matrix determination, the actual data collection consisted in a phi-scan followed by several omega-scans at different values of kappa, providing a completeness of 1 and a redundancy of 8.7 up to theta=35°.

The integrated intensities were extracted from the collected images using the EvalCCD software [79] and corrected for anisotropic effects using SADABS [80]. Structure refinement from the starting atomic positions taken from literature was performed with the Jana2006 program [81]. All atoms were given anisotropic atomic displacement parameters.

A merohedral twinning correction with twin domains related by a pseudo centre of symmetry had to be introduced. This is due to the presence of ferroelectric domains in the crystal. A gof (goodness of fit) of 1.6 was obtained at the convergence of the refinement. The Experimental conditions are summarized in table 4.1 (below).

Table 4.1. Data collection and refinement conditions for the X-ray single crystal diffraction experiment on $PbVO_3$.

Crystal Data (T= 298 K)	
Formula	$PbVO_3$
Molar weight (g/mol)	306.19
Symmetry	Tetragonal
Space group	P4mm
Unit cell (Å) and angle (°)	a = 3.798 (3)
	c = 4.662(11)
Volume ($Å^3$)	67.2 (2)
Z	1
Data Collection	
Equipment	KappaCCD goniometer, ApexII CCD camera detector, Incoatec *IμS* Microsource generator
λ (Ag Kα (multilayer optics); Å)	0.56087
Density calc. (g/cm^3)	7.559
Crystal shape & dimensions	Acicular, radius of average sphere 50μm
Color	black
Scan mode	ω, φ
θ (min-max) (°)	4.41-35
Absorption correction	SADABS + Sphere
μ (mm^{-1}; for λ Kα = 0.56087 Å)	35.799 (sphere)
T_{min}/T_{max}	T_{min} = 0.246 , T_{max} = 0.139
R(int) (%)	0.0576
Recording reciprocal space	-7≤h≤7, -7≤k≤7,-9 ≤l≤9
Number of measured reflections	3519
Independent reflections ($I > 3\sigma(I)$), total	405/405
Completeness (%), Redundancy	100, 8.7
Refinement	
Number of refined parameters	14
Refinement method	Least squares on F
Weighting scheme	W = 1 / [sigma^2(lFol) + (0.01 * Fo)^2]
Robs[$I > 3\sigma(I)$]/Rall [all data], %	2.36 /2.36
wRobs [$I > 3\sigma(I)$]/ wRall [all data], %	2.87 /2.87
GOF	1.63
Max/Min residual electronic density ($e^-/Å^3$)	5.14/-1.52
Merohedral twin ratio	0.19(3)

Table 4.2 presents the structural parameters obtained with this refinement. Table 4.3 provides the main inter-atomic distances.

As expected, the results are in good agreement with the previously proposed structure [31-34, 37]. The lattice parameters found are a=3.798(3) Å respectively c=4.662(11) Å. Nevertheless, the interatomic distances and anisotropic atomic displacements parameters are determined to a much better precision and accuracy. The non-centro symmetric nature of the structure is unambiguously confirmed, so as the ferroelectric nature of the compound which is even more supported by the presence of ferroelectric twin domains.

Table 4.2. Atomic positions and displacement parameters obtained from the refinement of single crystal diffraction data.

Positional parameters

Atom	Wyckoff	x	y	z	Ueq ($Å^2$)
Pb	1a	0	0	0	0.01008(5)
V	1b	0.5	0.5	0.5690(3)	0.0089(2)
O1	1b	0.5	0.5	0.215(2)	0.0145(14)
O2	2c	0.5	0	0.6900(14)	0.0120(11)

ADP harmonic parameters ($Å^2$)

Atom	U_{11}	U_{22}	U_{33}	U_{12}	U_{13}	U_{23}
Pb	0.00828(8)	0.00828(8)	0.01368(11)	0	0	0
V	0.0067(3)	0.0067(3)	0.0133(5)	0	0	0
O1	0.014(2)	0.014(2)	0.015(3)	0	0	0
O2	0.010(2)	0.0093(19)	0.017(2)	0	0	0

The anisotropic displacement parameters show the amplitude and direction of dynamical and/or static displacements of atoms from their mean value determined by diffraction. In the case of harmonic thermal displacements, the potential wells in which the atoms oscillate must also obey the local symmetry of the Wyckoff position given by the space group of the structure. For the P4mm space group, the displacement parameters U_{11} and U_{22} are thus constrained to have the same values for atoms at the 1a and 1b positions, i.e. sitting on the fourfold axis of the tetragonal cell (Pb, V and O1), but may differ for O2 on the 2c position. U_{33} which reflects atomic displacements along the c axis is independent from the other parameters for all atoms and is also much larger (except for O1). This might be a result of some disorder taking place along the c-axis direction, maybe related to the presence of ferroelectric domains.

Table 4.3. Inter-atomic distances (Å) in $PbVO_3$ calculated from the refinement of single crystal diffraction data.

Pb-O1 x4	2.867(5)	V-O1	1.649(12)
Pb-O2 x4	2.386(6)	V-O1	3.013(17)
		V-O2 x4	1.981(4)

The most striking feature that can be extracted from inspection of the $PbVO_3$ structure is probably the presence of a very short V-O1 bond at 1.649 Å. Such short V-O distances are well-known in crystal-chemistry for V^{4+} and V^{5+} cations and reflect the formation of a strongly covalent so-called "vanadyl" bond. The formation of such a vanadyl bond in the $PbVO_3$ compound containing V^{4+} cations is thus not unexpected. Moreover, the strongly covalent nature of this bond will have to be taken into account for the interpretation of the physical (magnetic and electric) properties of the $PbVO_3$ compound and of the cation substituted compounds, since Ti and Fe cations are not expected to form such bonds.

IV.1.2. Powder $PbVO_3$ low temperature XRD

Most of the physical property measurements we have performed on the $PbVO_3$ and substituted samples are carried out at low temperatures, typically down or below liquid helium temperature, e.g. 4.2K. Therefore it is important to check the existence of any structural anomaly in this temperature range and to follow the evolution of the structure. In order to gain insight into the low temperature structural evolution of $PbVO_3$, we have performed a low temperature x-ray powder diffraction experiment.

For the best $PbVO_3$ powder sample, labelled PVO_005, XRD patterns were recorded at different low temperatures with the D8 diffractometer of the Institut Néel. The diffractometer is set in reflection geometry for high resolution powder diffraction, with a Ge (111) primary beam focusing monochromator providing CuKα1 radiation, and a LynxEye solid state linear detector allowing fast data acquisition. The diffractometer is equipped with a closed-cycle Gifford-McMahon-type ARS cryostat capable of reaching temperatures as low as 6 K. Temperature is controlled via a Lake Shore controller using a Cernox type thermocouple attached to the cryostat copper cold head. The cold head is vacuum tight isolated by two caps equipped with x-ray

transparent capton windows. The cryostat and sample chamber are evacuated using a turbo pump. The powder sample is mixed with a small amount of thermally conductive grease and placed in a flat copper sample holder which is screwed to the cryostat cold head. Here also, thermal contact is insured by conductive grease between the sample holder and cold head. A homemade set of slits is placed between the cryostat and x-ray detector in order to eliminate diffuse scattering from the cryostat windows.

Measurements were taken from room temperature down to 10 K at every 20 K. Relatively short diagrams of about 30 minutes total acquisition time were collected for most temperatures with the exception of the 10 K, 150 K and 290 K temperatures. At these steps the same type of diagram was recorded 10 times over and the resulting diagrams were added to each other forming a single diagram having better counting statistics. All diagrams were Rietveld refined using the Fullprof program [82]. One has to notice that anisotropic broadening of the Bragg reflection had to be introduced in order to obtain high quality agreement factors (see next part for description of the anisotropic broadening effect). In order to minimize the number of structure parameters, all atoms were given fixed isotropic atomic displacement parameters and an overall a.d.p. was refined.

The results are given in table 4.4 for the three long diagrams. The corresponding Rietveld plots are shown in figure 4.4.

The main phase, marked by blue ticks is $PbVO_3$. The second phase, marked by red ticks is gold from the capsule used in the HP synthesis. The excluded regions correspond to contributions from the copper sample holder. Since the sample holder is not placed exactly in the true zero position of the goniometer, including the corresponding peaks in the refinement is inaccurate, therefore these peaks are excluded. Two very weak peaks are visible at about 25 and respectively 27 degrees and a third one appears at approximately 34 degrees. The first two peaks can be indexed with the hydrocerussite phase, $Pb_3(CO_3)_2(OH)_2$ [78], which appears in all samples. The third peak can still be explained by the same phase but also by PbV_6O_{11} [83, 84]. However, the latter is magnetically ordered (antiferromagnetic with T_N about 90 K) but no evidence of the presence of PbV_6O_{11} is found on magnetic measurements performed at the SQUID. Therefore we conclude that the only observed impurity is hydrocerussite, which was not included in the refinement because of the weakness of the corresponding peaks.

Table 4.4. Structural parameters, agreement factors and main interatomic distances for $PbVO_3$ found by Rietveld refinement of x-ray powder diffraction data as function of temperature

Temperature	10 K	150 K	290 K
Atom/coordinates	x, y, z	x, y, z	x, y, z
Pb	0 0 0	0 0 0	0 0 0
V	½ ½ 0.554(1)	½ ½ 0.552(1)	½ ½ 0.556(1)
O1	½ ½ 0.317(4)	½ ½ 0.331(4)	½ ½ 0.299(4)
O2	½ 0 0.684(2)	½ 0 0.674(2)	½ 0 0.686(2)
a (Å)	3.7734(1)	3.77342(9)	3.77213(9)
c (Å)	4.6085(2)	4.6216(1)	4.6368(1)
Rwp, RBragg chi^2	21.8, 5.63, 2.53	22.3, 6.28, 2.44	22.2, 6.22, 2.63
Pb-O1 (Å) x4	3.04	3.08	3.01
Pb-O2 (Å) x4	2.38	2.41	2.38
V-O1 (Å) x1	1.09	1.02	1.19
V-O2 (Å) x4	1.98	1.97	1.98

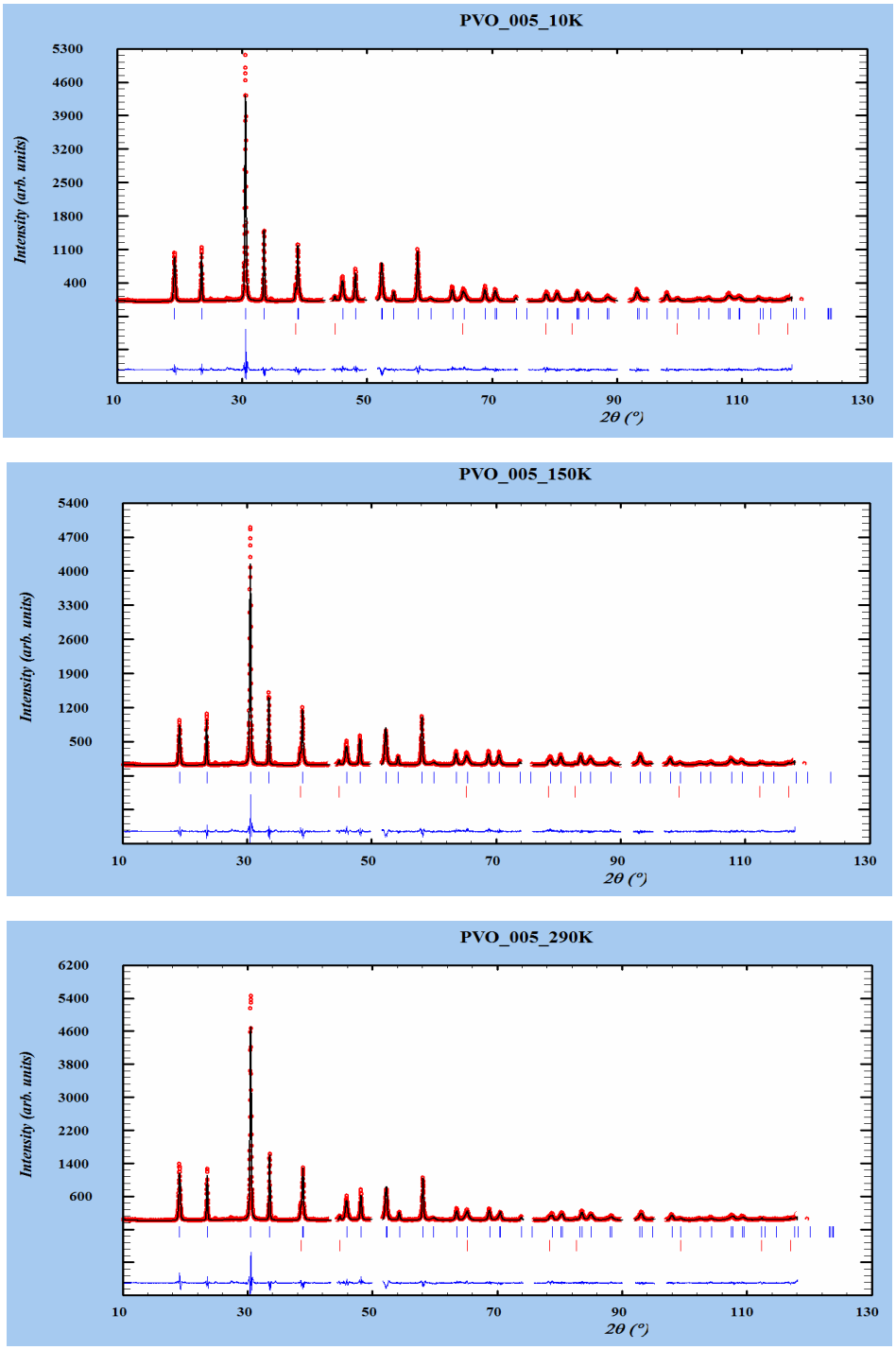

Fig. 4.4. Rietveld plots showing the refinement results for $PbVO_3$ (sample PVO_005) at 10 K (top), 150 K (middle) and 290 K (bottom).

Despite the good agreement between the experimental and calculated diagrams, the obtained structural parameters are clearly dubious, especially the position of atom O1 at z~0.3, whereas the value found by single crystal diffraction is 0.215. This results in an abnormally short V-O1 distance close to 1 Å which is unphysical. This

can be attributed to the low diffracting power of oxygen for x-rays, since the scattered intensity from atom O1 represents far less than 1% of the total diffracted intensity. Its position is then very sensitive to any systematic error, for example in the description of the complex peak profiles. This greatly limits the possibility of exploiting the atomic position obtained here and justifies the need for neutron powder diffraction for more accurate studies. Therefore, we will limit the discussion to the evolution of the cell parameters.

The evolutions of the cell parameters and volume are given in figure 4.5 below. A small decrease of the c parameter with the temperature is observed from 4.6368(1) Å at RT to 4.6085(2) Å at 10 K, in agreement with previous reports [33]. The a parameter remains practically unchanged.

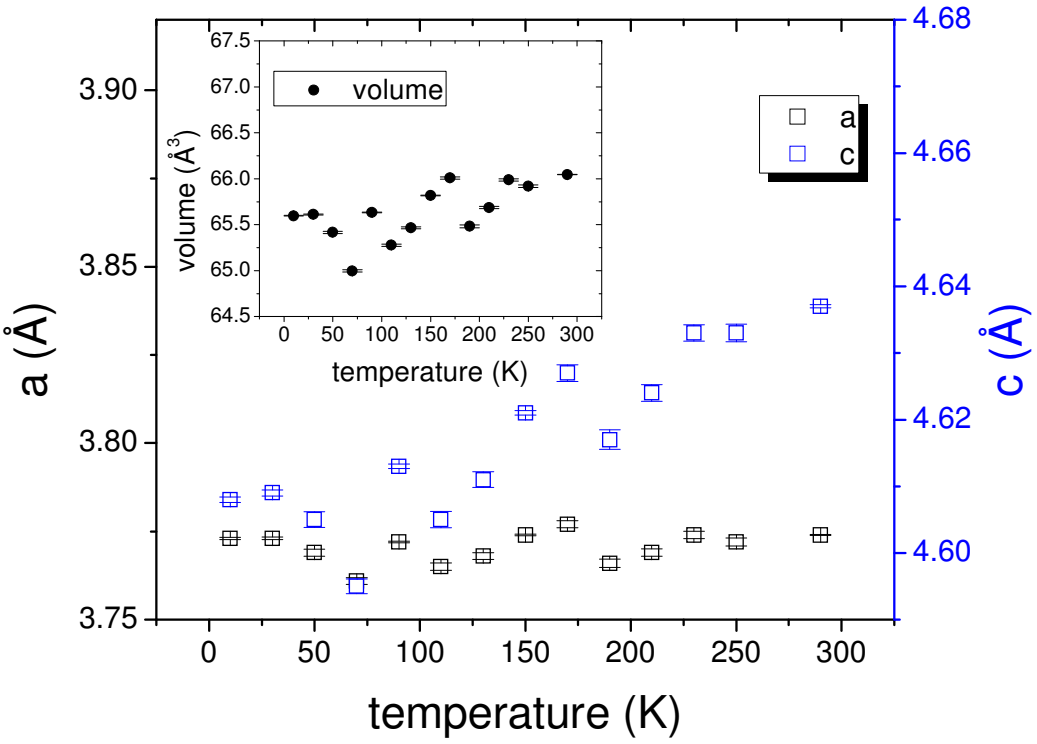

Fig. 4.5. Variation of lattice parameters with the temperature for $PbVO_3$ (sample labelled PVO_005). Insert shows the variation of the unit cell volume with the temperature.

IV.2. The influence of vanadium partial atomic substitution with Fe and Ti on the crystalline structure of $PbVO_3$

Most of the crystallographic information about the sample was obtained from diffraction measurements, whether these are XRD or NPD.

X-Ray diffraction patterns were taken for all the samples, regardless of the substitution. This includes "short diagrams" used just for phase identification and "long diagrams" used for structural Rietveld refinements and calculations of the grain size and mechanic strain. The "short diagrams" were measured with a Siemens D 5000 diffractometer equipped with a Cu anode and a monochromator filtering the CuKα1 radiation. Diffraction patterns were recorded in transmission geometry using a NaI scintillator detector, in the 2θ angle range of 10-90° with a step of 0.016° and 1 second counting time for every step. The "long diagrams" were measured at the same diffractometer, in the same range and with the same step size but with 10 seconds / step counting time. This became the standard method for XRD measurements.

For simplicity, only the "long diagrams" are discussed. All these diagrams are registered in the same way, in the same standard conditions, with the same detector and can therefore be compared one to another.

The first samples in which substitutions were made are the samples from the Ti series. Before investigating the substitution samples, a standard sample which gives no contribution to the broadening of the diffraction peaks was registered at the same device in the standard conditions. The standard sample was LaB_6. From the refinement of the XDR pattern of the standard sample the instrumental resolution function (IRF) was determined. The IRF controls the instrumental contribution to the broadening of diffraction peaks through the values of the U, V, W, and even X, Y parameters of the Thomson-Cox-Hastings (TCH) [85] description of the peak shape and width, which are available in the refinement. Once U, V, W, X and Y have been determined experimentally, they can be used in the refinements of the other (non-standard) samples to describe the contribution of the instrument to the reflection profiles. Only the contribution from sample effects remains to be determined, which makes the refinement much more stable and less likely to return unrealistic (negative) values for the width of reflections. From the values of the sample dependent profile

parameters obtained in the refinement, the program Fullprof is able to calculate the crystallite size and the amount of mechanical strain induced in the sample. The diagram and the LeBail refinement for the LaB_6 standard sample is shown in figure 4.6. The instrumental parameters returned by the refinement are:
U = 0.014(2), V = -0.014(2), W = 0.0064(4), X = 0.029(5) and Y = 0.002(2).

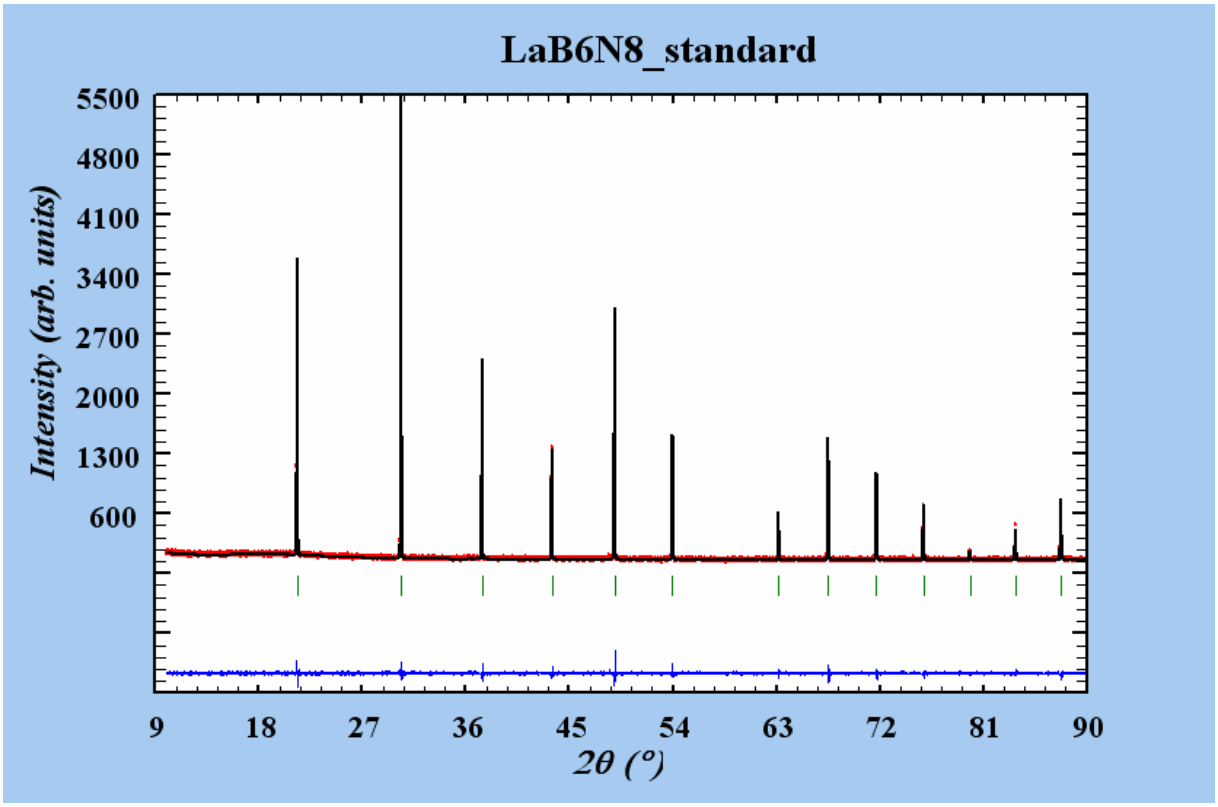

Fig. 4.6. LeBail refinement of LaB_6 standard sample, used for the determination of the instrumental contribution to the width of Bragg reflections.

Crystallographic results for $PbVO_3$ samples were discussed above. In the following pages the results for the Ti series and respectively for the Fe series will be presented.

IV.2.1. Ti series - variation of lattice parameters

Figure 4.7 shows the XRD patters for the Ti substituted samples at 0, 25, 50, 75 and 100 % substitution. The diagrams were recorded from 2θ = 10° to 2θ = 90° however the representation is stopped at 61° because the intensity of the diffraction peaks at higher angles is too small to be relevant at this point. The diagram at x = 1 was recorded with a counting step of 1 second while the other 4 diagrams were recorded with a counting time of 10 seconds per step. This explains the lower peak / background ratio for the $PbTiO_3$ diffractogram.

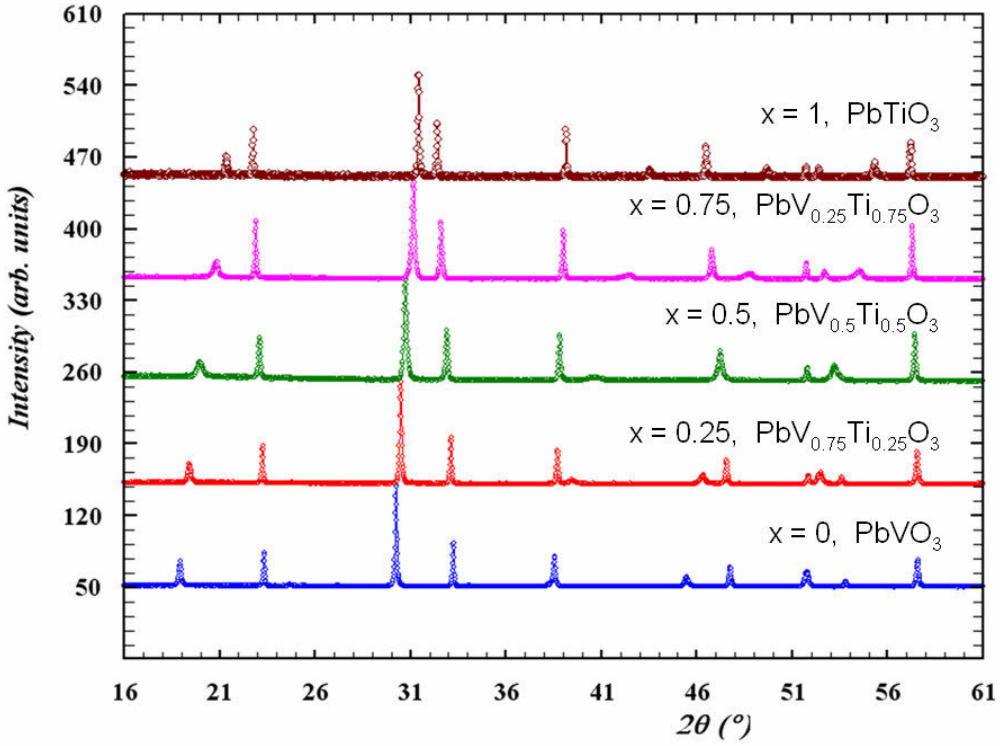

Fig. 4.7. XRD patterns obtained for 5 representative samples from the PVT ($PbV_{1-x}Ti_xO_3$) series, namely the samples for x = 0, 0.25, 0.5, 0.75 and 1.

As already mentioned in the synthesis chapter, for the Ti series we observed a linear change in lattice parameters with the degree of substitution. The lattice parameters of the $PbV_{1-x}Ti_xO_3$ compound converge towards the lattice parameters of $PbTiO_3$ as x increases from 0 to 1. A solid solution thus exists in between $PbVO_3$ and $PbTiO_3$. The variation of lattice parameters in function of the Ti concentration is plotted in figure 4.8.

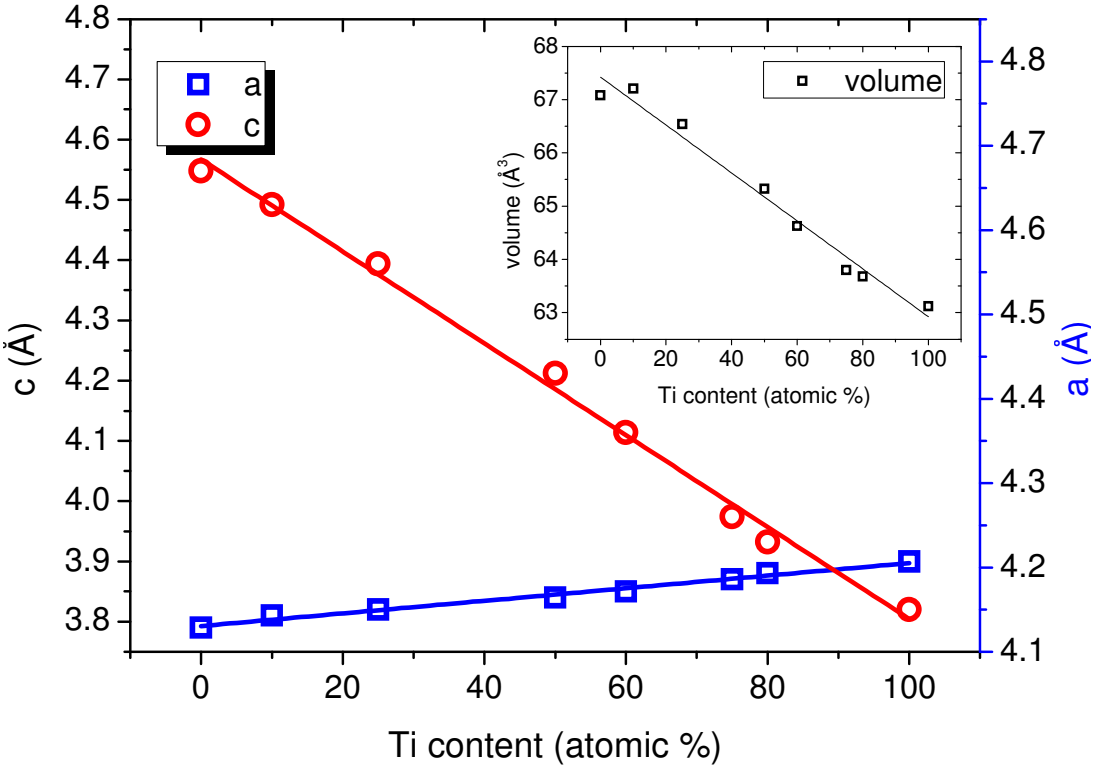

Fig. 4.8. Modification of the lattice parameters vs. nominal degree of substitution, x, in $Pb(V_{1-x}Ti_x)O_3$. The insert shows the evolution of the cell volume. Linear fits are drawn to guide the eyes.

The modification in lattice parameters is immediately observed when comparing the X-Ray diagrams of the sample in the series since the value of the lattice parameters determines the position of diffraction peaks. The displacement of the position of the diffraction peaks of samples in the Ti series is shown in figure 4.9. For simplicity peaks from only five samples are presented. Of the five samples, three of them contain substitutions, namely at x = 0.25, 0.5 and 0.75 and the other two are the "parent" compounds, $PbVO_3$ and $PbTiO_3$.

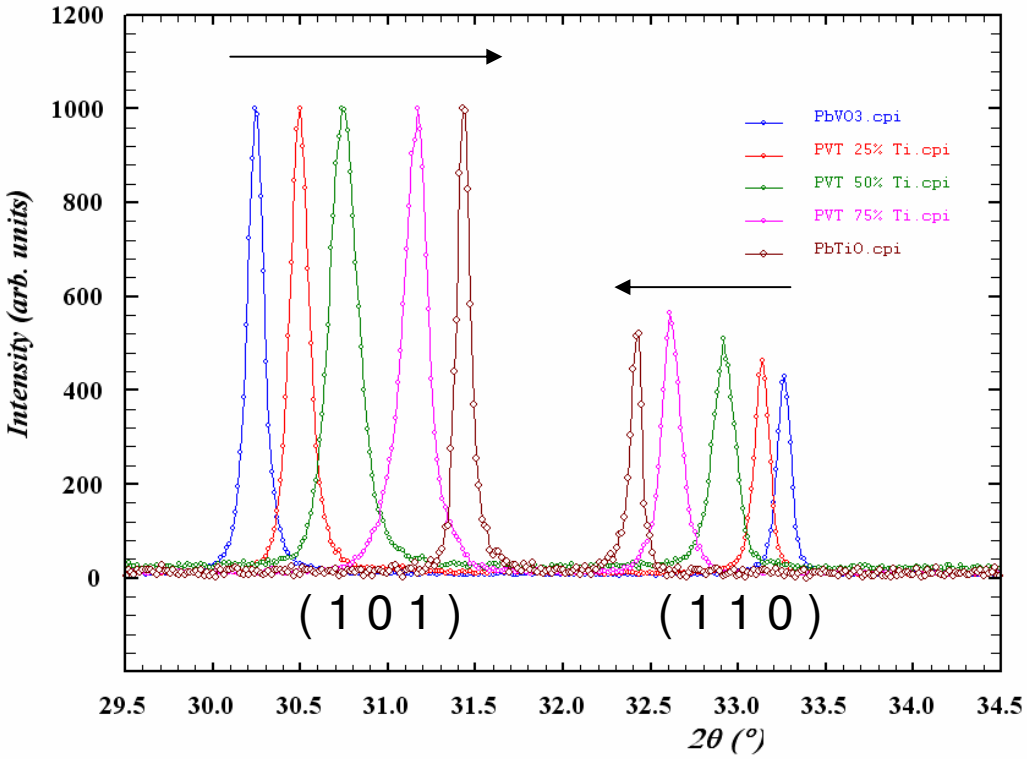

Fig. 4.9. The convergence of the diffraction peaks from $PbVO_3$ towards $PbTiO_3$ in the $Pb(V_{1-x}Ti_x)O_3$ compound. The arrows point in the direction in which the position of the diffraction peaks changes as the concentration of Ti is increased.

The convergence of the diffraction peaks of the $Pb(V_{1-x}Ti_x)O_3$ compound from the positions in which they appear in $PbVO_3$ towards the positions in which they appear in $PbTiO_3$ is visible for all the reflections, however, the displacement is more clearly visible for the (1 0 1) and (1 1 0) reflections. In the above figure, the tall peaks on the left side of the image correspond to the (1 0 1) reflection and the peaks on the right side correspond to the (1 1 0) reflection. The outermost peaks (in blue) belong to $PbVO_3$ and the innermost peaks (dark red) belong to $PbTiO_3$.

It is easy to see that when the amount of Ti is increased the peaks converge towards each other and finally to a single peak corresponding to a cubic structure. The cubic structure is not reached, since the solid solution stops at the tetragonal $PbTiO_3$. However, the direction towards a cubic structure is clearly visible. This is again stressed in figure 4.10 below which shows the evolution of the c/a ratio vs. the Ti content x.

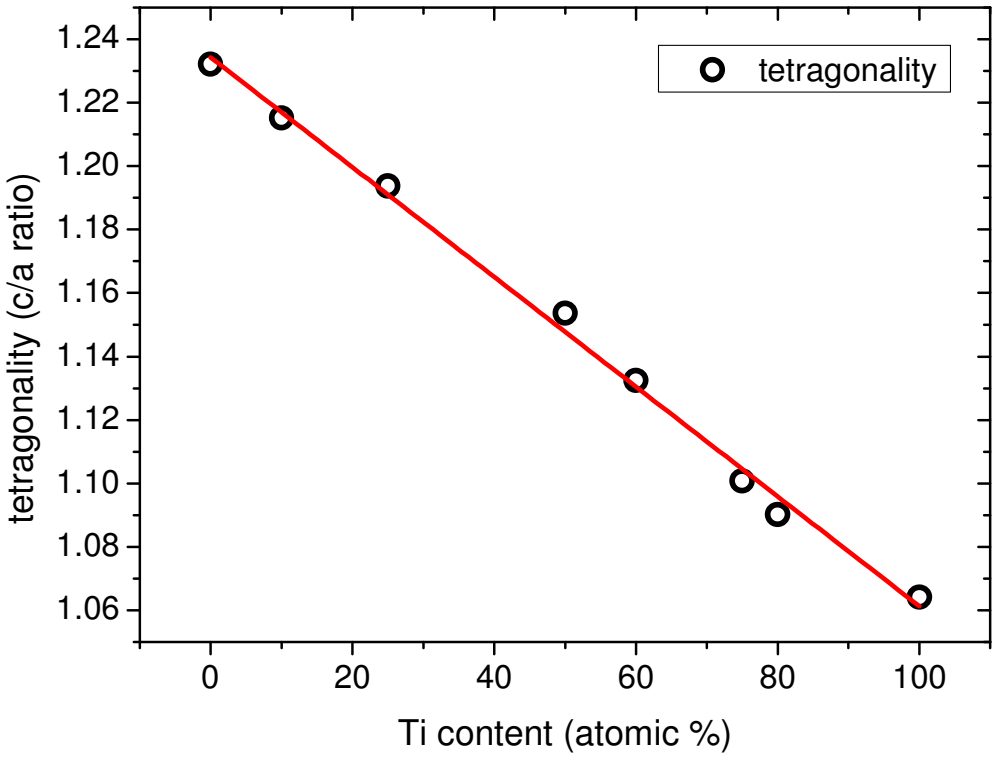

Fig. 4.10. c/a ratio vs. Ti content. The black hollow dots represent the tetragonal distortion calculated for each sample from the refined lattice parameters. The red line is the linear fit of the experimental results.

The ferroelectric distortion of these compounds decreases with the increase of the Ti concentration. The spontaneous polarization is therefore also expected to decrease from the value predicted for $PbVO_3$ to that of $PbTiO_3$ throughout the substitution range. See the section IV.4 for a detailed discussion about the calculation of the expected ferroelectric polarization.

IV.2.2. Ti series - microstructure

As can be clearly seen from fig. 4.8 the width of reflections shows a marked evolution with respect to substitution ratio. The broadening of peaks from sample effects is known to originate from two types of physical phenomena: the first one is the grain size, or more precisely the size of coherent domains for x-ray diffraction. The smaller the domain size is, the broader the diffraction peaks will be. The second one comes from the presence of local strain in the sample, due to some kind of mechanical stress. The presence of strain leads to local variations of atomic positions and therefore to diffraction peak broadening. Both effects can be separated using powder diffraction data, since there evolutions with the Bragg angle are different. This is why Rietveld refinement can provide precious information about the sample microstructure.

In the case of isotropic size/strain effects, the sample dependent width of the reflections can be described using the U, V, W, X and Y parameters from the TCH profile function, provided that the instrumental contribution parameters are given to the software (using the IRF file formalism in Fullprof, for example). The width of the reflection is then only dependent on the Bragg angle. In more complex cases, the broadening of the reflections can be anisotropic, i.e. it will depend on the orientation of the reflection in reciprocal space. In this case a more complex description of the sample microstructure has to be used in order to model the reflection profiles, which, when refined, yields in turn information on the microstructure and its anisotropy. On figure 4.8 it is quite clear that reflections (110) and (101) can have quite different widths, although they appear at relatively close Bragg angles. Therefore, anisotropic broadening effects will have to be taken into account in the refinement.

The precise knowledge of the microstructure is quite important for the interpretation of the physical properties of these materials, since it may reflect the presence of structural disorder and characterizes the structural coherence length.

The effect of microstructure is visible on all the diffractograms from the substitution series, whether the substitution is made with Ti or with Fe and even for the clean $PbVO_3$ samples.

We had observed that reflections close to the c* axis direction were systematically broader. This corresponds to an anisotropy with uniaxial symmetry and

preferred axis along c. This not unexpected, given the tetragonal symmetry and structure of the compound.

The model employed to describe this anisotropy for the Rietveld refinement using Fullprof was the following:

1) size effects were modelled using an uniaxial lorentzian size parameter which complements the isotropic part of the size broadening described by the Y parameter of the TCH profile function. The correction depends on the angle between the reflection direction and the direction of the c-axis chosen as preferred axis.

2) the effect of anisotropic strain was modelled using the formulation of Stephens [86], with, taken into account the tetragonal symmetry, lead to four additional parameters S400, S004, S220 and S202 plus a lorentzian strain coefficient.

The additional parameters to take account of anisotropic peak broadening effects were refined together with all others profile and structural parameters by Rietveld refinement using the Fullprof program.

The effects of strain and particle size on the width of the reflection were calculated for all the samples. The result is returned in the form of a list containing all the reflections and their corresponding widths and the physical parameters calculated from the width of the reflection. Thus for every reflection the refinement provides the associated apparent crystallite size and induced strain. The sizes of the crystallites are calculated in angstroms (Å) and the strain is expressed in double percentage (%%). The program also calculates an average crystallite size and an average strain.

The average coherent domain size and the size along the c axis for the samples in the Ti series are plotted in figure 4.11. The average size is represented in black and the size along the (0 0 1) direction is shown in red. It is immediately seen that the size of crystallites in the c direction is smaller than the average size, and thus smaller than the size in the (a,b) plane.

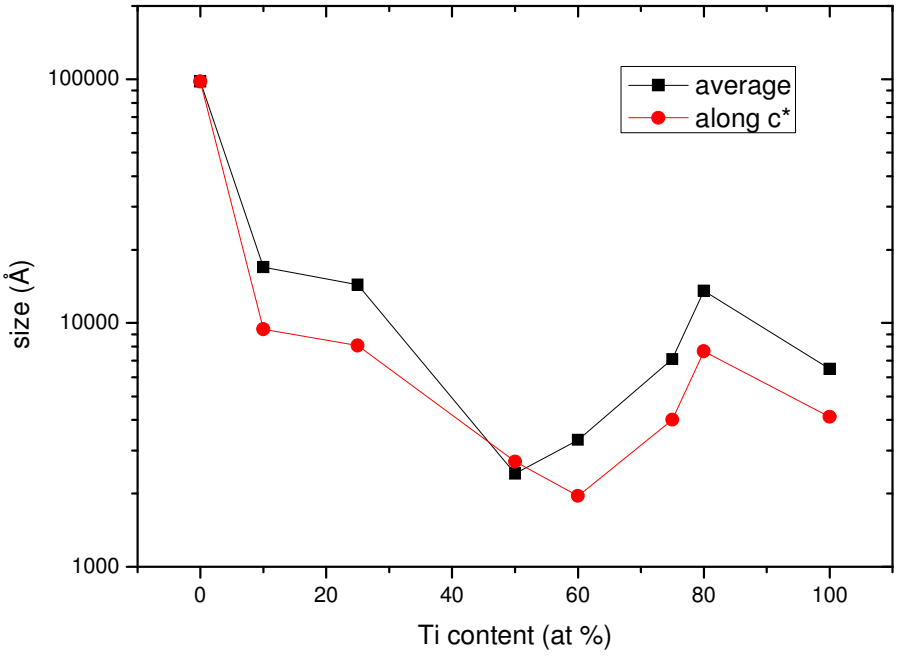

Fig. 4.11. Average crystallite size (black) and grain size along the c axis (red) in function of composition for the Ti series.

The domain size (either average or along c) has a minimum at about 50% Ti substitution, the half way between $PbVO_3$ and $PbTiO_3$. This can be understood for the reason that the crystallite size seen by XRD is also a measure of the size of a coherently diffracting domain and not just a measure of the actual size of the particles of powder. The small domain size is therefore associated with a larger number of defects present in the sample due to which the coherence of the diffraction process is progressively lost, rather than an actual size of the powder grains. The anisotropy of the broadening then points towards the presence of planar defects or stacking faults along the c-axis direction.

Strain for the same Ti series, follows an almost constant variation with the composition, as seen in figure 4.12. It can be seen however that the strain along the c axis (red) is far greater than the average strain (blue). This means that the crystallites are tensioned along the c direction and this causes an additional broadening of the corresponding peaks.

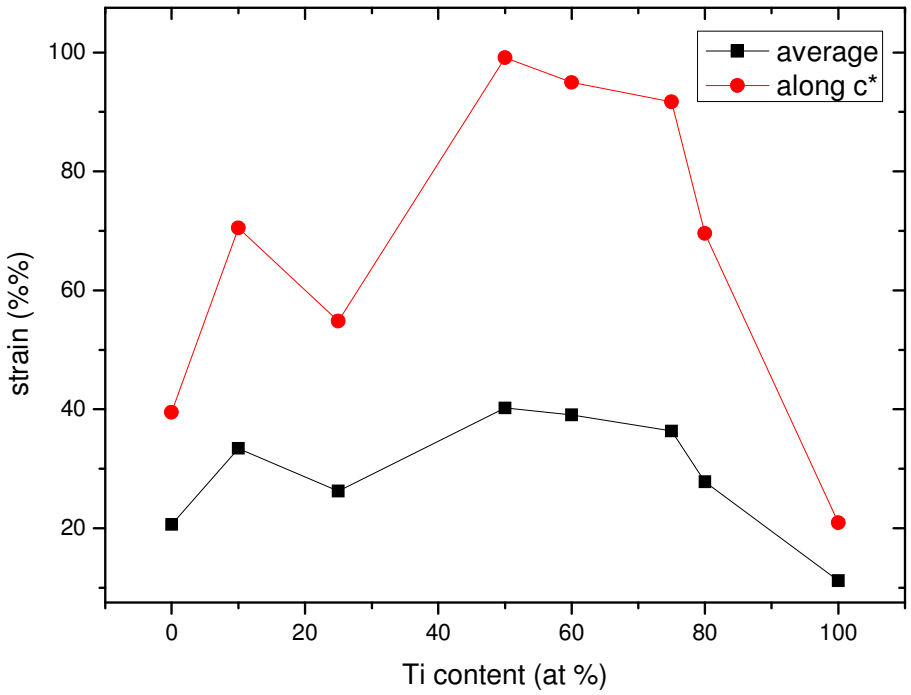

Fig. 4.12. Strain vs. composition for the Ti series. The black dots mark the evolution of average value of the strain. The black dots show the evolution of strain along the c direction.*

Contrary to the domain size, the strain does not seem to be strongly affected by the substitution. We have already seen in our single crystal x-ray diffraction study of $PbVO_3$ that the crystals are heavily strained to the point they are bent. The origin of the strain is then to be found in the presence of ferroelectric domains, which may be present in the whole solid solution, for which all compounds are isostructural and then ferroelectric. One may infer that the presence of defects related to cation substitution can decrease the size of the domains, but does not change their nature as ferroelectric domains. It is also interesting to note that ferroelectric domains are related by a pseudo centre of inversion, but in an equivalent way by a mirror perpendicular to the c axis (adding an inversion centre to the P4mm space group leads to P4/mmm). Thus the presence of such domains can generate faults perpendicular to the c-axis, leading to the observed peak broadening anisotropy.

IV.2.3. Structure refinements for $PbV_{1-x}Ti_xO_3$ samples

In the previous segment the values related to the position of the peaks and the width of the peaks was discussed. We will now discuss the refined values of the parameters related to the peak intensities, and therefore to the crystal structure of the sample.

The structure of the substitution series samples was first refined from XRD data. In the refinement we assumed the structure to remain in essence that of $PbVO_3$ and in that structure Ti (or Fe) atoms were added in the place of the substituted V ions. The substitution atoms were assumed to take the same crystallographic position as the Vanadium atoms. The chemical occupancy of both the remaining V atoms and the substitution atoms was calculated in agreement with the chemical composition of the samples. In this model the coordinates of the B site cations (V and Ti or Fe) and the coordinates of the two oxygen anions were refined. Since all these atoms are on special positions, the only parameter that could be left open for the refinement was the atom position along the z axis. The z coordinates of V and those of substitution atoms were refined at the same time and to the same value. This is not the best choice since it can be expected that V and Ti/Fe will not occupy exactly the same place in the unit cell, however, this was the only reasonable choice as an attempt to refine separately the z of V and the z of Ti/Fe lead either to non-realistic coordinates or to the coordinates reaching the same value.

The same method of refinement was applied to all the samples. Figures 4.13 and 4.14 show the Rietveld refinements for the two samples at the ends of the Ti series and table 4.5 gives the atom coordinates, cell parameters, agreement factors and main interatomic distances for all the Ti-series samples.

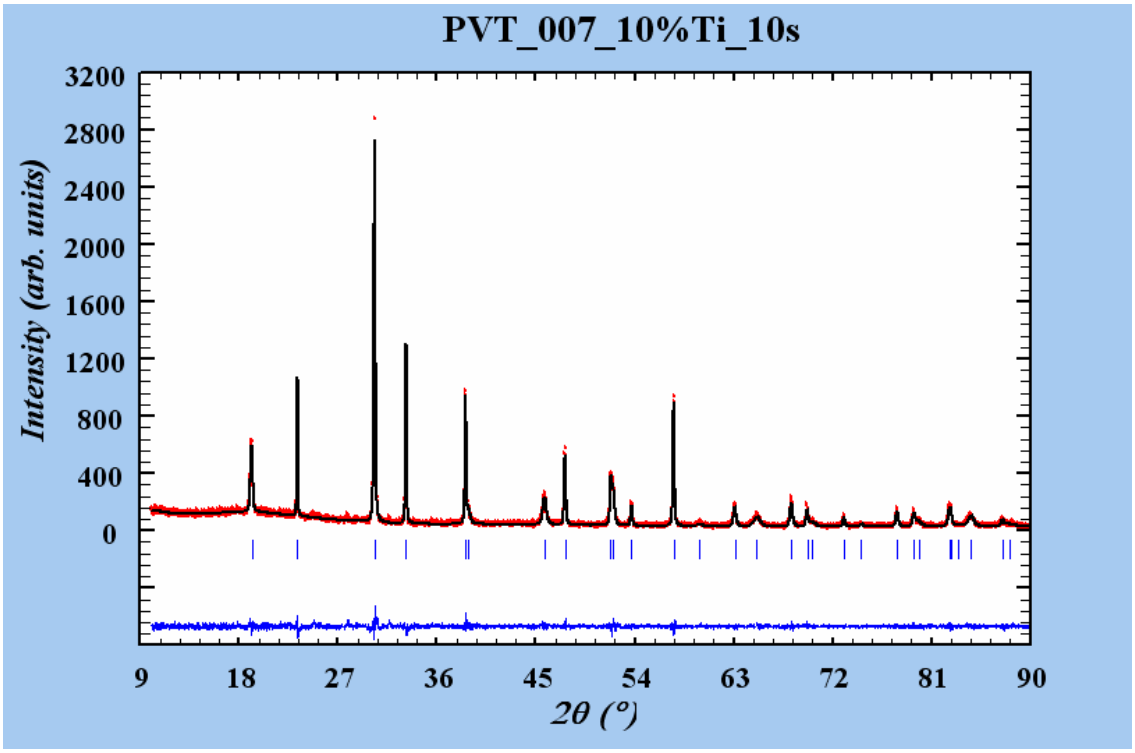

Fig. 4.13. Rietveld refinement for $PbV_{0.9}Ti_{0.1}O_3$ (the PVT_007 sample).

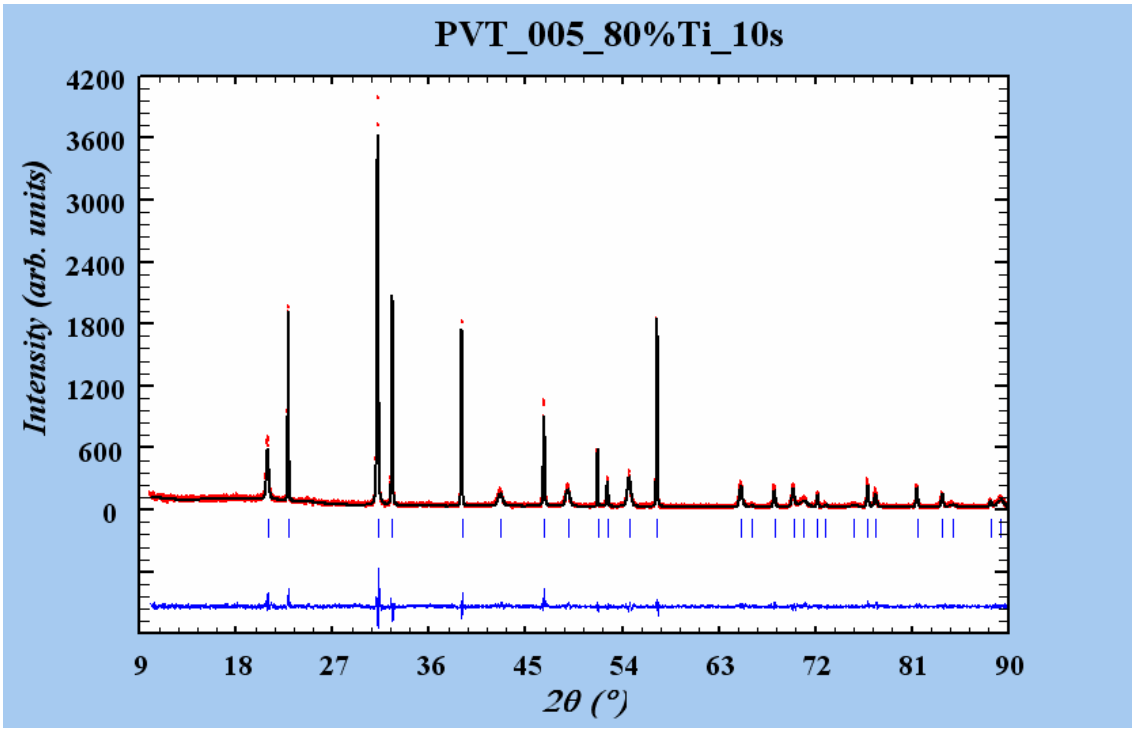

Fig 4.14. Rietveld refinement for $PbV_{0.2}Ti_{0.8}O_3$ (the PVT_005 sample).

For the Ti series small modifications in the atom coordinates are observed as the content of Ti is increased. The z for the B site cation decreases from z = 0.564(2) for

the 10% Ti sample to z = 0.545(1) for the 80% Ti sample. It seems the B site cation tends to go towards the centre of the unit cell (at z = 0.5), the apical oxygen moves towards the face of the unit cell (z = 0) and the other oxygen anions try to go to face centres (z = 0.5) as if the system begins to transform in a cubic structure. This is consistent with the evolution of the lattice parameters showing a decrease of the c/a ratio (figure 4.9). This is also consistent with a decrease of the ferroelectric distortion upon V substitution for Ti, which is expected since $PbTiO_3$ is known to be less distorted than $PbVO_3$. However, due to the dubious reliability of the oxygen positions determined by this method, these conclusions have to be taken with caution.

Table 4.5. Results of the Rietveld refinements based on XRPD data for the Ti series

Sample	10% Ti	25% Ti	50% Ti	60% Ti	75% Ti	80% Ti
Atom	x y z	x y z	x y z	x y z	x y z	x y z
Pb	0 0 0	0 0 0	0 0 0	0 0 0	0 0 0	0 0 0
V/Ti	½, ½, 0.564(2)	½, ½, 0.559(1)	½, ½, 0.550(1)	½, ½, 0.553(3)	½, ½, 0.547(2)	½, ½, 0.545(1)
O1	½, ½, 0.205(5)	½, ½, 0.205(4)	½, ½, 0.172(4)	½, ½, 0.151(5)	½, ½, 0.128(5)	½, ½, 0.127(4)
O2	½, 0, 0.686(3)	½, 0, 0.674(3)	½, 0, 0.652(3)	½, 0, 0.657(3)	½, 0, 0.642(1)	½, 0, 0.631(4)
a	3.81169(2)	3.82037(5)	3.84431(3)	3.85833(2)	3.87934(2)	3.88509(2)
c	4.63066(9)	4.56106(8)	4.4339(1)	4.36542(8)	4.26105(9)	4.23688(7)
Rwp, RBragg, chi^2	23.2, 3.86, 1.41	21.1, 5.04, 2.14	23.1 4, 1.38	19.8, 3.31, 1.51	22.6, 4.12, 2.08	22.4, 4.75, 1.95
Pb-O1 x 4 (Å)	2.85	2.85	2.82	2.8	2.79	2.79
Pb-O2 x 4 (Å)	2.39	2.42	2.46	2.43	2.46	2.49
V/Ti-O1 x1 (Å)	1.66	1.61	1.67	1.75	1.79	1.76
V/Ti-O2 x4 (Å)	1.98	1.98	1.97	1.98	1.98	1.97

It is known that for $PbVO_3$ the formation of the strongly covalent bond between V and O1 decreases the strength of the Pb-O1 bond, which is responsible for the

additional shift of the Pb cations towards the O2 plane, in order to reach charge balance [31].

Ti is not known to form similar bonds therefore when Ti is substituted in $PbVO_3$ the average bond between the B site cation and the apical oxygen becomes weaker so the Pb-O1 bond regains its strength. The bond length is inversely proportional to the bond strength. When Ti is added to the structure the V/Ti-O1 distance increases and the Pb-O1 distance is expected to decrease. If the Pb-O1 distance becomes smaller the shift of Pb towards the O2 plane should also be smaller because it was the decrease of the Pb-O1 bond strength that caused the displacement of the Pb cation towards the O2 plane for the clean $PbVO_3$. With the cause of the displacement of Pb toward the O2 plane gone, than the Pb-O2 bond length should increase.

This is indeed observed when the main interatomic distances of the Ti series are plotted (fig 4.15).

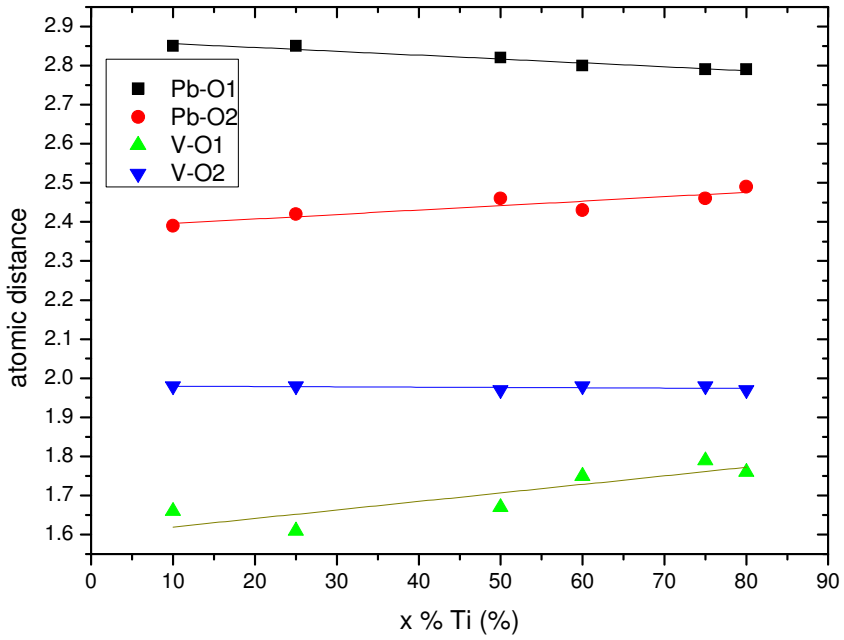

Fig. 4.15. Interatomic distances for the Ti series. Dots mark the interatomic distances obtained from the refinements of XRD patterns for the respective samples. Lines show the linear fits of the variation of the experimentally determined interatomic distances.

Figure 4.16 shows the variation of the atom coordinates with the substitution degree. The coordinates for both oxygen anions decrease much faster than the z of the B site cation. The weakening of the average B site cation – apical oxygen bond has

the effect of releasing the O1 anion which is then displaced toward the Pb plane. As the V/Ti-O1 distance is increased the oxygen pyramid is elongated along the c axis and distorted towards an octahedron, again, suggesting the tendency of the system to transform in a typical cubic perovskite.

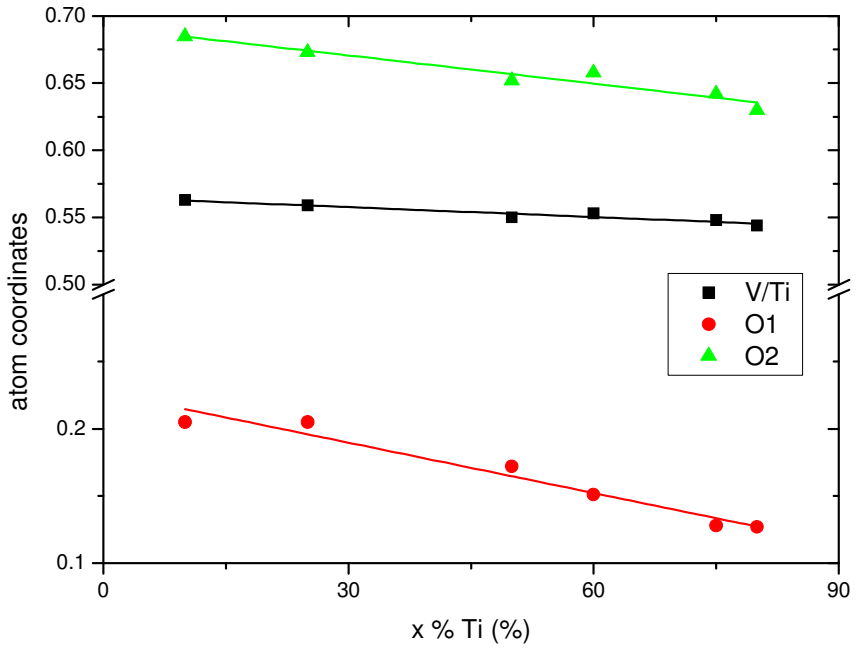

Fig. 4.16. The z coordinate for atoms on the $PbV_{1-x}Ti_xO_3$ compound. Dots represent experimental values. Lines represent linear fits of the experimental data.

The V/Ti-O2 distance appears not to be modified by the substitution although both the z coordinates of V/Ti and O2 change. However, the distance is not the same thing as the coordinate on z so although the coordinate can decrease on z the distance might remain constant because the cell is increased on the a-b plane and this can compensate for the diminution of the z.

The evolution of the structure with the substitution can be followed by performing a symmetry mode analysis. This was done with the help of Dr. Claire Colin. The analysis shows the displacement of the atoms from the coordinates they have in an ideal perovskite structure towards the coordinates they take in $PbVO_3$ and the substitution compounds up to $PbTiO_3$. These displacements are listed in table 4.6. All the displacements take place along the z axis. The values of the displacements are given in Å. The negative sign shows the direction of the displacement.

Table 4.6. Atomic displacements obtained for the samples from the Ti series ($PbV_{1-x}Ti_xO_3$ for x = 0, 0.1, 0.25. 0.5, 0.6, 0.75, 0.8 and 1)

Ti content (%)	global displacement (Å)	atomic displacement (Å)		
		V/Ti	O1 (apical)	O2
0	1.39(2)	-0.261(6)	-0.90(2)	-1.03(2)
10	1.36(2)	-0.255(6)	-0.82(2)	-1.05(2)
25	1.32(2)	-0.2555(3)	-0.81(2)	-0.99(2)
50	1.13(2)	-0.194(9)	-0.67(2)	-0.89(2)
60	1.10(1)	-0.212(7)	-0.61(1)	-0.89(1)
75	1.202(8)	-0.180(9)	-0.55(2)	-1.0503(3)
80	0.92(2)	-0.2119(3)	-0.51(2)	-0.74(2)
100	0.8479	-0.1602	-0.4727	-0.4847

The tendency of the $PbV_{1-x}Ti_xO_3$ system to form a less distorted structure when the concentration of Ti is increased can be seen by the progressive decrease of the atom displacement (for all of the 3 atoms analysed).

The global displacement (root-summed square of all atomic displacements within a primitive unit cell of the reference structure) takes into account the displacement of the 3 atom types and represents the magnitude of the ferroelectric distortion. The evolution of the global displacement again marks the decrease in the ferroelectric distortion of the compound with the degree of substitution.

This transformation of the system from an ideal perovskite structure to the structure of $PbVO_3$ is shown in figure 4.17 (a and b). Arrows are used to mark the displacement of ions from $PbTiO_3$. The magnitude of the arrow is proportional to the magnitude of the displacement.

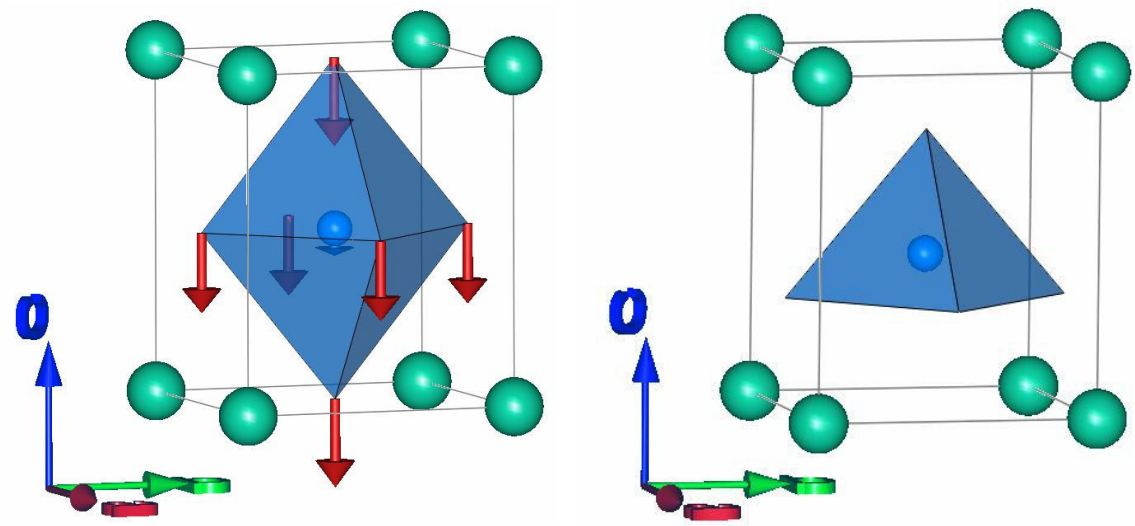

a) b)

Fig. 4.17. Atomic displacement from the atomic positions occupied in an ideal perovskite to the atomic positions taken in $PbVO_3$. a) structure of the ideal perovskite, b) structure of $PbVO_3$. Pb atoms are green, V/Ti atoms are blue. The oxygen octahedron / pyramid surrounding the B site cation is highlighted, however the oxygen cations themselves are not represented.

The changes in structure (and lattice parameters and tetragonal distortion and volume) can be correlated to the ionic radii of V^{4+} and Ti^{4+}. V^{4+} assumes a 5 fold coordination and has a radius of 0.53 Å. Table 4.7 gives the ionic radii for the species discussed. The (average) coordination of the Ti^{4+} cation tends to shift from 5 fold to 6 fold as the Ti substitution progresses. The radius of Ti^{4+} in a 5 fold coordination is 0.51 Å but in a 6 fold coordination the radius is 0.605 Å.

Table 4.7. Ionic radii for V^{4+} and Ti^{4+}

cation	coordination	radius (Å)
V^{4+}	V	0.53
Ti^{4+}	V	0.51
Ti^{4+}	VI	0.605

The radius and hence volume of the Ti^{4+} ion 6 fold coordinated is larger than the radius (volume) of the V^{4+} 5 fold coordinated cation. When the V ion is substituted with another ion having a larger volume one might expect the volume of the unit cell

to increases. However, for $PbV_{1-x}Ti_xO_3$ the inverse is observed, namely the unit cell volume decreases when a bigger atom is substituted. The apparent contradiction can be explained by considering not only the volumes of the cations changed during the substitution but also the bonds they form.

In an ideal perovskite the coordination of Ti would be VI. In the PVT compounds the Ti cation tends to adopt the 6 fold coordination. The larger radius of the Ti cation in this configuration places it closer to the base of the oxygen pyramid (centre of the oxygen octahedron). Also the larger radius determines the increase of the a and b lattice parameters. The unit cell expands in the a, b plane to accommodate the Ti cation. On the other hand, the absence of an equivalent vanadyl bond formed by the Ti cation reduces the tetragonal distortion of the system and therefore reduces the c parameter.

The rapid decrease in c and the increase in a reduces the tetragonal distortion of the system. The dilution of the average vanadyl bond appears to be a significant effect as the decrease of the c parameter is much more evident than the increase of the a or b parameters and determines the overall reduction of unit cell volume with the Ti substitution degree, even though the volume of the Ti cation is larger than the volume of the V cation.

It could also be inferred that the larger volume of the Ti cation and the tendency of it to occupy a central position on the unit cell increases the stacking efficiency of the ions. Indeed the theoretic density of $PbTiO_3$ (7.964 g/cm^3) is larger than the theoretic density of $PbVO_3$ (7.508 g/cm^3) even though the mass of Ti is smaller than the mass of V (47.9 for Ti respectively 50.94 for V).

IV.2.4. Fe series - variation of lattice parameters

Figure 4.18 shows the XRD patters for the Fe substituted samples at 0, 10, 20, 30 and 40 % substitution. All the diagrams were recorded on the 2θ range = 10 to 90° with a step size of 0.016° and 10 seconds counting time per step. At scattering angles higher than 2θ ≈ 60° the peak intensity becomes too small to be relevant here.

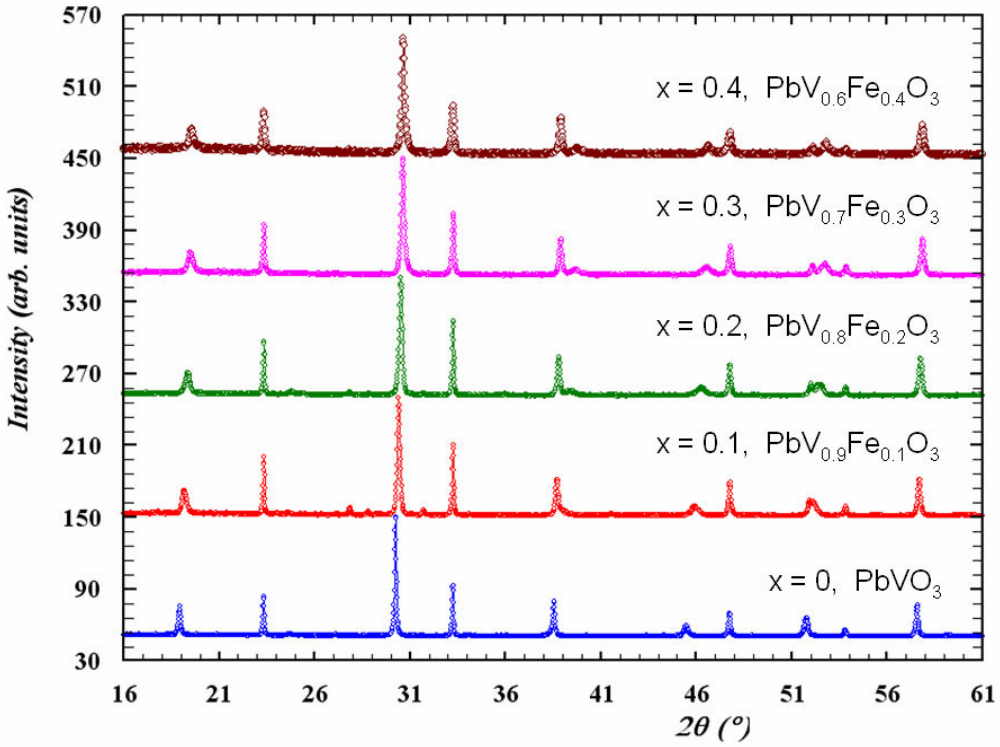

Fig. 4.18. XRD patterns of representative samples of the Fe substitution compounds, $PbV_{1-x}Fe_xO_3$, where x = 0, 0.1, 0.2, 0.3 and 0.4.

For the Fe series the solid solution stops at x = 0.5. The tetragonal structure of $Pb(V_{1-x}Fe_x)O_3$ is conserved until x = 0.5, i.e. 50% Fe substitution degree. Above 50% the tetragonal phase vanishes and a new cubic phase appears. The variation of lattice parameters and the leap to a new cubic phase are represented in figure 4.19.

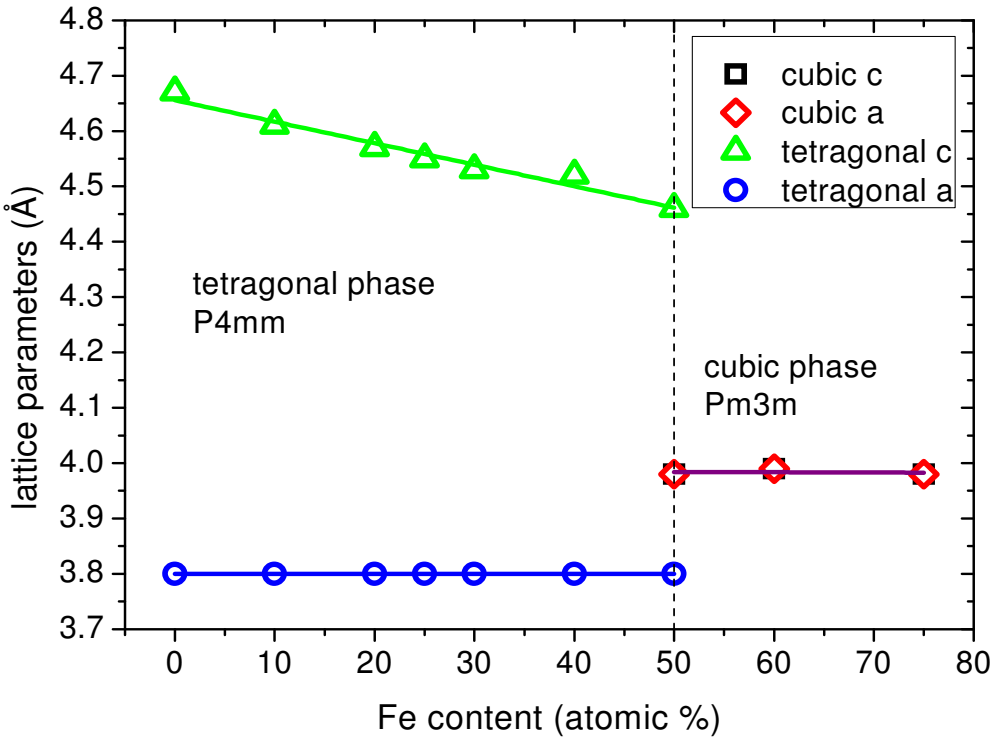

Fig. 4.19. Variation of lattice parameters vs. nominal Fe content x for the Fe series, $Pb(V_{1-x}Fe_x)O_3$, and emergence of a new cubic phase for x>0.5. Dots mark the experimentally obtained values of the lattice parameters. Continuous lines are linear fits of the sets of lattice parameters. The dashed vertical line at x = 50% marks the transition of the system from the tetragonal phase to the cubic phase.

In the tetragonal phase, the increase of iron percentage leads to a decrease of the c parameter from about 4.67 Å for x=0 to 4.49 Å for x=0.5, but the a parameter is not modified at 3.80 Å. At substitution degrees larger than 50% a new cubic phase appears with the space group Pm3m and lattice parameters that remain almost constant and close to 4 Å, whatever is the percentage of Fe. From preliminary investigations, this phase appears to have the structure of a disordered perovskite. However, it should be noted that in the figure 4.19 the x axis represents the nominal stoichiometry. This could differ noticeably from the sample's actual composition, since un-reacted starting oxides were found as impurities in the final product for x>0.5. EDX data were inconclusive in this case and much about the synthesis conditions and structure of the cubic phase remains a mystery to be solved by future research.

At 50% Fe substitution both phases, tetragonal and cubic, co-exist. Diffraction peaks corresponding to both phases are identified on the diffractogram of the sample (figure 4.20).

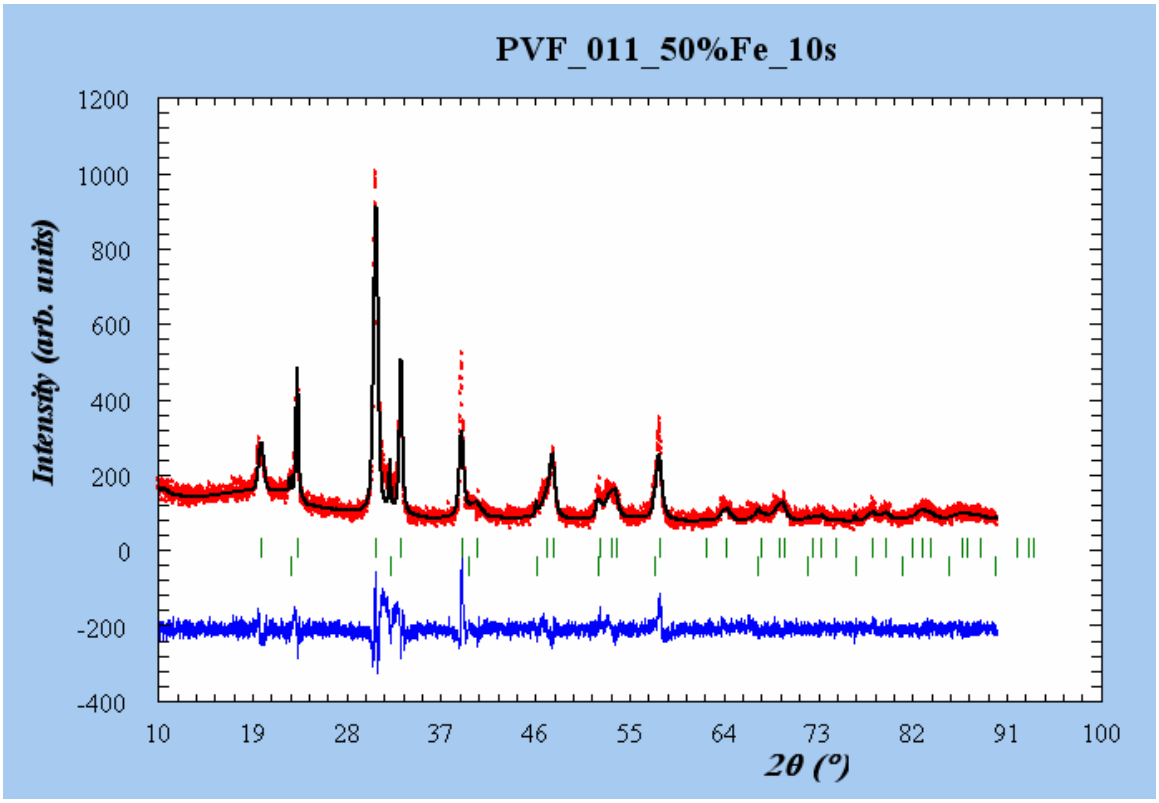

Fig 4.20. Rietveld refinement of the PVF_011 sample containing 50% Fe (nominal stoichiometry). One can notice the poor crystallinity of the sample.

As in the case of the Ti series, the variation in lattice parameters remains easy to observe when the XRD diagrams of different samples are superimposed and the position of diffraction peaks is examined. The changing in peak position with the increasing Fe concentration is shown in figure 4.21. The same peaks are studied, as in the case of the Ti series. The peak corresponding to the (1 0 1) reflection is on the left and the peak which belong to the (1 1 0) reflection is on the right of the plot.

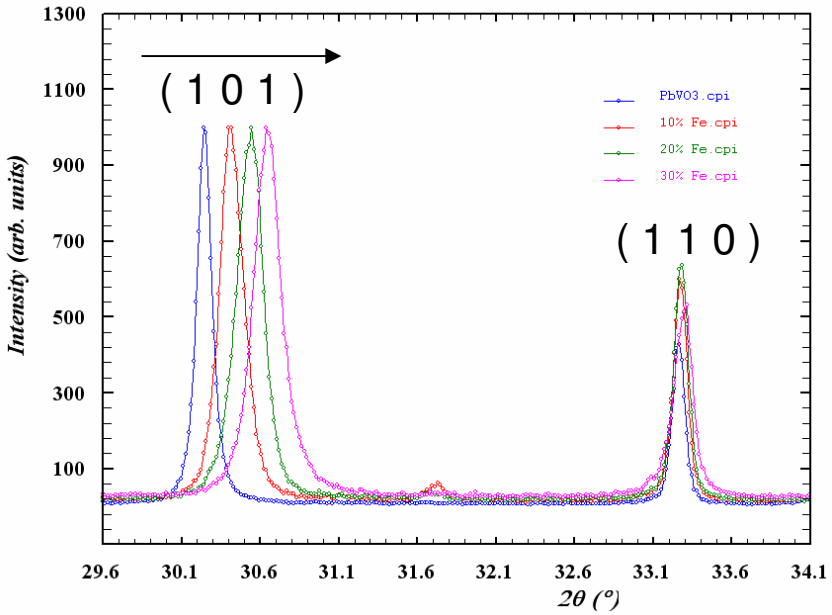

Fig. 4.21. Displacement of the peak position in $Pb(V_{1-x}Fe_x)O_3$. For clarity only the samples for x = 0 (blue), 0.1 (red), 0.2 (green) and 0.3 (pink) are shown. The arrow shows the direction in which the peaks are displaced as the Fe content is increased.

The evolution of the c/a ratio vs. x for the Fe series is shown in figure 4.22. Obviously, the discussion stops at 50% Fe.

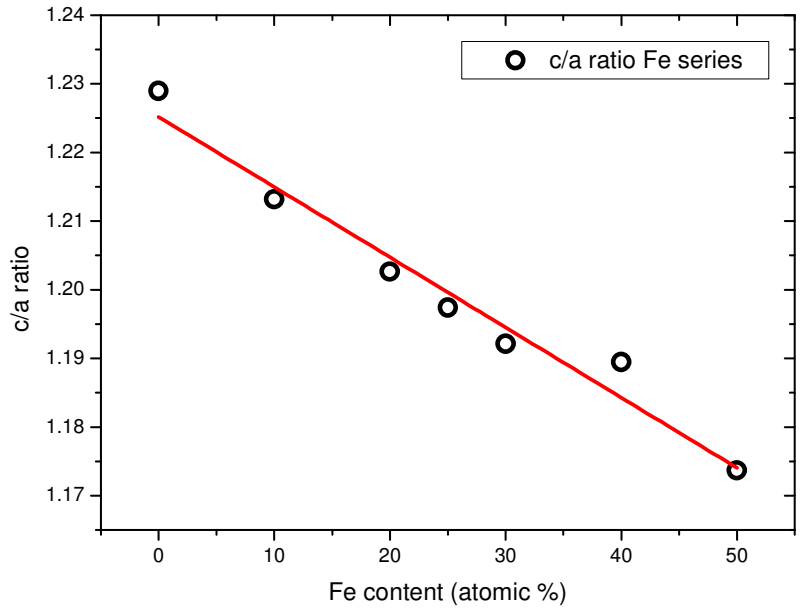

Fig. 4.22. Tetragonality for the Fe series. The dots mark the experimentally measured tetragonality. The red line is the linear fit of the experimental data.

The difference between the tetragonal distortions of the two substitution series is small (see figure 4.23).

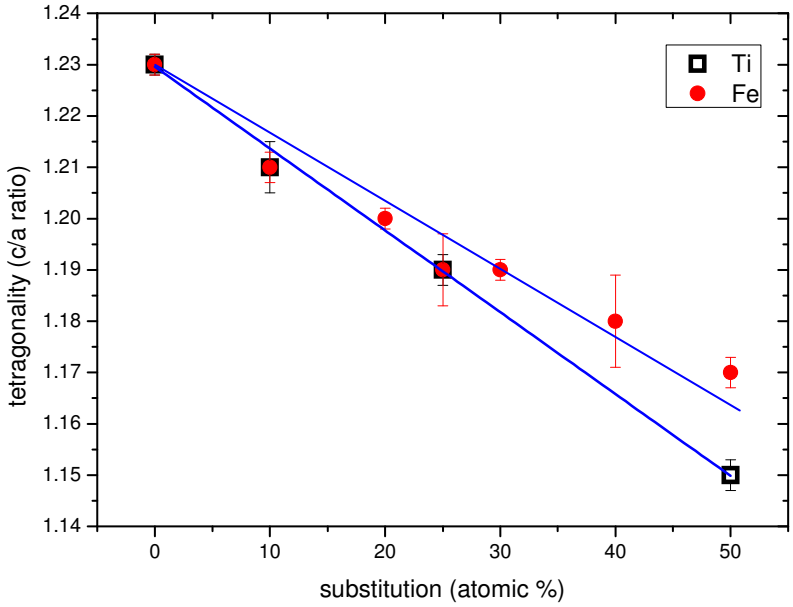

Fig. 4.23. Tetragonal distortions of samples from the Ti and Fe series. Blue lines are used for eye guidance.

Up to 25% substitution the c/a for the two sets of samples are almost identical. At substitutions higher that 25% the small differences become more easily visible and tend to increase as the substitution degree increases. The largest difference between the tetragonal distortions is only 0.02 (at 50% substitution). For $PbV_{0.5}Fe_{0.5}O_3$ the c/a $\approx$ 1.17 while for $PbV_{0.5}Ti_{0.5}O_3$ c/a $\approx$ 1.15.

This effect can be explained by the different radii of the Ti^{4+} and Fe^{3+} cations. The radius of the Fe^{3+} cation is 0.55 Å (assuming the 6 fold coordination) which is smaller than the radius of the Ti^{4+} cation (0.605 Å 6 fold coordination). It can be speculated that the Fe^{3+} cation does not form an equivalent of the vanadyl bond with the apical oxygen and therefore attempts to form a 6 fold coordination (like the Ti^{4+} cation) and to reduce the c parameter of the unit cell. The c parameters of the two types of samples follow an almost identical variation with the composition (figure 4.24). However, due to the smaller radius of the Fe^{3+} cation, compared to the radius of the Ti^{4+} cation, the substitution of V by Fe does not cause an increase of the a and b parameters, contrary to the substitution of V by Ti which does cause the increase of a

and b. Therefore the tetragonal distortion of the Fe substituted compounds is larger than the one of their Ti counterparts. However the tetragonal distortions are weak for both substitutions at high degrees of substitution.

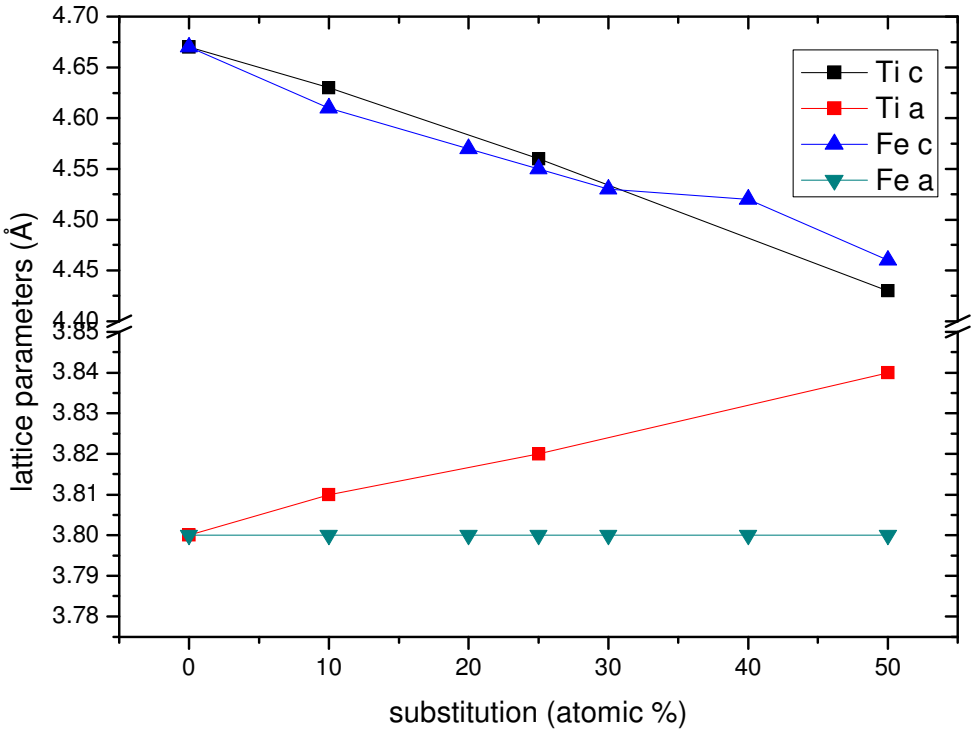

Fig. 4.24. Variation of lattice parameters for the 2 types of samples vs. substitution degree. Black and red dots and lines show the variations of the lattice parameters for the Ti series while blue and green dots and lines show the variation of lattice parameters for the Fe series.

IV.2.5. Fe series - microstructure

Strain/size effects are also seen to the samples of the Fe series. In figure 4.21 it can be seen that the width of the Bragg reflections increases with the substitution. Analogous to the situation found in Ti samples, the broadening is more significant for reflections close to the c* direction. For exemplification we will discuss the sample containing 30% Fe. Figure 4.25 shows the (0 0 1) peak (left) and the (1 0 0) peak (right). One can easily observe the difference in peak width.

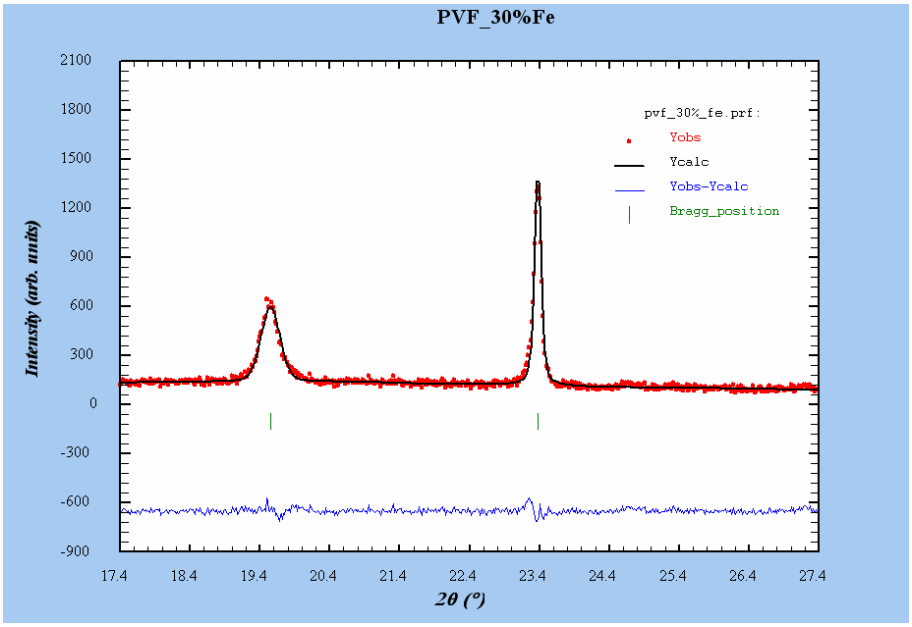

Fig. 4.25. Example of anisotropic peak broadening for the (001) and (100) reflections for $PbV_{0.7}Fe_{0.3}O_3$ *(PVF_004).*

The strain/size values obtained for the Fe series following the same analysis as for the Ti series are presented in figures 4.26 (size) and 4.27 (strain). Average size is shown in black and size along the c axis is shown in red. Again, the same pattern as in the Ti series can be observed. The size of the coherent domains is markedly smaller along the c axis (smaller along c than average size) and decreases as the Fe content is increased.

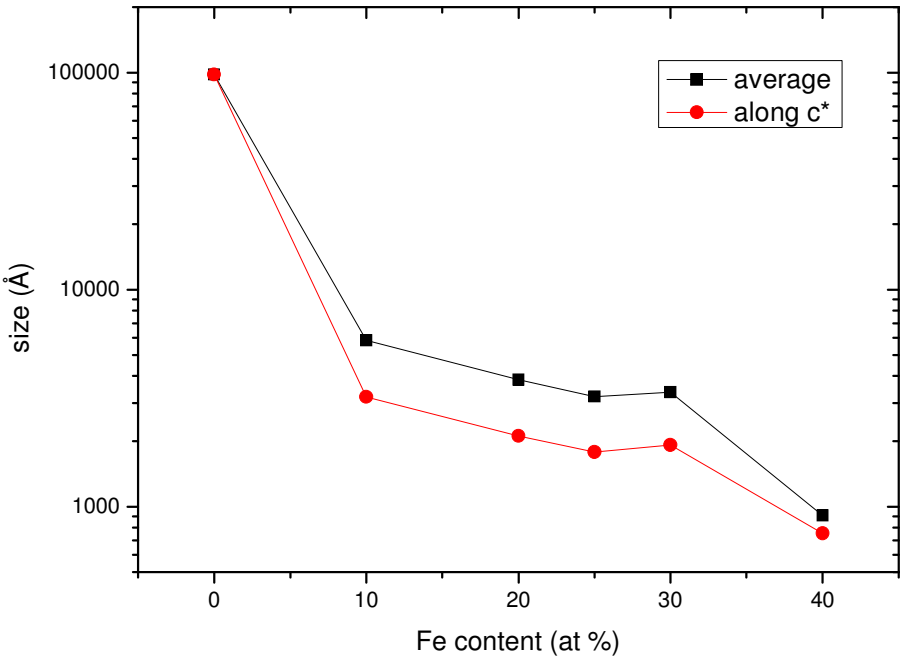

Fig. 4.26. Size effects in function of composition for the $PbV_{1-x}Fe_xO_3$ samples.

Conversely, this can be interpreted as an increase of the number of defects as the iron content is increased. The last single phase sample from the Fe series is the sample containing 40% Fe. For this reason the representation of size/strain in function of composition stops at 40% Fe. However, it can be observed that the domain size values are about 2 to 3 times smaller for the Fe-substituted than for the Ti-substituted compounds, which indicates that Fe substitution is probably more efficient at creating defects than the Ti- one. Table 4.8 gives the domain sizes along c* for a few samples from both substitution series.

Table 4.8. Domain size along c* for samples of equal degree of substitution from the Ti and respectively Fe series.

Ti content (%)	domain size along c* (Å) Ti series	Fe content (%)	domain size along c* (Å) Fe series
10	9423	10	3207
25	8069	25	1784
50	2700	40	753

The strain present in the sample is marked by black squares for the average values and by red dots for the values it has along the (0 0 1) direction (figure 4.27).

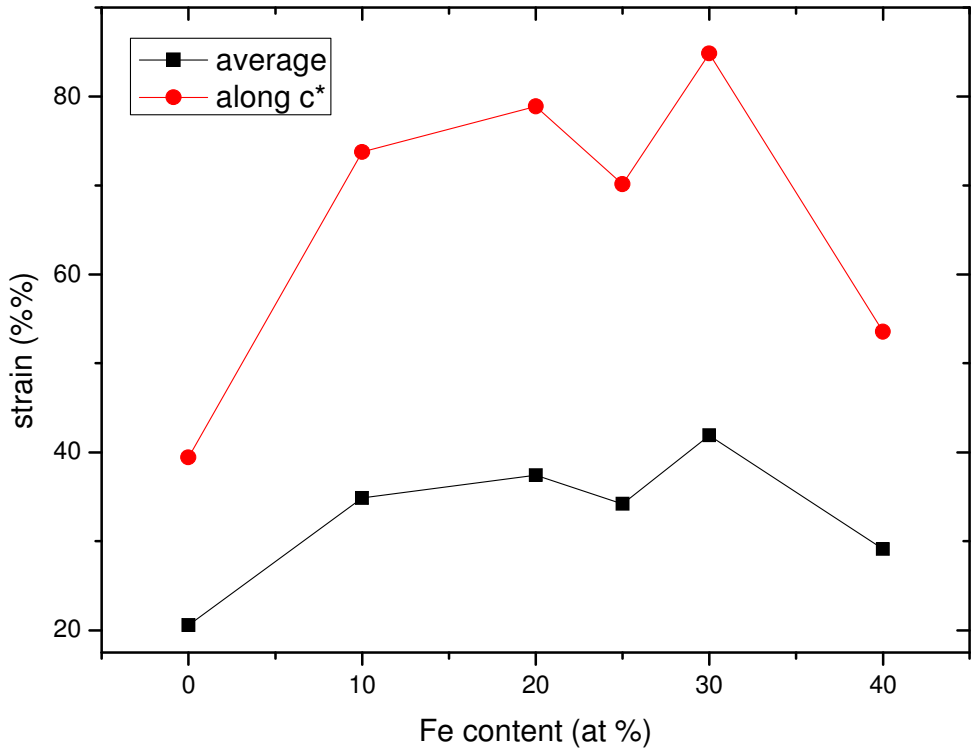

Fig. 4.27. Strain effect in function of composition for samples with the composition $PbV_{1-x}Fe_xO_3$.

Yet again as in the case of the Ti series, the strain does not vary significantly with the composition but remains nevertheless much larger along the (0 0 1) direction than the average value, indicating a strongly anisotropic strain with c as the preferred axis. The value of the strain parameters are similar to those obtained for the Ti series.

As a conclusion to this study of the microstructure of substituted samples, we have shown that substitution at the V site generates planar defects which can be interpreted as ferroelectric antiphase domains oriented perpendicular to the c axis. Such domains already exist in the pristine $PbVO_3$ compound, as shown in the single crystal study as well as in the low temperature x-ray powder diffraction study, where anisotropic peak broadening had also been observed. However, the disorder introduced by substitution decreases the coherent domain size, more efficiently for Fe than for Ti substitution, without additional change of the structural global strain.

IV.2.6. Structure refinements for $PbV_{1-x}Fe_xO_3$ samples

Rietveld refinements were performed on diffractograms of the samples from the Fe substitution series. Figures 4.28 and 4.29 are showing the Rietveld refinements for the samples containing 10% and 40% Fe respectively. Only the main phase is taken into consideration in the refinement. Table 4.9 gives the main parameters obtained from the refinements.

Table 4.9 Results of the Rietveld refinements based on XRPD data for the Fe series

Sample	10% Fe	20% Fe	25% Fe	30% Fe	40% Fe	50% Fe
Atom	x y z	x y z	x y z	x y z	x y z	x y z
Pb	0 0 0	0 0 0	0 0 0	0 0 0	0 0 0	0 0 0
V/Fe	½, ½, 0.557(2)	½, ½, 0.556(1)	½, ½, 0.550(2)	½, ½, 0.552(2)	½, ½, 0.545(3)	½, ½, 0.439(8)
O1	½, ½, 0.202(4)	½, ½, 0.200(4)	½, ½, 0.175(3)	½, ½, 0.181(3)	½, ½, 0.184(5)	½, ½, 0.207(8)
O2	½, 0, 0.670(3)	½, 0, 0.671(2)	½, 0, 0.666(2)	½, 0, 0.655(3)	½, 0, 0.636(2)	½, 0, 0.401(6)
a	3.80520(5)	3.80427(2)	3.80210(2)	3.80233(3)	3.80438(5)	3.8141(1)
c	4.6149(1)	4.5745(1)	4.55017(8)	4.5366(1)	4.5255(1)	4.4671(4)
Rwp, RBragg, chi^2	22.3, 3.41, 1.67	23.9, 3.93, 1.81	20.9, 4.63, 1.37	21.7, 3.24, 1.5	30.5, 6.13, 1.69	35, 6.13, 2.06
Pb-O1 x 4 (Å)	2.84	2.84	2.8	2.81	2.81	2.85
Pb-O2 x 4 (Å)	2.43	2.42	2.43	2.46	2.51	2.61
V/Fe-O1 x1 (Å)	1.65	1.62	1.7	1.68	1.63	1.03
V/Fe-O2 x4 (Å)	1.97	1.97	1.97	1.95	1.94	2.03

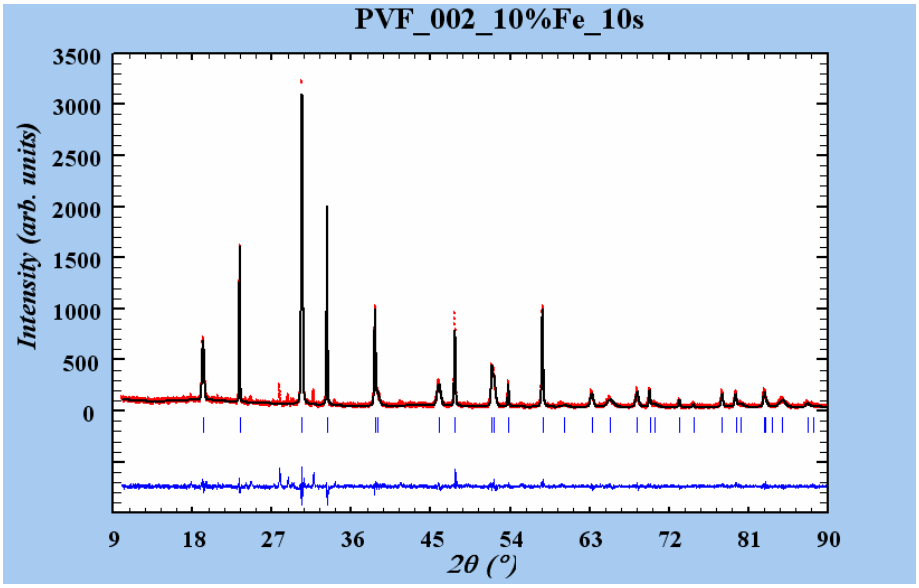

Fig. 4.28. Rietveld refinement for $PbV_{0.9}Fe_{0.1}O_3$ (the PVF_002 sample).

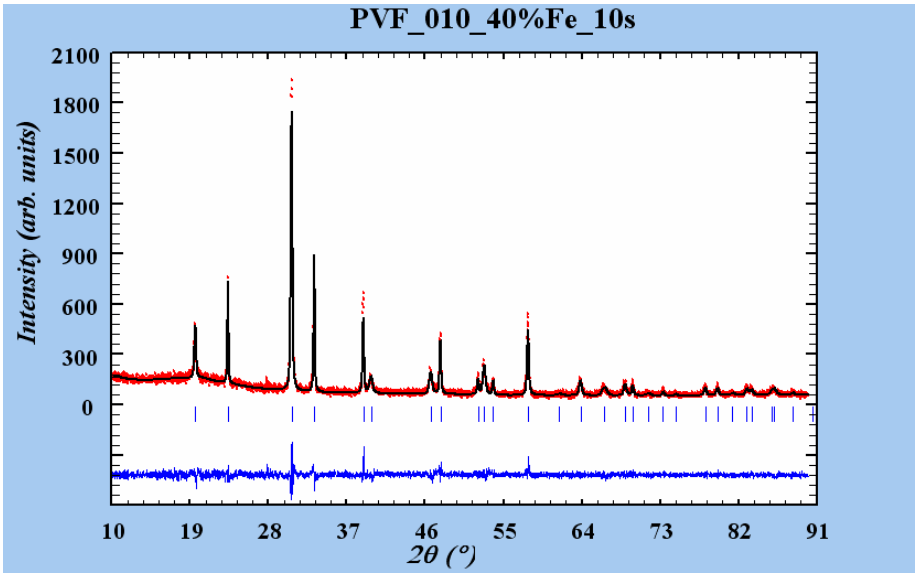

Fig. 4.29. Rietveld refinement of $PbV_{0.6}Fe_{0.4}O_3$ (the PVF_010 sample).

Again some small variations in atomic positions are seen and these variations appear to show the system slightly shifting towards a cubic structure. The interatomic distances obtained for the 50% Fe sample, particularly the B site cation - apical oxygen distance, are not reliable. The V/Fe - O1 distance returned by the refinement is close to 1 Å which is unphysical. The crystallinity of the Fe substituted sample decreases with the substitution degree and reaches the minimum value at the 50% Fe point. On the other hand the sample at 50% Fe substitution does not contain only a single phase. For these reasons the quality of the refinement for the 50% Fe sample is

seriously weighed down. The discussions about the structure of the $PbV_{1-x}Fe_xO_3$ compound will therefore stop at the 40% Fe sample.

For the Fe series a phenomenon similar to the one observed at the Ti series occurs. Fe does not form an equivalent to the short strong vanadyl bond so the average V/Fe-O1 distance increases slightly (figure 4.30). The Pb-O1 bond strength increases so Pb-O1 distance becomes smaller. Consequently the distortion of Pb towards the O2 plane is less effective so Pb-O2 distance increases. Just like for the Ti series, the reduction of overall vanadyl strength tends to release the O1, more than to change the z of the V/Fe cation. The atomic coordinates are plotted on figure 4.31.

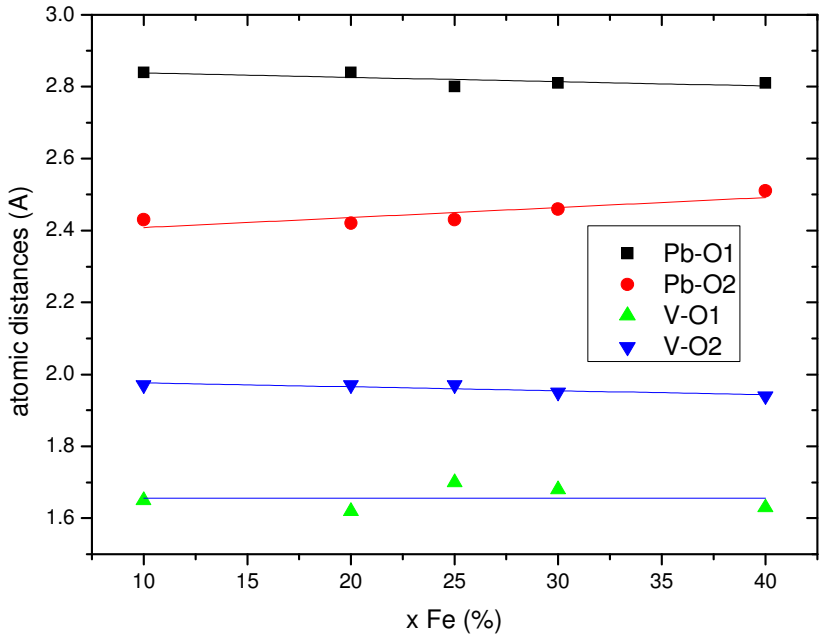

Fig. 4.30. Main interatomic distances for the Fe series. The points represent experimental data and the lines are linear fits of the experimental data.

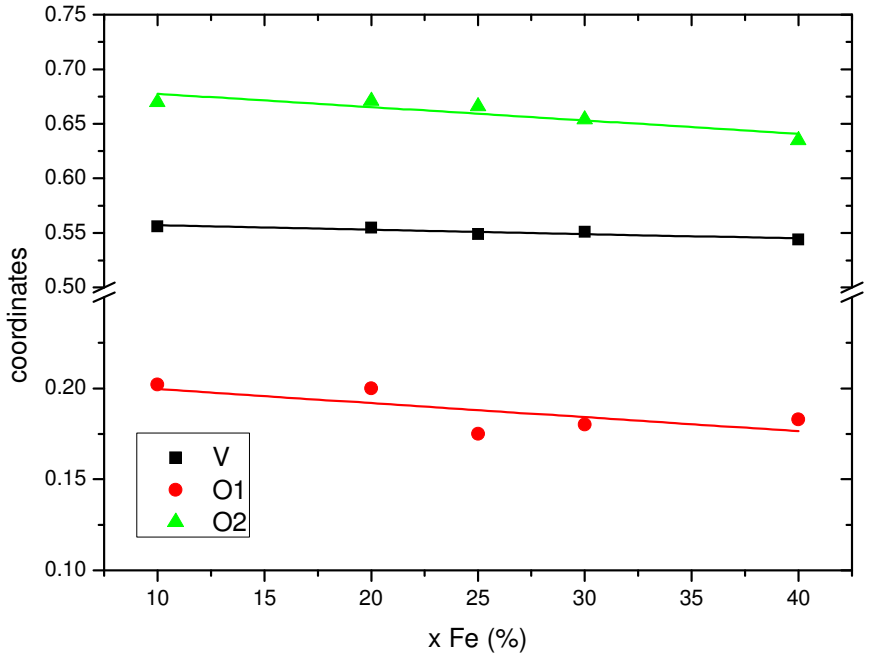

Fig. 4.31. Atomic coordinates for samples from the Fe series. The points represent experimental data and the lines are linear fits of the experimental data.

There are however noticeable differences between the Fe and the Ti series. The change in average z of V/Fe is smaller than in the Ti series. The increase of the V/Fe-O1 distance is seen from linear fits of the z values, however the decrease is not clearly visible in point by point calculated inter-atomic distances.

Both O1 and O2 decrease their z at the same rate in the Fe substitution samples whereas the decrease of z occurred at different rates in the Ti substituted samples.

Also, unlike for the Ti series, the a-b parameters remain constant and the V/Fe-O2 distance decreases. This indicates a displacement of the oxygen ions which causes the B site cation to approach the base of the oxygen pyramid.

IV.3. Neutron powder diffraction and NPD/XRD refinements

Although some idea about the structure evolution of the materials emerges, at this point the structure cannot be completely understood, mainly because the positions of the oxygen atoms are not accurately determined. So far we assumed that V and Ti or Fe occupy the exact same place in different unit cells however this may not be true. Also, the oxygen atoms connected to a Vanadium cation have no reason to be located at the same coordinates as the oxygen atoms connected to the Ti or Fe ions. The x-ray diffraction data provide average information which can be inaccurate for what concerns the oxygen positions. The diffraction pattern is dominated by the contribution of the Pb atoms due to the large number of electrons that Pb possesses and the subsequent scattering power of the Pb atom. The contribution of V (or Fe or Ti) is already much smaller and comes in the second place while the oxygen atoms only bring a very small contribution (on third place) to the information on a XRD diagram. Oxygen atoms represent only about 1% of the scattering power of Lead atoms. In order to increase the amount of information that can be extracted about the oxygen atoms neutron powder diffraction is needed. At NPD the strongest scattering atom remain the Pb but the scattering power of oxygen is much greater, at about half the scattering power of Pb. Table 4.10 gives the X-Rays and neutrons scattering powers for Pb, V, Ti, Fe and O.

Table 4.10. The scattering power of the atoms from the $PbV_{1-x}M_xO_3$ compound (M = Ti, Fe). For XRD the atomic form factor is provided only for zero scattering angle. For NPD the coherent Fermi length is provided.

atom	X-Ray scattering 0 scattering angle (Z)	Coherent neutron scattering Fermi length ($x10^{-12}$ cm)
Pb	82	0.9405
V	22	-0.0382
Ti	23	-0.3438
Fe	26	0.9450
O	8	0.5803

This makes NPD diffractograms particularly sensitive to the positions of oxygen atoms. With NPD it becomes possible to refine the data using a more sophisticated model in which the oxygen atoms corresponding to the V are separated from the oxygen atoms for the substitution atom. That way, the model contains two types of oxygen atoms that no longer occupy the exact same place in the unit cell.

However, for NPD, the great drawback is that Vanadium is not visible, because the Vanadium Fermi length is close to zero. Vanadium is almost completely transparent for neutrons. On the other hand Titanium and iron can be easily detected using NPD.

The problem of the low V signal to NPD is solved by conducting a simultaneous refinement of and XRD and an NPD pattern of the same sample. FullProf can refine two diffraction patterns using the same structural model for both patterns and trying to adjust the refined parameters of the model in such a way as to best explain the XRD and the NPD data. That way the NPD provides information about the positions of the oxygen atoms and the XRD about the position of Vanadium. Such refinements were performed on a number of samples and the results of these refinements are discussed below.

NPD measurements are more sophisticated than XRD measurements and have different requirements. Most notably NPD requires relatively large volumes of sample which are hard to prepare using HP-HT (which generally produces small quantities). Consequently 4 representative samples were chosen for NPD measurements. The 4 representative samples were obtained by mixing several small samples of the same composition.

Measurements were conducted at the D1B facility at the Laue-Langevin Institute (ILL), Grenoble, France.

The four representative samples that were measured are:

1. $PbVO_3$ as the witness sample (marked PVO)
2. $PbV_{0.75}Ti_{0.25}O_3$ as representative of the Ti series (marked PVT_25)
3. $PbV_{0.75}Fe_{0.25}O_3$ the counterpart from the Fe series (marked PVF_25)
4. $PbV_{0.6}Fe_{0.4}O_3$ the sample with the highest iron content that is still crystallized in only the tetragonal form. (PVF_40)

NPD measurements were conducted at two wavelengths, 1.28 Å and 2.52 Å. and several temperatures from 300 K to 2 K. The short wavelength was used for the acquisition of crystallographic information, more precisely the position of oxygen

atoms. The longer wavelength was used in the acquisition of information about the magnetic ordering of the sample. Data collected at the 2.52 Å wavelength are discussed in the next chapter.

As in the case of XRD, before starting to measure the samples, the IRF of the diffractometer was determined at both wavelengths by measuring a standard, which was this time a NAC sample ($Na_2Ca_3Al_2F_{14}$). Like the LaB_6 we used for XRD the NAC used for NPD gives no contribution to the broadening of the reflections so from the refinement of the NAC pattern the instrumental contribution is determined. Also, the lattice parameters of the NAC are known to a great precision and this allowed for the refinement of the wavelength of the neutrons. The refinements for the NAC at the two wavelengths are shown in figures 4.32 and 4.33 respectively.

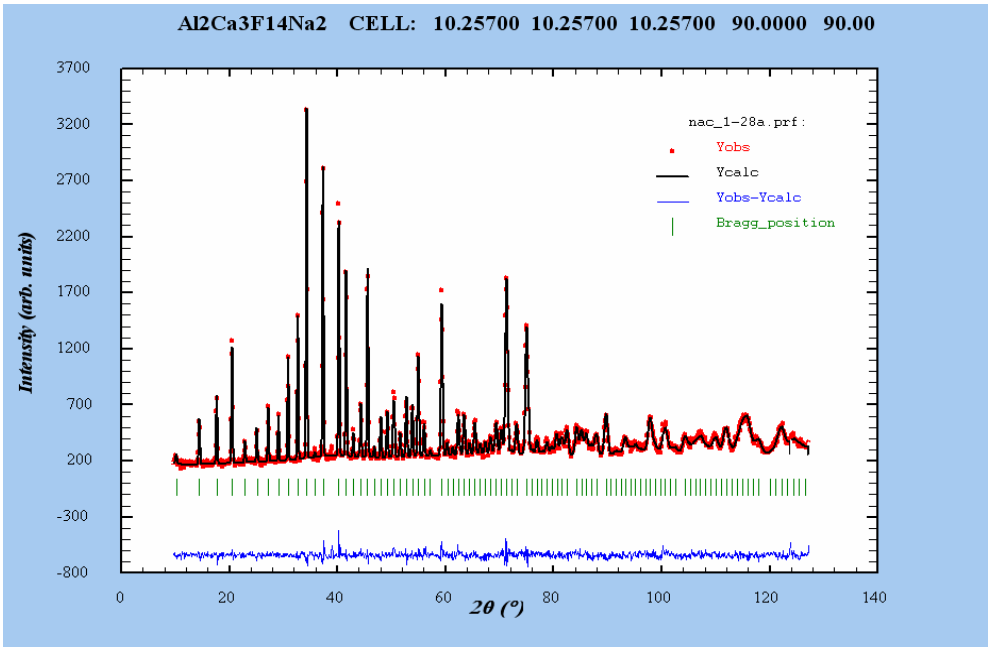

Fig. 4.32. Rietveld refinement for NAC sample measured at the 1.28 Å wavelength.

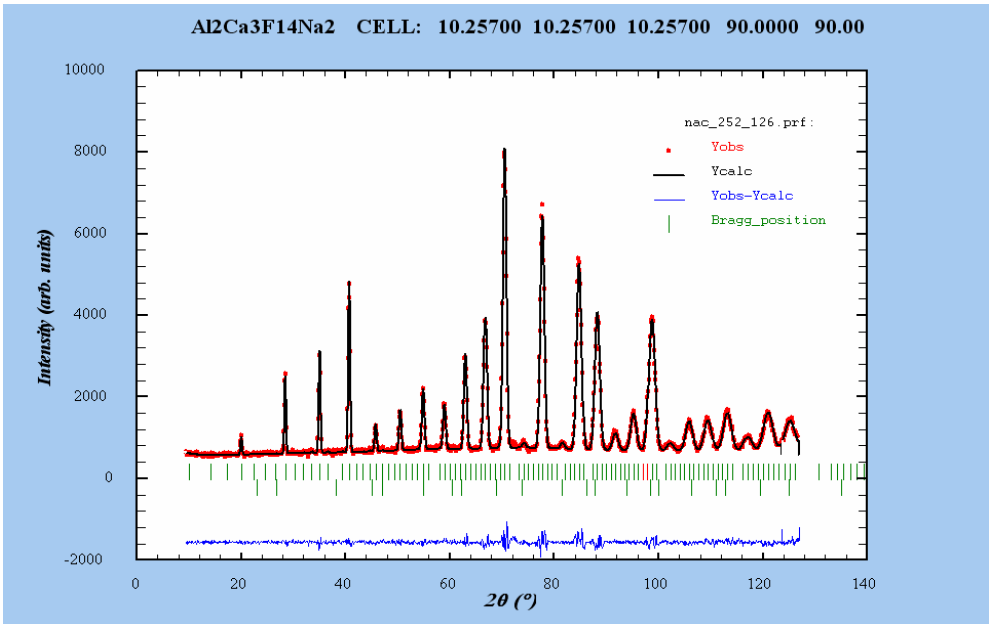

Fig. 4.33. Rietveld refinement for NAC sample at the 2.52 Å wavelength.

The parameters obtained from the refinements of the standard (NAC) sample are collected in table 4.11, below.

Tale 4.11. U, V, W, X and Y parameters of the D1B neutron diffractometer, obtained for the two wavelengths used during our experiments.

λ (Å)	U	V	W	X	Y
1.28921(5)	0.97(3)	-0.56(3)	0.142(5)	0.04(1)	0
2.52588(3)	1.93(5)	-0.79(5)	0.22(1)	0.02(1)	0

In a dual refinement one has to decide of the relative weights of the NPD and XRD diagram for the refinement. This will depend on the counting statistics of each pattern and diffracting power for each radiation. In other words if the NPD is statistically "heavier" then the refinement will be content to find a model that fits the NPD and tend to neglect the XRD. In FullProf however it is possible to choose the importance (or the weight) of each diffraction pattern, XRD or NPD. After several attempts, the weight of the patterns was distributed as 75% for XRD and 25% for NPD in order to extract sufficient information both on the oxygen and vanadium positions.

For dual refinements better results were obtained by constraining the lattice parameters for the XRD and NPD patterns to the same values and refining the neutron wavelength.

Since NPD diffractometers are less sensitive to strain/size effects because the instrumental resolution is poorer, the parameters that describe these effects were kept fixed to the values determined from XRD.

The results of the refinements are given in tables 4.12 and 4.13. Table 4.12 gives the atom coordinates, lattice parameters and agreement factors for the double refinements and table 4.13 gives the most important interatomic distances. The coordinates of the V and Ti or Fe cations are separated. The coordinates of the oxygen anions corresponding to each of the B site cations are also separated.

The interatomic distances are calculated between a B site cation and its surrounding oxygen anions. The distinction is made between V and oxygen's for its coordination and Ti or Fe and their oxygen neighbouring. The former distances are labelled M-O1M (for O1) or M-O2M (for O2) where M = Ti, Fe.

Table 4.12 Results of the joint XRPD and NPD Rietveld refinements for Pb(V,M)O3 (M=Ti, Fe) samples

Sample	$PbVO_3$		PVT_25		PVF_25		PVF_40	
Atom	x y z	Biso	x y z	Biso	x y z	Biso	x y z	Biso
Pb	0 0 0	0.73(5)	0 0 0	0.5	0 0 0	0.5	0 0 0	0.5
V	½, ½, 0.571(2)	1.66(8)	½, ½, 0.561(2)	0.7	½, ½, 0.557(3)	0.7	½, ½, 0.548(3)	0.7
Ti/Fe			½, ½, 0.563(4)	0.7	½, ½, 0.538(4)	0.7	½, ½, 0.543(3)	0.7
O1V	½, ½, 0.2170(1)	0.81(8)	½, ½, 0.1980(1)	0.80(8)	½, ½, 0.188(1)	1	½, ½, 0.180(2)	1
O2V	½, 0, 0.6890(1)	0.79(6)	½, 0, 0.6650(1)	0.34(6)	½, 0, 0.671(2)	0.80(7)	½, 0, 0.655(3)	0.85(6)
O1Ti/Fe			½, ½, 0.151(3)	0.85(8)	½, ½, 0.128(3)	1	½, ½, 0.130(3)	0.86(9)
O2Ti/Fe			½, 0, 0.706(2)	0.36(2)	½, 0, 0.626(3)	0.74(2)	½, 0, 0.638(2)	1
a	3.8054(1)		3.8205(1)		3.8019(2)		3.8044(2)	
c	4.6766(1)		4.5611(2)		4.5502(2)		4.5256(1)	

Rwp (Rx) RBragg (Rx)	23.4, 7	20.6, 3.66	21.7, 4.46	30, 6.48
Rwp (N) RBragg (N)	11.7, 8.73	9.33, 5.06	9.15, 3.57	14.2, 5.09
chi^2	29.74	57.49	210.8	45.25

Table 4.13 Main interatomic distances for the following compounds $PbVO_3$, $PbV_{0.75}Ti_{0.25}O_3$ (PFT_25), $PbV_{0.75}Fe_{0.25}O_3$ (PVF_25) and $PbV_{0.6}Fe_{0.4}O_3$ (PVF_40).

Sample	$PbVO_3$	PVT_25	PVF_25	PVF_40
Pb-O1V x 4 (Å)	2.8760(1)	2.8498(1)	2.8209(1)	2.811(3)
Pb-O2V x 4 (Å)	2.39550(2)	2.4458(2)	2.419(3)	2.461(1)
Pb-O1M x 4 (Å)		2.791(2)	2.751(3)	2.754(3)
Pb-O2M x 4 (Å)		2.334(5)	2.552(7)	2.510(1)
V-O1V x1 (Å)	1.65(3)	1.652(5)	1.678(5)	1.665(9)
V-O2V x4 (Å)	1.985(8)	1.9702(8)	1.9712(1)	1.963(4)
M-O1M x1 (Å)		1.872(6)	1.861(1)	1.869(3)
M-O2M x4 (Å)		2.020(5)	1.944(3)	1.950(6)

The first sample for which a dual refinement was performed is the PVT_25 (25% Ti). The diagrams and corresponding refinements are shown in the figures 4.34 and 4.35.

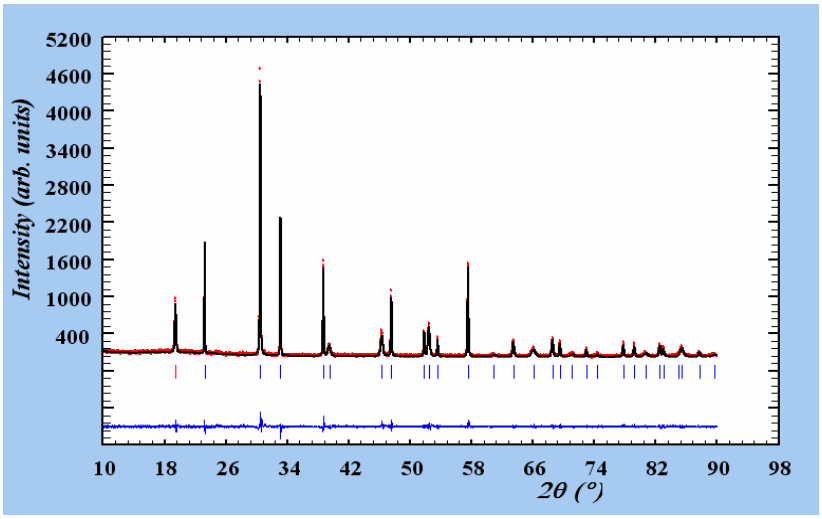

Fig. 4.34. Rietveld refinement of the XRD pattern for $PbV_{0.75}Ti_{0.25}O_3$ (the PVT_001 sample).

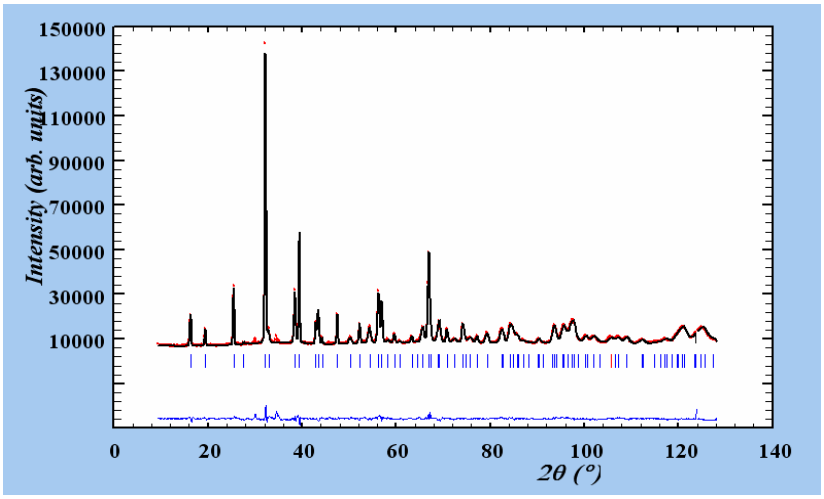

Fig. 4.35. Rietveld refinement of the NPD pattern for $PbV_{0.75}Ti_{0.25}O_3$ (the PVT_25 sample). The sample was obtained by mixing 5 different samples of the 25 % Ti composition.

From the single crystal refinement the V-O1 distance in $PbVO_3$ is 1.65 Å. For the PVT_25 sample from the double refinement (XRD / NPD) it appears that the V-O1 1.64 Å apical bond length and the 1.98 Å in-plane bong lengths are almost unchanged. The Vanadium coordination seems relatively unaffected by the isovalent substitution of Titanium. The Ti-O distances returned by the refinement of PVT_25 are Ti-O1=1.87 and TiO2=2.01 Å. In $PbTiO_3$ the corresponding Ti-O distances are

1.76 and 1.98 Å [42]. Although some caution must be taken with these results, such a change could reflect a compromise between the oxygen coordination for Ti cations in $PbTiO_3$ and as a substituting element in $PbVO_3$. The a cell parameter in the PVT_25 sample (3.8204 Å) is much smaller than that of $PbTiO_3$ (3.905 Å) and therefore the Ti coordination octahedron has to be more elongated along the c axis in the PVT_25 compound to compensate for the compression effect in the (a,b) plane. Figure 4.36 shows the unit cells of $PbTiO_3$ (a) and PVT_25 (b).

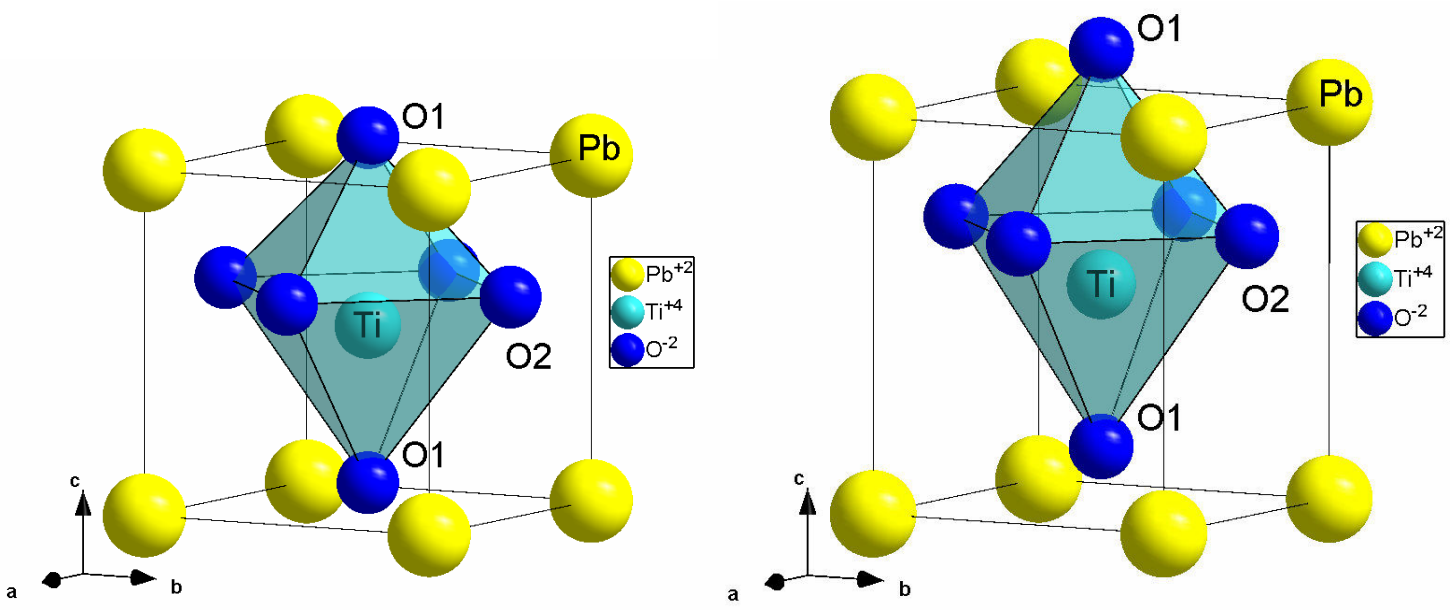

a) b)

Fig. 4.36. a) Representation of the unit cell of $PbTiO_3$, b) the unit cell of PVT_25. Only the Ti cation and its corresponding oxygen octahedron are represented. The V cations (and related oxygen coordination) have been omitted.

The Ti^{4+} cation radius is much closer to the V^{4+} cation radius when they both adopt the 5 fold coordination. Therefore the Ti cation will on one hand try to adopt a 5 fold coordination to respect the structure of the $PbVO_3$ but on the other hand will tend to adopt a 6 fold coordination to approach the structure of $PbTiO_3$ and eventually the structure of an ideal perovskite.

The next sample investigated by joint XRD / NPD refinements was PVF_25. The XRD and NPD refinements are shown in figures 4.37 and 4.38 respectively.

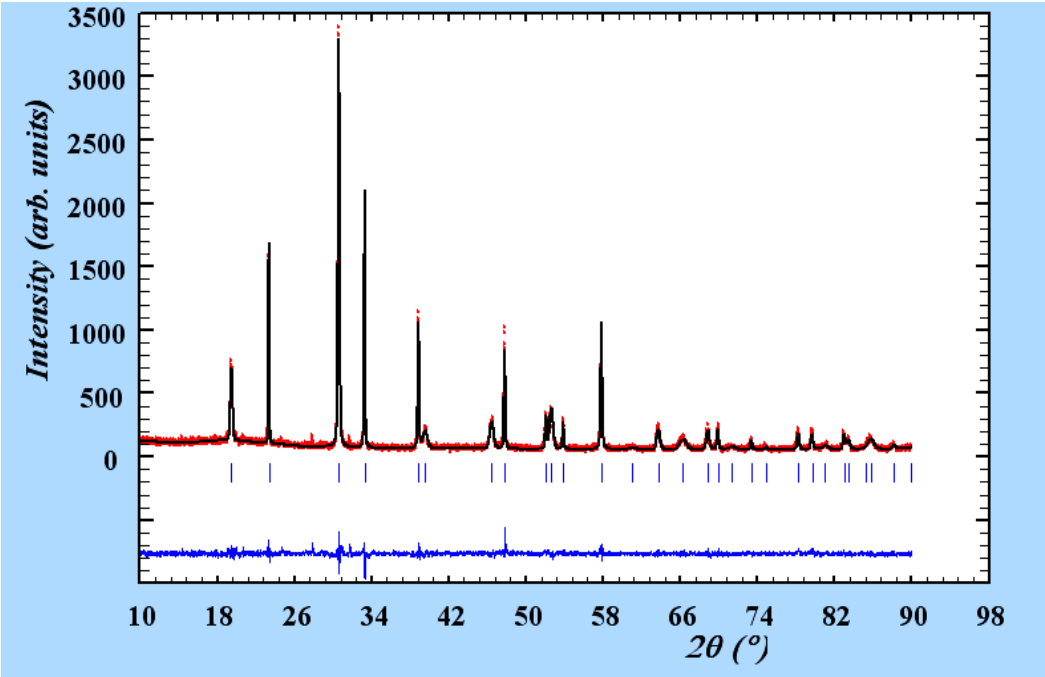

Fig. 4.37. Rietveld refinement for XRD on $PbV_{0.75}Fe_{0.25}O_3$ (sample PVF_001).

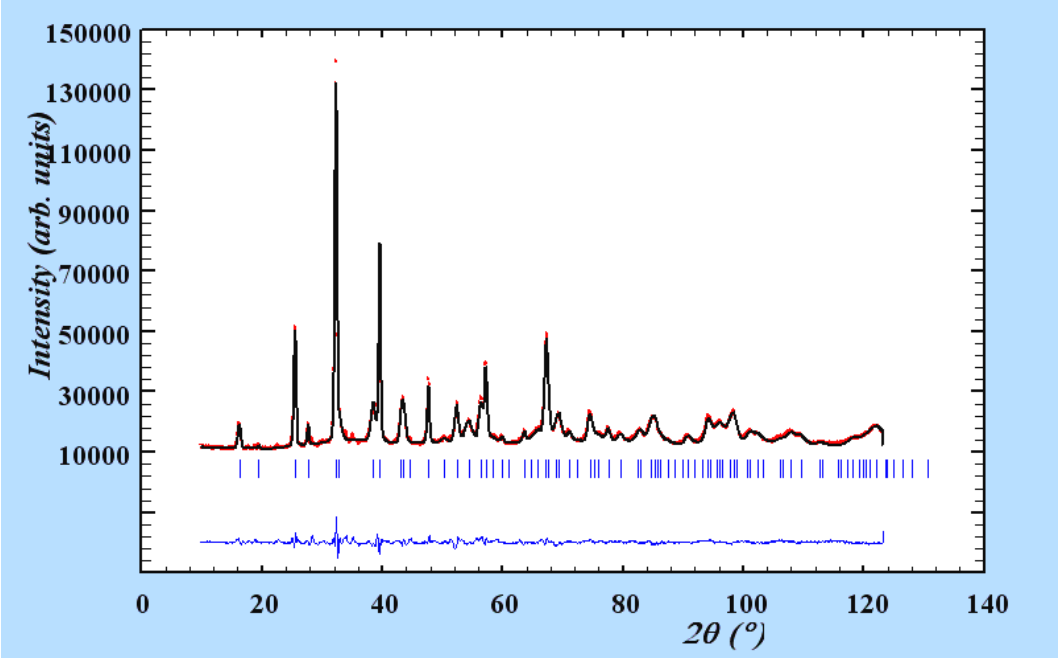

Fig. 4.38. Refinement for NPD data collected for the PVF_25 sample at the D1B. The PVF_25 sample is a mixture of different samples with the $PbV_{0.75}Fe_{0.25}O_3$ composition.

The last sample in the series is the 40% Fe product. The refinements for the XRD and NPD are shown in pictures 4.39 and 4.40.

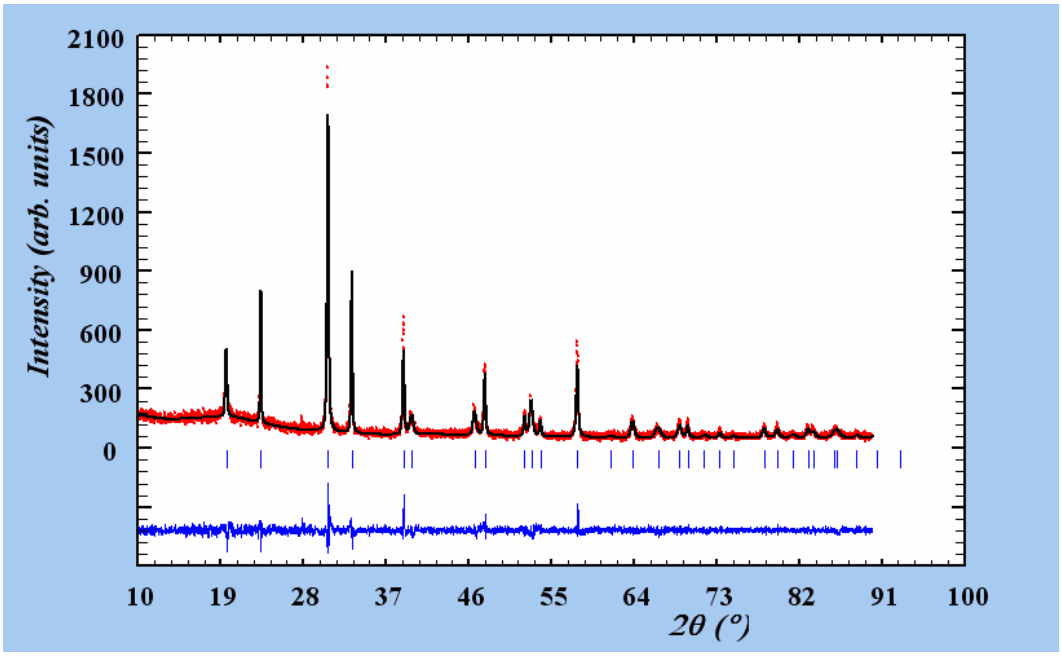

Fig. 4.39. $PbV_{0.6}Fe_{0.4}O_3$ (PVF_010) XRD Rietveld refinement. Standard synthesis and measurement conditions were employed.

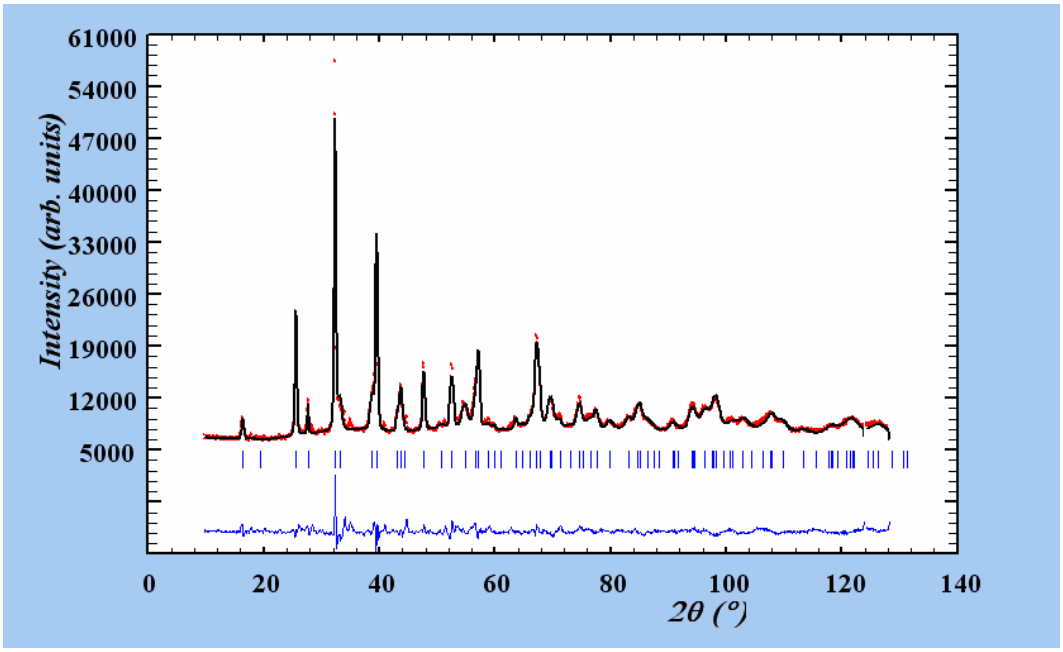

Fig. 4.40. PVF_40 (40% Fe) NPD Rietveld refinement. The PVF_40 sample is a mixture of several identical samples of the $PbV_{0.6}Fe_{0.4}O_3$ composition. The samples that were mixed are PVF_010, PVF_014, PVF_020 and PVF_022.

For both Fe substituted samples, the conclusions are similar to what was observed for the PVT_25 one, although the comparison to a hypothetical $PbFeO_3$ compound is not possible here since such a compound has not been prepared yet. Nevertheless, we still observe little change in the Vanadium coordination, and a

tendency for the Fe cations to adopt a less distorted coordination, with longer Fe-O1 bonds. When the amount of iron is increased, the quality of refinement becomes somewhat poorer. Contrarily to the case of Titanium, the substitution is no longer isovalent for Fe and the B cation site of the perovskite is now occupied by V^{4+}, V^{5+} and Fe^{3+}, each with its own coordination sphere. Table 4.14 gives the ionic radii and the coordination of the 3 cations.

Table 4.14. Ionic radii and coordination for V^{4+}, V^{5+} and Fe^{3+}.

cation	coordination	ion radius (Å)
V^{4+}	V	0.53
V^{5+}	VI	0.54
Fe^{3+}	VI	0.55 (low spin state)

The situation is now probably too complicated to expect an accurate description of each of them even in a joint XRD-NPD refinement, and our results are just the average picture from a quite complex situation.

Another aspect concerns the atomic displacement parameters, the Biso, for the oxygen atoms. No strict numerical values are given here but the evolution of the Biso during the refinement is described. The "default", initial, value for the oxygen atoms is chosen to be 1. In the model which contains a single type of oxygen atoms the refined value of Biso remains close to unity or increases slightly up to 1.2 for example. However when the unit cell is defined with separate oxygen atoms, assigned to their corresponding V or Ti/Fe atoms, the refined Biso decreases to a value from 0.8 to 0.5. The Biso shows how much the atom oscillates around its equilibrium position but the data can be interpreted, more or less, as an indication of how "diffuse" the electronic cloud of the atom is. In the single oxygen atom model, the program "sees" an oxygen atom distributed in a large volume, meaning it increases Biso in an attempt to fit the data. In the two oxygen atoms model, the program "sees" at the site of oxygen two atoms in slightly different coordinates and therefore no longer needs to increase the delocalization of the atom(s) to fit the data. In this way the Biso for each individual oxygen atom decreases to "reasonable" values. Looking at the problem backwards, the decrease in the Biso of the oxygen atoms in the two anions model gives validity to the model.

IV.4. Electric polarization calculated from the structural data

The tetragonal, ferroelectric structure of $PbVO_3$ is maintained for both substitutions so it can be expected that the substitution samples present a certain electric polarization. Having the structural information it is possible to predict the value of that spontaneous polarization using the point charge calculation, as described by [87]. The polarization defined as the sum of the dipole moments divided by the volume. For a unit cell, the polarization is then calculated as the sum over all the point charges q_i at their position r_i within the volume of the unit cell [87] according to the equation:

$$\mathbf{P_S = (\sum q_i * r_i) / V}$$

The dipole moment is defined as q*d, where q is the electric charge and d is the separation between centres of the charges. For $PbVO_3$ (and its substitution counterparts) the polarization is oriented along the z axis. Assuming that the Pb cations are located at the origin (so they are not displaced), their contribution to the spontaneous polarization is zero. The remaining cations generate the following contributions:

- V^{4+} generate a moment of $4*e*d_{Vz}$ (where e is the elementary charge and d_{Vz} it the atomic displacement of the V cation along the z axis)
- $O1^{2-}$ generates a contribution of $-2*e*d_{O1z}$ (where the last term is the displacement of the apical oxygen
- $O2^{2-}$ generate a contribution of $-4*e*d_{O2z}$ (where the last term is the displacement of the O2 oxygen anion. There are two O2 anions on the chemical formula of $PbVO_3$, hence the electric charge multiplied by 4.

The formula then becomes:

$$\mathbf{P_S = (4ed_{Vz} - 2ed_{O1z} - 4ed_{O2z}) / V}$$

The position occupied by the V cation is defined by the (x, y, z) coordinates as (1/2, 1/2, $1/2+\delta_V$) and the coordinates of the oxygen anions are (x, y, z) = (1/2, 1/2, δ_{O1}) for O1 and (x, y, z) = (1/2, 0, $1/2+\delta_{O2}$) for O2.

The atomic displacements are calculated as the differences between the coordinates occupied by the respective cations on $PbVO_3$ and the coordinates they would take on

an ideal perovskite, multiplied by the height of the unit cell. For that reason the atomic displacement for the vanadium cation is $d_{Vz} = \delta_V * c$, where δ_V has the significance discussed above and c is the height of the unit cell. Similar equations are used to calculate the atomic displacements of the oxygen anions. The volume of the unit cell is $V = a^2*c$. Considering these modifications the equation of the spontaneous polarization becomes:

$$\mathbf{P_S = e*(4\delta_V - 2\delta_{O1} - 4\delta_{O2}) / a^2}$$

Using this equation and the structural data obtained from XRD experiments the spontaneous polarization was calculated for the Ti and Fe substitution series, assuming the average charge at the B site cation equal to 4e and assuming a single (average) position for the B site cation and the oxygen anions. Table 4.15 gives the results of these calculations. When the unit cell parameters are expressed in SI units the result of the spontaneous polarization will be expressed in C/m^2. However, the results from table 4.15 are given as $\mu C/cm^2$ which is often used.

Table 4.15 Estimated electric polarization for Ti and Fe series

Ti composition (at %)	spontaneous polarization ($\mu C/cm^2$)
0	102.6
10	100.1
25	96.5
50	82.4
60	78.1
75	68.4
80	64.2
100	54.8
Fe composition (at %)	spontaneous polarization ($\mu C/cm^2$)
0	102.6
10	95.7
20	96.2
25	91.2
30	86.7
40	81.9

For the Fe series the table stops at the 40% Fe sample since this is the last Fe sample for which reliable structural information is available. The structural data for the 50% Fe sample is not sufficiently reliable.

For the 3 substitution samples investigated by NPD (PVT_25, PVF_25 and PVF_40) a better estimation of the spontaneous polarization can be obtained. The polarizations for V only (respectively Ti only and Fe only) containing unit cells is first calculated and the overall polarization is obtained by the weighted sum according to the chemical composition. Table 4.16 presents these results. For the PVT_25 sample the only modification concerns the atomic coordinates of oxygen anions from V or Ti unit cells. For the PVF_25 and PVF_40 samples supplementary modifications appear. The charge of the Fe cation is 3e and the coordinates of the Fe and V cations are better distinguished. At the B site (for Fe samples) there are 3 types of cations, Fe^{3+}, V^{5+} and V^{4+} but the precise coordination of the V cations is not known. Therefore the polarization of the V containing unit cell was calculated assuming a single set of vanadium and corresponding oxygen atomic coordinates, which is a simplification of the problem.

Table 4.16 Estimated spontaneous polarizations calculated from the separate contributions of the unit cells containing V, Ti or Fe.

sample composition (Fe at %)	calculated spontaneous polarization ($\mu C/cm^2$)			
	V^{4+} unit cell	V^{5+} unit cell	Ti^{4+} / Fe^{3+} unit cell	overall
25% Ti	90.1		97	91.8
25% Fe	93.2	86.8	72.4	86.4
40% Fe	88.2	82.8	76.4	81.3

Another estimation of the spontaneous polarization can be made using Glazer's formula [42] which states that:

$P_S = k*\delta z$, where k is a constant, evaluated by Glazer [42] at $k = 2.9\ C * m^{-2} * Å^{-1}$ for $PbTiO_3$ and δz is the distance between the B site cation position and the O2 plane.

For $PbTiO_3$ the experimentally determined spontaneous polarization is $P_S = 75\ \mu C/cm^2$ [88]. Glazer's equation [42] overestimates the spontaneous polarization at P_S

= 86.6 μC/cm^2 and the point charge calculation underestimates the value of P_S at 54.8 μC/cm^2. Used for $PbTiO_3$ both formulations give equally reasonable values of the spontaneous polarization but it is likely that for $PbVO_3$ and its substitutions, the point charge calculation is better suited. On one hand Glazer's formula [42] overestimates (considerably) the spontaneous polarization and on the other hand it is not sure if the k constant of $PbTiO_3$ can be transferred to $PbVO_3$.

When the values of the polarization are compared for substitution samples it is easy to observe that the polarization decreases with the substitution, for both series, regardless of the type of substitution. Figure 4.41 shows the variation of the spontaneous polarization with the composition.

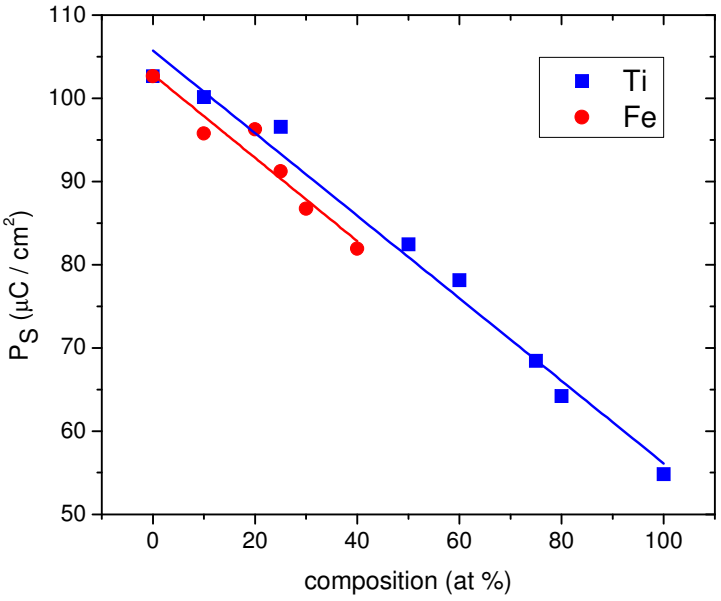

Fig. 4.41. Evolution of the spontaneous polarization with the composition for the Ti series (blue) and the Fe series (red). Dots mark the experimental points. Lines represent the linear fit of the experimental data.

The variation of the polarization seems to be linear and, interestingly, appears to have the same rate of change regardless of the substitution type as evidenced by the slopes of the two linear fits. The slopes are s = -0.496 for the Ti series and s = -0.500 for the Fe series.

IV.5. Raman spectroscopy measurements

X-ray diffraction (XRD) [89] and Raman spectroscopy [90-97] have been used for stress analysis of ferroelectric materials. Raman spectroscopy is complementary to XRD methods as it is a local probe and is sensitive to even subtle changes of symmetry. Moreover, ferroelectricity and thus Raman modes are strongly influenced by mechanical deformation of the sample resulting, for example, from hydrostatic pressure or stress [91, 92, 98-101].

Both $PbVO_3$ and $PbTiO_3$ adopt a tetragonal symmetry (space group P4mm or C^1_{4v}) with one formula per unit cell [31]. Both undergo a tetragonal to cubic phase transition. The transition of $PbTiO_3$ occurs at 490° C but the (T-C) transition of $PbVO_3$ only takes place under high pressure conditions where investigations are harder to perform.

Therefore the discussion's starting point will be the cubic structure of $PbTiO_3$. There are 12 vibration modes for the cubic phase which belong to the irreducible representation $3T_{1u} + T_{2u}$. The T_{1u} modes are only infrared (IR) active and the T_{2u} is a silent mode neither Raman nor IR active therefore no Raman signal should be obtained for the cubic phase. On the tetragonal phase, each T_{1u} mode splits and produces an A_1 and an E mode (for a total of $3A_1 + 3E$ modes) and the T_{2u} mode splits into B_1 + E modes. The A_1 and E modes are infrared and Raman active and the corresponding phonons are polarized in the z-direction or in the x-y plane, respectively. The B1 mode is only Raman active [102].

The Raman tensors are presented below, for each mode, and the direction of polarization is indicated in parentheses.

$$A_1(z) = \begin{bmatrix} a & \cdot & \cdot \\ \cdot & a & \cdot \\ \cdot & \cdot & b \end{bmatrix} \quad B_1 = \begin{bmatrix} c & \cdot & \cdot \\ \cdot & -c & \cdot \\ \cdot & \cdot & \cdot \end{bmatrix} \quad E(x) = \begin{bmatrix} \cdot & \cdot & -e \\ \cdot & \cdot & \cdot \\ -e & \cdot & \cdot \end{bmatrix} \quad E(y) = \begin{bmatrix} \cdot & \cdot & \cdot \\ \cdot & \cdot & e \\ \cdot & e & \cdot \end{bmatrix}$$

Due to long-range electrostatic forces, all A1 and E modes split into transverse (TO) and longitudinal (LO) components. Depending on the phonon propagation direction (x, y or z), only pure TO or LO can be observed in Raman spectra, as presented in table 4.16.

Table 4.16. Assignment of TO and LO modes according to the phonon propagation direction

Propagation direction	Phonon assignment		
	E(x)	E(y)	$A_1(z)$
x	LO	TO	TO
y	TO	LO	TO
z	TO	TO	LO

Raman spectra were collected for the same 4 representative samples, $PbVO_3$, PVT_25, PVF_25 and PVF_40 at RT using a laser radiation with a wavelength of 633 nm. The peaks of Raman spectra were attributed to vibration modes by comparing the spectra obtained by us to spectra reported in literature for $PbTiO_3$ [35, 103-105].

$PbVO_3$ and $PbTiO_3$ are isostructural and the Raman spectra they present are similar so $PbTiO_3$ is a good model for the interpretation of the Raman spectra of $PbVO_3$.

Figure 4.42 shows the Raman spectra obtained by measurements in different regions of the same sample $PbVO_3$. The striking feature for these spectra (and for spectra of the other 3 samples) is the change of some peaks intensities and the shift of peak positions depending on the regions from which data was collected. A reasonable explanation of this behaviour is the presence of local inhomogeneities and of the strain. Nevertheless the spectra are similar and the identification of (most of) the vibration modes is possible.

More probable, responsible for the presence of supplementary peaks in the samples is the presence of small quantities of impurities which are easily detected by the Raman spectroscopy.

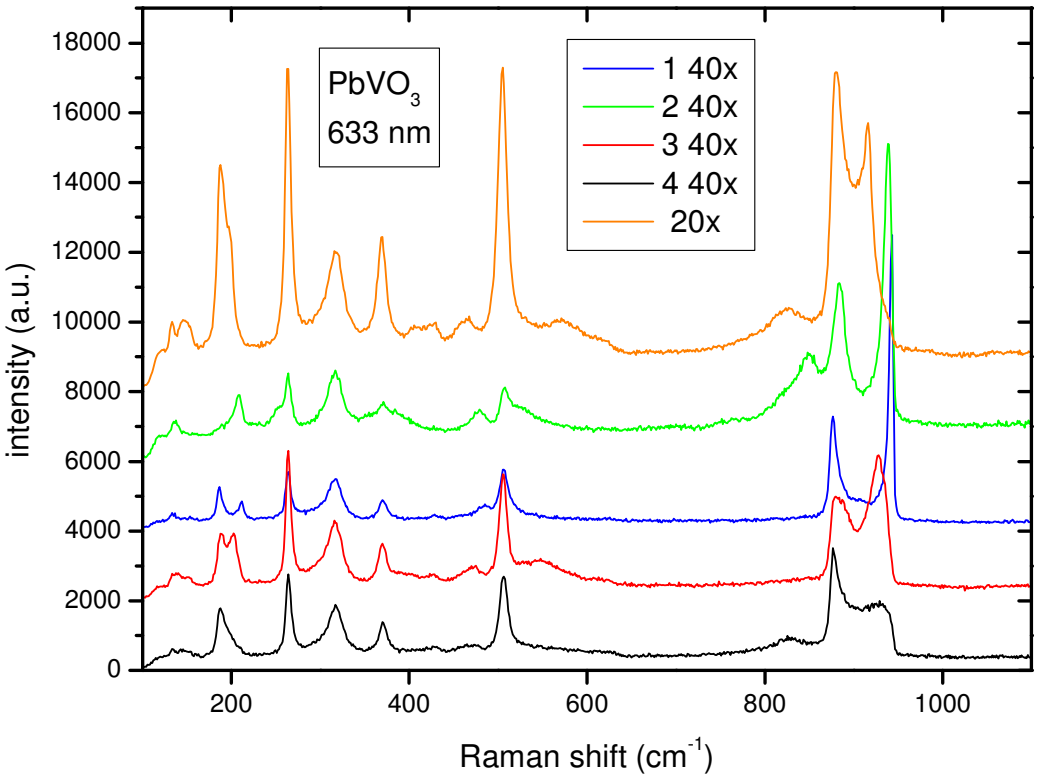

Fig. 4.42. Raman spectra for $PbVO_3$. The data was collected using a laser wavelength of 633 nm. Two objectives were used of 40X respectively 20X. The laser power was set a 5% and the integration time was 10 seconds. 9 integrations were made.

A representative Raman spectrum of PVO was selected in figure 4.43. The Raman peaks were attributed to vibration modes according to the rules discussed above and data available in literature. There are 3 regions on the spectra associated with the following vibrations of the cations of the $PbVO_3$ unit cell:

- Region I including peaks at low wavenumbers, up to 220 cm^{-1} associated with the vibrations of the Pb-O bonds. These peaks appear at approximately 147 188 and 200 cm^{-1}
- Region II, with peaks between 220 and 550 cm^{-1} attributed to the V-O2-V bending motion. These peaks appear at 318, 370 and 506 cm^{-1}
- Region III made of peaks at high wavenumbers (in the range 830 to 930 cm^{-1}) attributed to the V-O1 stretching with peaks appearing at 880 and 917 cm^{-1}

The spectrum is dominated by the peaks attributed of the V-O1 vibration of the strong short vanadyl bond. The small peaks marked with star are not identified.

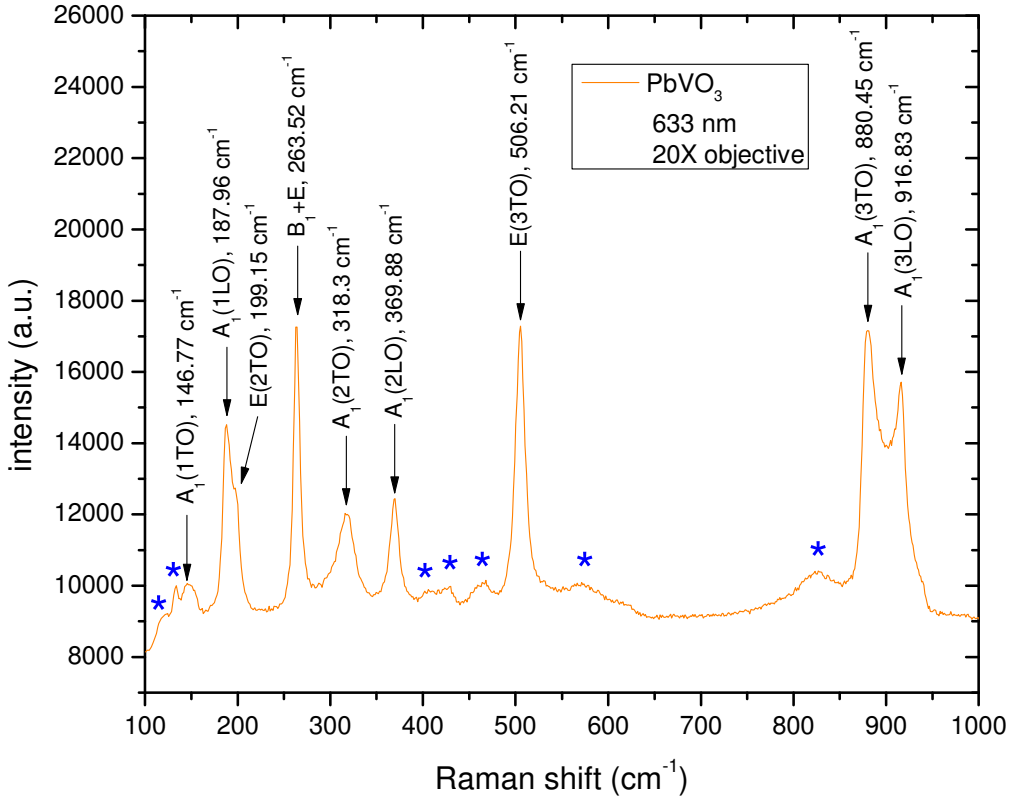

Fig. 4.43. Vibration modes for $PbVO_3$. The peaks marked with star are not identified. The data was collected using the 20X objective. The laser power was set a 5% and the integration time was 10 seconds. 9 integrations were made.

Figure 4.44 shows the vibration mode assignment for data collected for the PVT_25 sample. The spectra for PVT_25 and $PbVO_3$ are similarly, however the spectra for the PVF_25 sample are characterized by broad overlapping peaks. The peaks from the spectrum of PVT_25 can be related to the peaks of the parent compound, $PbVO_3$ and can be organized on the same 3 regions.

- Region I, from 100 to 230 cm^{-1}, where peak positions appear at 143 and 183 cm^{-1}.
- Region II between 230 and 520 cm^{-1}, where peak positions appear approximately at 270, 358, 458 and 508 cm^{-1}.
- Region III above 520 cm^{-1}, where peak positions appear approximately at 634, 804, 874 and 914 cm^{-1}.

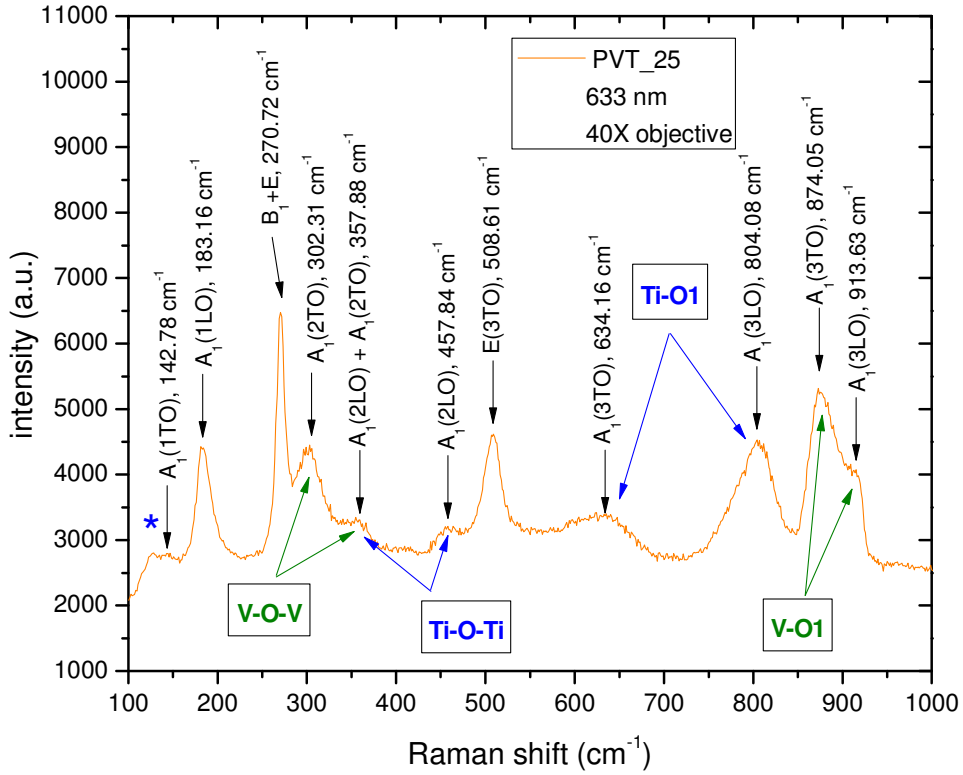

Fig. 4.44. Raman vibration modes for PVT_25. The peaks marked with star are not identified. The data was collected using the 40X objective. Laser power was set at 5% and the integration time was 10s. 9 integrations were made.

By comparing the Raman spectra for $PbTiO_3$ [105] and for $PbVO_3$ it appears that the A_1(3TO) and A_1(3LO) can be attributed separately to the Ti-O1 and to the V-O1 stretching vibrations. It might be inferred that the V-O1 bond is shorter and stronger than the Ti-O1 bond (where O1 denotes the apical oxygen) since it appears at higher wavenumbers. It can also be supposed that the sample contains local structural fluctuations caused by the fact that Ti^{4+} forms a weaker bond to the apical oxygen and hence a different coordination. This result is consistent with observations based on diffraction experiments.

It seems that the peaks from region II can also be separated according to the atom bonds that correspond to them. The peak observed at about 358 cm^{-1} appears to contain the contributions from the A_1(2TO) mode for the Ti-O-Ti bending oscillation and the A_1(2LO) mode for the V-O-V bending oscillation.

Figure 4.45 shows the vibration mode assignment for data collected for the PVF_25 sample. When Fe substituted V in $PbVO_3$, the effect of the substitution is

dramatically different from the effect of the Ti substitution. The spectra for the PVF_25 sample are different from the spectra of the Ti counterpart and the spectra of $PbVO_3$ as they present essentially only two very broad peaks. For PVF_25 it appears that there is a convolution of the A_1(3TO) and A_1(3LO) which generates a single broad peak cantered at about 842 cm^{-1}. This peak is associated to the B site cation – apical oxygen stretching oscillation. Similarly, the peak that appears at about 307 cm^{-1} seems to represent the convolution of the A_1(2TO) and A_1(2LO), attributed to the O–(B site cation)–O bending oscillations. The large width of the peaks at 842 and 307 cm^{-1} could be explained by the fact that the sample contains 3 different cations at the same crystallographic place (V^{4+}, V^{5+}, Fe^{3+}), each cation forming a different bond with the oxygen anions from the surrounding pyramid and each bonding is responsible for the development of a characteristic peak located at a slightly different wavenumber. Therefore what is observed is the convolution of these peaks. The peaks marked with star are not identified.

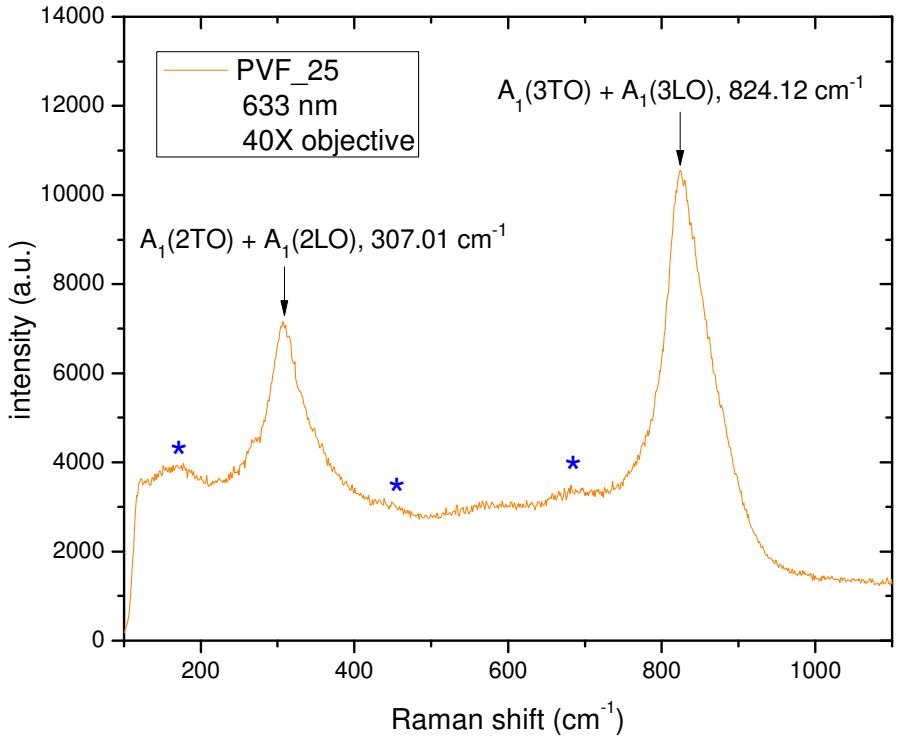

Fig. 4.45. Raman vibration modes for PVT_25. The data was collected using the 40X objective. Laser power was set at 5% and the integration time was 10s. 9 integrations were made.

Figure 4.46 shows the Raman spectra for the PVF_40 sample. The response of this sample is similar to the one of PVF_25, the other Fe substitution sample. The spectra for PVF_40 present (again) two broad peaks at 305 and 817 cm^{-1}.The intensity of peaks marked with star increases comparatively with the some peaks of sample PVF_25, suggesting the increase of the amount for impurity phases (see M(H) results).

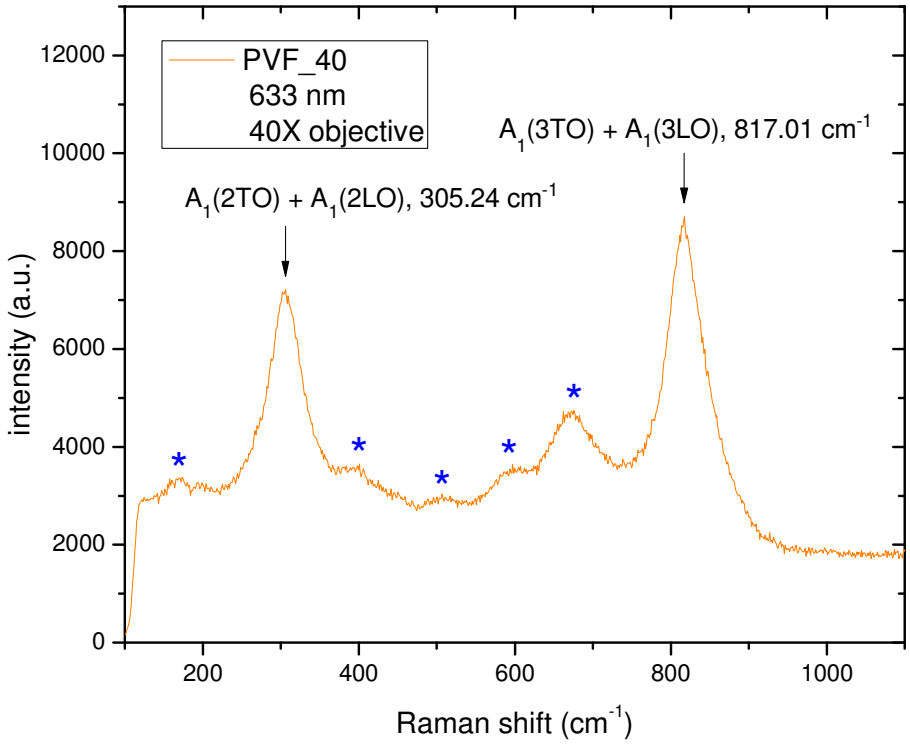

Fig. 4.46. Raman vibration modes for PVT_25. The data was collected using the 40X objective. Laser power was set at 5% and the integration time was 10s. 9 integrations were made. The peaks marked with star are not identified.

More information can be obtained by comparing the spectra of the four samples. This is shown on figure 4.47.

It can be observed that the most active vibrations are those that appear at high wavenumbers respectively A_1(3TO) and A_1(3LO) and belong to the B site cation - apical oxygen stretching. Their evolution is marked by line (1). Line (2) marks the evolution of the A_1(2TO) and by extension A_1(2LO) modes, associated to the bending of the O-B cation-O bond.

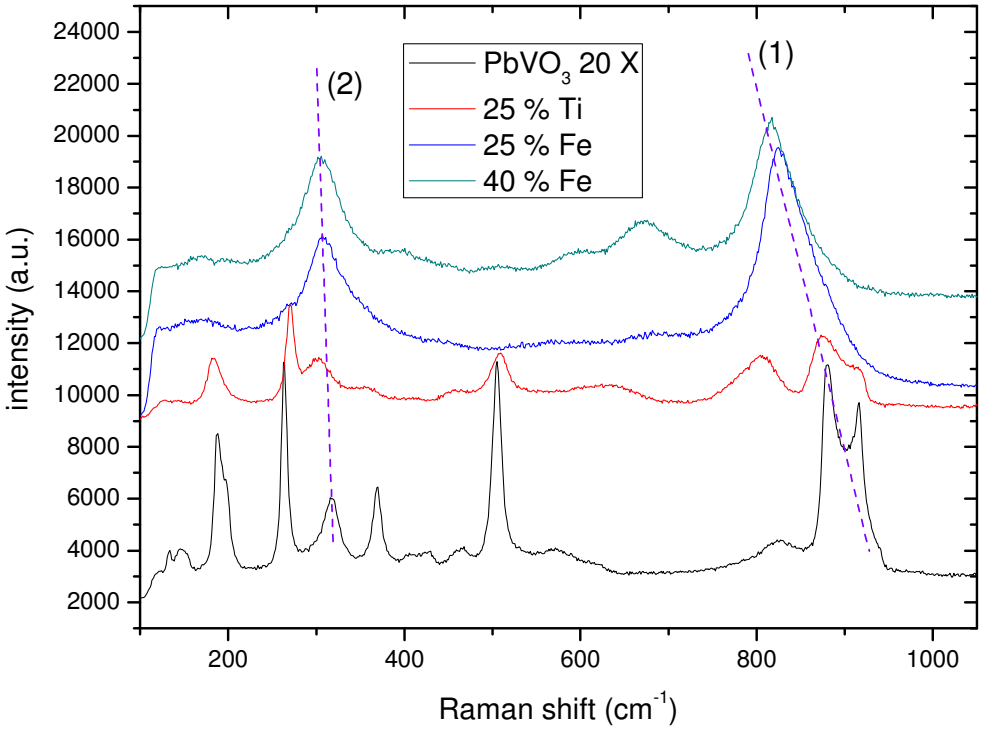

Fig. 4.47. Superposition of the Raman spectra for all 4 samples (see recording conditions above). Two lines are plotted for eye guidance and to indicate the evolution of the vibration modes considered.

Two main effects are visible. The first effect is the widening and coalescence of peaks, which was described earlier.

The second effect observed is the displacement of the peak position, more evident for line (1). The peaks at high wavenumbers (about 800 cm^{-1}) are displaced towards lower wavenumbers as the substitution degree increases. This suggests the weakening of the average B site cation - apical oxygen bond and is clearly observed between the samples containing 25% Fe and 40% Fe. This consequence is consistent with results obtained from XRD / NPD experiments.

Chapter V. Magnetic and dielectric properties of $PbV_{1-x}M_xO_3$ (where M = Fe, Ti) samples

Up to now we have discussed the structural properties of $PbVO_3$ and the substitution samples. We will now turn our attention to the physical (magnetic and dielectric) properties of the respective samples. The first part will discuss the magnetic behaviour while the second part will be centred on the dielectric properties.

It is very important to establish the type of magnetic interactions presented by a material that is a potential multiferroic. For $PbVO_3$ this subject is of particular interest, considering the complex magnetic properties it displays and the often contradicting results obtained between magnetic (and magnetic related) measurements and theoretic predictions.

V.1. The influence of vanadium partial atomic substitution with Fe and Ti on magnetic susceptibility of $PbVO_3$

The magnetic properties of the $PbV_{1-x}M_xO_3$ samples were investigated by means of dc susceptibility, isothermal magnetization, ac susceptibility and neutron powder diffraction. Susceptibility measurements were performed on a Quantum Design MPMS SQUID magnetometer at temperatures down to 2 K and filed intensities up to 5 T. A SQUID-VSM magnetometer was also used for measurements conducted at fields up to 7 T. Neutron diffraction experiments were performed at the D1B diffractometer of the ILL. Details about the diffraction measurements are provided at the chapter IV.

V.1.1. Magnetic properties of $PbVO_3$

In $PbVO_3$, the valence of the vanadium cation is 4+ with a $3d^1$ electronic structure and a spin of ½. The magnetic susceptibility in function of temperature for $PbVO_3$ was measured between 2 K and 350 K. The $\chi(T)$ graph for $PbVO_3$ is shown in figure 5.1. The general shape of the curve is similar to what has been reported in literature.

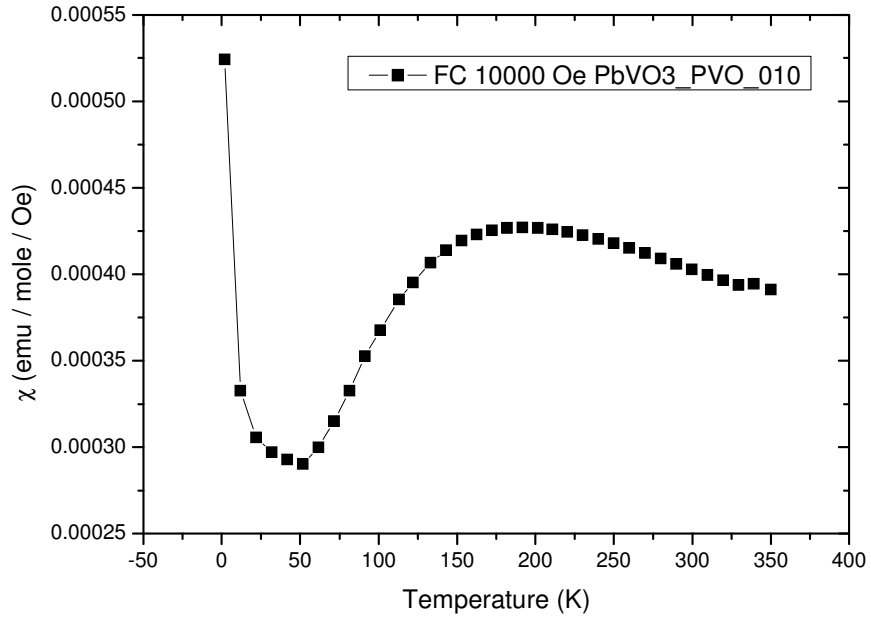

Fig. 5.1. $\chi(T)$ for $PbVO_3$. The measurement was performed by cooling the sample in a 1T field. The diamagnetic component of the film was subtracted. This sample is PVO_010.

The value of the susceptibility is very small, close to the detection limit of the SQUID. The diamagnetic signal given by the sample containing film has almost the same magnitude as the signal of the sample but opposite sign therefore this diamagnetic contribution had to be removed. This was done by measuring just the empty film (containing no sample) in the same conditions in which the sample was to be measured. The measurement on the film alone was then corrected to the mass of the film used to wrap the sample and the diamagnetic film contribution was removed by means of point by point subtraction. This procedure was conducted for all the

samples which presented a weak signal, namely for $PbVO_3$ and the samples from the Ti series.

The inverse susceptibility vs. T for $PbVO_3$ (figure 5.2) presents a linear region at temperatures higher than 240 K. This region can be exploited for a fit attempt with a Curie-Weiss law. The fit was performed between 250 K and 300 K, taking into account a diamagnetic component and it returned a negative θ temperature of -1144(1) K which indicates dominant antiferromagnetic interactions.

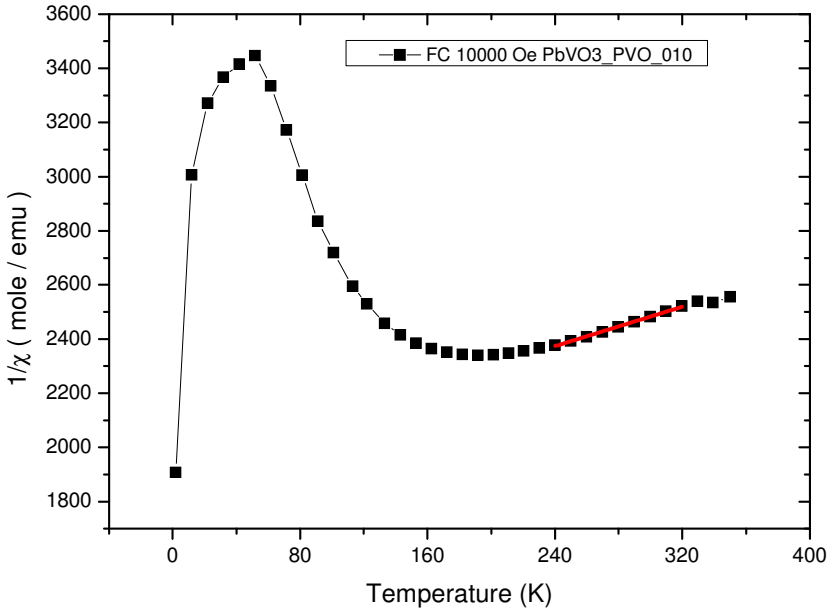

Fig. 5.2. 1/χ(T) plot for $PbVO_3$ (PVO_010).

The χ(T) graphs depend on whether the sample is cooled in the absence an external magnetic field (zero field cooling, ZFC) or in the presence of an external magnetic field (FC). The difference between the ZFC and FC measurements is seen at temperatures lower than 43K. The graphs of the two measurements are shown in figure 5.3. The same type of behaviour, with the splitting of the ZFC and FC curves is reported in literature [34, 37]. This might suggest that the difference is intrinsic to $PbVO_3$ but it could also be the effect of a magnetic impurity, not seen by XRD.

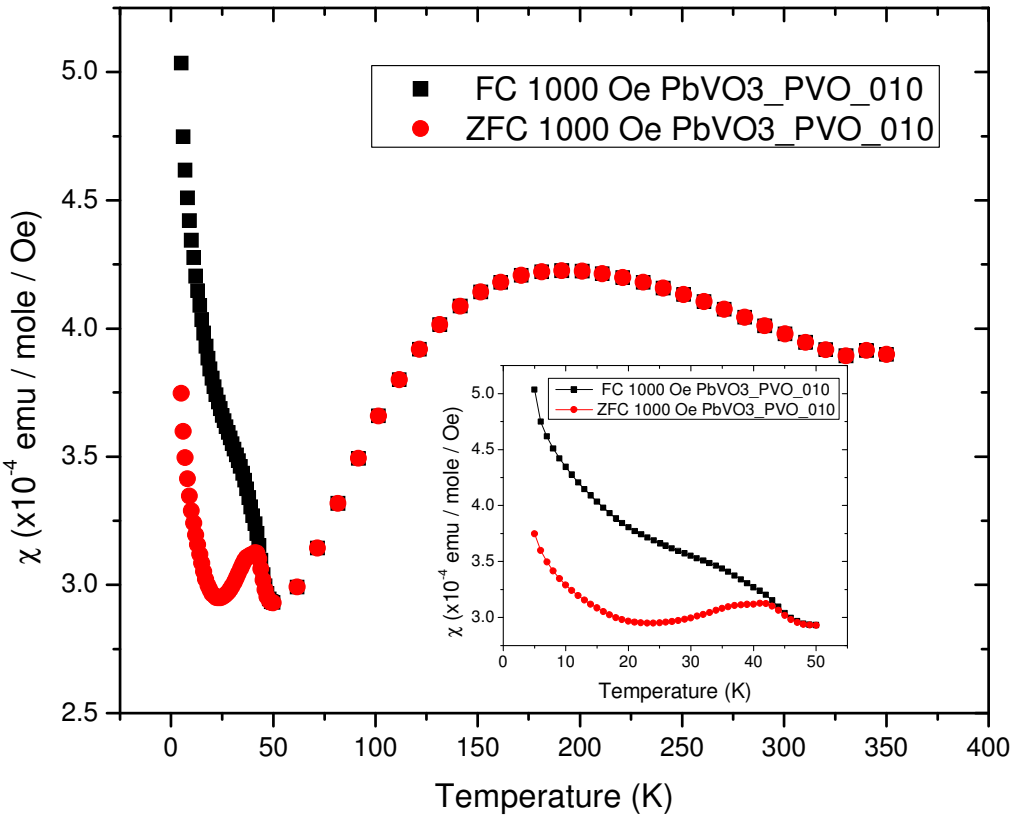

Fig. 5.3. Difference between ZFC and FC measurements for $PbVO_3$. The insert is the low temperature region of the $\chi(T)$ measurements.

Tsirlin [34] reports that the difference appears at about 50 K and is followed by two small humps at about 43 K. Oka [37] reports a rise in the susceptibility at 50 K followed by a peak at 40 K and the separation of the ZFC-FC below 40 K. Oka [37] also mentions the fact that these anomalies are more pronounced on single crystal data.

The nature of the anomalies is still a matter of debate. Susceptibility data alone is not sufficient to conclude on whether the ZFC-FC difference marks a transition and is intrinsic to $PbVO_3$ or it is just the result of some impurities, namely trapped oxygen that undergoes condensation below 50 K.

Tsirlin [34] supposes that the ZFC - FC difference is extrinsic since it is not detected by other experimental methods such as by neutron diffraction or by measurements of the specific heat.

On the contrary, Oka [37] presumes that the difference is intrinsic and marks a transition to a 2D AFM system as determined from μSR measurements. The

temperature at which this transition supposedly appears is determined by Oka at 42.5 K from μSR and 50 K from susceptibility measurements [37].

For the moment we are obliged to continue with the discussion about the magnetic properties of $PbVO_3$ failing to provide an immediate answer to the question of the low temperature anomalies.

The odd shape of the susceptibility curve for $PbVO_3$ (namely the broad peak at about 180 K) and the small value of the susceptibility were tentatively explained in literature by frustration in the magnetic structure or by 2D S=1/2 AFM models [34, 37]. Similar susceptibility curves, presenting a broad peak, are observed for another 2D compound containing V^{4+} cations, namely for $Pb_2V_5O_{12}$ [106].

Then the question about the formation of the 2D magnetic structure of $PbVO_3$ arises. The answer to this question might also be found in the formation of the vanadyl bond. The V cations are connected by a super-exchange interaction through the oxygen anion. The nature of this interaction is strongly dependent on the V-O distances. The V-O2 distance is 1.98 Å. The out of plane distance is affected by the formation of the vanadyl bond as it distorts the oxygen octahedron to the point at which the coordination of V is pyramidal. Thus the V-O1 distance is 1.64 Å to the apical oxygen but is elongated to 3.03 Å to the oxygen cation placed at the other corner of the distorted octahedron. This large distance prevents the formation of the super-exchange interaction perpendicular to the (a,b) plane therefore correlations of the V cations are confined to the 2D system.

On the other hand it has been shown by Uratani [43] that the 1d electron of V occupies the d_{xy} orbital which is parallel to the V-O2 layers this constituting a second reason for which the system is expected to be two dimensional.

Another possible explanation for the low value of the magnetic susceptibility is that the 1d electron of V^{4+} is taken on the formation of the vanadyl bond therefore the magnetic moment it posses becomes unavailable.

We considered two models that describe the 2D magnetism of $PbVO_3$. These two S=1/2 models are the Heisenberg square lattice model (SQL) and the frustrated square lattice model (FSL). SQL assumes the formation of a long range 2D antiferromagnetic lattice. The magnetic susceptibility for this case is described by the following equation [37]:

$$\chi(T) = \frac{Ng^2{\mu_B}^2}{4k_BT}\left[1 + \left(\frac{J}{k_BT}\right) + \frac{1}{2}\left(\frac{J}{k_BT}\right)^2 + \frac{1}{6}\left(\frac{J}{k_BT}\right)^3 + \frac{1}{64}\left(\frac{J}{k_BT}\right)^4\right]^{-1} + \chi_0$$

where J represents the exchange integral.

The FSL model considers the formation of a frustrated 2D antiferromagnetic structure. It takes into account the interactions of a magnetic moment with the nearest neighbours (NN) and also with the next nearest neighbours (NNN). The product between the temperature and the susceptibility for this case is described by the following equation [107]:

$$T\chi = \sum_n \beta_1^n \sum_m c_{m,n} x^m$$

where $\beta_1 = J_1/K_BT$ and J_1 represents the exchange integral between NN moments. The x term is equal to J_2 / J_1 and represents the ratio of the exchange integrals between NN and NNN, with J_2 describing the NNN interactions. The $c_{m,n}$ term represent a sequence of coefficients, developed up to the order 9.

Results for the values of the exchange integrals obtained by fitting the susceptibility data of $PbVO_3$ with both models are given on the next section.

Figure 5.4 shows the SQL and FSL fits for the $\chi(T)$ data of $PbVO_3$. Both fits were performed on the 200 K – 300 K temperature range, although the predicted susceptibility is shown for a wider range. A diamagnetic contribution was refined for all the fits.

The fits were performed with the help of Dr. Claire Colin.

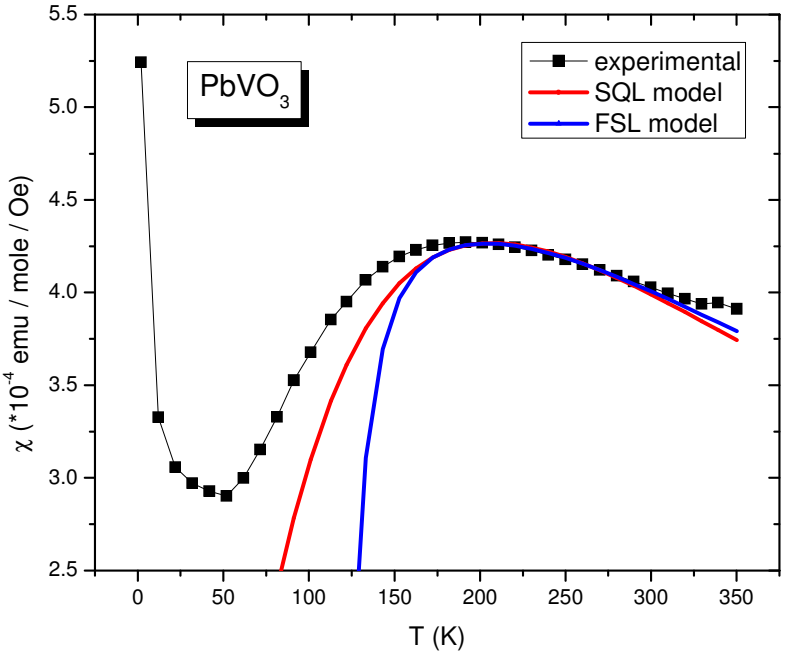

Fig. 5.4. SQL and FSL fits for the χ(T) data of $PbVO_3$. Black points are experimental data. The SQL fit is shown by the red line and FSL fit is the blue line.

The magnetization in function of field measurements, M(H), (figure 5.5) show a linear dependence on the field at 300 and 100K whereas a small non linearity is present at 5K.

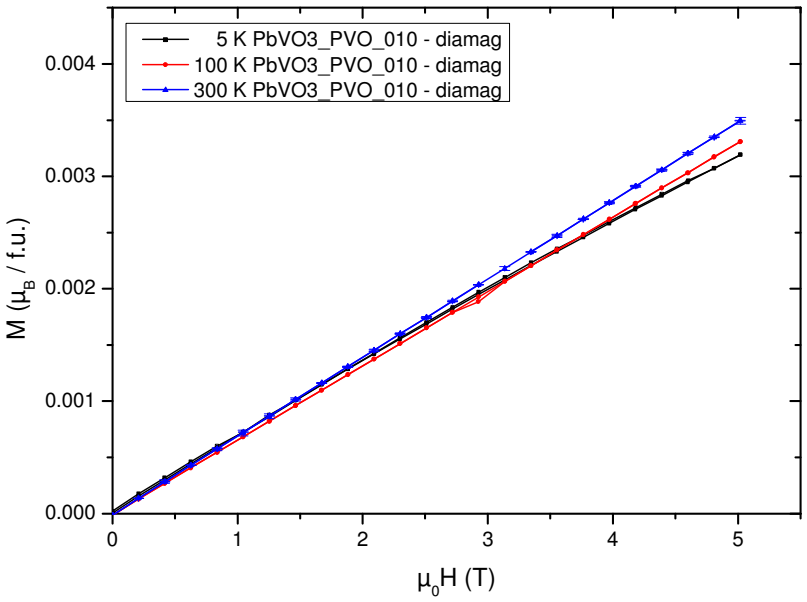

Fig. 5.5. M(H) for $PbVO_3$ (PVO_010) at 5 K, 100 K and 300 K.

V.1.2. Magnetic properties of the $PbV_{1-x}M_xO_3$ substitution compounds (M = Ti, Fe)

In order to provide further explanations on the magnetism of $PbVO_3$, the effects of partial substitution of V by Ti and by Fe on the magnetic properties of $PbVO_3$ have been investigated.

Several explanations for the weak magnetic signal observed despite the presence of the V^{4+} cations have been proposed. The formation of strongly covalent vanadyl bonds forming a 2D array in the (a,b) plane could lead to a 2D behaviour with a possibly reduced magnetic moment with the d^1 electron of vanadium engaged in covalent bonding. Replacing V by Ti or Fe should then reduce this 2D character and might allow 3D magnetic ordering to appear. Of course magnetic Fe cations would probably be more efficient for that purpose. In the hypothesis of frustration as the origin of the weak magnetic signal, disorder induced by substitution could release the frustration and lead to magnetic ordering through the "order by disorder" phenomenon.

The results of our magnetic measurements on the Ti- and Fe-substitution series are discussed below. There are specificities to both series so the discussion will vary accordingly, however, the main aspects followed are the same, namely the $\chi(T)$ of a representative sample for the series, $1/\chi$ for the samples of each series, calculations of magnetic moments, presence or absence of ZFC-FC differences and evolution of M(H).

a) Ti substitution series

For the Ti substitution it was observed that the system appears to take a paramagnetic behaviour. This effect is observed for all the samples of the Ti series (for all the tested compositions). To illustrate the effect of the Ti substitution, the magnetic susceptibility for the $PbVO_3$ sample substituted with 50 % Ti ($PbV_{0.5}Ti_{0.5}O_3$) is shown in figure 5.6.

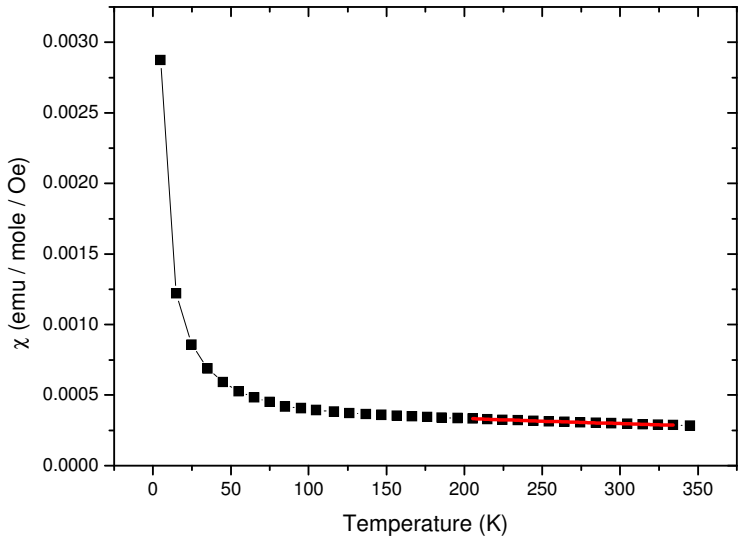

Fig 5.6. χ(T) for $PbV_{0.5}Ti_{0.5}O_3$ (PVT_002). The red line represents the fit of the experimental data with a Curie-Weiss law. The fit was made without taking into account the supplementary diamagnetic contribution from the sample itself (the contribution from the film was removed before the data processing).

The Curie-Weiss law fits the data very well in the region of high temperatures (from 200 K to 350 K) but the fit becomes less good for the entire data range. Also, the plot of the inverse susceptibility (figure 5.7) does not pass through zero as it is expected for a purely paramagnetic sample.

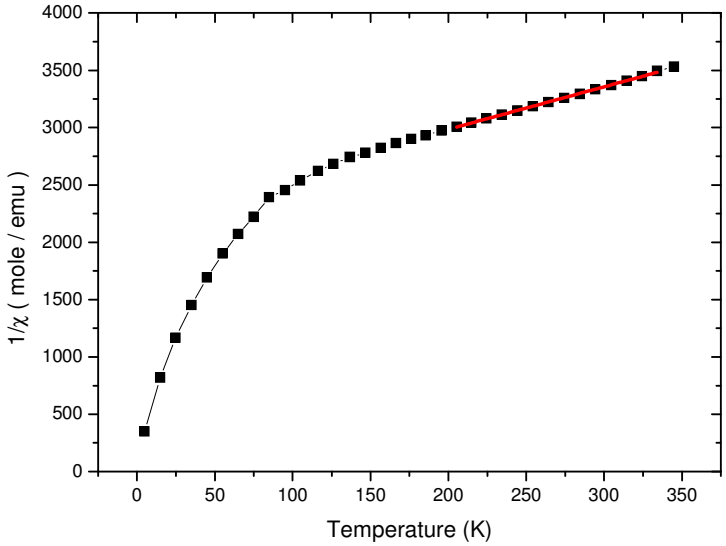

Fig. 5.7. 1/χ plot for $PbV_{0.5}Ti_{0.5}O_3$ (PVT_002).

There are two possible explanations for the nonlinearity of the $1/\chi$ plot. Either the sample contains magnetic impurities or there are nevertheless some interactions between the vanadium cations that remain after the substitution.

It would appear that in the case of the Ti substitution the magnetism of $PbVO_3$ becomes progressively diluted as the V atoms are substituted by Ti. The dilution of the magnetic moments of V^{4+} gradually transforms the system from a 2D AFM material to a paramagnetic material. The sample with 10% Ti is interesting because it still presents the very broad peak in susceptibility of $PbVO_3$, centred at about 170 K, which marks the presence of 2D AFM correlations, but it also shows an increase of the susceptibility with the decreasing temperature, which defines a paramagnet. The 10% Ti sample seems to be placed somewhere between the magnetic behaviour of $PbVO_3$ and the paramagnetism of the samples with higher degrees of substitution. Figure 5.8 shows the $\chi(T)$ for $PbVO_3$, the 10% Ti sample and the 50% Ti sample.

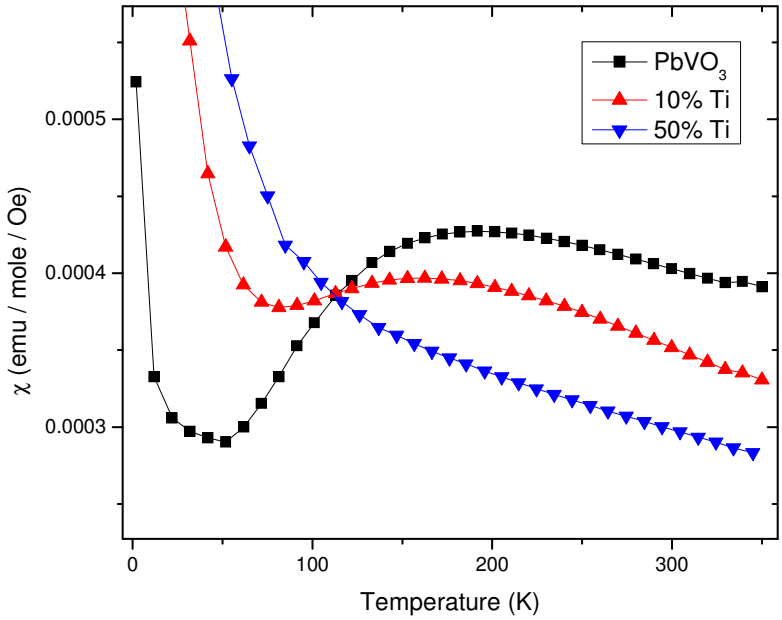

Fig. 5.8. $\chi(T)$ for $PbVO_3$ sample (PVO_010) and for the samples containing the 10% Ti (PVT_007) and 50% Ti (PVT_002) substitutions. A broad peak can be observed on the susceptibility of the 10% Ti sample, while the same peak is virtually gone for the 50% Ti sample.

Since the 10% Ti sample ($PbV_{0.9}Ti_{0.1}O_3$) retains some of the properties of $PbVO_3$ the two models used for $PbVO_3$ (SQL and FSL) were employed in order to fit

the χ(T). The SQL fits for the 10% Ti sample on two data ranges are shown below (figure 5.9). The fits were performed on the same manner for $PbV_{0.9}Ti_{0.1}O_3$ and $PbVO_3$ (on the 200–300 K range considering a diamagnetic component).

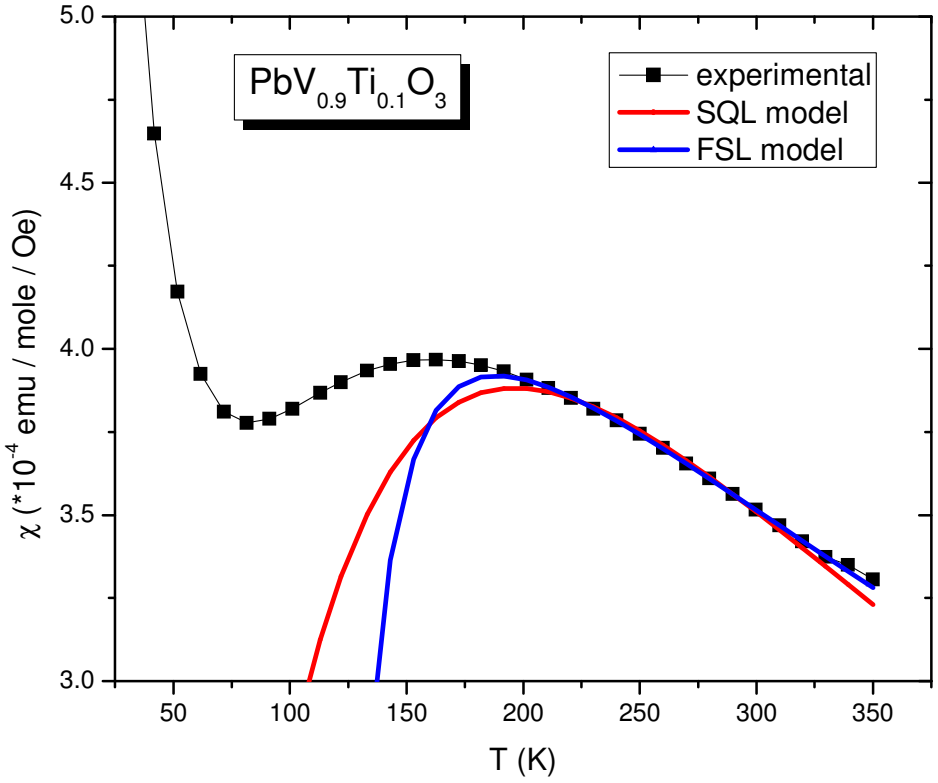

Fig. 5.9. SQL and FSL fits on the 10% Ti sample (PVT_007). The experimental data are the black dots. The low temperature region has been omitted to highlight the fit range. The SQL fit is red and the FSL fit is blue.

The results of the SQL and FSL fits for $PbVO_3$ and $PbV_{0.9}Ti_{0.1}O_3$ are listed below (table 5.1). The values for exchange integrals obtained from the two models (and x for the FSL model) as well as the diamagnetic component and the residue of the fit are provided. The residue is calculated as the square of the difference between the experimental and the predicted values, summed over the entire fit range.

Table 5.1 Calculation of J from the SQL and FSL models from $PbVO_3$ (PVO_010) and $PbV_{0.9}Ti_{0.1}O_3$ (PVT_007)

sample/model	SQL			FSL			
	J (K)	χ_0	residue	J (K)	x	χ_0	residue
$PbVO_3$	218	$-8*10^{-5}$	$3*10^{-11}$	216	$1.4*10^{-4}$	$-7*10^{-6}$	$1*10^{-11}$
10% Ti	207	$-1*10^{-4}$	$1*10^{-11}$	208	0.22	$-5*10^{-5}$	$4*10^{-13}$

The exchange interaction from both models decreases when Ti is added to the sample. The decrease of the exchange interaction suggests the dilution of the magnetic lattice, which is an expected result, considering that dilution of the moment carrying V^{4+} cations also triggers the reduction of the exchange interaction.

Both models appear to work reasonably well for both samples. However, the SQL model seems to describe the experimental data better for $PbVO_3$, thus indicating the absence of frustration. On the contrary the FSL model seem to give better results for the 10% Ti substituted sample, with $J_2/J_1 \approx 0.22$, indicating the presence of frustration within that sample. On the other hand the differences between the qualities of the fits are small and for the 10% Ti sample an almost equally good FSL fit can be obtained for J = 185 K and $J_2/J_1 \approx 1.5*10^{-4}$ which does not support the frustration theory.

For the other Ti substituted samples a similar effect (dilution of magnetic moments) is observed when the magnetic susceptibilities for samples with different substitution degrees are compared. As the concentration of Ti is increased the susceptibility of the samples decreases. Figure 5.10 shows the susceptibility for the following samples: $PbVO_3$, 10% Ti, 50% Ti, 80% Ti and $PbTiO_3$. For $PbTiO_3$ the susceptibility is expected to be zero since no cation in $PbTiO_3$ carries any magnetic moment. Indeed, the measured susceptibility is essentially zero. More precisely it is very small and negative (and almost constant in temperature) as it is produced by the diamagnetic contribution of the sample itself. The diamagnetic component of the film (sample holder) was subtracted. The 80% Ti sample has a particularity in that the weak, positive paramagnetic signal of the sample is neutralized at some point by the negative diamagnetic signal of the film. When that happens, the overall signal is zero

and the SQUID looses track of the sample and the measurement is corrupt. In an attempt to avoid this problem, the measurement is interrupted in the temperature range in which the two signals cancel out.

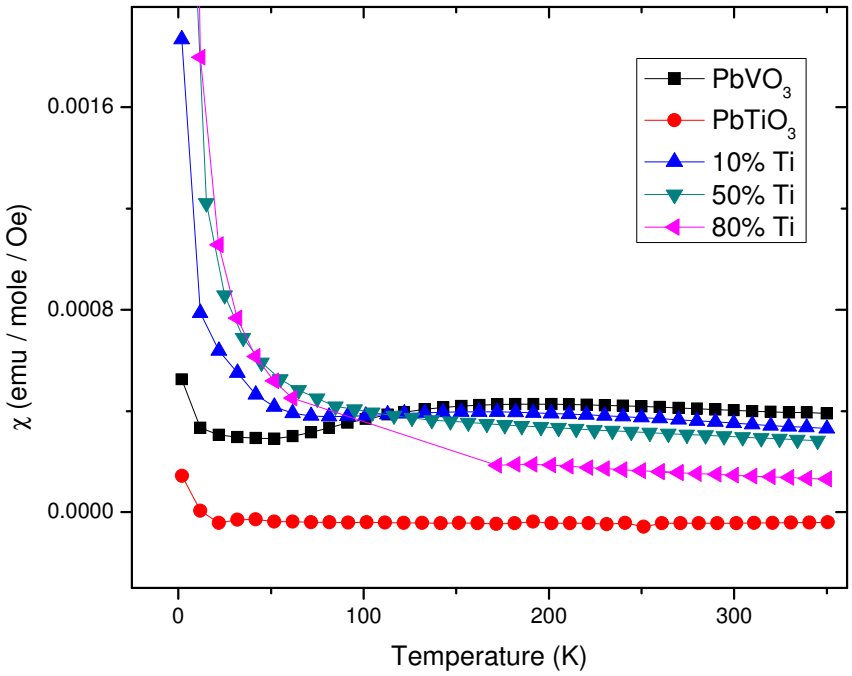

Fig. 5.10. χ(T) of the compound $Pb(V_{1-x}Ti_x)O_3$ for x = 0, 0.1, 0.5, 0.8 and 1. The sample labels are respectively PVO_010, PVT_007, PVT_002, PVT_005 and SPTO_001.

All the samples were measured in the same way (FC, 1T external field) and the signal was normalized for the sample quantity. It can be seen in the high temperature range (above 200 K) that the strength of the signal decreases as the content of Ti increases.

For all the samples in the Ti series the effective (overall) magnetic moment, μ_{eff}, was calculated from the Curie-Weiss law fit of the $1/\chi(T)$ data. The inverse susceptibility for the Ti samples, including $PbVO_3$, is shown in figure 5.11. When x increases, μ_{eff} decreases. The plot of the observed square effective moment for the Ti series is shown in figure 5.12. On the same graph the theoretic (or expected) square effective moment is also plotted. This magnetic moment was calculated assuming a moment of 1.73 μ_B for the V^{4+} cation and taking into account the chemical composition. Thus the overall moment was calculated as $\mu^2_{eff} = (1-x)\mu^2_V$. The overall moment is expressed in Bohr magneton / formula unit, μ_B / f.u.. The theoretic and

observed moments follow the same trend (decrease with Ti content), however, the values of the observed moment could be affected by weighing errors and/or calculation errors while performing the Curie-Weiss fit.

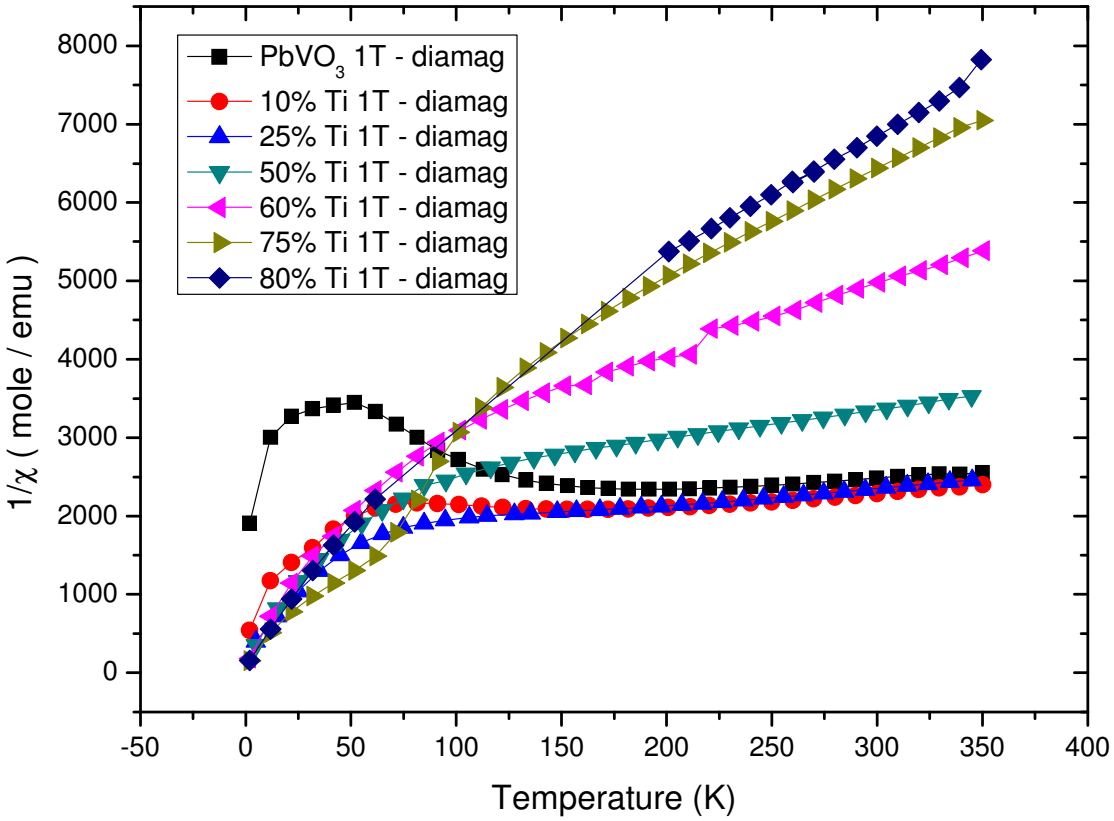

Fig. 5.11. 1/χ(T) for the $PbV_{1-x}Ti_xO_3$ compound for x = 0, 0.1, 0.25, 0.5, 0.6, 0.75 and 0.8. The samples are labelled with respect to x as PVO_010 (x=0), PVT_007 (x=0.1), PVT_001 (x=0.25), PVT_002 (x=0.5), PVT_004 (x=0.6), PVT_006 (x=0.75) and PVT_005 (x=0.8).

The values for the Curie constant, effective moment and θ temperature obtained from the linear fit of the 1/χ(T) for every sample containing a Ti substitution presented in table 5.2. The evolutions of the μ_{eff} and θ with the composition are shown in the subsequent figures (5.12 and 5.13).

Table 5.2. Values of the Curie constants, effective moments and Weiss temperatures for samples with the Ti substitution.

sample (% Ti)	Curie constant (emu*K/mole)	μ_{eff} (μ_B/f.u.)	θ (K)
0	0.5(1)	2.0(5)	-1144(1)
10	0.28(4)	1.50(9)	-518.0(9)
25	0.41(8)	1.82(9)	-685.8(4)
50	0.26(9)	1.46(9)	-609.1(9)
60	0.12(1)	0.98(1)	-273.7(4)
75	0.09(1)	0.85(1)	-232.0(6)
80	0.06(6)	0.73(1)	-155.5(4)

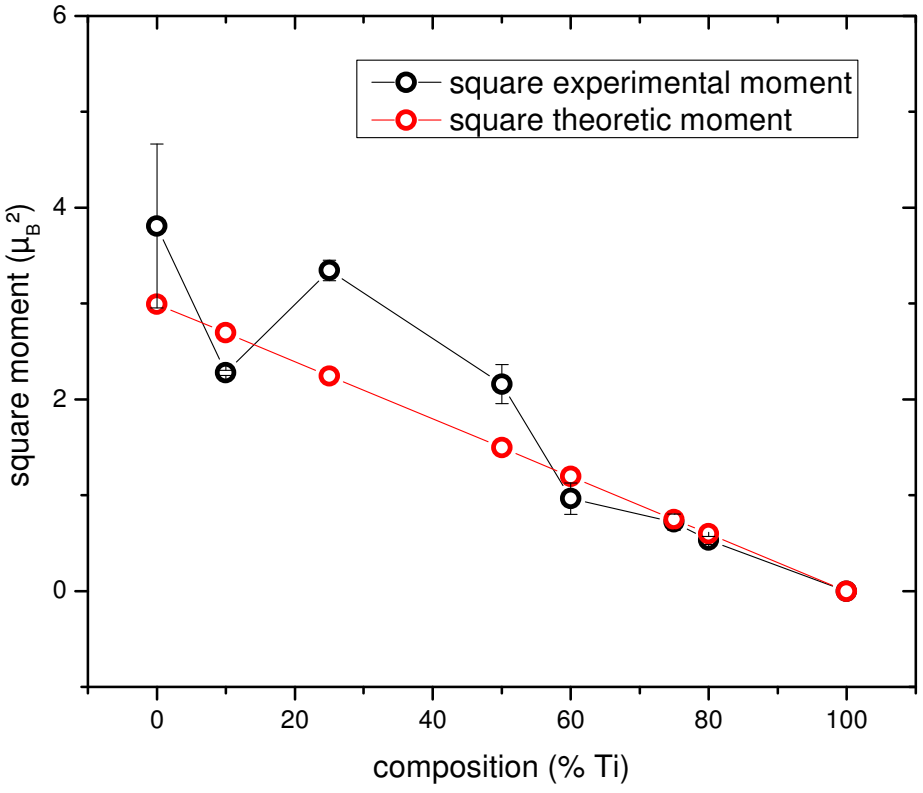

Fig. 5.12. Observed and calculated effective moments for the samples in the Ti series.

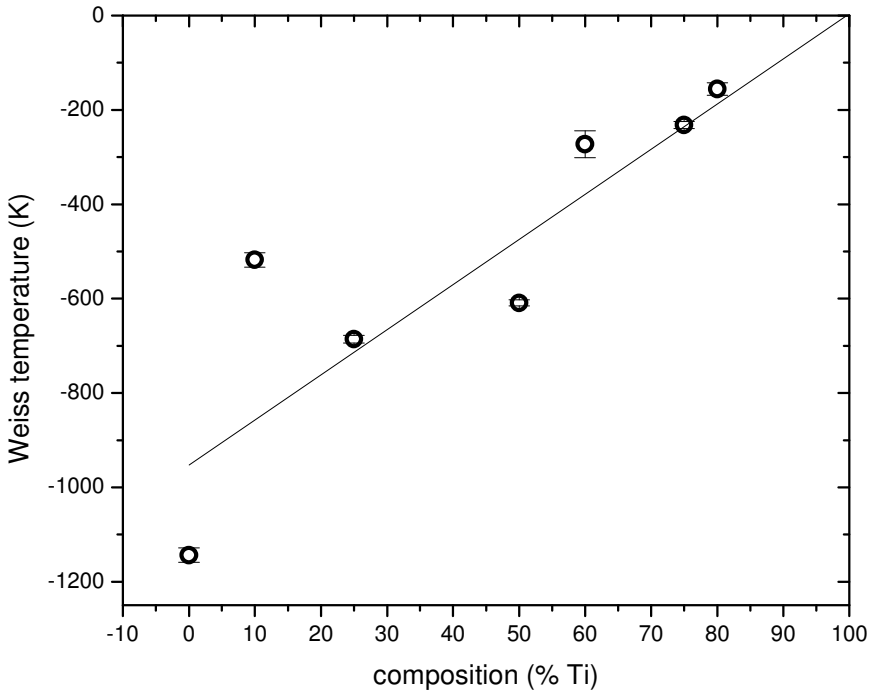

Fig. 5.13. Evolution of the Weiss temperature with the composition.

There is no difference between ZFC and FC graphs (figure 5.14) and the M(H) plot is linear at relatively high temperatures with only slightly deviation from linearity at 5 K (figure 5.15).

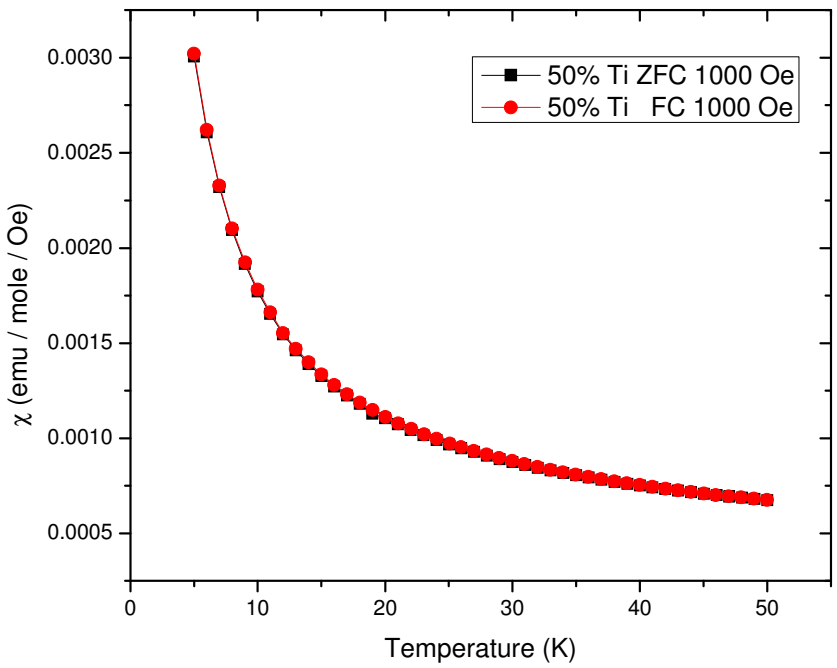

Fig. 5.14. ZFC – FC for $PbV_{0.5}Ti_{0.5}O_3$ in the low temperature domain.

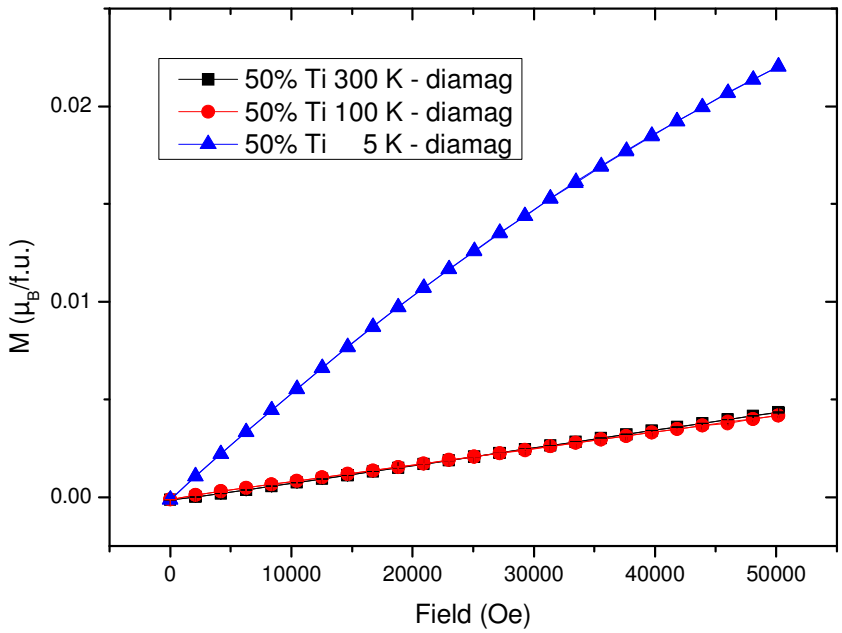

Fig. 5.15. M(H) for $PbV_{0.5}Ti_{0.5}O_3$ (PVT_002). Only a small deviation from linearity is observed at low temperatures.

The evolution of the effective moment shows the dilution of the magnetic cations which is explained by the lack of a magnetic moment of the substituting Ti^{4+}. The Weiss temperature presents a decrease in absolute value which marks the weakening of the antiferromagnetic interactions in the samples. An estimation of the exchange integral for $PbV_{0.9}Ti_{0.1}O_3$ again suggests the deterioration of the AFM interactions when Ti^{4+} replaces V^{4+} cations.

In a paramagnetic system, the magnetic moments on neighbouring atoms interact only weakly with each other and can be assumed to be independent. For the Ti series, the addition of Ti can be viewed as a dilution of the magnetic ions V4+: as Ti content is increased the number of magnetic moment decreases, at the same time the magnetic interaction between the magnetic moment decreases.

b) Fe substitution series

For the samples of the Fe series the same types of measurements were conducted. The first observed difference from the measurements on the Ti series is the increase of the signal strength. For samples in the Fe series, the diamagnetic component of the film (of the sample holder) is negligible and therefore it was no longer subtracted. Figure 5.16 shows susceptibility curve for $PbVO_3$, $PbV_{0.5}Ti_{0.5}O_3$, $PbTiO_3$ and the sample containing just 10% Fe ($PbV_{0.9}Fe_{0.1}O_3$).

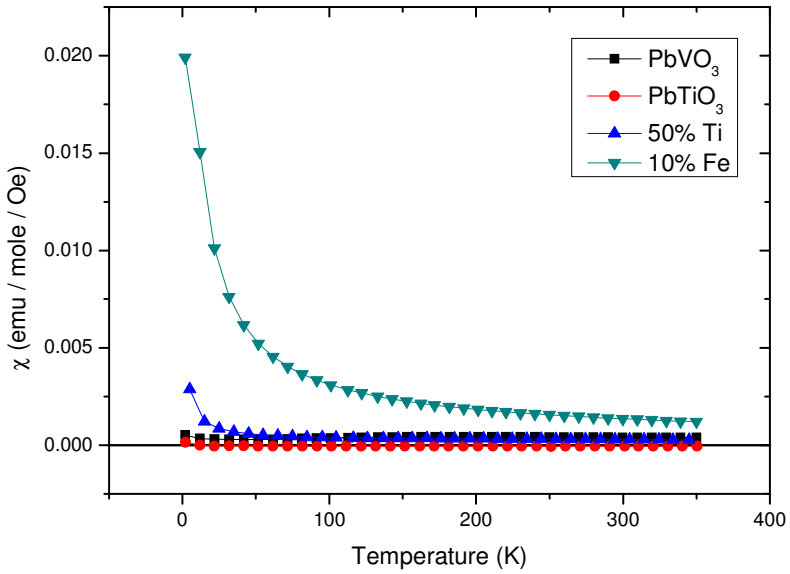

Fig. 5.16. χ(T) for $PbVO_3$ (PVO_010), $PbTiO_3$ (SPTO_001) and the substitution samples 50% Ti (PVT_002) and 10% Fe (PVF_002) respectively.

It can be observed that the signal of the Fe sample is much larger than the signal of the others. When plotted on a scale sufficiently large to observe the entire χ(T) graph of the 10% Fe sample, the susceptibility of the other samples appears to be zero. The susceptibility of the 10% Fe sample shown in figure 5.16 is measured by cooling the sample in a field of 1 T, that is, the same conditions of measurement were used for all the samples and the signal was corrected for the quantity of sample, therefore the difference in signal strength is the effect of the Fe substitution.

The FC susceptibility of $PbV_{0.9}Fe_{0.1}O_3$ (figure 5.17) is similar to the one of a paramagnetic material but the picture is more complicated.

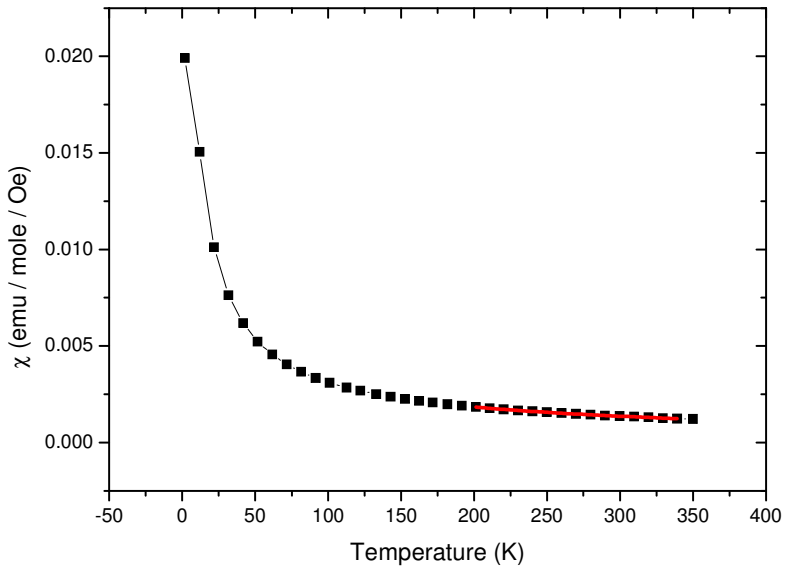

Fig. 5.17. χ(T) for 10% Fe sample (PVF_002). The red line represents the Curie-Weiss law fit.

The inverse of the susceptibility curve is not linear (figure 5.18) on the entire temperature range. The extension of the graph in the linear region (above 200 K) falls in the domain of negative temperatures, showing the presence of AFM interactions in the sample. This feature is seen in all the samples of the Fe series, regardless of their substitution degree. Figure 5.18 shows the inverse susceptibilities for all the single phase, tetragonal samples in which the V-Fe substitution is performed. The 50% Fe sample is also considered here even though it is not a single phase sample. The samples above 50% Fe substitution contain several secondary phases, therefore, the results of magnetization measurements for these samples are not reliable and will not be discussed here.

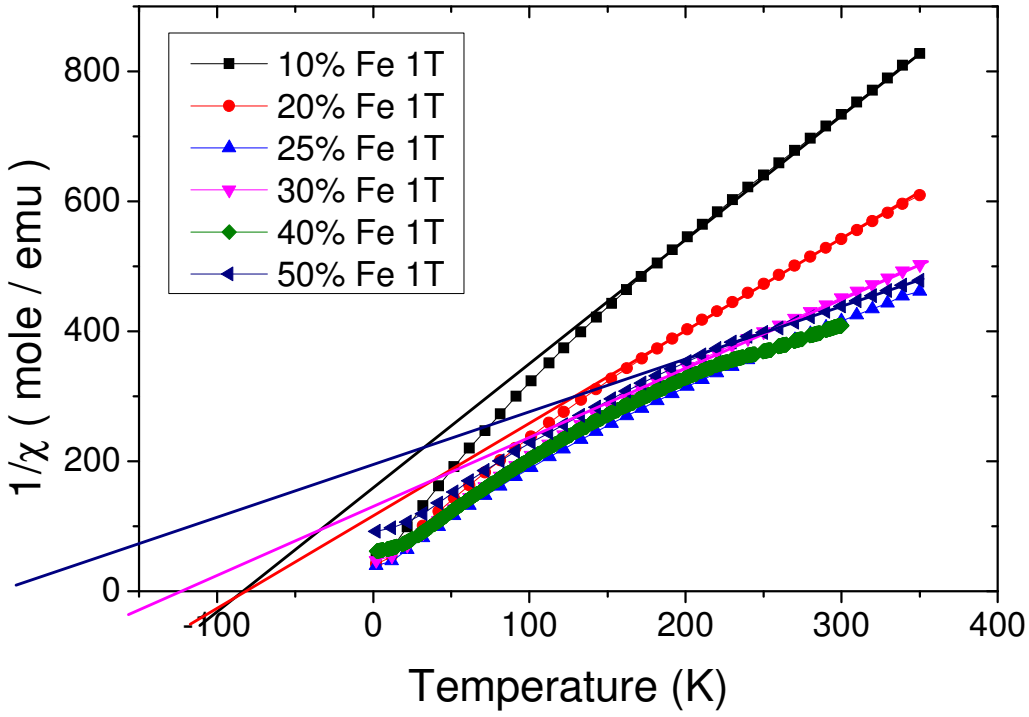

Fig. 5.18. 1/χ(T) for the $PbV_{1-x}Fe_xO_3$ compound for x = 0.1, 0.2, 0.25, 0.3, 0.4 and 0.5. The corresponding sample labels are PVF_002, PVF_007, PVF_001, PVF_004 and PVF_010. Lines extended from linear regions of the 1/χ graphs are traced and found to intersect the temperature axis in negative side, proving the existence of AFM interactions.

The Curie constant, effective magnetic moment and antiferromagnetic θ temperature are calculated from the Curie-Weiss fit of the linear region. Table 5.3 shows the values for the Curie constant, μ_{eff} and θ. All the refinements (fits with the Curie-Weiss model) were performed in the same manner. The temperature range was chosen between 200 K and 340 K because that region is the longest linear segment of the graph. No diamagnetic contribution was refined or subtracted for the systematic refinements as it was observed that the effect of the diamagnetic component on the measurements and on the values returned by the refinement is negligible. The χ(T) was refined using the equation:

$\chi = \chi_0 + c/(T-\theta)$

The refined parameters were c and θ. χ_0 was fixed to zero.

Conversely the $1/\chi$ plots were refined with a simple linear equation. The Curie constant and the θ temperature were thus extracted from the slope of the linear equation and respectively from the point at which $1/\chi = 0$.

Table 5.3. Curie constants, magnetic moments and Weiss temperatures for the Fe substitution samples.

sample (% Fe)	Curie constant (emu*K/mole)	μ_{eff} (μ_B/f.u.)	θ (K)
0	0.5(1)	2.0(5)	-1144(1)
10	0.52(7)	2.05(4)	-87.4(9)
20	0.71(8)	2.40(7)	-89.5(2)
25	1.00(2)	2.83(1)	-117.2(3)
30	0.95(1)	2.76(7)	-129.3(1)
40	1.22(1)	3.12(5)	-200.0(7)
50	1.21(5)	3.11(9)	-232.8(9)

Whatever the type of interactions between magnetic moments might exist in the samples at a sufficiently high temperature the system should be disordered by the thermal agitation. Under this assumption we attempted to measure the effective moment from the Curie-Weiss fit of the $1/\chi$ plots in the region above 200 K (the linear region) (see table above).

The evolution of μ_{eff} is shown in figures 5.19. The theoretic effective moment was found to approach the experimental values when it is calculated assuming the moments for the V^{4+} and for Fe^{3+} as $\mu_V = 1.73\ \mu_B$ and $\mu_{Fe} = 4.79\ \mu_B$ respectively and considering that each Fe^{3+} ion introduced in the sample replaces two V^{4+} ions. One V^{4+} ion is the ion replaced directly by Fe^{3+} and the other V^{4+} becomes oxidized to V^{5+} in order to maintain an average oxidation state of 4+ at the B site cation (see the XAS results). Thus, the effective moment is calculated by using:

$\mu^2_{eff} = (1-2x)*\mu^2_V + x*\mu^2_{Fe}$, where x is the iron content.

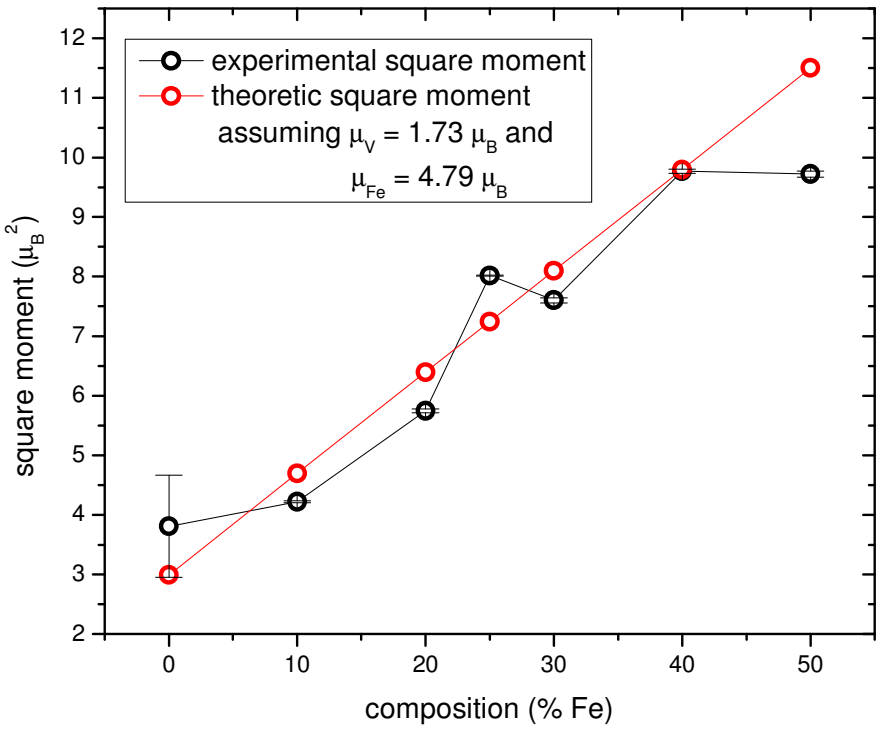

Fig. 5.19. Observed (black) and calculated (red) effective moment for Fe series.

The magnetic moment of the Fe^{3+} cation is expected to be μ_{Fe} = 5.92 μ_B assuming the relation for the spin only contribution $\mu_{eff} = g\sqrt{S(S+1)}$ for S = 5/2 and that the Fe^{3+} cation takes a high spin state. However, using this model the calculated (predicted) effective moment for the Fe series is larger than the observed moment. The better result is obtained assuming a magnetic moment of the Fe cation of only $\mu_{Fe} \approx 4.8\ \mu_B$ instead of the expected 5.92 μ_B. The reason for the discrepancy could reside in the fact that the Curie-Weiss fit was performed in a region that was not far enough from the transition temperature so the sample did not had a purely paramagnetic behaviour yet and some antiferromagnetic correlations of the Fe^{3+} moments were still present. The presence of these antiferromagnetic correlations could be responsible for the decrease of the magnetic moment of the Fe^{3+} cation.

Another possible explanation is that not all the Fe^{3+} cations from a sample have a high spin state and some Fe^{3+} by a low spin state with μ_{Fe} = 1.73 μ_B. The ionic radius of Fe^{3+} cations 6 fold coordinated having a low spin state is 0.55 Å which is close to the ionic radius of the V^{4+} cation (0.53 Å, 5 fold coordination). Even though the $PbV_{1-x}Fe_xO_3$ system does not form an oxygen octahedron, the oxygen pyramid is

elongated and tends to form an octahedron, as it was observed from diffraction experiments (chapter IV).

Figure 5.20 shows the variation of the θ with Fe content.

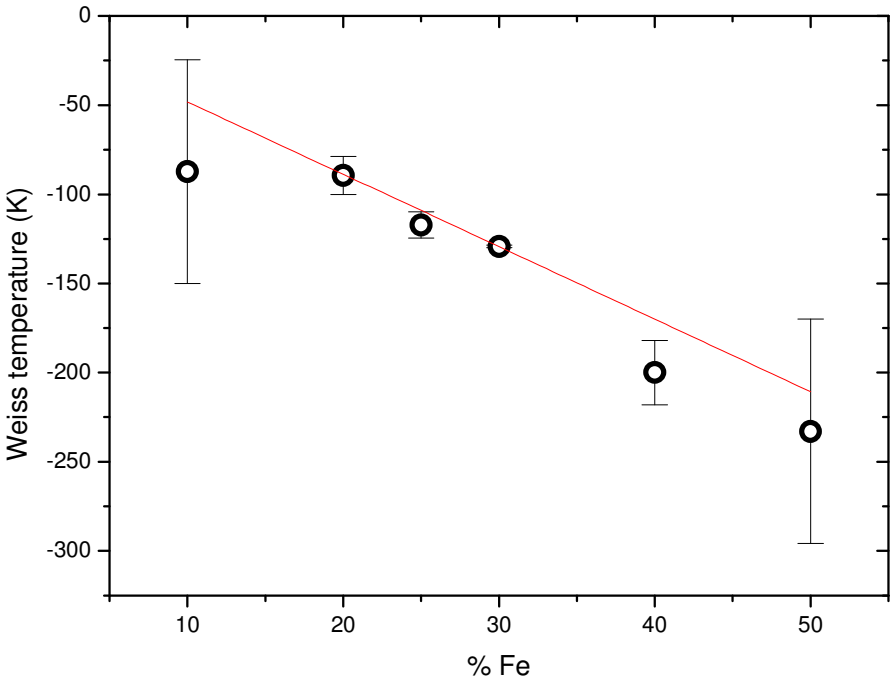

Fig. 5.20. Variation of the antiferromagnetic θ temperature in function of the Fe concentration.

The θ increases in modulus, linearly with the Fe content. This suggests an increase of the strength of the antiferromagnetic interactions. Deviations from linearity are caused by calculation errors, more precisely by the imperfections of the fit.

Stepping foreword with the magnetic measurements it is observed that for the Fe samples there is a clear difference between ZFC and FC measurements. The ZFC-FC for the 10% Fe sample is shown in figure 5.21. The same difference is seen for all the samples of the series.

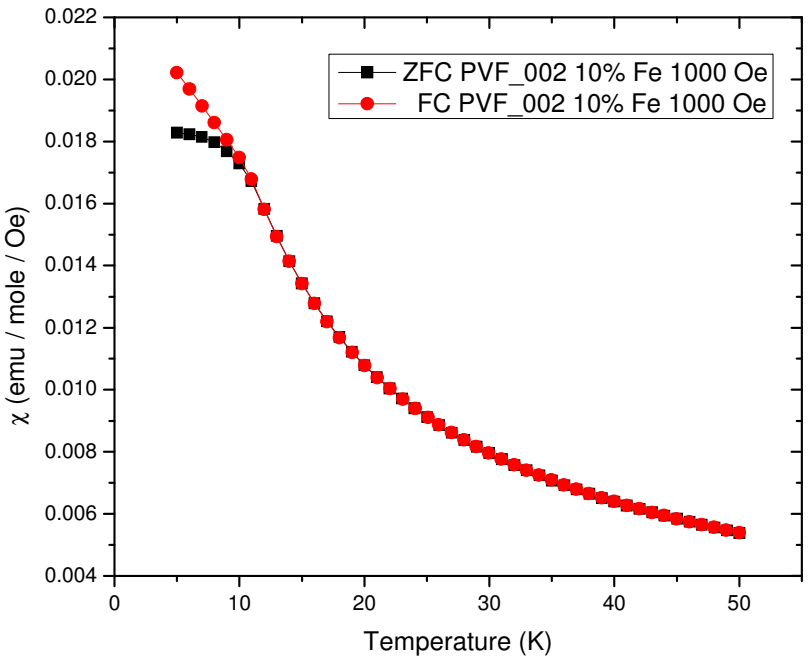

Fig. 5.21. ZFC-FC for 10% Fe sample. At approximately 10 K it is observed that the two curves separate.

All the samples in the Fe series show a maximum in the ZFC measurements of magnetization in function of temperature. This peak in magnetization is characteristic of an antiferromagnet. Figure 5.22 shows the ZFC for the Fe series samples and figure 5.23 shows the evolution of the transition temperature with the increase of the Fe content. The transition temperature (Néel temperature) is calculated from the first derivative of the ZFC graph.

The effect of the substitution is an increase of the transition temperature with the substitution degree. This suggests an increase of the average strength of the AFM interactions and that the Fe^{3+} cations form these correlations. The increase of the Fe content therefore causes the increase of the overall strength of the AFM interactions.

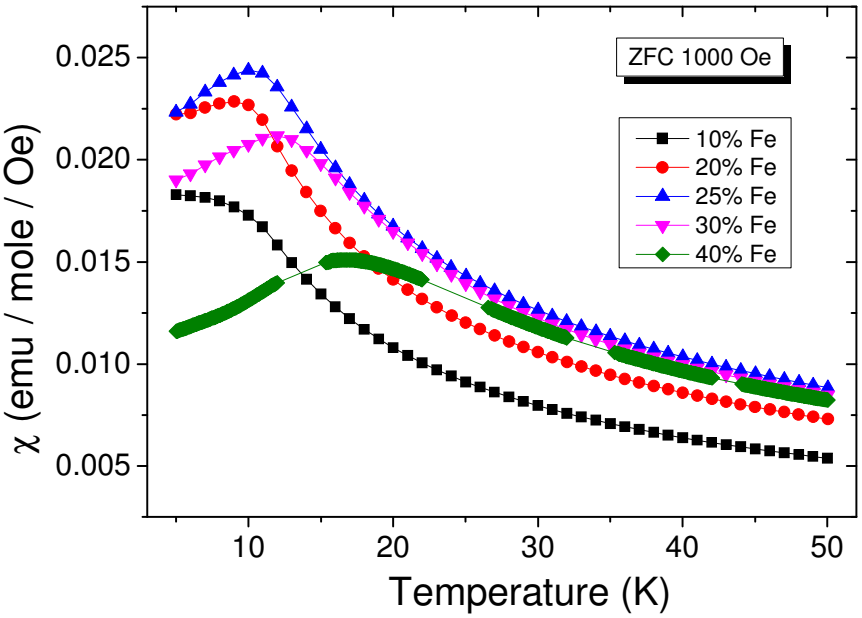

Fig. 5.22. ZFC for samples in the Fe series. The same peak in susceptibility is observed in all the samples and the position of the peak is displaced to higher temperatures as the amount of Fe is increased.

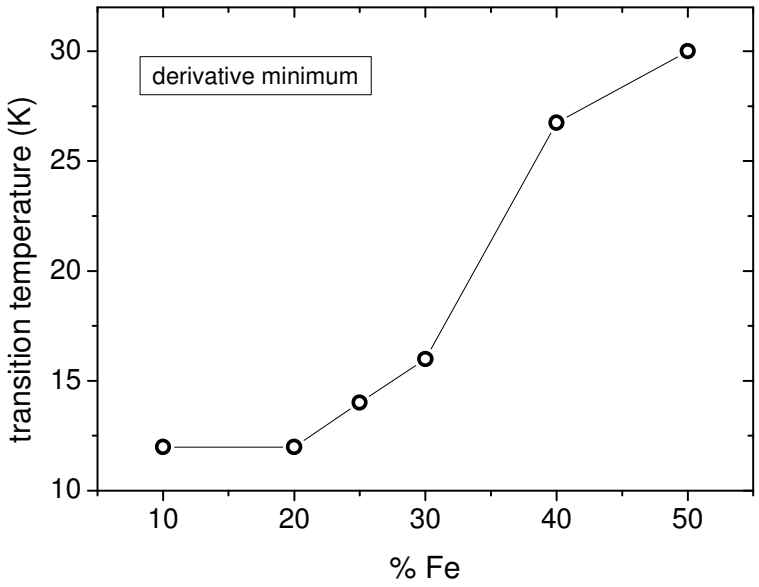

Fig. 5.23. The temperature at which the transition occurs, in function of the Fe degree of substitution.

The susceptibility measured in function of field, M(H), for the Fe samples is linear at relatively high temperatures but at very low temperatures (2K) the M(H) graph is slightly curved. Figure 5.24 shows the M(H) for the 10% Fe sample. Upon closer investigation it can be seen that the M(H) at low temperature presents some

hysteresis. Even more interestingly, while all the samples follow the same M(H) behaviour, the area occupied by the hysteresis circuit increases with the concentration of Fe. At 40% Fe the hysteresis is clearly visible. Figure 5.25 shows the M(H) for the 40% Fe sample.

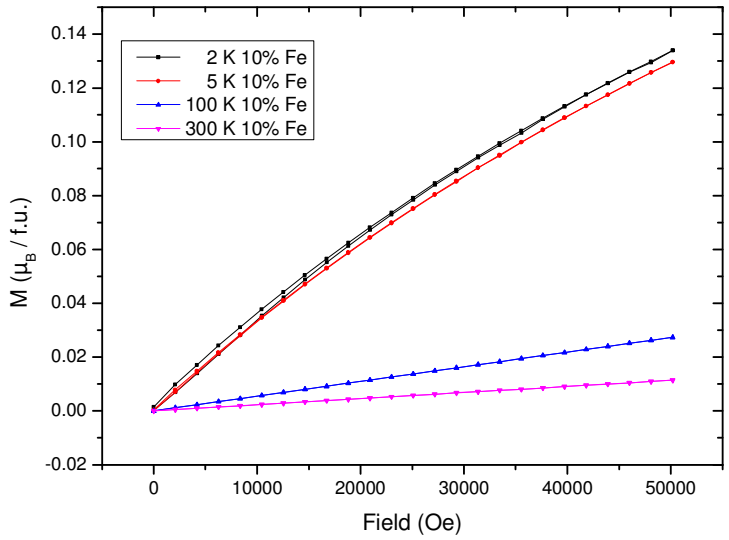

Fig. 5.24. The first two quadrants of the M(H) graph for the 10% Fe sample.

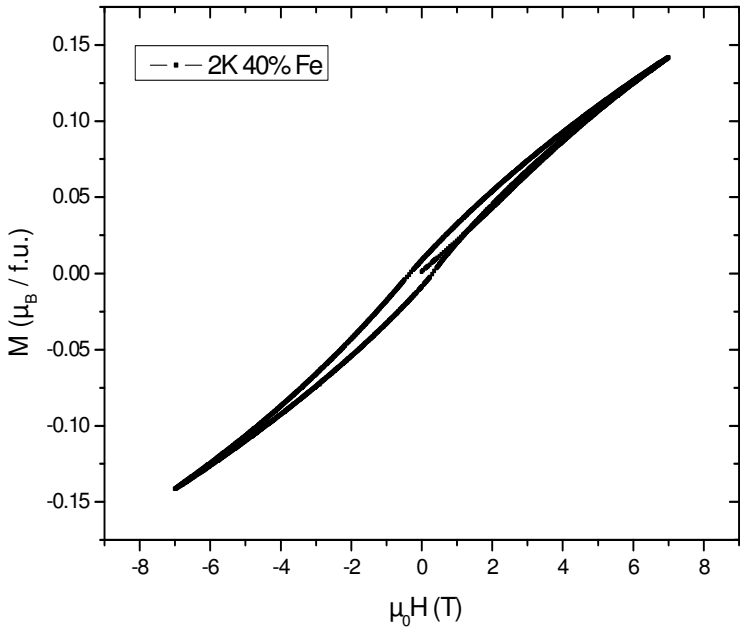

Fig. 5.25. Five quadrants M(H) hysteresis for the 40% Fe sample (PVF_010).

The appearance of a hysteresis circuit marks the existence of ferromagnetic interactions in the sample. The ferromagnetic component is nevertheless weak. Saturation is not reached even at $\mu_0 H$ = 7 T and the temperature T = 2 K. The remanent magnetization is $8.49*10^{-3}$ μ_B/f.u. and it is about 2 orders of magnitude smaller than the maximum magnetization reached (which is $1.413*10^{-1}$ μ_B/f.u.).

V.2. Magnetic order investigated with neutron diffraction

We assumed that there is an overall magnetic moment in the PVF samples (Fe series) and we have determined the magnitude of that moment, however, the magnetic structure is still unknown. In order to determine the magnetic structure NDP measurements were conducted on two representative samples. These samples are the 25% Fe and the 40% Fe (the same samples were discussed at the crystallography chapter). For doing this, NPD diffractograms were recorded at the D1B facility at the 2.52 Å wavelength at various temperatures ranging from 300K down to 2 K. An Orange cryostat was used to control the temperature.

Figure 5.26 shows the NPD patterns recorded for the 25% Fe sample at 2 K (well below the transition temperature, which is about 20 K) and 100 K respectively (well above the transition temperature).

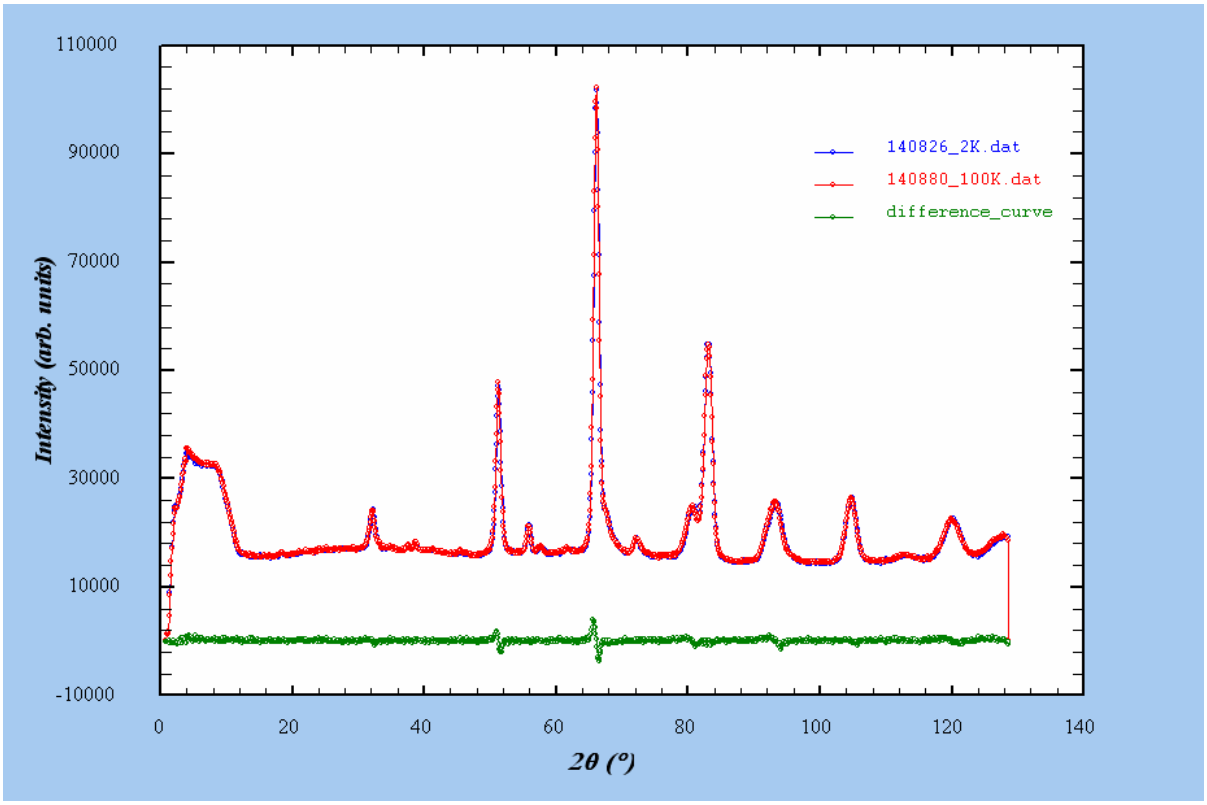

Fig. 5.26. NPD for the 25% Fe sample at 2 K (blue) and at 100 K (red). The green line shows the difference curve between the two diagrams. This is the PVF_25 sample.

No difference is seen between the two diffractograms. There is no new extra (magnetic) peak and no change in the intensities of the crystallographic peaks therefore no sign of long range magnetic ordering can be evidenced. The peaks seen in the difference curve are due to the variation of lattice parameters over the wide temperature range and not a change of peak intensity and therefore not sign of long range ordering. For this sample, the variation of lattice parameters with decreasing temperature was also investigated during the same event (the experiments at the D1B). In this measurement, again, no phase transition is observed. Their values of the lattice parameters are plotted in figure 5.27.

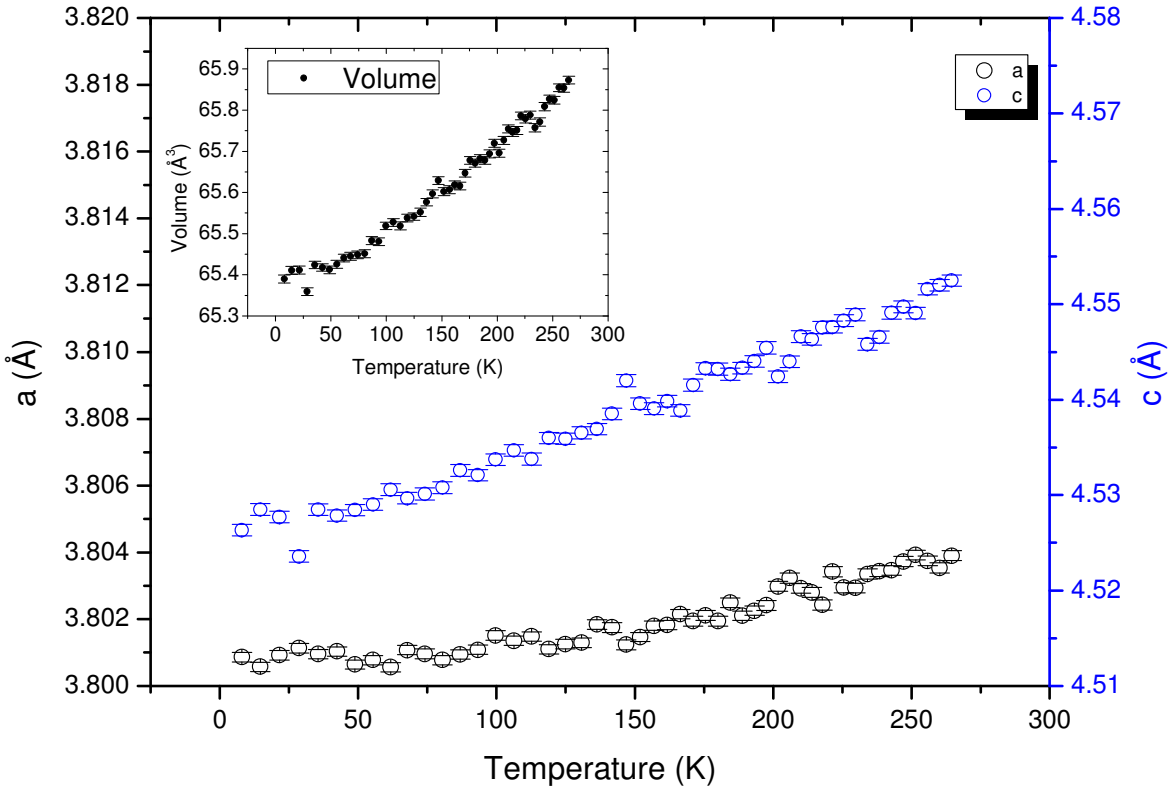

Fig. 5.27. Variation of lattice parameters with temperature for the 25% Fe sample PVF_25. The "a" parameter is shown in green and the c parameter is shown in black. The insert shows the variation of the volume.

The same conduct is observed for the 40% Fe sample. Again, neither extra peaks nor any changes in the already existing peaks can be detected in diffraction patterns recorded down to 2 K. Figure 5.28 shows the diagrams recorded at 2 K and 40 K for the sample. The temperatures are placed on each side of the transition temperature.

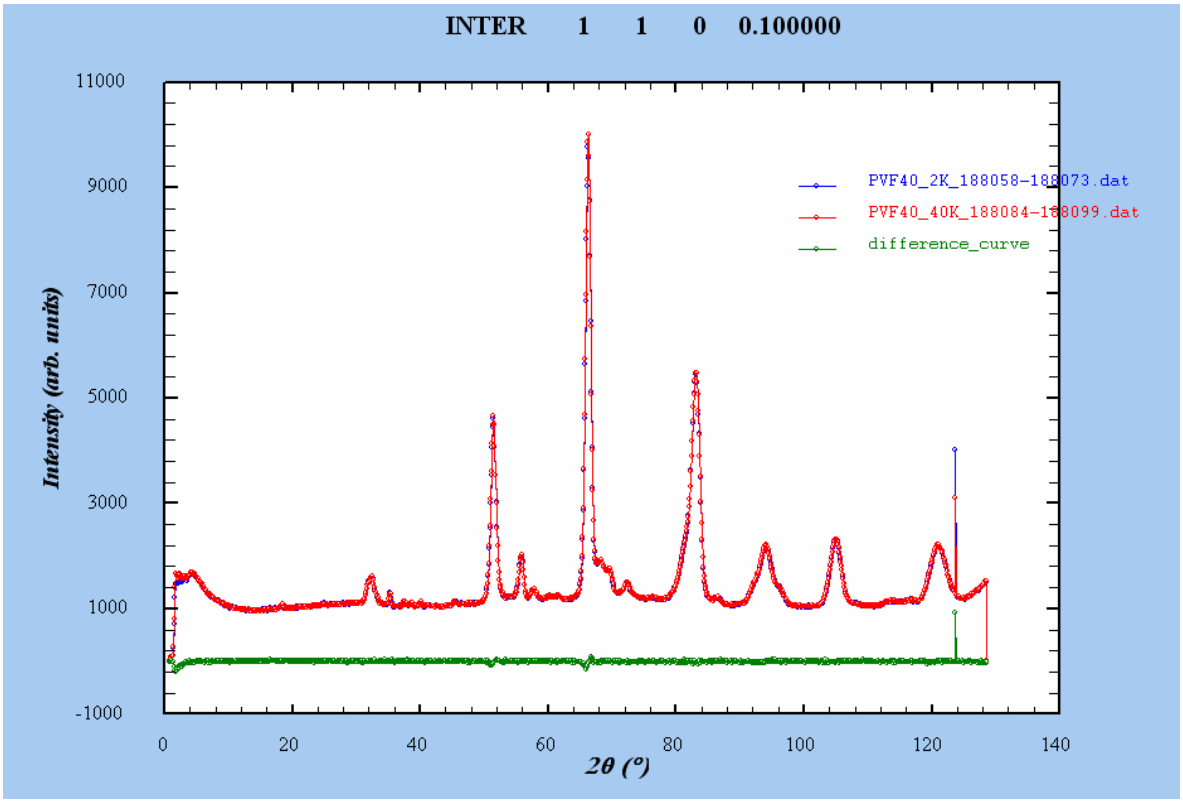

Fig. 5.28. NPD patterns at 2 K (blue) and 40 K (red) for the 40% Fe. The green line is the difference curve.

The lattice parameters for the 40% Fe sample reveal no structural phase transition (figure 5.29).

The only difference between the two diagrams (at 2 K and at 40 K) for the 40% sample is a small drop in the background of the lower temperature diagram. This drop in background could indicate that some local, short range ordering does occur nevertheless and this ordering reduces the diffuse magnetic scattering and hence the background. The small drop in background is evidenced in figure 5.30.

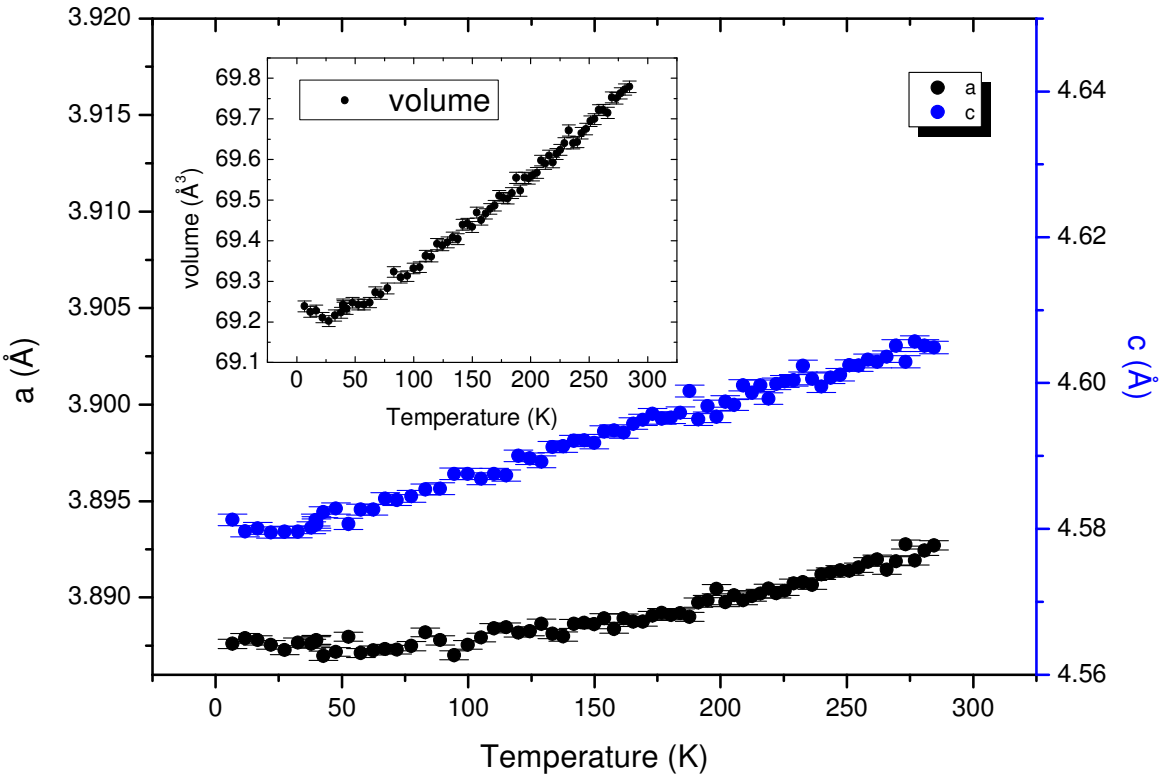

Fig. 5.29. Lattice parameters in function of temperature for the 40% Fe sample. A is green and c is black. The insert shows the evolution of the unit cell volume.

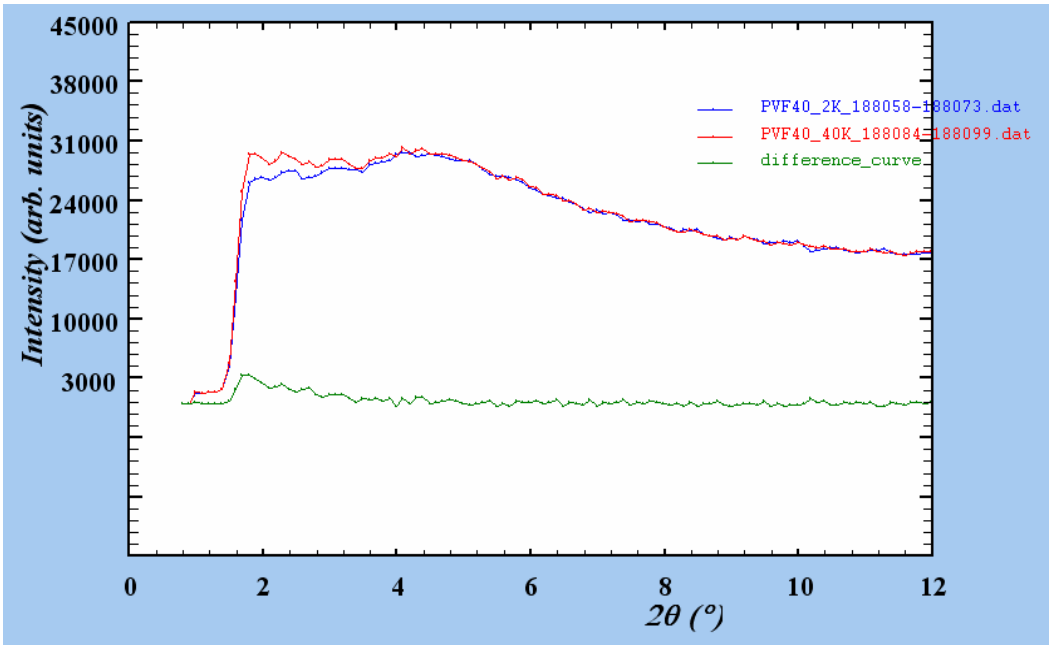

Fig. 5.30. Zoom in the small 2θ region of figure 5.28. The small difference between diffraction patterns is easier o observe in this picture.

A similar small drop in background could also be observed in the 25% Fe sample but the diagrams for that sample were not recorded with the same counting time so the difference is harder to be evidenced.

The $PbV_{1-x}Fe_xO_3$ samples present features indicating both AFM interactions (peak of susceptibility, negative Weiss temperature) and FM interactions (hysteresis curve). The AFM transition is evidenced by susceptibility measurements but no transition is observed by NPD (no extra peak, no structural change/phase transition related to magnetic ordering). This suggests that the system might be a spin glass.

A spin glass is a magnetic system characterized by the lack of long range order presenting randomly distributed clusters of ferromagnetic and antiferromagnetic coupled magnetic moments (i.e. short range order). Some of the characteristics observed on measurements on spin glass systems include a sharp peak of susceptibility and separation of ZFC-FC curves, the displacement of the peak with the frequency of measure for a.c. susceptibility measurements, the lack of any supplementary peak observed on NPD measurements and the lack of a visible transition of the specific heat.

The experimental data collected (presented) up to this point are not sufficient for drawing a conclusion on whether the system is indeed a spin glass so additional experiments (measurements) were performed. These are frequency dependent ac susceptibility measurements and specific heat measurements. Also additional magnetic measurements of $\chi(T)$ and M(H) are performed, aiming to search for signs of spin glass organization. The results from these measurements are discussed below.

V.3. Testing for spin glass behaviour

From the samples used at NPD, two samples were chosen as representative for the spin glass system. These are the 25% Fe (PVF_25) and the 40% Fe (PFV_40) samples. The first measurement considered is the $\chi(T)$ measurement performed in the ZFC and FC modes. Both samples present a sharp peak on the ZFC measurement. The peak appears at 10 K for PVF_25 and at 16 K for PVF_40. Figures 5.31 and 5.32 show the ZFC-FC measurements collected at different fields for PFV_25 and PVF_40 respectively. The ZFC-FC graphs are separated at low temperatures. The separation

decreases as the field intensity increases, eventually vanishing completely at 10 kOe for PVF_25 and at 50 kOe for PVF_40. This behaviour is typical for a spin glass.

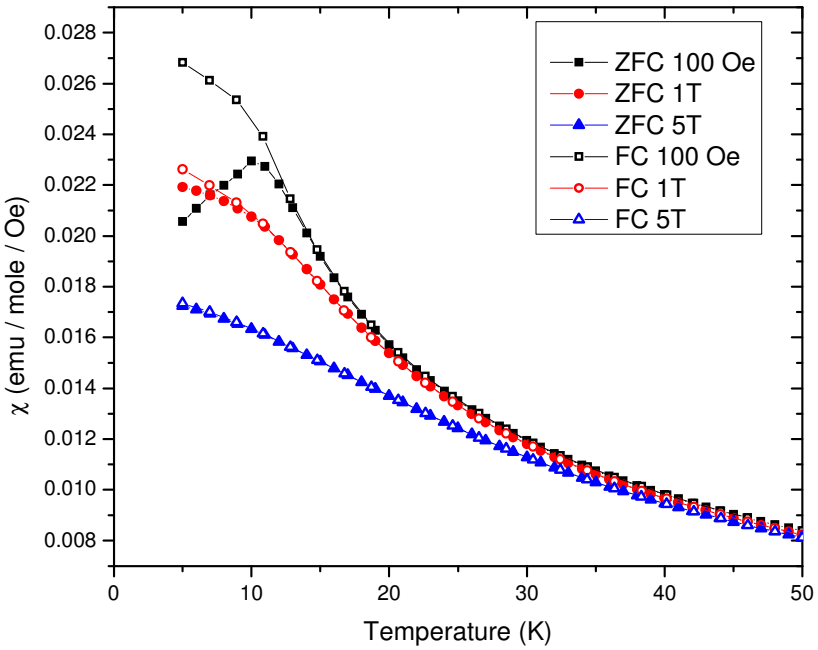

Fig. 5.31. ZFC-FC plots for PVF_25.

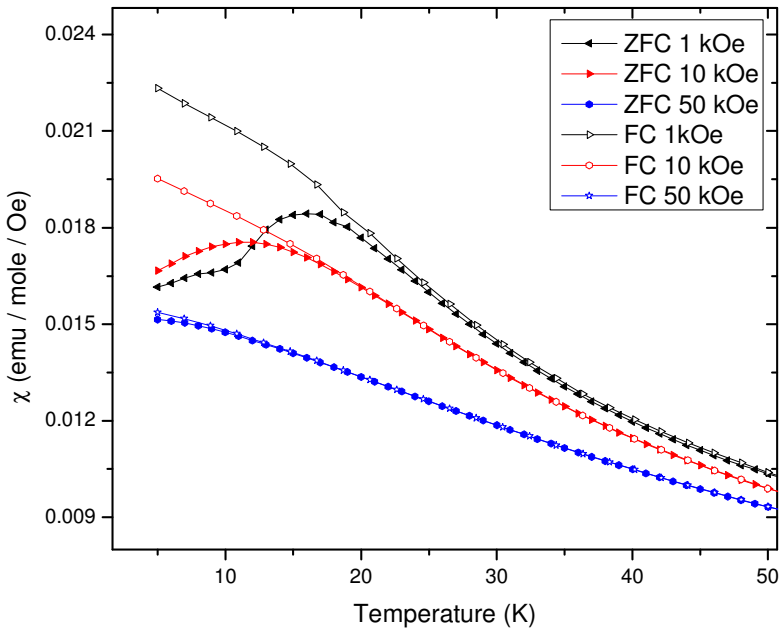

Fig. 5.32. ZFC-FC plots for PVF_40.

A second measurement that returns a result typical for a spin glass is the measurement of the isothermal magnetization. The M(H) measurements performed at different temperatures for PVF_25 and PVF_40 are shown in figures 5.33 and 5.34.

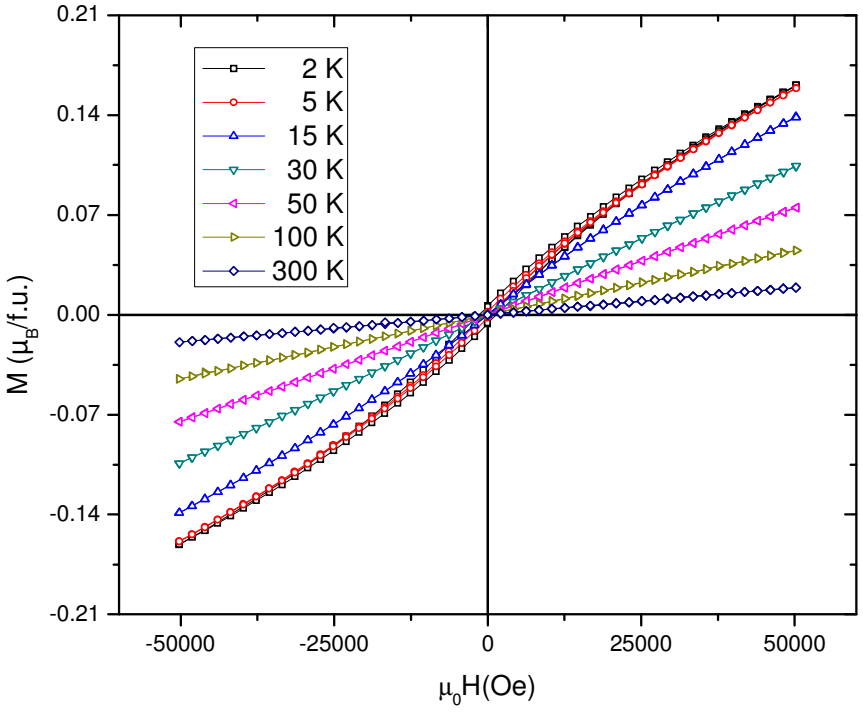

Fig. 5.33. M(H) for PVF_25 taken at different temperatures.

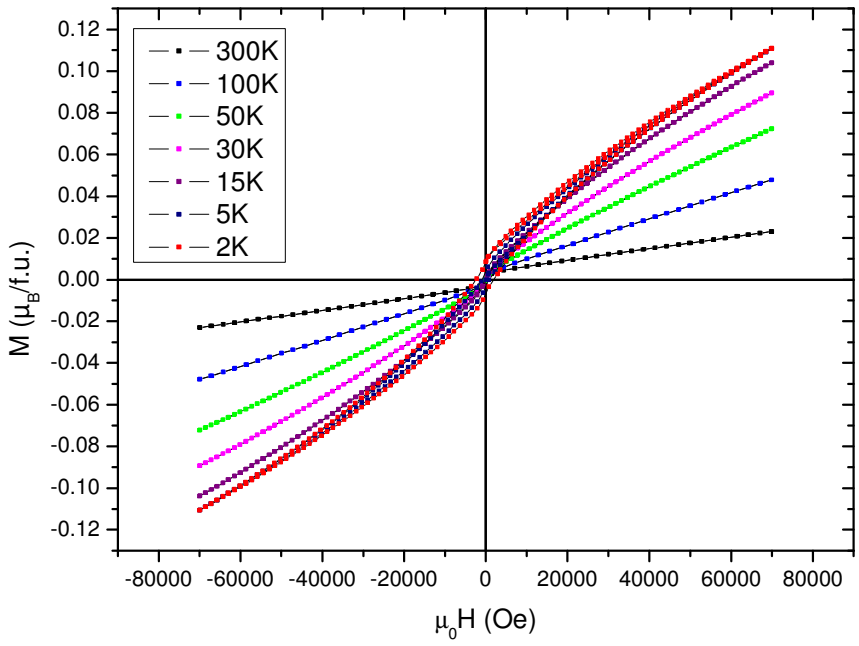

Fig. 5.34. M(H) for PVF_40. This sample contains a ferromagnetic impurity (not visible by XRD) which causes the deviation from linearity of the M(H) curves at the high temperatures.

These M(H) measurements have a rounded shape which is characteristic for a spin glass and lack a saturation value which reflects the randomness of the magnetic moments. Even at T = 2 K and $\mu_0 H$ = 5 T (for PVF_25) and $\mu_0 H$ = 7 T (for PVF_40) saturation is not reached. The maximum magnetization reached under these conditions is only 0.16 μ_B for the 25% Fe sample, respectively 0.12 μ_B for the 40% Fe. This is well under the expected values of 2.12 μ_B for PVF_25 respectively 3.12 μ_B for the other sample.

The third type of measurement is the measurement of the a.c. susceptibility. The real part of the a.c. susceptibility for the 40% Fe sample is shown in figure 5.35.

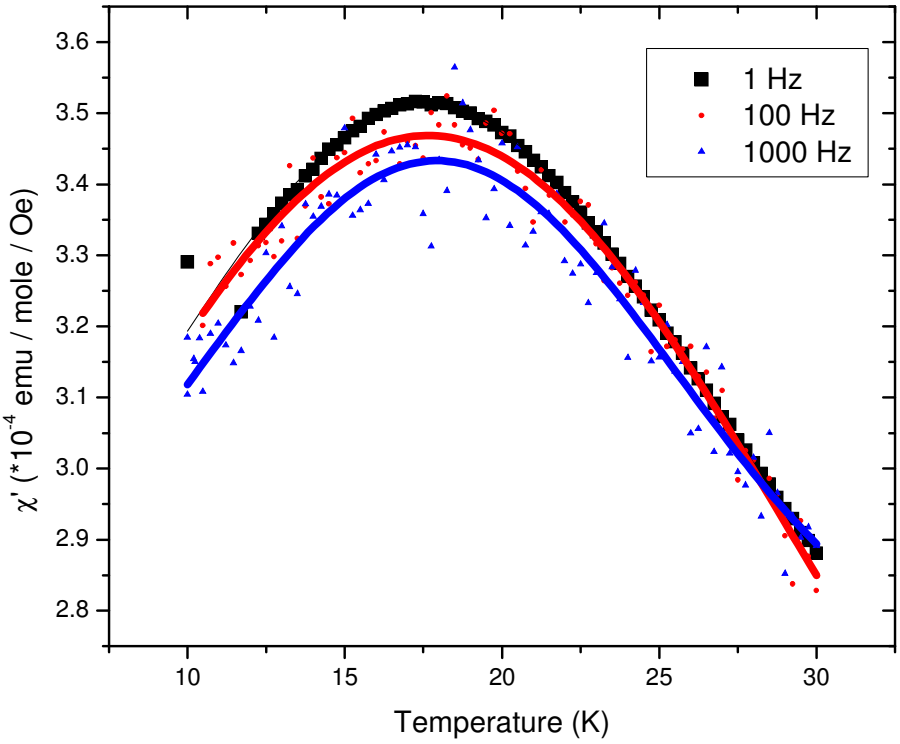

Fig. 5.35. χ'(T) for $PbV_{0.6}Fe_{0.4}O_3$ collected at 3 different frequencies. The signal is affected by electronic noise at higher frequencies so for these measurements Gaussian fit curves are drawn to guide the eyes.

The χ'(T) presents a maximum at 17.6 K for the measurement performed at 1 Hz. The peak shifts towards higher temperatures as the frequency increases and this is another typical behaviour of a spin glass.

The shift can be quantified by the so called "p" parameter which is given by the equation:

$p = \Delta T / [T*\Delta(\log(\omega))]$, where $\omega = 2\pi f$

The p parameter obtained for this sample is p = 0.010(2). A spin glass system is characterized by a p which varies between 0.004 and 0.08 [108]. The fourth type of measurement employed to verify whether the PVF system is a spin glass is the measurement of the specific heat. The specific heat was measured in the absence of an external field for $PbVO_3$ and for the two Fe substituted samples, PVF_25 and PVF_40. The curve of the specific heat (figure 5.36) shows no sign of any transition (no peak) on the temperature range from 2 K to 150 K (which includes the domain on which magnetic transitions are visible on $\chi(T)$ measurements). Some magnetic contribution to the specific heat is nevertheless detected.

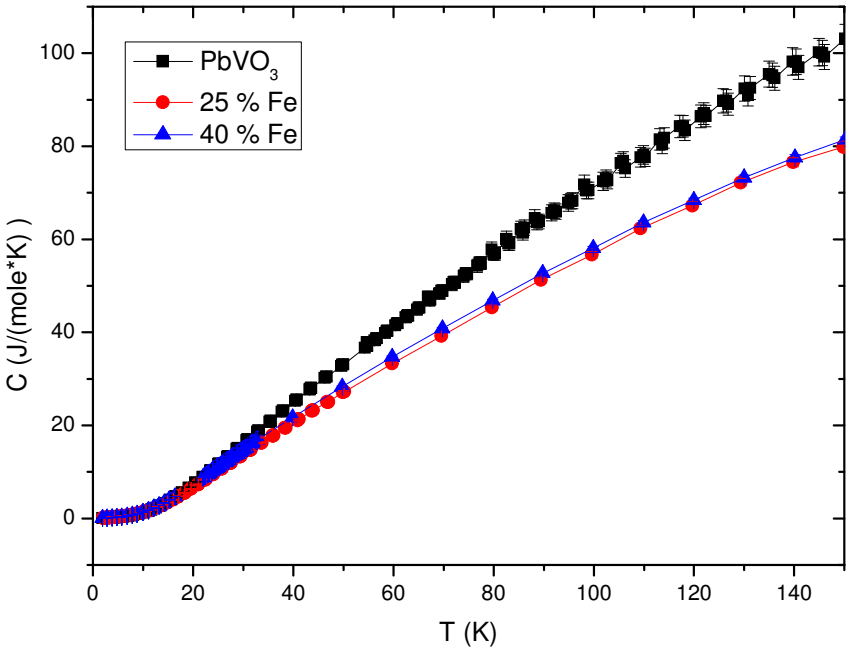

Fig. 5.36. Specific heat for $PbVO_3$, PVF_25 and PVF_40. No sign of any phase transition is visible.

The low temperature part of the specific heat curve is expected to be dominated by the magnetic contribution as the phononic contribution is small at low T. The C/T vs. T^2 plot (figure 5.37) shows a difference between $PbVO_3$ and the substitution samples at the low temperature domain. This difference is attributed to the magnetic contribution.

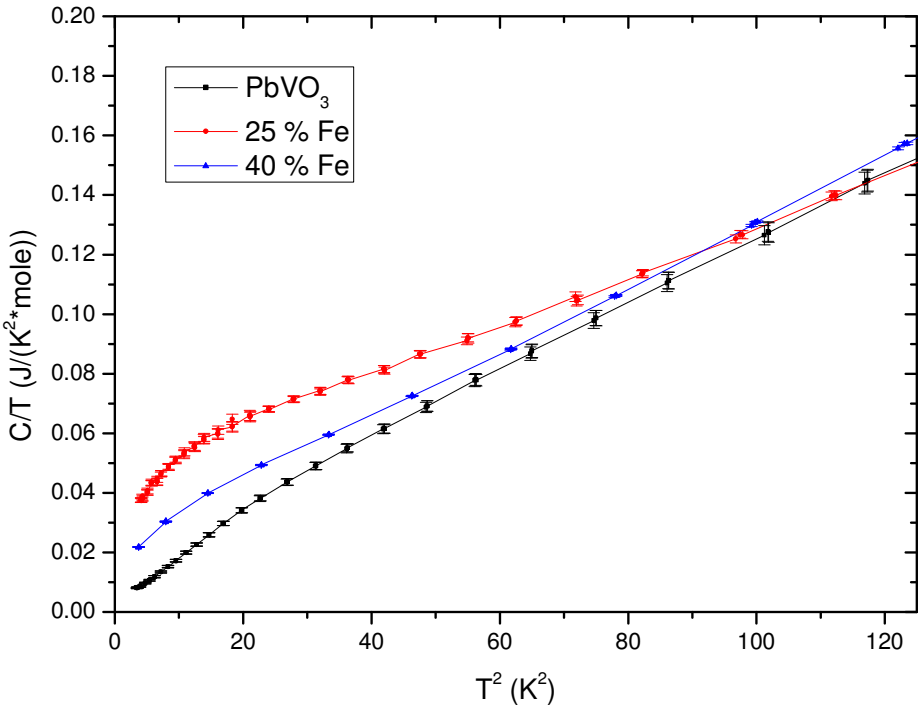

Fig 5.37. C/T vs. T^2 for $PbVO_3$ (PVO_010), $PbV_{0.75}Fe_{0.25}O_3$ (25% Fe, PVF_008) and $PbV_{0.6}Fe_{0.4}O_3$ (40% Fe, PVF_014). It can be observed that the curves of the samples containing the Fe substitution become separated from the curve of the $PbVO_3$ sample.

On the basis of these results it can be concluded that the $PbV_{1-x}Fe_xO_3$ system (for $x < 0.5$) displays a spin glass behaviour. The formation of the spin glass state could be explained by the existence of different types of magnetic exchanges, randomly distributed at the B site cation. It is possible that the distribution of V^{4+} cations and Fe^{3+} cations determines the formation of 3 types of interactions as follows:

- weak AFM interactions between V^{4+} cations (V-V),
- strong AFM interactions between Fe^{3+} cations (Fe-Fe)
- weak FM interactions between V^{4+} and Fe^{3+} cations (V-Fe).

The simultaneous presence of these interactions could create a very disordered magnetic state.

This model is supported by the Goodenough Kanamori rules. These rules predict the sign of the superexchange integral based on the electronic configuration and the position of the ions forming the interaction. According to these rules when two cations are correlated through an oxygen anion the interaction will be:

- antiferromagnetic if the magnetic cations have half-filled orbitals
- ferromagnetic if one cation has a filled (or half-filled) orbital and the other a half-filled (or empty) orbital.

The V^{4+} cation contains a single 3d electron so it might be consider that the d orbital is nearly empty. Fe^{3+} contains 5 3d electrons so the d orbital is half filled. Considering this configuration and the angle between the cation-oxygen-cation bond to be 180°, the interactions between V-V and Fe-Fe are the interactions between cations containing half filled orbitals and are therefore antiferromagnetic. The V-V interaction is weak and is sometimes considered negligible [109] while the Fe-Fe interaction is strongly antiferromagnetic. The interactions between Fe^{3+} and V^{4+} could be considered as interactions between half-filled and empty orbitals and could be therefore ferromagnetic. Table 5.4 gives the types of interaction between cations containing d^1 and respectively d^5 cations.

Table 5.4 Interactions between d^1 and d^5 cations, from [109]. S means strong, W – weak and NEGL – negligible.

	d^1	d^5
d^1	↑↓ NEGL	↑↓ M
d^5	↑↓ M	↑↑ S

V.4. Study of local magnetic interactions by EPR spectroscopy

The EPR measurements were performed at the INDTCIM Institute with the help of Dr. Oana Raita. The EPR measurements were carried out on a Bruker Elexsys E500 spectrometer in the X band (at 9.4 GHz) at low temperature. Spectra were collected in the temperature range of 110 K to 290 K for every 10 K. The magnetic field was swept from 0 to 10000 Gs.

Measurements were performed on 4 representative samples:

- $PbVO_3$
- $PbV_{0.75}Ti_{0.25}O_3$ (PVT_25)
- $PbV_{0.75}Fe_{0.25}O_3$ (PVF_25)
- $PbV_{0.6}Fe_{0.4}O_3$ (PVF_40)

These are the same samples that were used at the NPD experiments. The interpretation of the results was made with the help of Prof. Dr. Aurel Pop.

V.4.1. EPR studies of $PbVO_3$

The EPR signal of V is of two types:

(i) due to the high concentration of vanadium. If the vanadium content in the compound is high, it gives a broad resonance line. Therefore the line from ^{51}V cannot be resolved. The g value for this resonance is less than 2.

(ii) due to the interaction with the nuclear magnetic moment. The VO^{2+} ion has S= 1/2 and I = 7/2. The EPR spectrum shows a hyperfine pattern of eight equidistant lines. In the C4v symmetry two sets of eight lines are expected (i.e. a sixteen-line pattern whereas in the C2v symmetry three sets of eight lines are expected).

In our sample, the EPR spectra of $PbVO_3$ show a well-resolved hyperfine structure consisting of eight lines of equal peak-to-peak width. This is the only feature of the spectra. A zoom on this region of the experimental data is shown in figure 5.38. The presence of the 8 lines is typical for V^{4+} cations. These lines are formed by the hyperfine coupling of the unpaired electron of the V^{4+} cation (S =1/2) with the nuclear spin (I =7/2) of ^{51}V.

These spectra can be explained by the following spin Hamiltonian:

$$H = \beta[g_{\parallel}B_zS_z + g_{\perp}(B_xS_x + B_yS_y)] + A_{\parallel}S_zI_z + A_{\perp}(S_xI_x + S_yI_y),$$

where β is the Bohr magneton, $g_{\parallel}$, $g_{\perp}$, $A_{\parallel}$ and $A_{\perp}$ are components of gyromagnetic factor and hyperfine structure tensor , B_x, B_y, B_z are the components of the magnetic field , S_x, S_y, S_z are the components of spin operators and I_x, I_y and I_z are the nucleus components respectively.

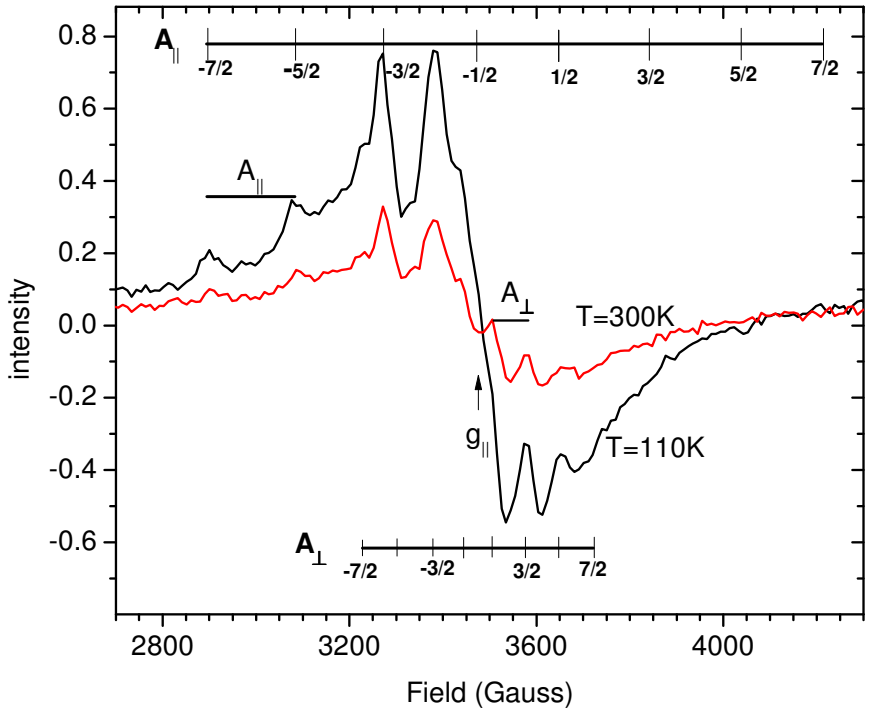

Fig. 5.38. EPR spectra for $PbVO_3$.

The spectrum in figure 5.38 shows that both parallel and perpendicular features can be seen. At higher temperatures we have a better resolved hyperfine structure than in the low temperature range. At low temperatures the EPR spectrum change to a V^{4+} anisotropic powder spectra. In the high temperature range, all anisotropic interactions are averaged to zero [110]. These results are in agreement with the small decrease of the unit cell height, c, with decreasing temperature, previously evidenced from XRD measurements.

Table 5.5 shows the EPR parameters for V^{4+} ions obtained from experimental spectra. The results are consistent with a square–pyramidal C_{4v} coordination specific for vanadyl ions [111-114]. The hyperfine coupling constants $A_{\parallel}$ and $A_{\perp}$ are sensitive to the local bonding environment for V^{4+} coordinated with oxygen ligands. The small

decrease of the hyperfine coupling $A_{\parallel}$ and $A_{\perp}$ suggest the increase of ligand field with increasing temperature from 110 K to 300 K.

Table 5.5 EPR parameters for V^{4+} ions.

Temperature	$g_{\parallel}$	$g_{\perp}$	$A_{\parallel}$ [Gauss]	$A_{\perp}$ [Gauss]
110 K	1.941	1.995	184	70
300 K	1.933	1.998	180	68

V.4.2. EPR results for $PbV_{0.75}Ti_{0.25}O_3$ (sample PVT_25)

When any Ti (III) compound in the form of powder is placed in a magnetic field, it gives a resonance signal. The single d-electron of Ti^{3+} has spin, S = 1/2. The abundance of isotopes is reported as $^{46}Ti \approx 87\%$, $^{48}Ti \approx 7.7\%$ and $^{50}Ti \approx 5.5\%$. These isotopes have the nuclear spins I = 0, 5/2 and 7/2 respectively. Electron spin and nuclear spin interactions give rise to (2I+1) hyperfine lines (0, 6 and 8) which appear as satellites. Since ^{46}Ti is more abundant, the EPR signal contains only one resonance line which is similar to the one shown in figure 3. The g value for this resonance is slightly less than 2.0. The g value of 1.95 indicates that Ti^{3+} is in a tetragonally distorted octahedral site.

Figure 5.39 shows the EPR spectra for PVT_25 (25% Ti) at 5 different temperatures. The spectra for this sample present a single, very intense transition which is shifted at lower values of the magnetic filed with the decrease of the temperature.

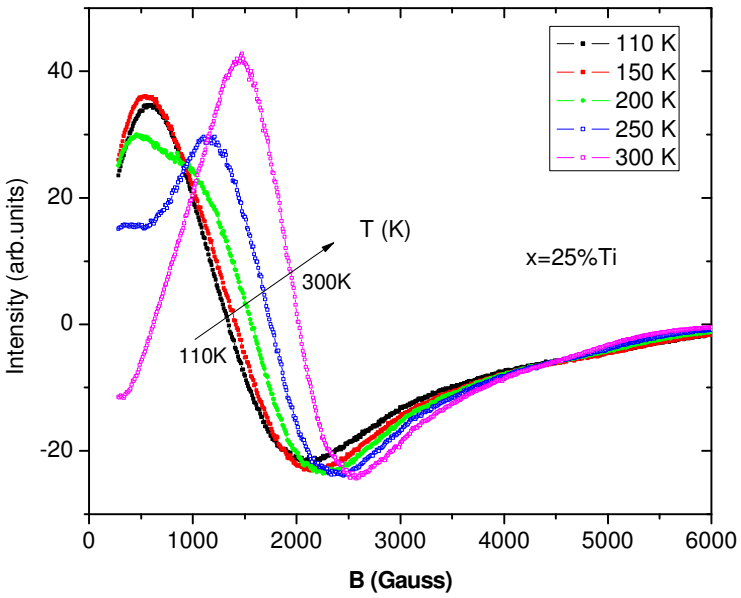

Fig. 5.39. EPR spectra at different temperatures for PVT_25.

The plots of both the width of the line and the intensity of the line in function of temperature (figures 5.40 and 5.41a) present a broad peak around 190K.

The abrupt changes of linewidth of the EPR line around 190K, directly reflects the change in the spin-lattice relaxation rate and most importantly, the dynamic averaging of the g-anisotropy.

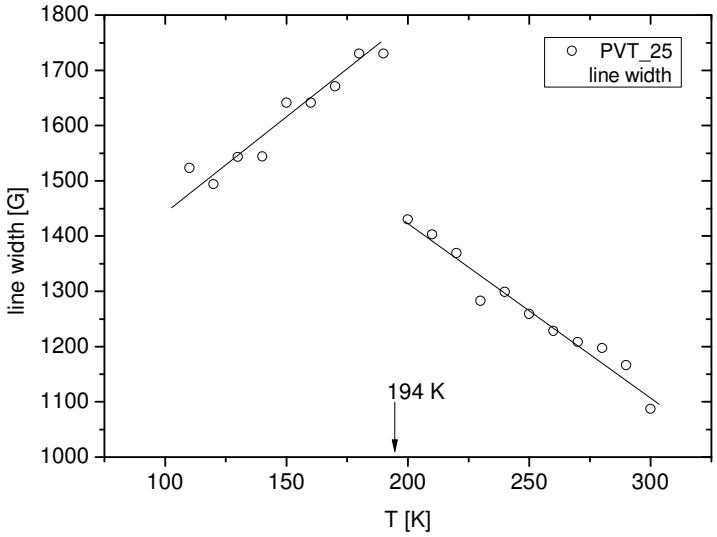

Fig. 5.40. Temperature dependence of the line width in function of temperature for PVT_25.

The linewidth of the narrow EPR line, which reflects any variation in the spin-lattice relaxation, is increasing with decreasing temperature in the range (300-200K). The sharp increase of the linewidth at temperature T=194 K pertains to the behaviour similar to frustration of magnetic systems, with the resonance line broadening connected to the onset of a magnetic order at a high-temperature region [115, 116].

Figures 5.41a and 5.41b show the temperature dependence of the EPR integrated intensity, I(T), and the inverse of intensity 1/ I(T).

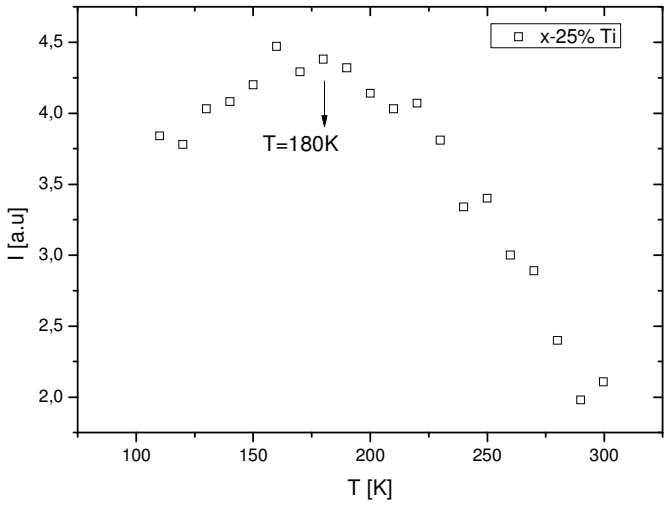

a)

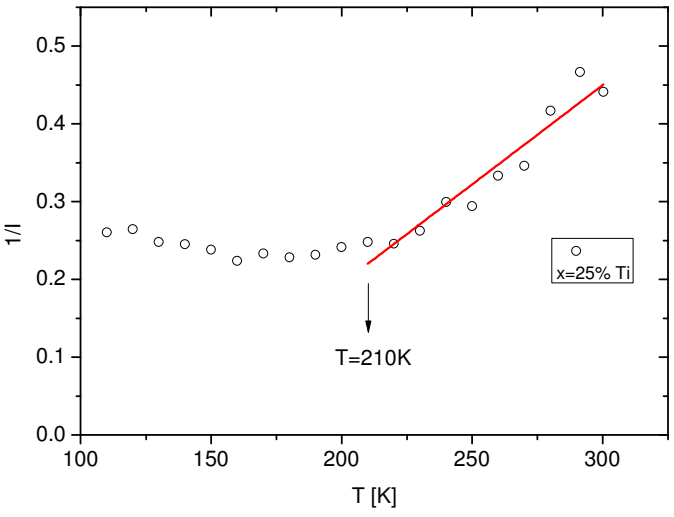

b)

Fig. 5.41. a) Temperature dependence of the intensity, I, and of the inverse integrated intensity, I(T) (fig 5.41b) for the PVT_25 sample.

As the EPR integrated intensity, defined as the area under the absorption resonance curve, is proportional to the imaginary part of the complex magnetic susceptibility, the Curie or Curie-Weiss type dependence of I(T) might be expected.

For the PVT_25 sample, the *g*-factor increases linearly with decreasing temperature with a noticeable change of slope observed about ~250K (Fig. 5.42). The approximate temperature rate of change (slope of linear dependence) for the g-factor is $\Delta g/\Delta T \sim 17.3 \cdot 10^{-3}\ K^{-1}$ in the temperature range 300K-260K and $\Delta g/\Delta T \sim 8.3 \cdot 10^{-3}\ K^{-1}$ for the 260–130K range. The g-values are sensitive to the local internal fields. A similar strong increase of the g-value at lower temperatures was reported for the $Ba_{0.9}La_{0.1}Ti_{1/2}Mn_{1/2}O_3$ perovskite where it was explained as an effect of the internal fields associated with the onset of magnetic order and/or strong magnetic fluctuations [117]. We believe that in our sample the competition between the magnetic interaction and the spin ordering processes could be responsible for this complex behaviour of the *g*-factor.

The narrowing of the absorption line below 194K and the shift in the g factor (resonance field, H_{res}*)* indicates an internal field contribution, caused by the exchange interaction.

In the PVT_25 sample the range of the g-value is between 3.1 and 4.9. These values are higher that the g-values for Ti^{3+} (g around 2).

A short range magnetic order, confined to distinct spatial regions could cause a sharp variation of the EPR parameters and inhibit the onset of a long-range magnetic order. A similar behaviour was observed for paramagnetic centres in quite different compounds – in ternary vanadates [118, 119].

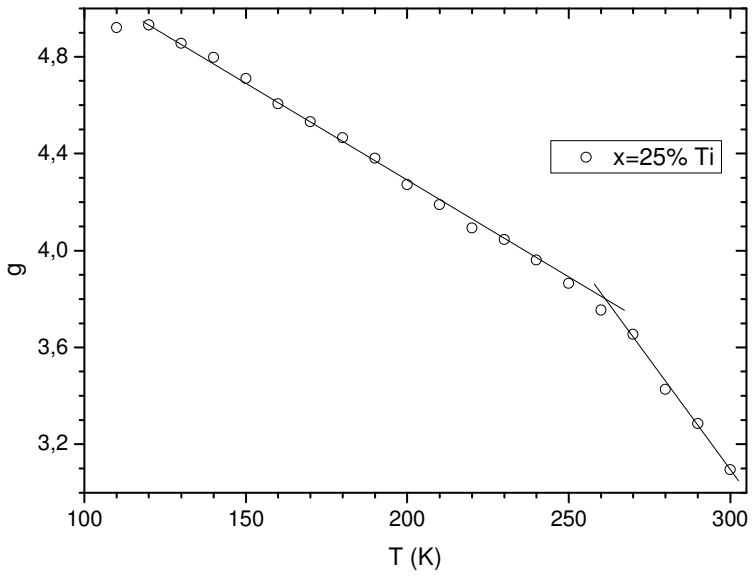

Fig. 5.42. Temperature dependence of the g – factor for the sample PVT_25 (with x = 25% Ti).

Unexpected jumps observed at certain temperatures for linewidth, *g*-factor and integrated intensity (e.g. at 194 K in linewidth) could be yet some more evidences of a magnetically inhomogeneous state.

To reveal different temperature ranges of relaxation processes, a double logarithmic plot of linewidth ΔH_{pp} versus a shift of resonance field $\delta H_r = H_r(\infty)-H_r(T)$ has been proposed (see Fig. 5.43). Here Hr(∞) is the resonance field in a very high temperature limit. Any detected change of slope on this type of figure should be a sign of a relaxation type variation in the observed samples [119].

Figure 5.43 shows the existence of two relaxation modes with positive slopes in the high temperature ranges (300-260K), (260K-200K) and a different relaxation mechanism with negative slope in temperature range (200-110K), respectively.

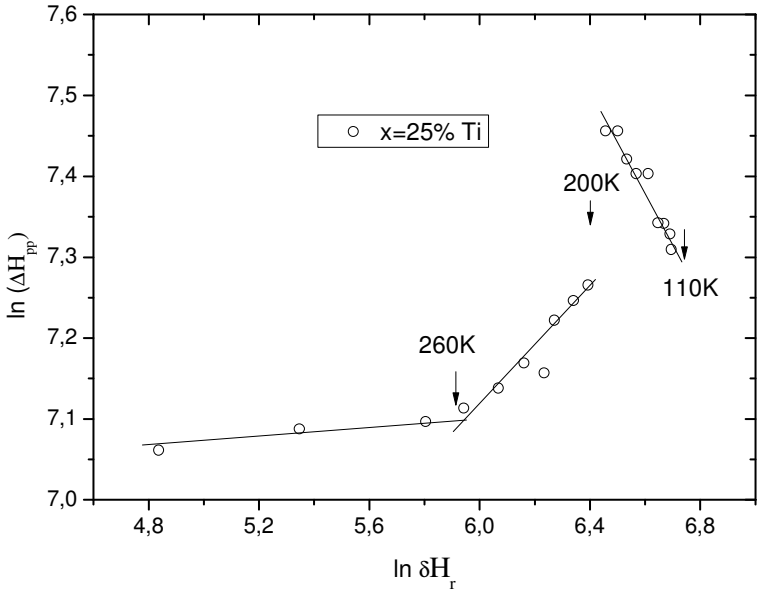

Fig. 5.43. Plot of ln(ΔH_{pp}) vs. ln(δHr) for sample PVT_25. Crossover temperatures are indicated.

Figure 5.44 shows the reciprocal magnetic susceptibility curve function of temperature (obtained by SQUID measurements). The deviation from linearity of the reciprocal magnetic susceptibility vs. temperature around 200 K confirms the anomaly evidenced from EPR measurements.

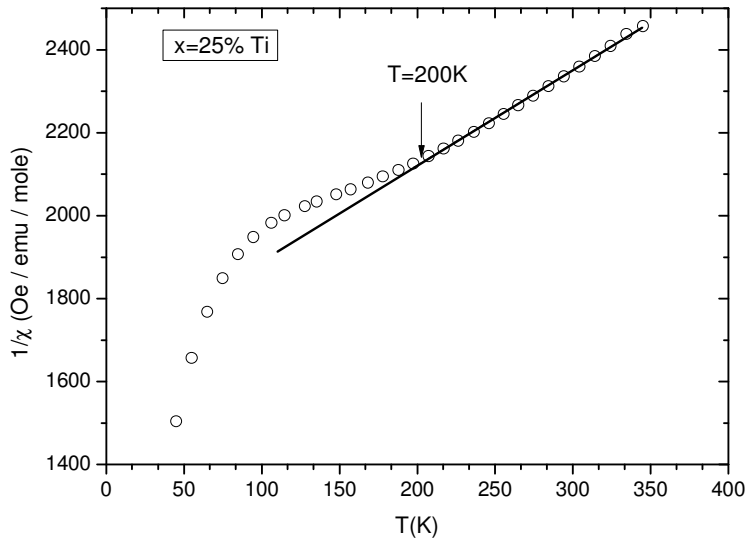

Fig. 5.44. The reciprocal magnetic susceptibility vs. temperature for sample with x=25%. The line is the fit of experimental data from 200 K to room temperature.

V.4.3. EPR results for $PbV_{1-x}Fe_xO_3$ (x=25%, 40%) samples

When dealing with dopants on a sub percentage level, a sensitive test of the local environment around the functional centre can only be provided by electron paramagnetic resonance (EPR).

Three signals are invariably reported for Fe^{3+} [120-122]

– a sharp line around g=4.3, interpreted as Fe^{3+} in a tetrahedral environment with strong rhombic distortion

– a broad line around g=2.3 due to oxidic Fe species

– a line around g=2, interpreted as Fe^{3+} in (distorted) octahedral environment

In the case of paramagnetic Fe^{3+} dopants, the sextet spin ground state is strongly influenced by the ligand field originating from the nearest-neighbour oxygen anions. The resulting fine-structure (FS) interaction is a measure of the local symmetry. With its five unpaired electrons, the free Fe^{3+} ion possesses a half-filled 3d shell and can be described as orbital singlet. Its ground-state configuration is $^6S_{5/2}$ (S = 5/2) and the sixfold spin degeneracy can be lifted by the FS interaction and an external magnetic field. Neglecting hyperfine interactions, because the magnetic active isotope ^{57}Fe is present in only 2.2% natural abundance, an approximate spin Hamiltonian for this high-spin system can be written as:

$$H = gBS + D\left(S_z^2 - \frac{1}{3}S(S+1) + E\left(S_x^2 - S_y^2\right)\right)$$

The second and third terms in the equation represent the effects of axial and rhombic components of the crystal field respectively. When D=E=0, it corresponds to a free ion in the magnetic field, B and if E = 0, it implies a field of axial symmetry.

If λ = (E/D) increases, it results in the variation of rhombic character.

- Maximum rhombic character is seen at a value of λ=1/3 and further increase in λ from 1/3 to 1 results in the decrease of the rhombic character.
- When λ = 1, the axial field situation is reached.
- When λ=1/3, the g value is around 4.27 and when λ is less than 1/3, g value is 4. Hence, the resonance is no longer isotropic and the powder spectrum in that region is a triplet corresponding to B along each of the three principle axes. For Fe^{3+}, in fields of high anisotropy, the maximum g value is 9. If g values are limited from 0.80 to 4.30, the Fe^{3+} ion is under the influence of a strong tetragonal distortion.

This is due to the fact that the three Kramer's doublets of |S=5/2> are split into |S±5/2>, |S±3/2> and |S±1/2> separated by 4D and 2D respectively where D is the zero field splitting parameter.

The widths of the line are larger in low magnetic fields when compared to high magnetic fields. If the lowest doublet, |S±1/2> is populated, it gives a g value of 2 to 6 whereas if the middle Kramer's doublet |S±3/2> is populated, a g value 4.30 is expected. If the third doublet |S±5/2> is populated, it gives a g value of 2/7 to 30/7. A few systems are known which exhibit resonances from all the three Kramer's doublets.

The Fe substitution samples investigated by EPR spectroscopy are PVF_25 (x=25%Fe) and PVF_40 (40%Fe). Figure 5.45 shows the spectra for the PVF_25 sample at 5 temperatures (from 300K to 110K).

It can be observed that all the resonance spectra exhibit a broad line, centred on g = 2 due to the spin of the Fe^{3+} ions. An additional resonant mode is situated around g = 4.2. By decreasing the temperature the signal around g = 4.2 is well resolved and the signal intensity decreases.

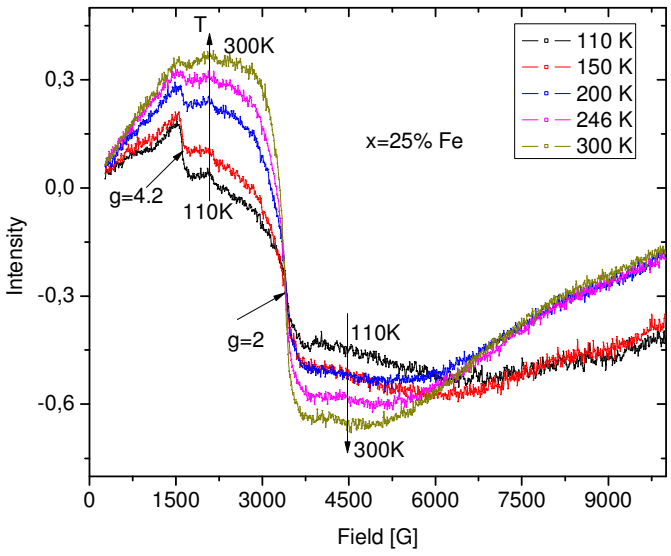

Fig. 5.45. EPR spectra for PVF_25 (25 % Fe).

The presence of the additional resonant mode is interpreted as an indication of the presence of Fe^{3+} cations in a tetrahedral environment with a strong rhombic distortion.

The complete evolution of the EPR line intensity/concentration of the paramagnetic Fe^{3+} centres with the temperature, as determined in the present investigation, is presented in figure 5.46. One finds that the EPR line intensity of the Fe^{3+} centre decreases with decreasing temperature. This result suggests the increase of the number of antiferromagnetic Fe^{3+}-Fe^{3+} pairs by decreasing temperature.

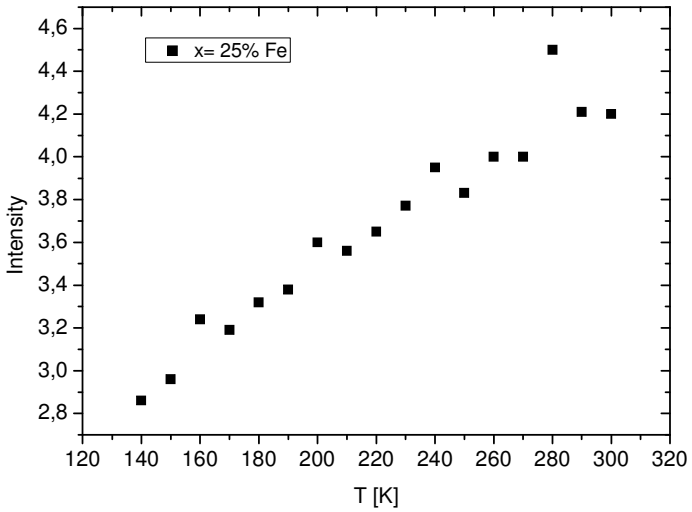

Fig. 5.46. Temperature dependence of the EPR integrated intensity of the x=25% Fe sample.

Figure 5.47 shows that the linewidth ΔH_{pp} increases by decreasing temperature. The large value of ΔH_{pp} is the result of a strong magnetic dipolar interaction between the Fe^{3+} ions [123].

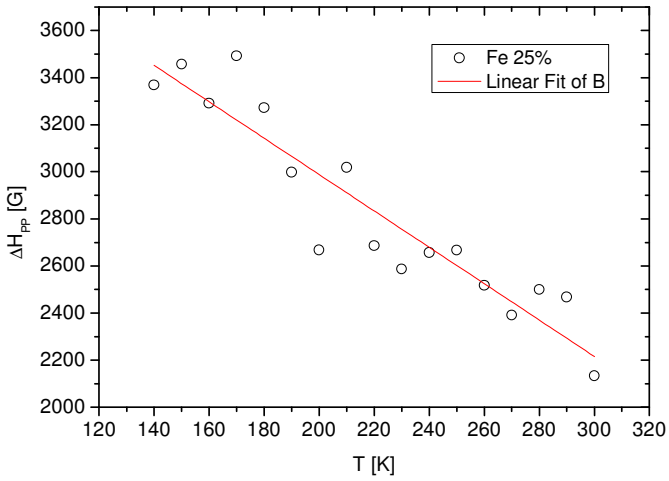

Fig. 5.47. Temperature dependence of the line width in function of temperature for PVF_25 sample.

The g-factor increases linearly with decreasing temperature, presenting a change of the slope around ~176 K (Fig. 5.48). The approximate temperature rate of change for the g-factor is $\Delta g/\Delta T \sim 0.17 \cdot 10^{-3}$ K^{-1} in the temperature range of 300 to 180 K and $\Delta g/\Delta T \sim 1.26 \cdot 10^{-3}$ K^{-1} (170 –138 K).

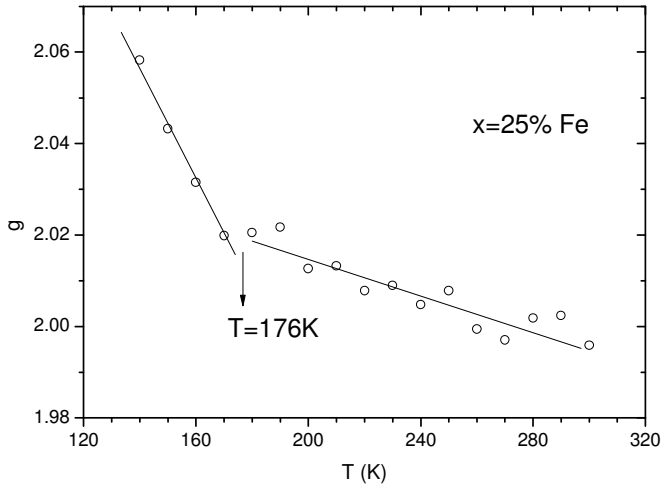

Fig. 5.48. Temperature dependence of the g–factor for PVF_25.

The double logarithmic plot of linewidth ΔH_{pp} versus a shift of resonance field ΔH_r (see Fig. 5.49) reveals the existence of two relaxation types with negative slope in the high temperature ranges (300 - 180 K), (175 - 130 K), with a crossover temperature T_S around 175 K.

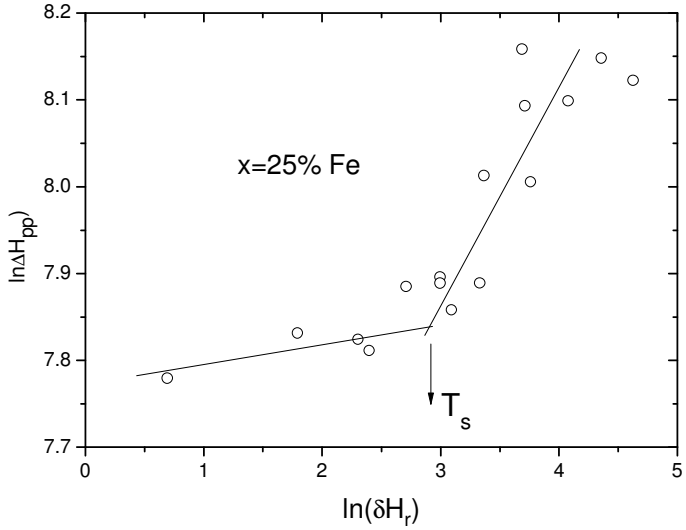

Fig. 5.49. Plot of ln(ΔH_{pp}) vs. ln(δHr) for the PVF_25 sample. The crossover temperature is indicated by the arrow.

Figure 5.50 shows the spectra for the PVF_40 sample (x=40% Fe) at the same 5 temperatures as PVT_25. The signal seems to contain two components: a large transition attributed to Fe^{3+} ions (assigned to the central fine structure $\Delta M_S = -1/2 \rightarrow 1/2$ transition) and a hyperfine structure, respectively.

The EPR line intensity of a paramagnetic centre is proportional with its concentration. For the PVF_40 sample the decrease of the EPR signal with the decreasing temperature shows that the concentration of free Fe^{3+} ions decreases. This behaviour is related with the antiferromagnetic order evidenced from magnetic susceptibility measurements.

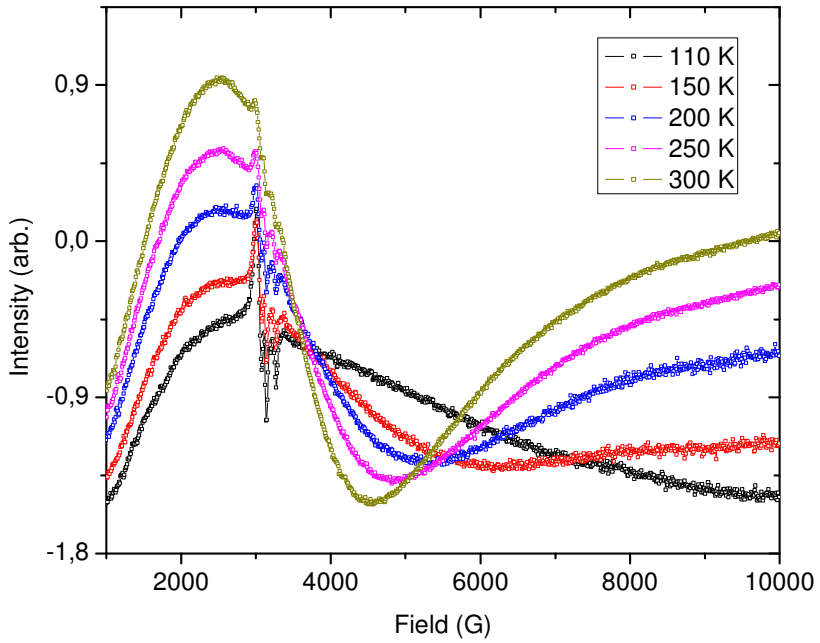

Fig. 5.50. EPR spectra for the PVF_40 sample at different temperatures.

Figure 5.51 shows that by decreasing the temperature, the hyperfine structure becomes well resolved.

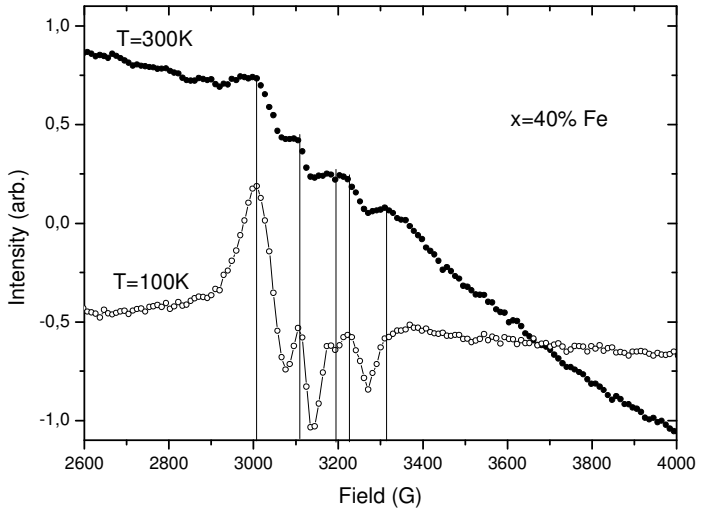

Fig. 5.51. The hyperfine structure of PVF_40 sample at temperatures T=300K and T=100K, respectively.

Figure 5.52 shows that the linewidth ΔH_{pp} increases by decreasing temperature with a slope of $\Delta H_{pp}/\Delta T$ = -6.5 G/K, a value lower comparatively with the one obtained for the x=25% Fe sample ($\Delta H_{pp}/\Delta T$ = -7.7 G/K). The large value of ΔH_{pp} confirms the presence of a strong magnetic dipolar interaction between the Fe^{3+} ions.

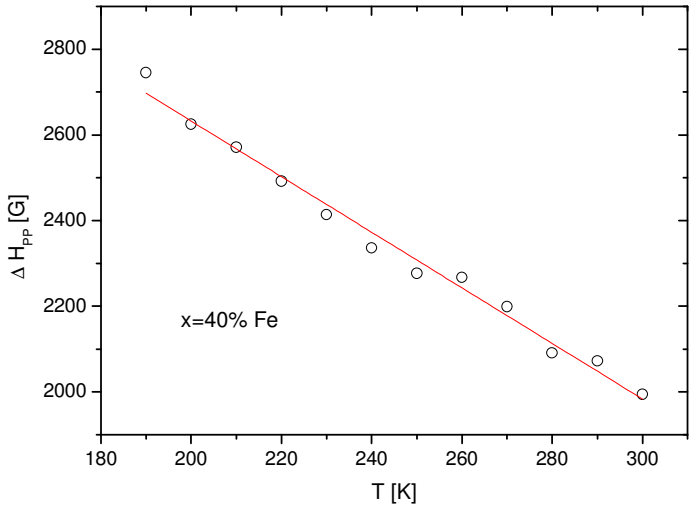

Fig. 5.52. Temperature dependence of the line width function of temperature for PVF_40 sample.

Figure 5.53 shows that the *g*-factor decreases with decreasing temperature, with a noticeable change observed about ~260 K and 200 K. The temperature change for the g-factor is $\Delta g/\Delta T = 1.95*10^{-3}$. The shift of g-factor and the decrease of ΔH_{pp} suggest the increase of the exchange interaction in the sample with x=40% Fe comparatively with the x=25% Fe sample.

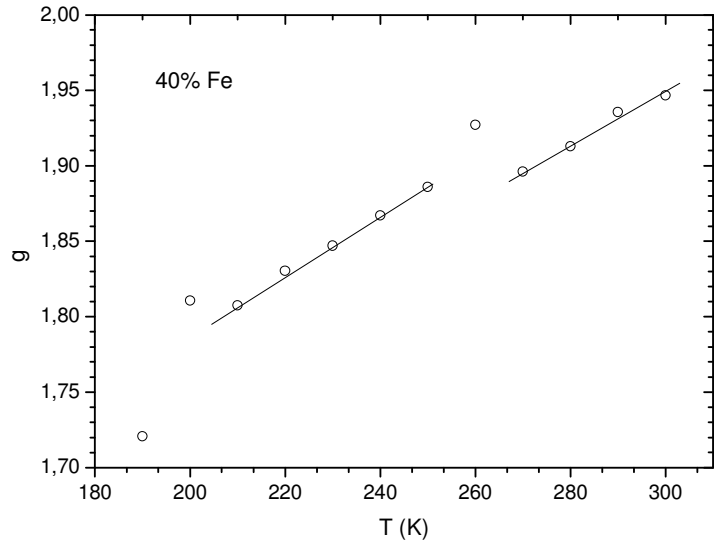

Fig. 5.53. Temperature dependence of the g – factor for sample PVF_40.

The double logarithmic plot of linewidth ΔH_{pp} versus a shift of resonance field ΔH_r (see Fig. 5.54) shows the existence of a single relaxation type with positive slope in the high temperature range (300-200 K).

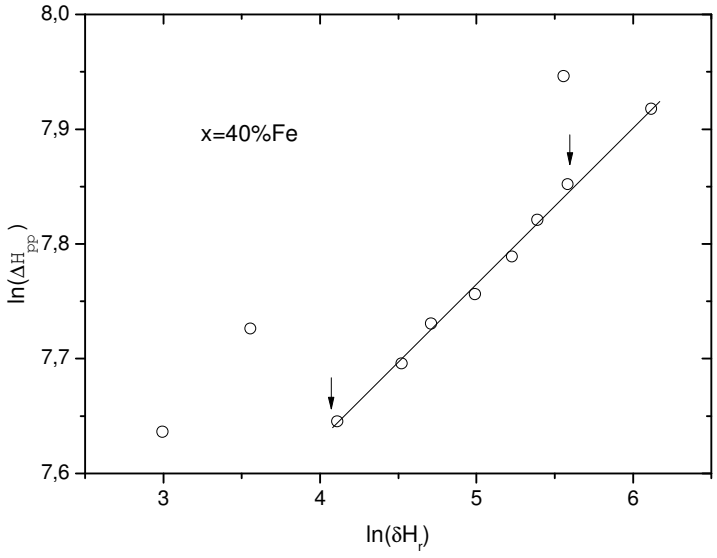

Fig. 5.54. Plot of ln(ΔH_{pp}) vs. ln(δHr) for sample PVF_40.

Figure 5.55 shows comparatively the fine structure of the $PbVO_3$ and of PVF_40 samples. The shift to lower fields of fine structure for x=40% Fe sample (PVF_40) suggest the existence of a different internal field because of the Fe ions. Most likely, the fine structure can be attributed to the vanadium ions.

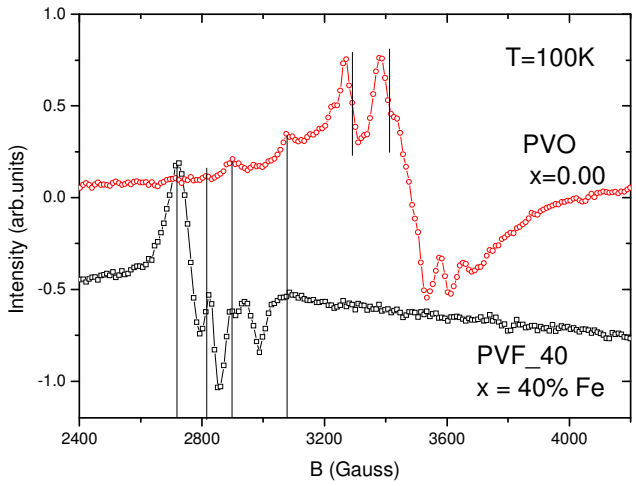

Fig. 5.55. Hyperfine structure of $PbVO_3$ and of the PVF_40 x=40%Fe samples.

Conclusions

1. EPR results function of temperature for $PbVO_3$ are consistent with the presence of V^{4+} paramagnetic ions in a square–pyramidal C_{4v} coordination (with hyperfine coupling constants $A_{\|}$ and $A_{\perp}$). The evolution of the hyperfine coupling constants function of temperature is in agreement with the small increase of unit cell height c with increase of the temperature.

2. The sharp variation of the EPR parameters with the temperature for the sample with x = 25% Ti is in relation with the presence of short range magnetic order, confined to distinct spatial regions.

a) The sharp increase of the linewidth at the temperature T = 194 K is similar to the behaviour of frustrated magnetic systems.

b) The competition between magnetic interaction and spin ordering processes could be responsible for the behaviour of the g-factor.

c) By analysing the linewidth and resonance field, three different relaxation mechanisms were evidenced with the decreasing temperature.

3. All resonance spectra function of temperature, for samples x=25% and 40% exhibit a broad line, centred on g=2 due to the spin of the Fe^{3+} ions.

a) For the x = 25%Fe sample, an additional resonant new absorption mode situated around g=4.2 was evidenced. It is attributed of the presence of Fe^{3+} ions on a tetrahedral environment with a strong rhombic distortion.

For sample with x=40% Fe, the superimposed hyperfine structure around g=2 can be attributed to the vanadium ions.

b) The large value of ΔH_{pp} is the result of strong magnetic dipolar interaction between the Fe^{3+} ions in both the x=25% and 40% Fe samples.

c) The shift of g-factor and the decrease of ΔH_{pp} suggest the increase of the exchange interaction in sample with x=40% Fe comparatively with the x=25% Fe sample.

d) The decrease of EPR line intensity attributed to Fe^{3+} paramagnetic centre with decreasing temperature, suggest the increase of the number of antiferromagnetic pairs Fe^{3+}-Fe^{3+}.

c) For the sample x=25% Fe two relaxation mechanisms were evidenced with a crossover temperature T_s around 175K, while for the x=40% Fe sample only a single relaxation type is present.

V.5. Characterization of electrical resistivity and dielectric constant of samples

A multiferroic material must present must present at least two types of order (magnetic and electric) so the investigation of the electric properties of a candidate to a new multiferroic is just as interesting and important as the investigation of its magnetic properties. The investigation of the electric properties of $PbVO_3$ (+ substitution samples) was conducted by means of electrical resistivity measurements and dielectric constant measurements. Resistivity measurements were made in order to confirm the high resistivity which is one of the requirements for a multiferroic. Dielectric constant measurements were performed in order to search for a possible ferroelectric transition since such a transition is usually accompanied by another transition in the dielectric constant [12].

V.5.1. Electrical resistivity

Electrical resistivity was measured by the 2 contacts method on $PbVO_3$ single crystals. Several measurement attempts were made on different crystals and at different setups before the optimum conditions for the measurements were found. We used a setup working in DC for measurements at low temperature (from RT to 4.2K) and another apparatus working in AC (at 10 kHz) for measurements at higher temperatures (from RT up to 500K). Details about the measurement principle are given in the experimental methods chapter. For the AC resistivity measurements, the model of a parallel RC circuit was used to describe the sample and calculate the ohmic resistivity component of impedance of the sample.

Figure 5.56 shows a picture of one of the $PbVO_3$ single crystals used for resistivity measurements.

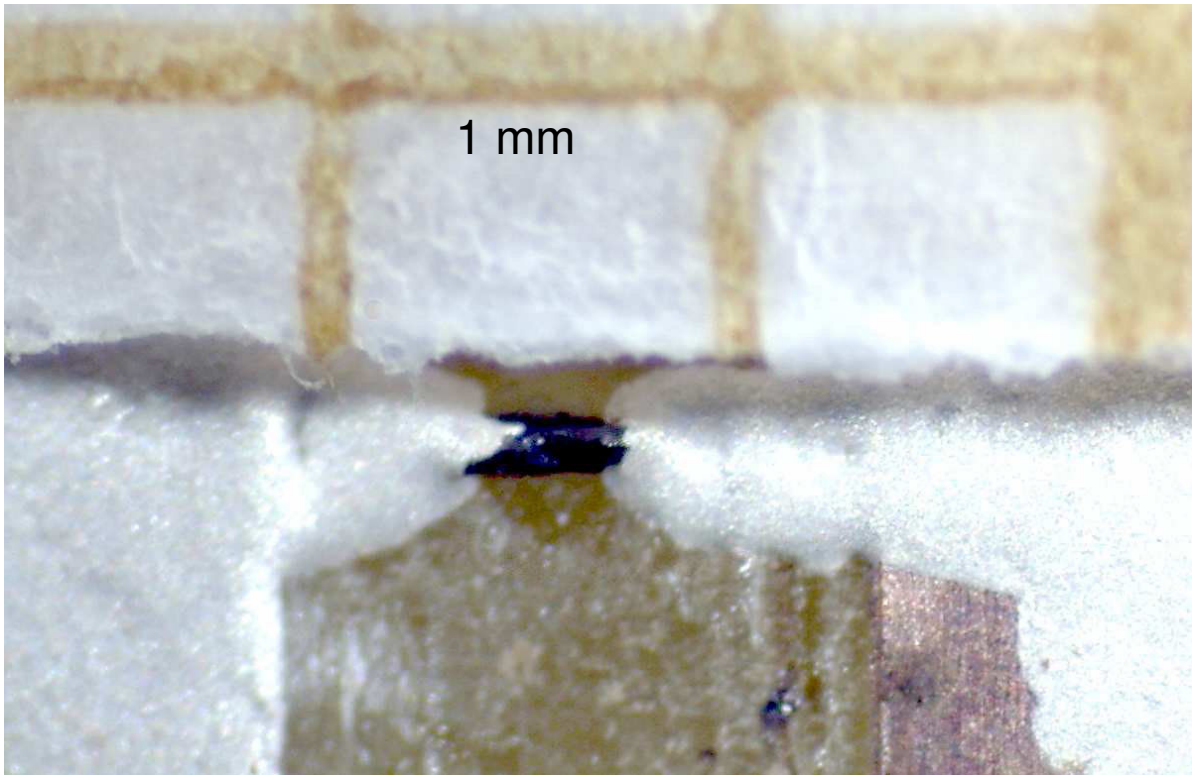

Fig. 5.56. $PbVO_3$ single crystal (black) with the two contacts made on each side with silver paste.

The crystal is placed on piece of PCB (printed circuit board) and silver paste is used to make contacts between the crystal and two traces on the PCB. A piece of millimetric paper was placed next to the crystal to give an estimation of the crystal's size.

The ρ(T) measurement revealed a semiconductor behaviour for the $PbVO_3$ sample with resistivity decreasing exponentially with the increase of temperature. Figure 5.57 shows the ρ(T) graph, obtained for a $PbVO_3$ single crystal in the low temperature domain. For the same measurement the ln(ρ) plot is also shown. Figure 5.58 shows the logarithmic plot of the resistivity measurement. The band gap energy was extracted from both representations in the following way:

For the ρ(T) graph, the energy band gap was returned by from the fit of the experimental data with the equation: $\rho = \rho_0 * \exp(Eg/2K_BT)$ where K_B is expressed in eV ($K_B = 8.61*10^{-5}$ eV/K). The band gap was also calculated from the ln(ρ) vs. 1/T plot. Considering that in this representation the equation for the resistivity becomes:

$\ln(\rho) = \ln(\rho_0) + Eg/2K_BT$ the slope of the graph is Eg/K_B. The gap energy is calculated from the slope of the graphic using $Eg = 2K_B$*slope.

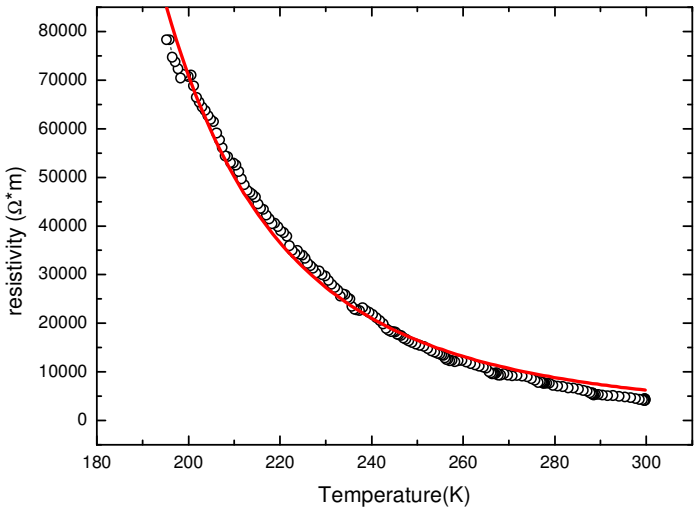

Fig. 5.57. Dependence of resistivity in function of temperature for a $PbVO_3$ single crystal. The hollow black dots represent the experimental data points and the red line is the exponential fit of the ρ(T) graph.

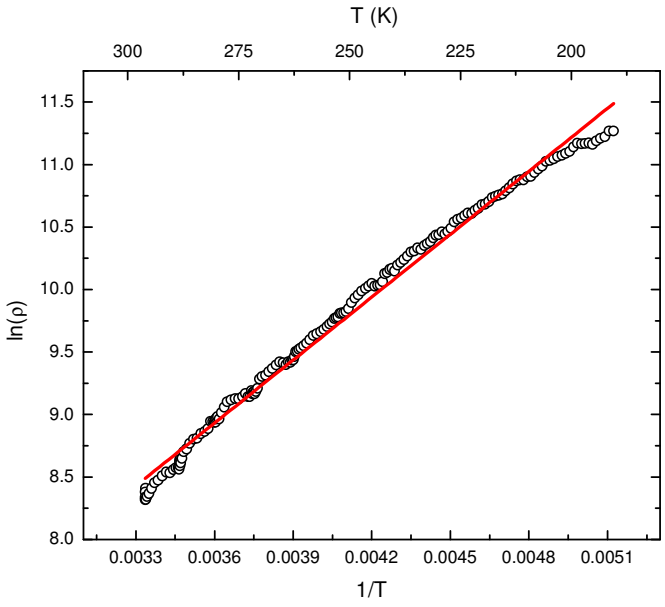

Fig. 5.58. ln(ρ) vs. 1/T plot for the low temperature part of the resistivity measurement.

The exponential fit for the resistivity data returns a gap energy for $PbVO_3$ of approximately 0.25(1) eV. The linear fit of the ln(ρ) data returns the value of the gap

energy as Eg = 0.28(8) eV. The difference is most likely caused by measurement errors which affect the quality of the fit and is therefore interpreted as the limit in the precision by which we could determine the gap energy.

For the same crystal (the same sample) the resistivity measured in the high temperature domain continues to present the semiconductor behaviour evidenced by the exponential decay of ρ with increasing temperature (figure 5.59.a) and the linearity of the ln(ρ) plot (figure 5.59.b).

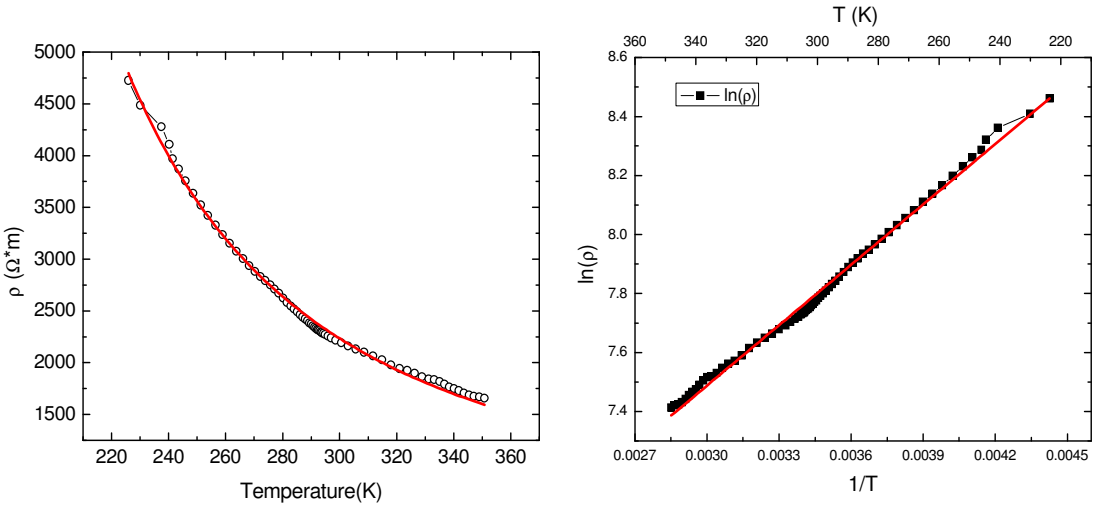

a) b)

Fig. 5.59. a) ρ (T) for high temperature domain of resistivity measurement, b) ln(R) in function of 1/T plot for $PbVO_3$ in the high temperature domain. Black points represent experimental data and the red line is the linear fit. The small fluctuations in the experimental data are caused by the instabilities in temperature.

Attempts to determine the band gap of the sample in the high temperature domain were made using the same equations as for the low temperature range, however, the results returned are not consistent with the value of the band gap obtained from the low temperature part nor with the observed semiconductor type behaviour of the sample's resistivity. The results of the band gap determinations are summarized in table 5.6.

Table 5.6. Band gap determination from ρ(T) and ln(ρ) vs. 1/T at different temperature domains and different setups

	Low T (DC)		High T (AC at 10 kHz)	
Fit	ρ (T)	ln(ρ)	ρ (T)	ln(ρ)
Eg (eV)	0.25(1)	0.28(8)	0.120(3)	0.11(7)

There are some drawbacks on the resistivity measurements.

Not all the measurements were made at the same setup. The temperature sensor is not placed relative to the sample in the exact same place in the two setups therefore there is an offset in temperature when comparing measurements performed at the two devices.

The resistance of the $PbVO_3$ sample at RT is in the order of magnitude of 100 MΩ. When the sample is cooled the resistance increases up to 1 GΩ. At that point the current flowing through the sample decreases to a few pA and can no longer be detected by the measuring equipment. This process begins to take place at approximately 200 K. Below 200 K the measurement saturates, as the detection limit of the ammeter is reached, and no further increase in the resistivity can be observed.

Potentially the most dangerous drawback arises from the way the contacts are made. The sample is a semiconductor but the contacts are metallic. In this way a metal-semiconductor junction is formed and this junction may work like a Schottky diode. There are two contacts therefore there are two diodes and worse still, these diodes are connected cathode to cathode. In this configuration each diode will block the current the other one normally allows to pass through so the circuit behaves like a good electrical insulator. A diagram of such a circuit is shown in figure 5.60.

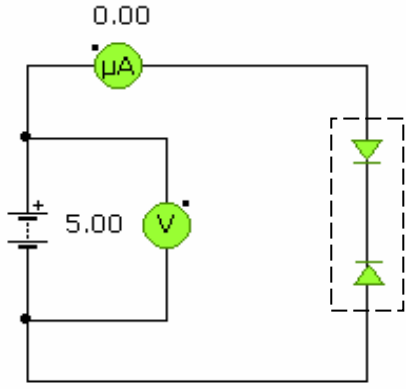

Fig. 5.60. Possible electric diagram of the circuit used to measure the resistivity of the $PbVO_3$ crystals. The sample (with the two contacts) is represented by the diodes surrounded by a dashed line.

Such a circuit could also explain the large resistance of the sample. Considering the possibility to (unwillingly) construct the circuit discussed above, the true characterization of the sample is obtained be registering the volt-ampere, I(V), characteristic of the sample. This was done by sweeping the voltage applied to the sample from -10 V to 10 V and measuring the current at a set temperature. The measure was repeated for temperatures from 300 K to 170 K for every 20 K. The results of these measurements are shown in figure 5.61. For simplicity of only 4 measurements are shown.

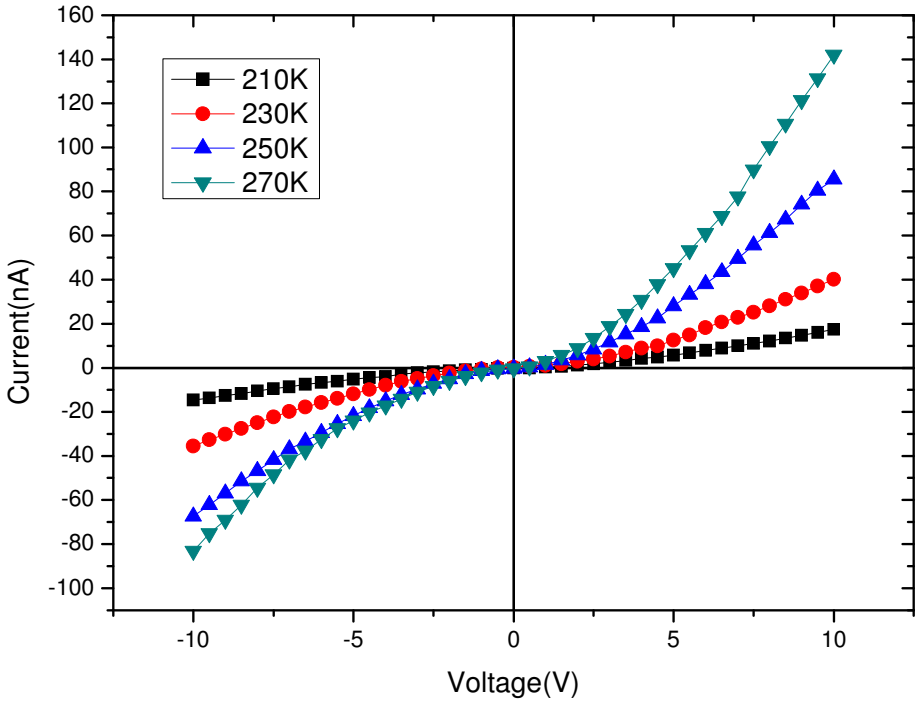

Fig. 5.61. I(V) characteristic of $PbVO_3$ single crystal with metal contacts.

The I(V) characteristic is non-linear and very close to the shape of an IV plot of a typical diode suggesting the fact that the metal contacts act indeed like diodes. On top of that the VA characteristic is not symmetric suggesting that the two diodes formed at the contacts are not equivalent. The formation of diodes at metal-semiconductor junctions is hard to avoid. One possibility is to use a 4 contact probe with asymmetrically placed contacts. However, for our sample this method might not be needed. The linear region of the I(V) curve indicates that the sample behaves like a resistor rather than a diode. The DC measurements were performed in the linear region of the I(V) so there measurements are reliable. The estimations of the gap energy from those measurements are therefore also reliable.

V.5.2. Polarization measurements

Considering that ferroelectric domains are expected in this structure and were indeed indirectly detected by single crystal diffraction, we attempted to switch the polarization with an electric field, i.e. to evidence a P-E hysteresis, and to measure the polarization for $PbVO_3$. In literature other similar attempts are reported [33] but generally the P-E hysteresis is hard to be evidenced. There are two reasons for that. Firstly, the spontaneous polarization of $PbVO_3$ is predicted to be very large, about 100-160 $\mu C/cm^2$ [31, 33, 35] and that would require large electric fields to turn the polarization. The second problem is related to the first one. Previous polarization measurement attempts were made on polycrystalline samples in the shape of sintered pellets but the electrical resistance of such pellets was too low to support the massive electric field so the pellets broke before the E field reached a high enough value [33].

We attempted to register a P-E hysteresis on a $PbVO_3$ single crystal using a Sawyer–Tower circuit. The result is shown in figure 5.62. The circuit was driven by a step up transformer that could output a voltage of about 1000 V. The length of the crystal was approximately 500 μm so the order of magnitude of the electric field applied had an intensity of about 2.10^6 V/m, far below the predicted 1.10^9 V/m field supposedly required to reach the saturation of the sample.

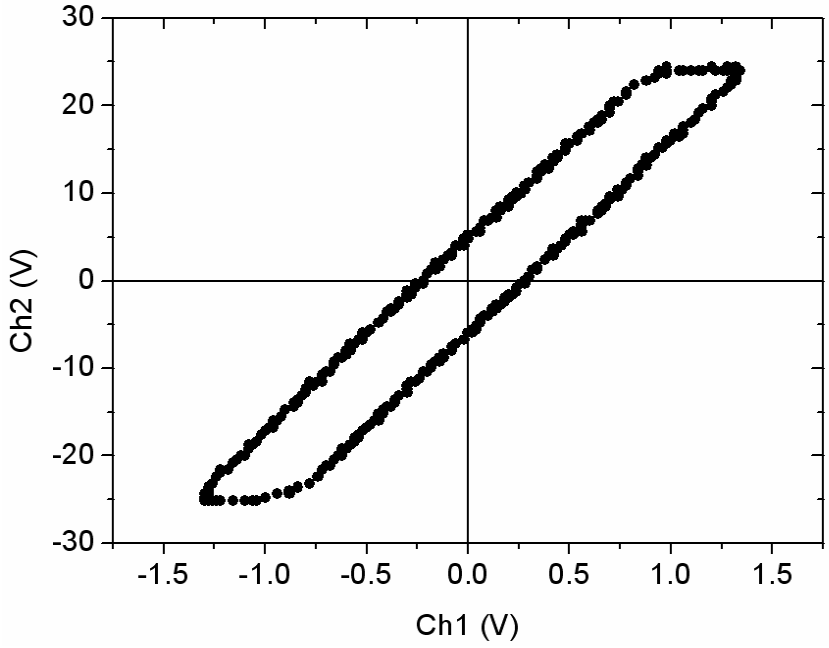

Fig. 5.62. Polarization hysteresis for $PbVO_3$. The measurement is made at RT with a frequency of the applied AC signal of 150 Hz.

On the above figure Ch1 (channel 1) is the voltage measured on the contacts to the sample and Ch2 is the voltage measured across the reference capacitor.

A hysteresis in the polarization can be observed. However the value of saturation polarization of $PbVO_3$ could not be reached and reasonable values for the applied field and electrical polarization could not be extracted from the raw signal, because of electronic equipment failure.

The result must be treated with caution anyway as it was evidenced by Dawber and Scott [124, 125] the Sawyer–Tower circuit can generate artefacts (the main drawback of the circuit). Moreover, a circuit made from cathode to cathode connected diodes, like the one discussed in the previous section, can also present a misleading P-E hysteresis.

V.5.3. Dielectric constant

Measurements of dielectric constant, ε_r, were performed on a small piece of sintered powder with the composition containing 40% Fe ($PbV_{0.6}Fe_{0.4}O_3$). In essence this measurement is conducted in the same manner in which the R(T) in AC measurements are registered. Again the impedance of the sample is measured and the sample is modelled with a parallel RC circuit for which the interesting value is the capacitance. With this setup the capacitance of the sample was measured in function of temperature at 3 different frequencies, at 1, 10 and 100 kHz. The evolution of the dielectric constant with the temperature and frequency is shown in figure 5.63. The evolution of tanδ is shown in figure 5.64.

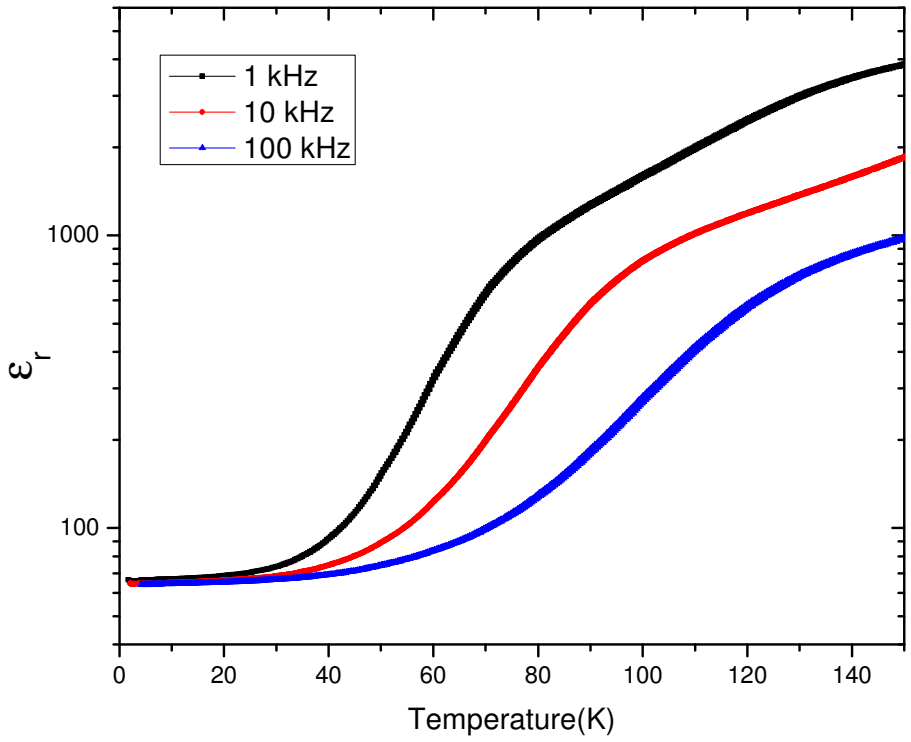

Fig. 5.63. Variation of dielectric constant with T at different frequencies for $PbV_{0.6}Fe_{0.4}O_3$ *(PVF_020).*

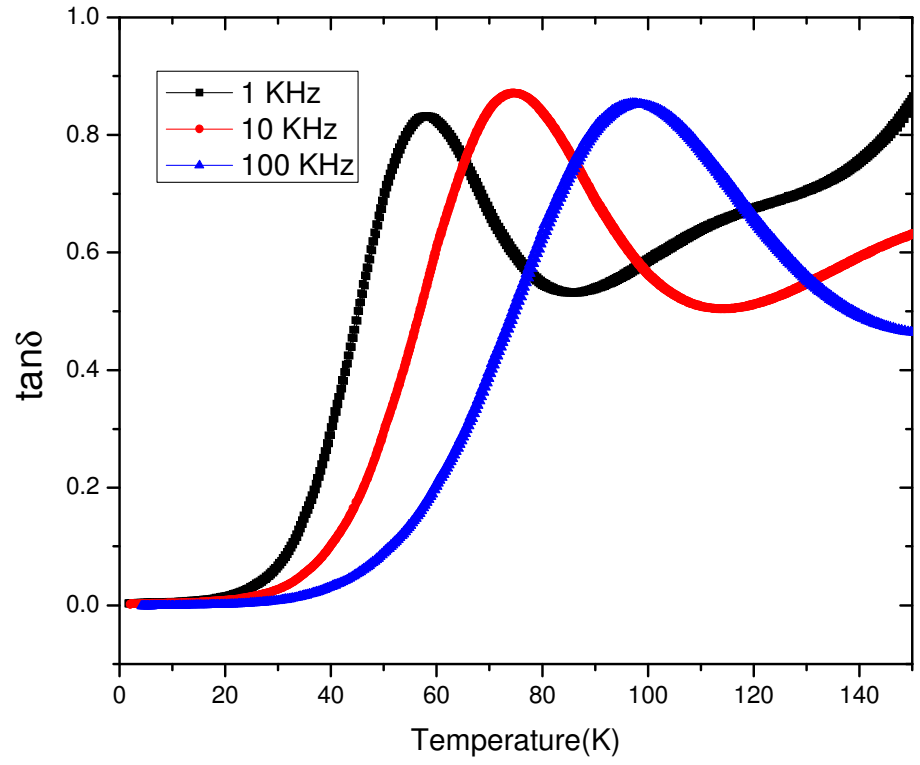

Fig. 5.64. Variation of tanδ in function of temperature and frequency for $PbV_{0.6}Fe_{0.4}O_3$ *(PVF_020).*

A board peak can be observed in the graph of tanδ and the position of the peak shifts towards higher temperatures as the frequency of the signal used for the measurement is increased. This is a typical behaviour of a ferroelectric relaxor.

Relaxor ferroelectrics, just like classic ferroelectrics present a hysteresis of the polarization with the applied electric field. The dielectric constant shows the ease at which the dipole moments change the direction on which they are aligned when the electric field is reversed.

As the temperature decreases the dipole moments begin to freeze and are consequently harder to turn by the electric field. The frequency response is determined by the small size of the polar domains, which characterizes a ferroelectric relaxor. One simple model which explains the frequency dependence is the dipole glass model proposed by Cross [126, 13]. The model supposes that the small size of the polar domains of a relaxor (several tens of nanometres) causes these domains to behave like superparaelectric domains by equivalence to the superparamagnetic domains from magnetism. Each domain has its own return frequency f_R. The frequency dependence becomes:

$f_R = f_0 * \exp(-E_A/K_BT)$ where E_A is the activation energy.

The maximum value for the dielectric constant is therefore obtained at the temperature for which $f = f_R$.

Conversely, the temperature shift of the maximum of the dielectric constant can be described using the relaxation time of the dipole moments with the equation:

$\tau = \tau_0 * \exp (E_A/K_BT)$

For the 40% Fe (PVF_020) sample, the plot of the relaxation time vs temperature of maximum and the fit with the Arrhenius law are shown below (figure 5.65).

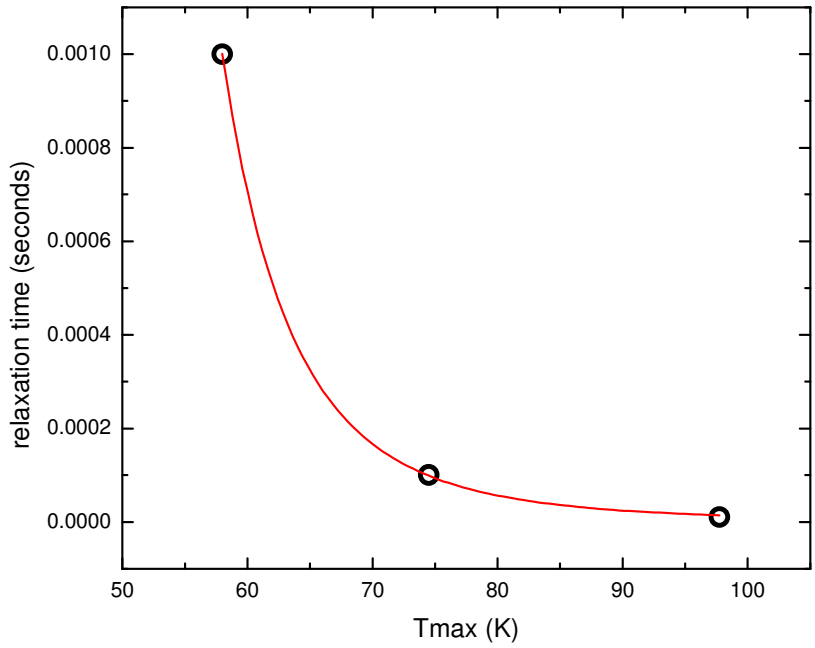

Fig. 5.65. Relaxation time vs. temperature of the maximum of the dielectric constant.

The values returned by the fit are E_A = 0.0522(1) eV and $\tau_0 \approx 2.89*10^{-8}$ s which is consistent with the values expected for a ferroelectric relaxor (E_A between 0.05 and 0.075 eV and τ_0 between $5*10^{-13}$ and $7*10^{-6}$ s) [127].

It is interesting to note that the departure material, the pristine $PbVO_3$ is a true ferroelectric. The long range ferroelectric ordering appears to be destroyed when V is substituted with Fe. This could be tentatively explained considering that ferroelectric relaxors are inhomogeneous materials presenting local structural fluctuations. The perovskite relaxors are almost always disordered crystals which contain some substitution (isovalent or not) at the B site cation. The compositional disorder is essential for the formation of a relaxor material. This is for example the case of $PbMn_{1/3}Nb_{2/3}O_3$.

$PbV_{1-x}Fe_xO_3$ (for x<0.5) contains 3 different cations at the B site, namely V^{4+}, V^{5+} and Fe^{3+} all presenting close ionic radii (0.53 Å for V^{4+}, 0.46 Å for V^{5+}, 0.58 Å for Fe^{3+}). The small differences of ionic radii could favour a random distribution of the cations which tends to reduce the tendency for long range ordering, possibly by a similar phenomenon as the one observed on Sr_2FeTiO_6 [127]. Also the presence of mixed valence states appears to favour the formation of a relaxor ferroelectric.

It should be noted that these B site cations have different coordination spheres which coupled with the random distribution of the cations could generate local structural fluctuations and small sizes of polar domains. Both these features are fingerprints of relaxor ferroelectrics.

The reduced size of the polar domains is known to be responsible for the transformation of other typical ferroelectrics to relaxor ferroelectrics. This is for example the case of the Pb-La substitution on $PbTiO_3$ [128, 129]. Although the substitution takes place at the A site it causes the development of vacancies at the B site and the reduction of the polar domain size.

A rough estimation of the size of the polar domains could be obtained from SEM imaging. From the pictures of the domains of $PbV_{0.6}Fe_{0.4}O_3$ (figures 5.66, 5.67) such domains can be visualized as the alternation of darker and lighter parallel stripes. It can be observed that indeed the domain size is limited to a few tens of nanometres, as expected for a ferroelectric material.

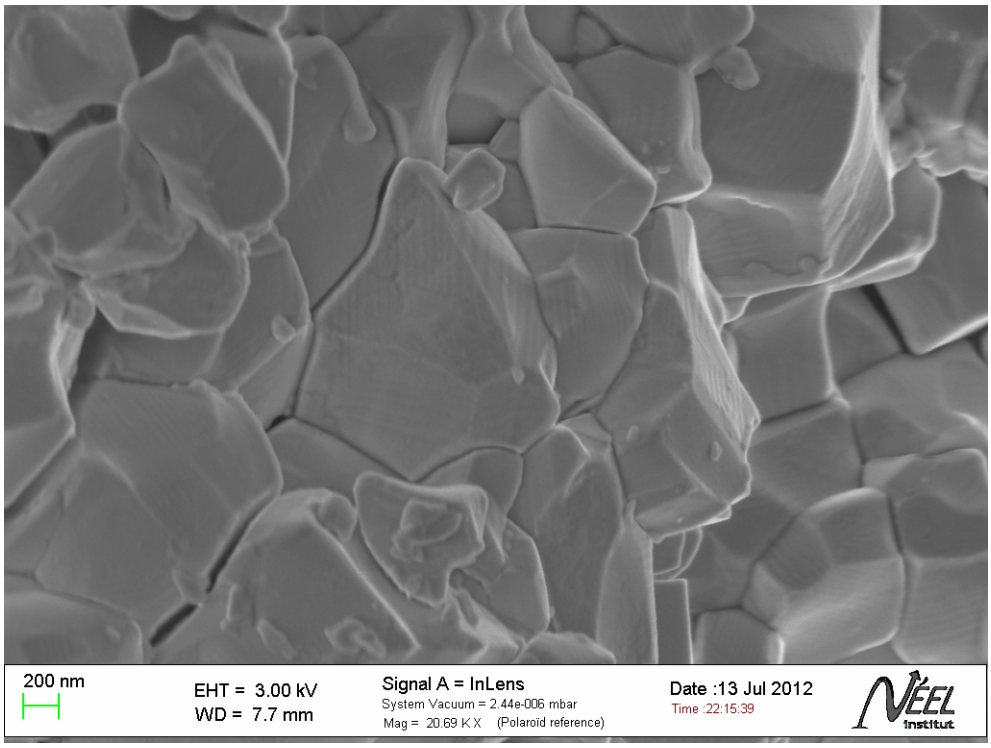

Fig. 5.66. Ferroelectric nano-sized domains in $PbV_{0.6}Fe_{0.4}O_3$ (PVF_010).

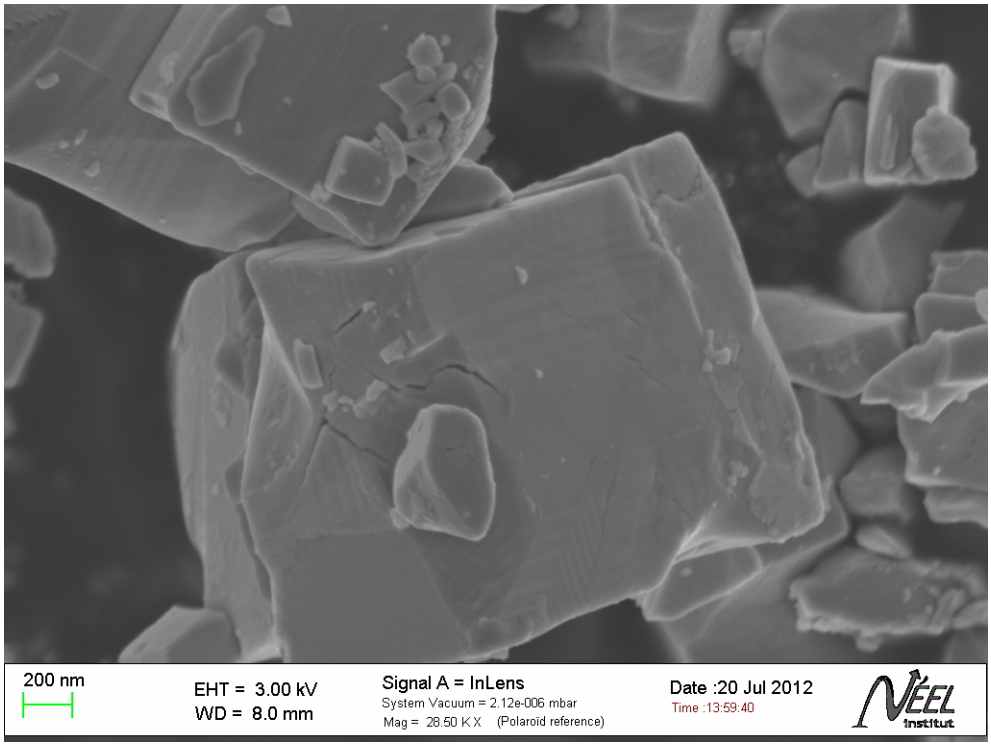

Fig. 5.67. Nanometre scale sized ferroelectric domains in $PbV_{0.6}Fe_{0.4}O_3$ *(PVF_014).*

V.5.4. Future directions

It would be very interesting to conduct a study of the evolution of the dielectric constant for samples from the Ti series. These samples form a solid solution between two known ferroelectric materials so an investigation of their electric properties might produce interesting results. The ferroelectric domains of samples from the Ti series (for example on $PbV_{0.4}Ti_{0.6}O_3$ shown in figure 5.68) are slightly larger than their counterparts from the Fe series but still on the same order of magnitude. It could be interesting to test whether this domain size also determines a relaxor behaviour…

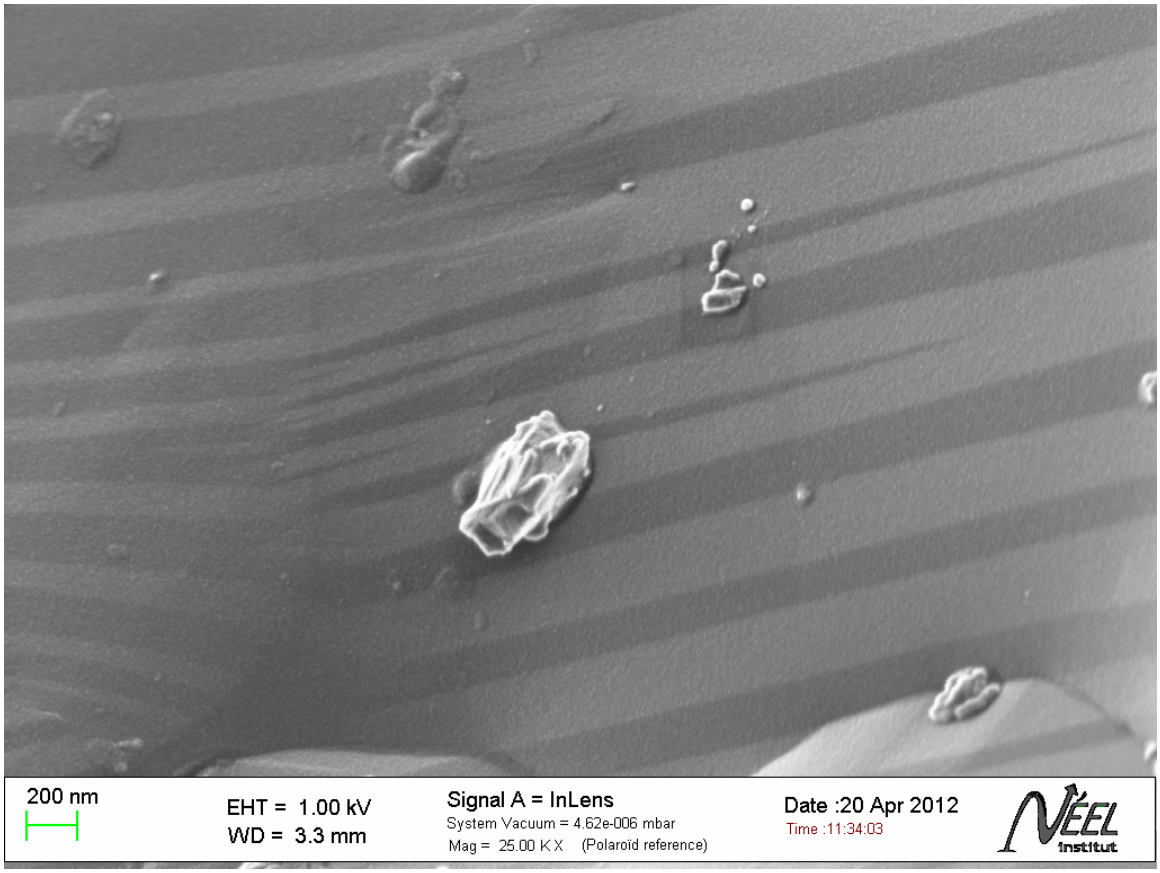

Fig. 5.68. Ferroelectric domains in $PbV_{0.4}Ti_{0.6}O_3$ (PVT_004).

Conclusions

1. Synthesis and chemical characterization:

Solid state reaction under HP-HT conditions (6 GPa and 950°C), and the hydrothermal method under HP-HT lead to practically single phase bulk $PbVO_3$ and $PbV_{1-x}M_xO_3$ (with M = Ti, Fe) compounds and $PbVO_3$ single crystals, respectively.

EDX method confirmed the nominal chemical composition of samples.

The knowledge of the oxidation states of V, M = Ti and Fe in $PbV_{1-x}M_xO_3$ is important for the explanation of the structural and magnetic properties of the samples. XAS investigations show that the partial substitution with Ti is isovalent (in Ti substituted samples Vanadium is 4+ oxidized), but the substitution with Fe is not isovalent (for the substitution sample with x=25 % at. Fe a mixture of V^{4+} and V^{5+} was evidenced).

2. Structure:

XRD data and a combination of XRD and NPD data led to a refined structure of samples.

X-Ray diffraction (XRD) data show that $PbVO_3$ sample crystallizes on the tetragonal space group P4mm with the lattice parameters a = 3.79 Å and c = 4.66 Å.

After the isovalent substitution (V with Ti), the samples maintain the tetragonal symmetry for all the Ti concentrations.

The non-isovalent substitution (V with Fe) lead to the decrease of the tetragonality structure by increasing x, and above x=50% Fe substitution of V a new cubic phase appears.

By using anisotropic broadening of the Bragg peaks (observed for all samples) the uniaxial strain and size effects were calculated. The crystallites are compressed and subjected to strain along the c* direction. For $PbVO_3$ sample the strain anisotropy (which is two times larger along the c axis as in (a, b) plane) has a pronounced effect on the peak broadening comparatively with the size anisotropy.

The strain effects are related to the presence of ferroelectric domains. The size effects were attributed to the reduced dimensions of coherent X-ray diffraction domains and to the increase of the number of defects.

Vanadium establishes a short vanadyl bond which places it on an off-centre distorted, 5 fold coordination, but Ti and Fe do not form an equivalent bond and hence tend to adopt a less distorted coordination.

Raman spectra of the $PbVO_3$ show the specific bands of non-centrosymmetric structure, space group P4/mm. The bands belonging the $V\text{-}O_1$ stretching with TO and LO components dominate the Raman spectra.

The length of the bond between the B site cation (V, Ti or Fe) and the apical oxygen depends on the nature of the B site cation and is also evidenced from Raman spectroscopy measurements.

3. Magnetic and dielectric properties:

The broad maximum of magnetic susceptibility vs. temperature for $PbVO_3$ and for sample with x=10% Ti is typical for 2D spin systems and the upturn at low temperatures is ascribed to the paramagnetic contribution of impurities and defects. The broad peak of the magnetic susceptibility curve is resonably fitted by the frustrated square lattice model (FSL).

In samples with Ti, the temperature dependence of the magnetic susceptibility is well fitted by using two contributions from 2D AFM model and from paramagnetic Curie-Weiss, respectively.

The fitting parameters (the decrease of the effective moment and Weiss temperature with increasing Ti content) reveal a decrease of the interactions between the magnetic moments, which is consistent with the dilution of magnetic moments.

The effect of partial substitution of V with Fe in $Pb(V_{1-x}Fe_x)O_3$ samples is the occurrence of both AFM and FM interactions (from temperature dependence of magnetic susceptibility measurements and the hysteresis in magnetisation curve) Specific heat measurements and NPD reveal no transition of any type. This suggests the formation of a spin glass system. The DC and AC susceptibility results also support the spin glass model. The formation of a spin glass system is explained by the disorder induced at the B site cation and by the different types of interactions between the magnetic cations which are themselves explained by the Goodnenough Kanamori rules.

EPR hyperfine structure of V^{4+} and the characteristic EPR signals for Fe^{3+} and Ti^{4+} substitution samples confirm the paramagnetic contribution evidenced in

susceptibility measurements and possibly traces of the 2D AFM magnetism of the Ti substituted samples.

The electrical resistivity for $PbVO_3$ single crystals yields a semiconductor behaviour with a gap energy of $E_A = 0.25 - 0.29$ eV.

An electric polarization hysteresis was evidenced for $PbVO_3$ single crystals confirming the ferroelectric nature of $PbVO_3$. However, the saturation value could not be reached.

For the $PbV_{0.6}Fe_{0.4}O_3$ compound measurements of dielectric constant indicate that the sample is a ferroelectric relaxor. The onset of the ferroelectric relaxor properties can be explained by inhomogeneities and local structural fluctuations which are caused by the disorder of the B site cations.

4. Perspectives:

The results presented here are, of course, not the end of the work as there are still many questions to be answered. As already mentioned it would be interesting (and important) to conduct a thorough investigation of the electric properties of the Ti substituted samples. It would also be interesting to grow single crystals of the substitution compounds and use the superior insulating properties of single crystals for polarization measurements. It would also be very interesting to conduct Mössbauer spectroscopy investigations on the Fe compounds as this technique could provide extremely valuable information about the magnetic structure of the sample.

References

1. J. Kreisel, Le défi du couplage entre magnétisme et ferroélectricité, *Reflets de la Physique*, 2008, 8, 10.

2. N. Hill, Why Are There so Few Magnetic Ferroelectrics?, *J. Phys. Chem. B*, *104,* 6694-6709, 2000.

3. L.W. Martin, Multiferroic and magnetoelectric heterostructures, *Acta Materialia*, 60, 2449–2470, 2012.

4. Eerenstein W., Multiferroic and magnetoelectric materials, *Nature*, 442:759, 2006.

5. C. Darie, Magnetic and crystal structures of $BiCrO_3$, *Solid State Sciences,* 2009.

6. F. Kubel, H. Schmid, Structure of a Ferroelectric and Ferroelastic Monodomain Crystal of the Perovskite $BiFeO_3$, *Acta. Cryst.,* B 46, 698-702, 1990.

7. D.L. Stein, Topical Review: Ordering and Broken Symmetry in Short-Range Spin Glasses, *Journal of Physics: Condensed Matter.,* 15, R1319 -- R1364, 2003.

8. http://inac.cea.fr/en/Phocea/Vie_des_labos/Ast/ast_visu.php?id_ast=508

9. http://www.physik.uni-leipzig.de/~janke/CompPhys08/Folien/Young.pdf

10. http://www.lorentzcenter.nl/lc/web/2006/172/moessnerP.pdf

11. Hidetoshi Nishimori, Statistical Physics of Spin Glasses and Information Processing - An Introduction, Clarendon Press Oxford, 2001.

12. Franco Jona, G. Shirane, Ferroelectric Crystals, Dover Publications, INC. New York, 1993.

13. Claire Laulhé, Structure locale dans un ferroélectrique relaxeur: $BaTi_{1-x}Zr_xO_3$, 2007.

14. Maxim Morozov, softening and hardening transitions in ferroelectric $Pb(Zr,Ti)O_3$ ceramics, thesis, 2005.

15. D.C. Agrawal, Ferroelectric ceramics – A Unique Class of Smart Materials, *App. Phy. Let.* 70, 138, 1997.

16. Charles D.E. Lakeman, Sol-gel processing of electrical and magnetic ceramic, *Materials Chemistry and Physics* 38, 305-324, 1994.

17. Seweryn Miga, Jan Dec and Wolfgang Kleemann, Non-Linear Dielectric Response of Ferroelectrics, Relaxors and Dipolar Glasses, *Ferroelectrics – Characterization and Modeling,* 2011. ISBN: 978-953-307-455-9.

18. Noel W. Thomas, A new framework for understanding relaxor ferroelectrics, *J. Phys. Chem. Solids,* 51, 2, 1419-1431, 1990.

19. Yuichi Shimakawa, Multiferroic Compounds with Double-Perovskite Structures, *Materials*, *4*, 153-168, 2011.

20. K.F. Wang, J.M. Liu, Z.F. Ren, Multiferroicity: the coupling between magnetic and polarization orders, *Advances in Physics,* 58, 4, 321-448, 2009.

21. S-W. Cheong, M. Mostovoy, Multiferroics: A magnetic twist for ferroelectricity. *Nature Mater.,* 6, 13–20, 2007.

22. D. J. Singh, Polar Behavior in a Magnetic Perovskite from *A*-Site Size Disorder: A Density Functional Study, *Physical Review Letters*, 100, 087601, 2008.

23. G Lawes, G Srinivasan, Introduction to magnetoelectric coupling and multiferroic films, *J. Phys. D: Appl. Phys.*, 44, 243001, 2011.

24. Ponniah Ravindran, Magnetic-Instability-Induced Giant Magnetoelectric Coupling, *Adv. Mater.,* 20, 1353–1356, 2008.

25. N. Hur, S. Park, Electric polarization reversal and memory in a multiferroic material induced by magnetic fields, *Nature,* 429, 2004.

26. Jennifer A. Rodgers, High-pressure / High-temperature Synthesis of Transition, Metal Oxide Perovskites, *Z. Naturforsch.*, 61b, 1515 – 1526, 2006.

27. Liu Hongbo, Investigation of New Multiferroic Materials with Coexistence of Several Ferroic and Structural Instabilities, thesis, 2012.

28. H. Béa, M. Gajek, M. Bibes, A. Barthélémy, Spintronics with multiferroics, *J. Phys.: Condens. Matter.,* 20, 434221, 2008.

29. http://en.wikipedia.org/wiki/Multiferroics

30. http://www.readcube.com/articles/10.1038/nmat1868?locale=en

31. P. Bordet, C. Bougerol, C. Brachet, S. de Brion, G. Chouteau , F. Hipper, J. Kreisel, « Recherche par Synthèse haute pression de Nouvelles Perovskites Multiferroïques de Type (Bi,Pb)MO_3, (M=métal de transition) », Meeting of the GDR NEEM, Aspet, France, 29 June-2 July 2004.

32. Roman V. Shpanchenko, Synthesis, Structure, and Properties of New Perovskite $PbVO_3$, *Chem. Mater.,* 16, 3267-3273**,** 2004.

33. Alexei A. Belik, Crystallographic Features and Tetragonal Phase Stability of $PbVO_3$, a New Member of $PbTiO_3$ Family, *Chem. Mater.,* 17, 269-273**,** 2005.

34. Alexander Tsirlin, Frustrated spin 1/2 square lattice in layered perovskite $PbVO_3$, *Physical Review B,* 77, 092402, 2008.

35. Lane W. Martin, Growth and structure of $PbVO_3$ thin films, *Applied Physics Letters,* 90, 062903, 2007.

36. Amit Kumar, Lane W. Martin, Polar and magnetic properties of $PbVO_3$ thin films, *Physical Review B,* 75, 060101(R), 2007.

37. Kengo Oka, Magnetic Ground-State of Perovskite $PbVO_3$ with Large Tetragonal Distortion, *Inorg. Chem.,* 47, 7355-7359, 2008.

38. Atahar Parveen, Thermal properties of a novel compound $PbVO_3$, *Journal of Physics: Conference Series,* 377, 012059, 2012.

39. Wei Zhou, Structural properties of $PbVO_3$ perovskites under hydrostatic pressure conditions up to 10.6 GPa, *J. Phys. Condens. Matter.*, 24, 435403, 2012.

40. Takeshi Tsuchiya, High-pressure synthesis and characterization of a novel perovskite $PbFe_{1/2}V_{1/2}O_3$, *Journal of Ceramic Society of Japan,* 117 [1] 102-105, 2009.

41. Angel Arévalo-Lopez, Miguel Alario-Franco, Structural Percolation in the $PbM_{1-x}M'_xO_3$ (M, M' =Ti, Cr, and V), *Perovskites Inorg. Chem.,* 50, 7136–7141, 2011.

42. Glazer A. M., Powder Profile Refinement of Lead Zirconate Titanate at Several Temperatures. II. Pure $PbTiO_3$, *Acta. Cryst.,* B34, 1065-1070, 1978.

43. Yoshitaka Uratani, First principles on the Magnetic Anisotropy in Multiferroic $PbVO_3$ and $BiCoO_3$, *Journal of the Physical Society of Japan,* 78, 8, 084709, 2009.

44. I. V. Solovyev, Magnetic structure of the noncentrosymmetric perovskites $PbVO_3$ and $BiCoO_3$: Theoretical analysis, *Physical Review B,* 85, 054420, 2012.

45. Xing Ming, First-Principles comparative study of multiferroic compound $PbVO_3$, *Solid State Sciences,* 12, 938-945, 2010.

46. Aleksandar S. Miloševic, An ab initio study of electronic structure and optical properties of multiferroic perovskites $PbVO_3$ and $BiCoO_3$, *Optical Materials,* 2013.

47. http://www.microscopy.ethz.ch/bragg.htm

48. http://chemwiki.ucdavis.edu/Analytical_Chemistry/Instrumental_Analysis/Diffraction/Powder_X-ray_Diffraction

49. http://www.doitpoms.ac.uk/tlplib/xray-diffraction/powder.php

50. Pierre Bordet, Affinement de diagrams de diffraction de poudres par la méthode de Rietvled, 18^{e} Formation Permanente Diffraction Par Les Materiaux Polycristallins, 2009.

51. http://www.ncnr.nist.gov/AnnualReport/FY2003_html/RH2/

52. http://www.ill.eu/instruments-support/instruments roups/instruments/d1b/description/instrument-layout/

53. http://www.purdue.edu/rem/rs/sem.htm

54. http://www.ammrf.org.au/myscope/sem/background/concepts/interactions.php

55. http://nptel.iitm.ac.in/courses/103106075/Courses/Lecture39.html

56. http://fr.wikipedia.org/wiki/Microscopie_%C3%A9lectronique_%C3%A0_balayage

57. http://en.wikipedia.org/wiki/Energy-dispersive_X-ray_spectroscopy

58. http://www.nrel.gov/pv/measurements/xray_energy_loss.html

59. http://www.microscopy.org/images/posters/Castaing.pdf

60. W. Jansen, M. Slaughter, Elemental mapping of minerals by electron microprobe, American Mineralogist, 67, 521-533, 1982.

61. http://www.cmp.liv.ac.uk/frink/thesis/thesis/node60.html

62. http://www.gitam.edu/eresource/Engg_Phys/semester_2/supercon/appl.htm

63. http://fr.wikipedia.org/wiki/Circuit_de_Sawyer-Tower

64. http://en.wikipedia.org/wiki/Electron_paramagnetic_resonance

65. http://en.wikipedia.org/wiki/Raman_spectroscopy

66. H. Tracy Hall, Ultra-High-Pressure, High-Temperature Apparatus: the "Belt", *The Review of Scientific Instruments*, 31, 125-131, 1960.

67. Céline Goujon, Quoi de neuf sur la Haute Pression au MCMF ?, Journées du département MCMF 11 et 12 Juin 2007.

68. C. Goujon, M. Legendre, A new differential thermal analysis setup for measuring high pressure phase transitions, *High Pressure Research,* 31, 375-387, 2011.

69. L. G. Khvostantsev Vereshchagin L.F., Novikov A.P., Device of Toroid for high pressure generation, *High Temp. High Press.,* 9, 639-639, 1977.

70. http://www.hppi.troitsk.ru/products/conac_n.htm

71. http://www.hppi.troitsk.ru/products/Toroid2/Toroid1.htm

72. N.A. Nikolaev and M.D. Shalimov, Device for producing superhigh pressure and temperature, Patent SU1332598, 1990.

73. L.G. Khvostantsev,V.N. Slesarev, andV.V. Brazhkin, Toroid type high-pressure device: history and prospects, *High Press. Res.,* 24, pp. 371–383, 2004.

74. John N. Lalena, David A. Cleary, Everett E. Carpenter, Nancy F. Dean – Inorganic Materials Synthesis and Fabrication - John Wiley & Sons, Inc. Hoboken, New Jersey, 2008.

75. http://ltl.tkk.fi/research/theory/typicalpt.html

76. J.M. Kiat, Structural Study of Lead Ortophoshpovanadates: Role of the Electron Lone Pairs in the Phase Transitions, *Journal of Solid state chemistry,* 103, 490-503, 1993.

77. J.M. Kiat, P. Garnier, M. Pinot, Neutron and X-Ray Rietveld analysis of the Three Phases of Lead Orthovanadate $Pb_3V_2O_8$, *Journal of Solid State Chemistry,* 91, 399-349, 1991.

78. J.M. Cowley, Electron-Diffraction Study of the Structure of Basic Lead Carbonate, $2PbCO_3 \bullet Pb(OH)_2$, *Acta Cryst.,* 9, 391-396, 1956.

79. A.J.M. Duisenberg, L.M.J. Kroon-Batenburg and A.M.M. Schreurs, An intensity evaluation method: *EVAL*-14, *J. Appl. Cryst.* 36, 220-229, 2003.

80. Sheldrick, G. M. (1996). *SADABS.* University of Göttingen, Germany.

81. Petricek,V., Dusek,M. & Palatinus,L.(2006). Jana2006. The crystallographic computing system. Institute of Physics, Praha, Czech Republic.

82. http://www.ill.eu/sites/fullprof/

83. O. Mentre, F. Abraham, New mixed valence compounds in the Pb-V-O system: Synthesis and Crystal Structure of Hollandite-Related $Pb_{1.32}V_{8.35}O_{16.7}$ and *R*-Type Hexagonal Ferrite PbV_6O_{11}, *Journal of Solid State Chemistry,* 125**,** 91–101, 1996.

84. Montre Olivier Mentre, Anne - Claire Dhaussy, Francis Abraham, Effect of Iron Substitution on the Structural, Electric, and Magnetic Properties in *R*-Type $PbFe_xV_{6-x}O_{11}$, a Frustrated System, *Journal of Solid State Chemistry 130,* 223-233, 1997.

85. Thompson, Cox and Hastings, Rietveld Refinement of Debye-Scherrer Synchrotron X-ray Data from $A1_2O_3$, *J. Appl. Cryst.,* 20, 79, (1987).

86. P. W. Stephens, Phenomenological model of anisotropic peak broadening in powder diffraction, *J. Appl. Cryst.,* 32, 281-289, 1999.

87. Frantti J., S. Ivanov, S. Eriksson, Phase transitions of $Pb(Zr_xTi_{1-x})O_3$ ceramics, *Physical Review B,* 66, 064108, 2002.

88. Gavrilyachenko V.G. et al, Sov. Phys. Solid State, 12, 1203, 1970.

89. E. Ching-Prado, A. Reynes-Figueroa, R.S. Katiyar, S.B. Majimder, and D.C. Agrawal, Raman spectroscopy and X-ray diffraction of $PbTiO_3$ thin films, *J. Appl. Phys.,* 78, 1920-1925, 1995.

90. D. Valim, A.G. Sauza Filho, P.T.C. Freire, J. Mendes Filho, C.A. Guavany, R.N. Reispaud, and E.B. Araujo, Evaluating the residual stress in $PbTiO_3$ thin films prepared by a polymeric chemical method, *J. Phys. D: Appl. Phys.,* 37, 744-747, 2004.

91. J.A. Sanjurjo, E. Lopez-Cruz, and G. Burns, High-pressure Raman study of zone-center phononos in $PbTiO_3$, *Phys. Rev. B,* 28, 7260-7268, 1983.

92. F. Cerdeira, W.B. Holzapfel, and D. Bauerle, Effect of pressure on the zone-center phonons of $PbTiO_3$ and on the ferroelectric-paraelectric phase transition, *Phys. Rev. B,* 11, 1188-1192, 1975.

93. D. Fu, T. Ogawa, H. Suzuki, and K. Ishikawa, Thickness dependence of stress in lead titanate thin films deposited on Pt-coated Si, *Appl. Phys. Lett.,* 77, 1532-1534, 2000.

94. A.-D. Li, D. Wu, C.-Z. Ge, P. Lu, W.-H. Ma, M.-S. Zhang, C.-Y. Xu, J. Zuo, and N.-B. Ming, Raman spectroscopy and X-ray diffraction study of $PbTiO_3$ thin films prepared by sol-gel technique, *J. Appl. Phys.,* 85, 2146-2150, 1999.

95. P.S. Dobal, S. Bhaskar, S.B. Majamder, and R.S. Katiyar, Micro-Raman investigation of stress variations in lead titanate films on sapphire, *J. Appl. Phys.,* 86, 828-834, 1999.

96. L. Sun, Y.F. Chen, L. He, C.Z. Ge, D.S. Ding, T. Yu, M.-S. Zhang, and N.B. Ming, Phonon mode hardening in epitaxial $PbTiO_3$ ferroelectric thin films, *Phys. Rev. B,* 55, 12218-12222, 1997.

97. S.-H. Lee, H.M. Jang, S.M. Cho, and G.-C. Yi, Polarized Raman scattering of epitaxial $PbTiO_3$ thin film with coexisting c and a domains, *Appl. Phys. Lett.,* 80, 17, 3165-3167, 2002.

98. H. Zheng, J. Kreisel, Y.H. Chu, R. Ramesh, and L. Salamanca-Riba, Heteroepitaxially enhanced magnetic anisotropy in $BaTiO_3$-$CoFe_2O_4$ nanostructures, *Appl. Phys. Lett.,* 90, 113113 1-3, 2007.

99. I.A. Kornev, L. Bellaiche, P. Bouvier, P.E. Janolin, B. Dkhil, and J. Kreisel, Ferroelectricity of perovskites under Pressure, *Phys. Rev. Lett.,* 95, 196804 1-4, 2005.

100. I.A. Kornev and L. Bellaiche, The nature of ferroelectricity under pressure, *Phase Transitions,* 80, 385-413, 2007.

101. G.A. Samara and E.L. Venturini, Ferroelectric/relaxor crossover in compositionally disordered perovksites, *Phase transitions,* 79, 21-40, 2006.

102. Ausrine Bartasyte, Raman Spectroscopy and X-ray Diffraction Studies of Stress Effects in $PbTiO_3$ Thin Films, *IEEE Transactions on Ultrasonics Ferroelectrics and Frequency Control,* 54, 2623-2631, 2007.

103. S.D. Cheng, Sol-gel derived nanocrystalline thin films of $PbTiO_3$ on glass substrate, *Thin Solid Films,* 375, 109-113, 2000.

104. Emre Erdem, Size effects in Fe^{3+}-doped $PbTiO_3$ nanocrystals—Formation and orientation of $Fe_{Ti} – V_O$ defect dipoles, *Journal of the European Ceramic Society,* 30, 289–293, 2010.

105. A. Bartasyte, Domain structure and Raman modes in $PbTiO_3$, *Phase Transitions*, 84, 509–520, 2011.

106. Enrique Eduardo Kaul, Experimental Investigation of New Low-Dimensional Spin Systems in Vanadium Oxides, thesis, 2005.

107. H. Rosner, High-temperature expansions for the J1-J2 Heisenberg models: Applications to *ab initio* calculated models for Li_2VOSiO_4 and Li_2VOGeO_4, *Physical Review B,* 67, 014416, 2003.

108. J. A. Mydosh, Spin Glass an Experimental Introduction, Taylor and Francis, London, 1993.

109. http://people.virginia.edu/~saw6b/summerschool/pdf/dionne.pdf

110. O. Cozar, I. Ardelean, IR and EPR studies on some lithium-borate glasses with vanadium ions, *Journal of molecular structure,* 563-564, 421-425, 2001.

111. O. R. Nascimento, C. J. Magon, Magnetic Resonance Study of Vanadium Pentoxide Gels, *Molecular Crystals and Liquid Crystals,* 447, 1, 233-242, 2006.

112. A. Agarwall, A. Sheoran, Structural investigation and electron paramagnetic resonance of vanadyl doped alkali niobium borate glasses, *Spectrochimica Acta, Part A,* 75, 3, 964-969, 2010.

113. R. P. Sreekanth Chakradhar, A study of electron paramagnetic resonance and optical absorption spectra of VO^{2+} ions in alkali calcium borate glasses, *Physica B,* 293, 1-2, 108-117, 2000.

114. N. Vedeanu, O. Cozar, I. Ardelean, V. Ioncu, Raman and EPR investigation of some lead-phosphate glasses with vanadium and copper ions, *Journal of Otpelectronics and Adv.Mat.*, 9, 4, 844-847, 2007.

115. K. Wakabayashi, M. Fujita, Electronic and magnetic properties of nanographite ribbons, *Phys. Rev. B*, 59, 12, 8271-8282, 1999.

116. V. Rode, Unconventional magnetism in all-carbon nanofoam, *Phys. Rev. B,* 70, 054407, 2004.

117. F. A. Garcia, P. Marques-Ferreira, Effects of La-substitution on the magnetic properties of the $Ba_{1-x}La_x(Ti_{1/2}Mn_{1/2})O_3$ (x= 0.0, 0.1) 12R-type Perovskite, *arXiv: 1206.3813v1 [cond-mat .str-el]8 Jul.2012.*

118. N.Guskos, EPR study of $Cd_4Fe_8V_{10}O_{41}$ vanadate, *J. Appl. Phys.*101,103922, 2007.

119. Gouskos, EPR study of Ti-Si-C-N system, Rev. Adv. Mater. Sci. 23, 189-195, 2010.

120. Grommen R, Manikandan P, Geometry and Framework Interactions of Zeolite-Encapsulated Copper(II)-Histidine Complexes, *J. Am. Chem. Soc.,* 122, 11488-11496, 2000.

121. Lin DH, Coudurier G, Vedrine J, Zeolites: Facts, Figures and Future, Proc 8'th Int. Zeolite Conf., Amsterdam, The Netherlands, July 10–14 1989, *Elsevier, Amsterdam,* Stud. Surf. Sci. Catal. 49, 1431, 1989.

122. Bert M.Weckhuysen, Ralf Heidler, Electron Spin Resonance Spectroscopy, *Mol. Sieves* 4, 295–335, 2004.

123. John A. Weil, James R. Bolton, and John E. Wertz - Electron Spin Resonance: Elementary Theory and Practical Applications - John Wiley & Sons, New York, 1994.

124. M. Dawber, A classroom experiment to demonstrate ferroelectric hysteresis, *Am. J. Phys.*, 71, 819-822, 2003.

125. J. F. Scott, Ferroelectrics go bananas, *J. Phys.: Condens. Matter*, 20, 021001, 2008.

126. L.E. Cross, Ferroelectrics, 76, 241, 1987.

127. P. Neenu Lekshmi, Room temperature relaxor ferroelectricity and spin glass behavior in Sr_2FeTiO_6 double perovskite, *Journal of Alloys and Compounds*, 522, 90– 95, 2012.

128. Hyun M. Jang, Nano-sized polar clusters with tetragonal symmetry in $PbTiO_3$-based relaxor ferroelectrics, *Solid State Communications,* 127, 645–648, 2003.

129. Tae-Yong Kim, Short-ranged clusters with tetragonal symmetry in La modified $PbTiO_3$ relaxor ferroelectrics, *Solid State Communications,* 119, 527-532, 2001.

Acknowledgements

It is not just a duty and an honour, but also a great joy for me to give my acknowledgements to all of those who, one way or another have contributed to the conclusion of this work.

I feel honoured and indebt to express my respect and gratitude towards the entire team of true professionals which were my model to follow and towards the friends I made who were the shoulder upon which I relied.

A special tank you is reserved for Professor Dr. Aurel POP for the long hours of conversations and wonderful explanations needed for structuring the work and data interpretation, for the time and effort he invested, for the painstaking work, for his patience and for maintaining a good working atmosphere even when I made severe mistakes.

I would like to thank Professor Dr. Pierre BORDET for leading me through the basis of crystallography, refinements, computers and virtually every scientific (or not) topic I brought to discussion. I also thank him for the patience he has proven during the long hours of conversation.

Special thank you-s also go to Professor Dr. Claire COLIN who introduced me to practically every type of measurement that was ever conducted during this thesis, from the relatively simple ones (like the switching of electrical polarization), passing through the SQUID and going all the way to really sophisticated measurements (XAS or specific heat).

I would now like to step over to the microscopy side and send a special tank you to Professor Dr. Céline DARIE for introducing me to the wonderful Jeol SEM and for teaching me almost everything I know about using a SEM and trusting me. I also owe Professor Céline DARIE another thank you for the synthesis of our samples.

Again on the realm of crystallography, I would like to address a big thank you to Dr. Olivier LEYNAUD, for the patience he had while handling the cumbersome tiny $PbVO_3$ crystal, but also for the patience in showing me any mechanism I might have been interested on.

Of course I cannot forget to thank Professor Dr. Sébastien PAIRIS for teaching me with endless patience and understanding everything I know about the scanning electron microscopy, that I have not learned from Professor Céline DARIE.

There is yet one more microscopist, to whom I owe many, many, thank you-s, and I am talking here about Professor Dr. Stéphanie KODJIKIAN, who helped me overcome my fears of failure and introduced me to the electron diffraction technique.

I would also like to thank my other mentors on magnetization measurements, Dr. Eric EYRAUD and Dr. Didier DUFEU.

Stepping to the closely related field of measurements of dielectrical properties, I owe many thanks to Professor Dr. Jacques MARCUS and Professor Dr. Frédéric GAY, for the patience they had handing my delicate samples and for staying extra hours when I needed their help. I sincerely thank them for the effort. Following the same thread I would like to thank Dr. Jérôme DEBRAY for his much needed help at constructing mirror-like polished surfaces on sintered samples used during dielectric measurements.

I also want to thank Dr. Murielle LEGENDRE and Dr. Céline GOUJON for the effort they invested on repairing the HP-HT equipments over and over again. Without their hard work the research could not have been possible.

Another big thank you goes to Professor Dr. Pierre STROBEL for every synthesis that was not carried out under HP – HT conditions and for the help with chemistry related problems and annealing treatments.

I owe a big thank you to Professor Dr. Olivier ISNARD for handling the paperwork and the organizing problems.

A lot of effort was (and still is) invested on Mössbauer spectroscopy measurements and for this I express my gratitude to Professor Dr. Bernard MALAMAN.

I want to thank Prof. Dr. Laurent RANNO for the effort and long hours spent in the attempt to synthesize $PbVO_3$ thin film samples by using the PLD technique.

I am sincerely thankful to all the persons from the staff of the big instruments, the ILL and the ESRF, professors and engineers for their hard work and dedication, for their long, late, extra-hours spent supervising and programming the sophisticated instruments. Without their sacrifice we would have never obtained the answers we were seeking.

On the Romanian team I would like to thank Professor Dr. Viorel POP for introducing me to the French laboratory.

I sincerely thank professors Prof. Dr. Nicolae LEOPOLD and Prof. Dr. Vasile CHIS for their hard and stubborn work against the unmanageable Raman spectroscopy data.

Furthermore I would like to thank Professor Dr. Marin COLDEA for the strong interest manifested towards our research, interest that was matched by the help provided on the interpretation of magnetic measurements.

For further productive discussion and clarifications on the contradicting magnetic properties displayed by our samples I would like to bring a big thank you to Professor Dr. Iosif DEAC.

I am also deeply thankful to Professor Dr. Daniel ANDREICA for his interest and his efforts invested in the acquisition of new types of experimental data.

Also I would like to think Dr. Oana RAITA and Dr. Ovidiu PANA for their hard work at the acquisition and interpretation of EPR data and other data which shed a new light on the subject of $PbVO_3$ and open the door on new perspectives of research on this material.

Lastly, I cannot forget to thank Dr. Daniel MARCONI for good advices and practical help in bringing the work to its final form.

For all the things mentioned I thank everybody one more time. And one other thing, equally important: I thank all for the trust they bestowed in me (although there were some moments which did not fully justified it), for the patience they had with me, and the understanding they proved, even during tensioned and stressful moments; for their encouragements, for their scolding, for all they gave me, for all they took from me, for all I have stolen from them, because I have seen and understood side by side with them what team work means and what research means and what is the meaning of a common purpose.

Paraphrasing Antoine de Saint-Exupéry who used to say: “Aimer, n’est pas se regarder l’un l’autre, mais regarder tous les deux dans la même direction” I can certainly say that I am a privileged of fate because I had the chance to watch in the same direction with my mentors in the field of research, even for an, unfortunately limited, period of time.

List of publications and conferences

Publications:

1. Alexandru Okos, Aurel Pop, Céline Darie, Pierre Bordet, High pressure - high temperature synthesis and phase characterization of $PbVO_3$ perovskite compound, STUDIA UBB CHEMIA, LVIII, 3, p 57-62, 2013.

2. Alexandru Okos, Aurel Pop, Céline Darie, Pierre Bordet, Crystal structures and microstrucutres of $PbV_{1-x}Fe_xO_3$ perovskites with $x \leq 0.3$, accepted for publication in Optoelectronics and Advanced Materials.

3. Alexandru Okos, Aurel Pop, Céline Darie, Pierre Bordet, The influence of partial substitution of V with Fe on structure, phase purity and microstructure of the multiferroic $Pb(V_{1-x}Fe_x)O_3$ compound, accepted for publication in STUDIA UBB PHYSICA.

Conferences:

1. Alexandru Okos, Claire V. Colin, Murielle Legendre, Olivier Leynaud, Sébastien Pairis, Aurel Pop, Pierre Bordet and Céline Darie, "Synthèse haute pression, structure, propriétés physiques de $Pb(V,A)O_3$, A = Fe,Ti", 13-ième Journées de la Matière Condensée (JMC 13), Montpellier 27-31 Août 2012.